

**SLIDING SHEAR BEHAVIOUR  
OF  
FIBREGLASS RETROFITTED  
CONCRETE MASONRY**

**IN PLANE SLIDING SHEAR BEHAVIOUR  
OF  
UNREINFORCED CONCRETE MASONRY  
RETROFITTED WITH  
SURFACE-BONDED FIBREGLASS LAMINATES**

By  
**FRANCESCO M. CAMPANARO, B.Eng.**

A Report  
Submitted to the School of Graduate Studies  
in Partial Fulfilment of the Requirements  
for the Degree  
Master of Engineering (M.Eng.)

McMaster University  
© Copyright by Francesco M. Campanaro, November 2006



*To my dear Uncle Gino...*

*Who unfortunately passed away in March, 2001 while I was pursuing my undergraduate degree. Uncle Gino was the closest to a grandfather I've ever had, and I was the closest to a son he ever had. Many years ago he once told me: "Before I die I want to see you become someone." I know he'd be proud of me today.*

*Per il mio caro Zio Gino...*

*Che purtroppo ha lasciato questa terra in Marzo, 2001 mentre stavo perseguire il mio grado di studente non laureato. Zio Gino era per me come un nonno, e io per lui come un figlio. Molti anni fa, mi disse: "Prima che io muoio desidero vederti diventare qualcuno." So che sarebbe oggi fiero di me.*

MASTER OF ENGINEERING (2006)  
(Civil Engineering)

McMASTER UNIVERSITY  
Hamilton, Ontario

TITLE: In Plane Sliding Shear Behaviour of Unreinforced Concrete Masonry  
Retrofitted with Surface-Bonded Fibreglass Laminates

AUTHOR: Francesco M. Campanaro, B.Eng. (McMaster University, 2003)

SUPERVISOR: Dr. Robert G. Drysdale (McMaster University)  
Dr. Ahmad A. Hamid (Drexel University)

NUMBER OF PAGES: xii, 182

## ABSTRACT

Lateral loads on buildings, either caused by wind or seismic events, are resisted primarily by the in-plane strength and stiffness of the walls oriented parallel to the direction of the applied load. The concern associated with relying on unreinforced masonry (URM) shear walls to transfer the load to the foundation is that the typical modes of failure are characterized by brittle behaviour, with rapid decreases in capacity and very limited deformations once the ultimate load is reached.

Traditional strengthening techniques have several undesirable properties, including being labour intensive and adding weight to the structure. Past research has shown that fibre reinforced polymer (FRP) reinforcement is an effective method of increasing both the strength and ductility of URM. One of the most desirable properties of FRP is that it has a high strength to weight ratio.

An experimental investigation was conducted to study the influence of surface-bonded fibreglass laminates on the sliding shear resistance of URM. The investigation was conducted in three phases:

**1 Phase One:** Analyzing the performance of five different test specimen shapes retrofitted with GFRP to determine the most adequate configuration for further shear slip tests. The data was also of direct use as an evaluation of strength and behaviour of FRP reinforced masonry subjected to shear-slip failure. Thirty-seven shear slip specimens were tested to failure. The average increase in shear strength ranged from 3.1 to 7.7 times that of the unretrofitted counterparts.

- 2 **Phase Two:** Assessing the feasibility of obtaining two sets to data from each test specimen.
- 3 **Phase Three:** Assessing the shear-slip strength and behaviour of URM reinforced with fibreglass mesh, of different weights, adhered at two different orientations to the bed joint slip planes ( $0^{\circ}/90^{\circ}$ ,  $\pm 45^{\circ}$ ) using a modified mortar parging. Twenty-one shear slip specimens were tested to failure. Typically, for any given mesh weight, orienting the fibres at  $\pm 45^{\circ}$  resulted in failure characterized by higher strength and less ductility compared to tests with fibres oriented at  $0^{\circ}/90^{\circ}$  to the bed joints. At  $\pm 45^{\circ}$  orientation, the fibres ruptured at failure. When the mesh was oriented at  $0^{\circ}/90^{\circ}$ , the fibres pulled out of the cement parging, which limited the strength, but enabled specimens to undergo large deformations while maintaining fairly constant residual capacity.

## ACKNOWLEDGEMENTS

I wish to express my appreciation to Dr. Robert Drysdale (co-supervisor), Dr. Ahmad Hamid (co-supervisor), and Dr. Wael El-Dakhakhni for their advice, encouragement and insight during the experimental work and the writing of this report. Thank you to Dr. Ghani Razaqpur for being the second reader of this report and providing valuable comments.

Special thanks go to Edward Fyfe and Peter Milligan of Fyfe Co., San Diego, California for their donation of the Tyfo® WEB Composite and the Tyfo® S Epoxy, the Ontario Masonry Contractors' Association and the Canada Masonry Centre for the mason's time, and Boehmers for the donation of the concrete blocks. The financial support for this research from the ORDCF funded Centre for Effective Design of Structures at McMaster University is gratefully acknowledged.

I would also like to thank all the professors who have taught me during my time as an undergraduate and graduate student. They have all contributed to my success.

Many thanks to McMaster University technicians Bernard Nieuwenhuis, Dave Perrett, Maurice Forget and Peter Koudys, and fellow graduate students Shawn Miller Cameron Baker and Marwan Shedid, who were always willing and able to provide either a helping hand, technical advice or a good laugh. Many thanks to fellow graduate student Daman Panesar for being my unofficial psychiatrist. No matter how busy, she would always take the time to listen to my problems and ease the frustrations which inevitably come when undertaking graduate work.

I also wish to thank my current employer, the Canada Masonry Centre, for allowing me to work part-time upon completion of my Master of Engineering degree. Last, but not least, thank you to my family for their patience and support during my undergraduate and graduate career.

Thanks a million, everyone! I couldn't have done it without you!

*Francesco M. Campanaro*

## TABLE OF CONTENTS

	<b>PAGE</b>
<i>Abstract</i>	<i>ii</i>
<i>Acknowledgments</i>	<i>iv</i>
<i>Table of Contents</i>	<i>v</i>
<i>List of Figures</i>	<i>viii</i>
<i>List of Tables</i>	<i>xii</i>
<b><i>Chapter 1: Introduction</i></b>	<b><i>1</i></b>
1.1 Background	1
1.2 Fibre Reinforced Polymers (FRPs)	7
1.2.1 History	7
1.2.2 General	8
1.3 Fibre Cement Matrix (FCM)	10
1.4 Codes and Standards	11
1.5 Research Objectives	12
1.6 Literature Review	13
1.6.1 Shear Slip Failure of URM	13
1.6.2 Masonry Sub-Assemblages Strengthened with FRP	16
1.6.3 Full-Scale Masonry Walls Strengthened with FRP	19
1.6.4 Full-Scale Masonry In-Fill Walls Strengthened with FRP	22
1.6.5 Other Research	24
1.7 Conclusion	24
<b><i>Chapter 2: Design and Construction of Test Specimens</i></b>	<b><i>26</i></b>
2.1 Introduction	26
2.2 Phase One	27
2.2.1 Specimen Types and Designation	27
2.2.2 Construction and Preparation of Phase One Test Specimens	31
2.2.3 Material Properties	36
2.2.4 Test Setup and Instrumentation	41
2.3 Phase Two Primer	46
2.4 Phase Three	46
2.4.1 Specimen Types and Designation	46
2.4.2 Construction and Preparation of the Test Specimens	48
2.4.3 Material Properties	53
2.4.4 Test Setup and Instrumentation	55
2.5 Phase Two	58
2.6 Summary	59

**Chapter 3: Phase One and Two Experimental Results** **61**

3.1	Introduction	61
	<b><u>PHASE ONE</u></b>	62
3.2	A – 0.5 Specimens	62
	3.2.1 Unreinforced (AU – 0.5)	62
	3.2.2 Reinforced (AR – 0.5)	63
3.3	A – 1.5 Specimens	65
	3.3.1 Unreinforced (AU – 1.5)	65
	3.3.2 Reinforced (AR – 1.5)	67
3.4	A – 2.5 Specimens	71
	3.4.1 Unreinforced (AU – 2.5)	71
	3.4.2 Reinforced (AR – 2.5)	72
3.5	T – 0.5 Specimens	74
	3.5.1 Unreinforced (TU – 0.5)	74
	3.5.2 Reinforced (TR – 0.5)	75
3.6	T – 1.5 Specimens	77
	3.6.1 Unreinforced (TU – 1.5)	77
	3.6.2 Reinforced (TR – 1.5)	79
3.7	Discussion of Phase One Experimental Results	81
3.8	Selection of Specimen Configuration	83
	<b><u>PHASE TWO</u></b>	87
3.9	Phase Two Experimental Results	87
	3.9.1 Specimen 1: Test 1 –Epoxy Applied 4.5 oz./yd. <sup>2</sup> and 15 oz./yd. <sup>2</sup> Mesh at 0°/90° (No applied clamping force)	87
	3.9.2 Specimen 2: Test 1 – Epoxy Applied 4.5 oz./yd. <sup>2</sup> and 15 oz./yd. <sup>2</sup> Mesh at 0°/90° (15 oz./yd. <sup>2</sup> mesh reinforced slip planes clamped)	89
	3.9.3 Specimen 2: Test 2 – Epoxy Applied 4.5 oz./yd. <sup>2</sup> and 15 oz./yd. <sup>2</sup> Mesh at 0°/90° (Damaged 4.5 oz./yd. <sup>2</sup> mesh reinforced slip planes repaired)	91
	3.9.4 Specimen 3: Test 1 – Mortar Parging Applied 4.5 oz./yd. <sup>2</sup> and 15 oz./yd. <sup>2</sup> Mesh at 0°/90° (No applied clamping force)	94
	3.9.5 Specimen 4: Test 1 – Mortar Parging Applied 4.5 oz./yd. <sup>2</sup> and 15 oz./yd. <sup>2</sup> Mesh at 0°/90° (15 oz./yd. <sup>2</sup> mesh reinforced slip planes clamped)	96
	3.9.6 Phase Two Conclusions	97
3.10	Summary	98

**Chapter 4: Phase Three Experimental Results** **100**

4.1	Introduction	100
4.2	Introduction of Typical Phase Three Crack Patterns	100
4.3	Specimens Retrofitted with 4.5 oz. Mesh Oriented at 0°/90° to the Bed Joints	101
4.4	Specimens Retrofitted with 4.5 oz. Mesh Oriented	103

	at $\pm 45^\circ$ to the Bed Joints	
4.5	Specimens Retrofitted with 6 oz. Mesh Oriented at $0^\circ/90^\circ$ to the Bed Joints	105
4.6	Specimens Retrofitted with 6 oz. Mesh Oriented at $\pm 45^\circ$ to the Bed Joints	106
4.7	Specimens Retrofitted with 9 oz. Mesh Oriented at $0^\circ/90^\circ$ to the Bed Joints	108
4.8	Specimens Retrofitted with 9 oz. Mesh Oriented at $\pm 45^\circ$ to the Bed Joints	110
4.9	Specimens Retrofitted with 12 oz. Mesh Oriented at $0^\circ/90^\circ$ to the Bed Joints	112
4.10	Failure Modes of the Strengthened Specimens	114
4.11	Influence of Fibre Weight with Fibre Orientation	120
	4.11.1 Fibres at $\pm 45^\circ$ Orientation	120
	4.11.2 Fibres at $0^\circ/90^\circ$ Orientation	124
4.12	Summary	126
<b><i>Chapter 5: Conclusions and Recommendations</i></b>		<b>129</b>
5.1	Final Summary	129
5.2	Comparison of Experimental Results with Code Equations	131
5.3	Conclusions and Recommendations	136
5.4	Suggestions for Future Research	137
<b><i>References</i></b>		<b>139</b>
<b><i>Appendix A: Material Data Sheets</i></b>		<b>144</b>
<b><i>Appendix B: Finite Element Analysis</i></b>		<b>152</b>
B.1	Introduction	152
B.2	Finite Element Analysis Details	152
B.3	Shear Stress Along Slip Planes	153
B.4	Normal Stress Along Slip Planes	157
B.5	Revised Finite Element Analysis	160
B.6	Conclusion	162
<b><i>Appendix C: Raw Experimental Data</i></b>		<b>162</b>
C.1	Introduction	162
C.2	Phase One Raw Data	162
C.3	Phase Three Raw Data	174



## LIST OF FIGURES

FIGURE	PAGE
<i>Chapter 1: Introduction</i>	
1.1 Behaviour of Unreinforced Masonry Under Combined Shear And Normal Stress Along the Mortared Bed Joints	5
1.2 Failure Modes of Unreinforced Masonry Shear Walls	6
<i>Chapter 2: Design and Construction of Test Specimens</i>	
2.1(a) Phase One Test Specimens: A-0.5 Specimen	28
2.1(b) Phase One Test Specimens: A-1.5 Specimen	28
2.1(c) Phase One Test Specimens: A-2.5 Specimen	28
2.1(d) Phase One Test Specimens: T-0.5 Specimen	29
2.1(e) Phase One Test Specimens: T-1.5 Specimen	29
2.2 Phase One Specimen Labelling Sample	31
2.3 Construction of Phase One Specimens	34
2.4 Excess Mortar Removed from Open Head Joints	35
2.5 Process of Applying GFRP to Phase One Specimens	37
2.6 Tests to Determine Mortar Properties	40
2.7 Grouted End Cells	41
2.8 Tinius Olsen Testing Machine	42
2.9 Phase One Mechanical Displacement Gauge Setup for Smaller Specimens	43
2.10 Customized Testing Apparatus	44
2.11 Phase One LPDT Setup for Larger Specimens	45
2.12 Phase Three Fibreglass Mesh	49
2.13 Shear Deformation and Tension Stresses Along the Bed Joints During Testing	51
2.14 Strong Fibre Direction Per Quadrant	51
2.15 Application of Glass Mesh Using Modified Parging	54
2.16 Phase Three LPDT Setup for All Specimens	57
2.17 15 oz./yd.2 (Finished Weight) Mesh	58
2.18 Phase Two Mesh Reinforcement Scheme	59
<i>Chapter 3: Phase One and Two Experimental Results</i>	
3.1 Specimen AU-0.5: Load/Metre versus Displacement	63
3.2 Typical Damage Along Slip Plane of Reinforced A-0.5 Specimen	64
3.3 Specimen AR-0.5: Load/Metre versus Displacement	65

3.4	Typical Failure Mode of AU–1.5 Specimens	66
3.5	Block Crushing at Lower Support Point of Specimen AU–1.5–1	66
3.6	Specimen AU–1.5: Load/Metre versus Displacement	67
3.7	Block Crushing at Lower Support Point of Specimen AR–1.5–1	68
3.8	Damaged GFRP for Specimen AR–1.5– 2	69
3.9	Block Crushing at Lower Support Point of Specimen AR–1.5–2	69
3.10	Damaged GFRP for Specimen AR–1.5– 3	70
3.11	Specimen AR–1.5: Load/Metre versus Displacement	71
3.12	Specimen AU–2.5: Load/Metre versus Displacement	72
3.13	Typical Block Crushing at Lower Support Point of Specimen AR–2.5	72
3.14	Specimen AR–2.5: Load/Metre versus Displacement	73
3.15	Typical Failure Mode of TU–0.5 Specimens	74
3.16	Specimen TU–0.5: Load/Metre versus Displacement	75
3.17	Typical Damage Along Slip Plane of Reinforced TR–0.5 Specimen	76
3.18	Damaged GFRP for TR–0.5 Specimens	76
3.19	Specimen TR–0.5: Load/Metre versus Displacement	77
3.20	Typical Failure Mode of TU– 1.5 Specimens	78
3.21	Specimen TU–1.5: Load/Metre versus Displacement	78
3.22	Minor damage to GFRP Along Bed Joint (Prior to Full Fabric Tearing)	79
3.23	Typical Failure Modes of TR–1.5 Specimens	80
3.24	Specimen TR–1.5: Load/Metre versus Displacement	80
3.25	Schematic Diagram of Shear Force Distribution	83
3.26	Atkinson et al. (1998) Shear Slip Specimens	86
3.27	Load/Metre vs. Average Displacement of Epoxy Applied 4.5 oz./yd. <sup>2</sup> and 15 oz./yd. <sup>2</sup> Mesh at 0/90° (No applied clamping force)	88
3.28	Damage of Epoxied Mesh Applied at 0°/90°	88
3.29	Clamping Apparatus	90
3.30	Load/Metre vs. Average Displacement of Epoxy Applied 4.5 oz./yd. <sup>2</sup> and 15 oz./yd. <sup>2</sup> Mesh at 0/90° (15 oz./yd. <sup>2</sup> mesh reinforced slip planes clamped)	90
3.31	Repaired Specimen	91
3.32	Load/Metre vs. Average Displacement of Epoxy Applied 4.5 oz./yd. <sup>2</sup> and 15 oz./yd. <sup>2</sup> Mesh at 0/90° (Damaged 4.5 oz./yd. <sup>2</sup> mesh reinforced slip planes repaired)	92
3.33	Damaged Epoxied 15 oz./yd. <sup>2</sup> Mesh Applied at 0°/90°	93
3.34	Load/Metre vs. Average Displacement of Mortar Parging Applied 4.5 oz./yd. <sup>2</sup> and 15 oz./yd. <sup>2</sup> Mesh at 0/90° (No applied clamping force)	94
3.35	Damage to Mortar Applied Mesh at 0°/90° from Specimen 3, Test 1	95
3.36	Load/Metre vs. Average Displacement of Mortar Parging Applied 4.5 oz./yd. <sup>2</sup> and 15 oz./yd. <sup>2</sup> Mesh at 0/90° (15 oz./yd. <sup>2</sup> mesh reinforced slip planes clamped)	97

#### ***Chapter 4: Phase Three Experimental Results***

4.1	Typical Phase Three Specimen Crack Patterns	101
4.2	Load/Metre vs. Average Displacement (4.5 oz./yd. <sup>2</sup> mesh at 0°/90°)	102
4.3	Typical Torn Fibre Damage of Bed Joints Reinforced with 4.5 oz. Mesh at 0°/90°	103
4.4	Load/Metre vs. Average Displacement (4.5 oz./yd. <sup>2</sup> mesh at ±45°)	104
4.5	Typical Torn Fibre Damage of Bed Joints Reinforced with 4.5 oz. Mesh at ±45°	104
4.6	Load/Metre vs. Average Displacement (6 oz./yd. <sup>2</sup> mesh at 0°/90°)	105
4.7	Typical Damage of Bed Joints Reinforced with 6 oz./yd. <sup>2</sup> mesh at 0°/90°	106
4.8	Load/Metre vs. Average Displacement (6 oz./yd. <sup>2</sup> mesh at ±45°)	107
4.9	Typical Torn Fibre Damage of Bed Joints Reinforced with 6.0 oz. Mesh at ±45°	108
4.10	Load/Metre vs. Average Displacement (9 oz./yd. <sup>2</sup> mesh at 0°/90°)	109
4.11	Typical Damage of Bed Joints Reinforced with 9 oz. Mesh at 0°/90°	110
4.12	Load/Metre vs. Average Displacement (9 oz./yd. <sup>2</sup> mesh at ±45°)	111
4.13	Typical Torn Fibre Damage of Bed Joints Reinforced with 9 oz. Mesh at ±45°	112
4.14	Load/Metre vs. Average Displacement (12 oz./yd. <sup>2</sup> mesh at 0°/90°)	113
4.15	Typical Damage of Bed Joints Reinforced with 12 oz. Mesh at 0°/90°	113
4.16	Average Load/Metre vs. Average Displacement Curves for 0°/90° Mesh	115
4.17	Average Load/Metre vs. Average Displacement Curves for ±45° Mesh	115
4.18	Average Load/Metre vs. Mesh Weight for ±45° Fibre Orientation	120
4.19	Resolved Force Components	121
4.20	Average Load/Metre vs. Mesh Weight for 0°/90° Fibre Orientation	124
4.21	Fibreglass Mesh Weaves	127

#### ***Appendix A: Material Data Sheets***

A.1	Fibreglass Cloth	144
A.2	Epoxy	146
A.3	4.5 oz./yd. <sup>2</sup> (Finished Weight) Fibreglass Mesh	148
A.4	6 oz./yd. <sup>2</sup> (Finished Weight) Fibreglass Mesh	149
A.5	12 oz./yd. <sup>2</sup> (Finished Weight) Fibreglass Mesh	150
A.6	Modified Mortar Parging	151

#### ***Appendix B: Finite Element Analysis***

B.1	Specimen A–0.5: Shear Stress Distribution Along Slip Planes	154
B.2	Specimen A–1.5: Shear Stress Distribution Along Slip Planes	155
B.3	Specimen A–2.5: Shear Stress Distribution Along Slip Planes	155

B.4	Specimen T–0.5: Shear Stress Distribution Along Slip Planes	156
B.5	Specimen T–1.5: Shear Stress Distribution Along Slip Planes	156
B.6	Specimen A–0.5: Normal Stress Distribution Along Slip Planes	157
B.7	Specimen A–1.5: Normal Stress Distribution Along Slip Planes	158
B.8	Specimen A–2.5: Normal Stress Distribution Along Slip Planes	158
B.9	Specimen T–0.5: Normal Stress Distribution Along Slip Planes	159
B.10	Specimen T–1.5: Normal Stress Distribution Along Slip Planes	159
B.11	Specimen T–1.5: Revised Shear Stress Distribution Along Slip Planes	161
B.12	Specimen T–1.5: Revised Normal Stress Distribution Along Slip Planes	161

***Appendix C: Raw Experimental Data***

C.1	Orientation of Slip Planes in the Custom-Made Testing Apparatus	163
-----	---	-----

## LIST OF TABLES

TABLE	PAGE
<i>Chapter 2: Design and Construction of Test Specimens</i>	
2.1 Phase One Test Matrix and Specimen Dimensions	32
2.2 Phase One Mortar Properties	38
2.3 Tyfo® WEB Composite GFRP Properties	39
2.4 Phase Three Testing Schedule	48
2.5 Phase Three Mortar Properties	56
2.6 Fibreglass Mesh Properties	57
<i>Chapter 3: Phase One and Two Experimental Results</i>	
3.1 Phase One Experimental Results	84
3.2 Phase Two Experimental Results	98
<i>Chapter 4: Phase Three Experimental Results</i>	
4.1 Phase Three Experimental Results	118
<i>Chapter 5: Conclusions and Recommendations</i>	
5.1 Comparison of Phase One GFRP Reinforced Specimen Results with CSA S806-02	135
<i>Appendix B: Finite Element Analysis</i>	
B.1 Multiplication Factors for Scaling Finite Element Analysis	153
B.2 Correlation Between Experimental and Finite Element Analysis Results	154
<i>Appendix C: Raw Experimental Data</i>	
C.1 Phase One Table of Contents	163
C.2 Phase Three Table of Contents	175

## **CHAPTER 1: INTRODUCTION**

### **1.1 BACKGROUND**

Masonry has a rich history as one of the oldest and most widely used construction material. It was used for thousands of years until modern materials (i.e., concrete and steel) appeared in the 19<sup>th</sup> century (Velazquez-Dimas et al., 2000). It has several inherent advantages, such as its aesthetic and architectural appearance, heat and sound insulation, fire resistance and economical construction.

Masonry structures still constitute a high percentage of the total building stock around the world, much of which can be classified as low-rise buildings, having only one or two storeys (Hall et al., 1997). Unfortunately, many of these structures are situated in seismic regions and were either constructed before appropriate seismic design provisions were available or do not meet current seismic design requirements (Ehsani et al., 1999). They were designed primarily to resist wind and gravity loads. Therefore, it is typical for these structures to be constructed of brick or block units bonded together by cement mortar with little or no reinforcing steel. Steel reinforced masonry was not introduced in the United States until the 1930s (Ehsani et al., 1997). The lack of steel exacerbates the problem of resisting seismic forces because masonry structures have well defined mortar joint patterns that provide relatively weak potential failure planes (planes of weakness). Also, in existing buildings, mortar joints may have reduced capacity due to aging and associated deterioration.



Unreinforced masonry (URM) structures are vulnerable to failure under seismic loading because they are not capable of dissipating energy through inelastic deformation during earthquakes. The Masonry Society and the Federal Emergency Management Agency have identified that, in earthquake prone areas, failure of URM walls result in the most property damage, injuries and loss of life (Tumialan et al., 2003; Ehsani et al., 1999). Property damage and injury are typically caused by the failure of masonry parapet walls (because of inadequate connections to the roof), veneers and unanchored loadbearing walls.

Lateral loads on buildings, either caused by wind or seismic events, are resisted primarily by the in-plane strength and stiffness of the walls oriented parallel to the direction of the applied load; strength and stiffness of a wall in the out-of-plane direction is much less. Since lateral loads can come from any direction it is essential that the layout of a building incorporate structural walls along the two major axes in the plan view. The concern associated with relying on these URM shear walls to transfer the load to the foundation is that the typical modes of failure are characterized by brittle behaviour, with rapid decreases in capacity and very limited deformations once the ultimate load is reached. In many low-rise masonry buildings subjected to lateral load, shear is the controlling mode of failure. It is well documented in the literature (Applied Technology Council, 1997; Bosiljkov et al., 2003; Drysdale et al., 1999; Mangenes et al., 1997) that the failure modes associated with the in-plane loading of URM shear walls depend on the combination of the applied load, wall geometry and properties of the constituent materials. The three failure modes are:

**1. *Tension Controlled/Rocking Failure:***

Rocking failure is essentially a rigid body rotation about or near the toe of the wall. This failure mode is most likely to occur if the applied axial compression load is low and the aspect ratio (height over length) is high. The overturning moment will cause tension at the base of the wall resulting in cracking which will propagate along the entire length. As the bearing area decreases, localized compression failure may occur at the toe of the wall. The severity of the compression failure depends on the compressive strength of the masonry units, the level of axial load, and the displacement.

**2. *Sliding/Shear-Slip Failure***

Shear-slip failure is characterized by the relative motion of masonry above and below a mortar bed joint. This failure mode is most likely to occur when both the aspect ratio (height to length) and compressive axial load are relatively low, as is the case with most low-rise buildings. In most cases, the slip failure occurs along the interface of the mortar and the unit rather than through the mortar joint (Drysdale et al., 1999). The capacity of a wall to resist shear-slip, or sliding failure, is a combination of the adhesion and shear-friction resistance between the mortar and the masonry units.

Experimental investigations (Drysdale et al., 1979; Atkinson et al., 1998; Bosiljkov et al., 2003) have shown that the shear-slip strength along a mortar joint is composed of the initial shear bond strength between the mortar and the unit, plus the shear-friction capacity due to the vertical load. The following Mohr-



Coulomb shear strength relationship (Equation 1.1) is commonly used to model this phenomenon.

$$\tau = \tau_o + \mu\sigma_n \quad (1.1)$$

where  $\tau$  is the total joint shear strength,  $\sigma_n$  is the compressive stress normal to the bed joints,  $\tau_o$  is the initial shear bond strength and  $\mu$  is the coefficient of friction. In the absence of experimental data, Paulay et al. (1992) estimated  $\tau_o = 0.04f'_m$ . Atkinson et al. (1998) reported  $\mu$  ranging from 0.7 to 0.85, El-Dakhakhni et al. (2003) reported  $\mu$  ranging from 0.3 to 1.2, Hegemier et al. (1978) reported  $\mu$  ranging from 0.61 to 0.88 for concrete masonry, Paulay et al. (1992) reported  $\mu$  equal to 0.5 and Zhao et al. (2003) reported  $\mu$  equal to 0.4. However, in Canadian design,  $\mu$  is set equal to 1.0 (CSA S304.1, 2004) for masonry-to-masonry contact. The Mohr-Coulomb shear strength relationship assumes that the shear friction capacity is proportional to the applied compressive stress. Experimental investigations (Hegemier et al., 1978; Drysdale et al., 1979; Atkinson et al., 1998) have shown that this is the case in the linear elastic region associated with relatively low axial compression.

### **3. Diagonal Tension Failure**

As both the axial and lateral load increase, the combination of shear and compressive stress results in principal tensile stresses at various angles to the bed joints. This results in diagonal cracking. Whereas rocking failure and shear-slip failure are dependent on the strength of the mortar bond, diagonal tension failure

also depends on the tensile strength of the units. However, depending on the combination of vertical and shear forces, stepped diagonal cracking can occur. This stepped diagonal cracking is caused also by slip along one or more of the bed joints. This is most likely to occur near the threshold between sliding failure and diagonal tension failure, as illustrated in Figure 1.1.

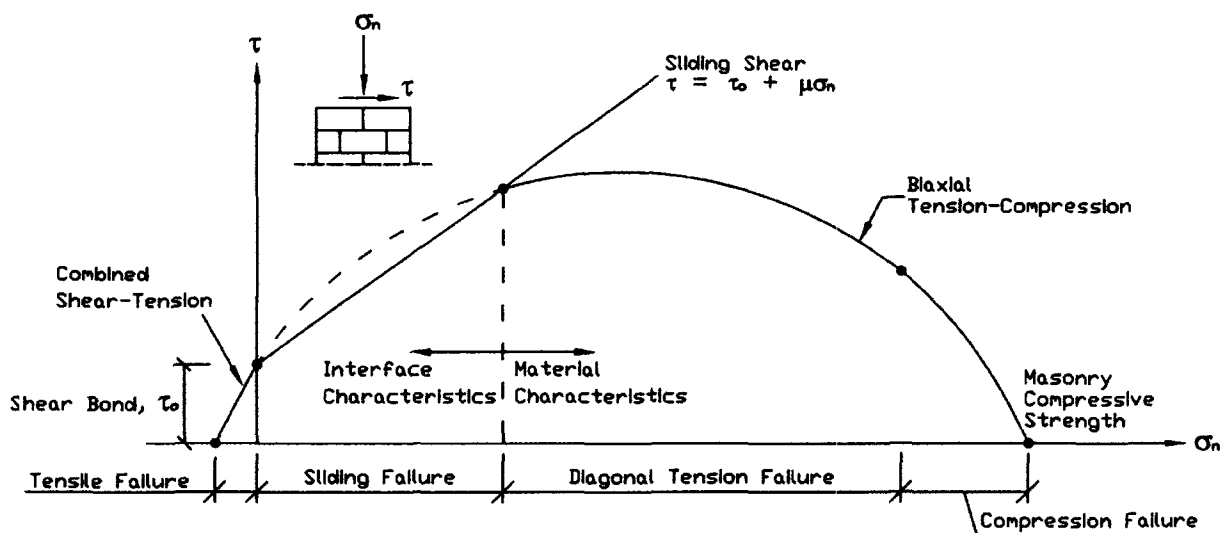
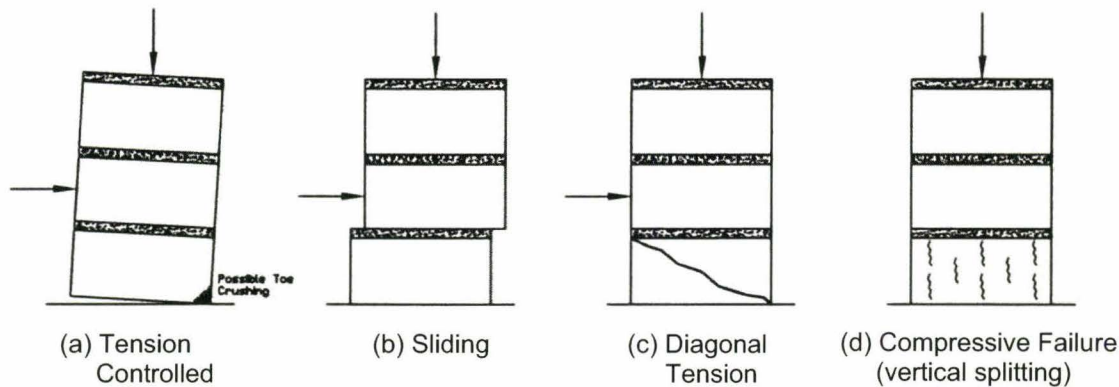


Figure 1.1 – Behaviour of Unreinforced Masonry Under Combined Shear and Normal Stress Along the Mortar Bed Joints [reproduced from Drysdale et al., 1999]

#### 4. Compressive Failure (Vertical Splitting)

In the case of high axial compressive stress and little or no lateral load, failure is the result of vertical splitting. As the masonry assemblage is compressed, the softer mortar wants to laterally expand more than the units. The units are in a state of biaxial tension which results in vertical splitting.

For masonry buildings subjected to lateral loading caused by earthquakes the two dominating failure modes are diagonal tension and shear slip failure (Atkinson et al., 1989). Illustrations of the aforementioned failure modes are found in Figure 1.2.



**Figure 1.2** – Failure Modes of Unreinforced Masonry Shear Walls  
[reproduced from Drysdale et al., 1999]

A building may require structural retrofitting for several reasons:

- Increased minimum design loads from updated building code requirements (i.e., seismic load requirements)
- Change of building use
- Redistribution of equipment
- Renovations
- Corrosion damaged reinforcement

Regardless of the reason, the existing structure may contain structural components that no longer meet the requirements for loadbearing capacity, serviceability, or durability (Kolsch, 1998). The need for an effective strengthening technique is apparent when one considers that as of 2001, 96% of the URM buildings in California alone required seismic retrofitting, at an estimated cost of \$4 billion U.S. dollars. Retrofitting of URM has proven effective in the past. For example, after the Northridge Earthquake (Los Angeles, California) in 1994, a survey showed that 67% of the unretrofitted buildings suffered damage, compared to 55% for those that were retrofitted (Bajpai et al., 2003).

Before the introduction of FRP as a potential strengthening technique, traditional methods of retrofitting URM structures included, but are not limited to:

- Adding structural elements such as steel or cast in-situ reinforced concrete frames
- Sprayed shotcrete, reinforced with steel mesh
- Grouting reinforced bars within vertical cores drilled through the URM walls
- Externally applying epoxy-bonded steel plates

All of the aforementioned methods are capable of adding strength and ductility, but they do have several disadvantages. Generally these techniques are labour intensive and, therefore, expensive. They can add considerable mass to the structure and can cause significant disturbance and inconvenience to the occupants. Also, increases in the cross-sectional dimensions of elements may reduce the structure's usable space. The additions may be susceptible to corrosion, and may negatively impact the aesthetics of a building. In light of these disadvantages, the owner may decide that the risk of economic loss and occupant injury does not justify the significant cost of strengthening (Eshani et al., 1999; Bakis et al., 2002; Bajpai et al, 2003). In seismic areas, adding any weight to a structure will alter the inertial forces and hence alter its earthquake response (Triantafillou et al., 1998). Furthermore, existing structural elements may be unable to support the additional weight, requiring them to be strengthened as well, adding additional cost to the retrofit.

## **1.2 FIBRE REINFORCED POLYMERS (FRPs)**

### **1.2.1 HISTORY**

Masonry reinforced with FRP is truly the coming together of the old and new world. While masonry has existed since the beginning of recorded history, FRP is one of the most recent additions to structural engineering rehabilitation. The earliest FRP products were produced following World War II due to the expanding petrochemical



industry (Bakis et al., 2002). During the 1960s, FRPs made with high performance fibres were used to meet the challenges of space exploration and air travel. At this time FRP was too expensive to be used for other applications. This all changed in the 1970s when entrepreneurs began marketing FRPs to the sporting goods industry (Bakis et al., 2002). This increased the use of FRPs which in turn lowered its cost. By the late 1980s/early 1990s, the need for infrastructure renewal in developed countries was identified by engineers. It was believed that FRP could be used in such a capacity. This led to an increase in industry and government funded research which resulted in the accepted use of FRP for infrastructure renewal.

Today a variety of FRP composite products are produced through processes such as filament winding, filament weaving, extrusion and compression moulding. These products include structural members of standard or customized cross-sections, reinforcing bars for prestressed and nonprestressed applications, external surface lay-up (ESLU) fabrics and meshes with unidirectional or bidirectional fibres. FRP lay-up fabrics are generally applied on the external surface of members, while FRP bars can be used for both internal and near-surface-mounted (NSM) reinforcement.

### **1.2.2 GENERAL**

FRP is a composite material composed of high-strength, high-stiffness structural fibres, made from carbon (CFRP), glass (GFRP) or Aramid (AFRP), embedded in a vinylester, polyester, or epoxy resin matrix. The fibres provide the strength and stiffness required to satisfy the design requirements while the matrix allows for the even distribution of load to the fibres, provides dimensional stability, and protects the fibres

from the environment and potential damage. As a composite material, it has mechanical properties that are better than any of its constituent materials alone.

FRP has many ideal properties for structural engineering applications (Bakis et al., 2002; Capozucca, 2001; El-Dakhakhni, 2003; Ehsani et al., 1997; Ehsani et al., 1999; Hamilton III et al., 2001; Kolsch, 1998; Velazquez-Dimas et al., 2000). These include:

- High tensile strength-to-weight ratio; typically greater than most metals
  - It does not add significant additional weight to the structure.
- High stiffness
- Corrosion resistance
  - Negligible moisture permeability
- Fatigue resistance
- Thermal stability
- Versatility of installation:
  - It can be tailor made to satisfy a specific application by selecting an appropriate fibre, matrix, fibre direction, and geometry.
  - It is available in virtually unlimited lengths. Therefore, when laminates or fabric strips are adhered to a wall they can be long and continuous.
  - It is suitable for repairing both plane and curved surfaces.
- Versatility of structural applications:
  - It can be used for flexural strengthening, shear strengthening, or confinement
- Relatively easy and quick installation; especially surface mounted laminates
  - This reduces the cost of installation and limits the downtime of the occupied structure.
- Reduce the anisotropic nature of masonry to assist in modeling

The mechanical properties of FRP are influenced by the fibre-to-matrix ratio. Typically, for construction applications, 40% of the total volume is the matrix, which contributes a minimal amount to strength and stiffness (Velazquez-Dimas et al., 2000). FRP has very high tensile strength and rigidity along the fibre direction, but negligible strength in the transverse direction. When loaded along the fibre direction, it will behave linearly up to failure. The strength and ductility provided is primarily dependent on the

fibres. CFRP will provide the greatest strength while GFRP will provide the greatest ductility (Bastidas et al., 2003):

- Strength and Stiffness: CFRP > AFRP > GFRP
- Max Strain: GFRP > CFRP  $\approx$  AFRP

FRP also has several disadvantages that must be given some consideration when used in a retrofit design (Bakis et al., 2002; Ehsani et al., 1999; Kolsch, 1998; Velazquez-Dimas et al., 2000). These include:

- Comparatively low transverse (i.e., shear) strength
- Low interlaminar strength
- Sensitivity to ultraviolet (UV) radiation degradation
- Temperature dependence of mechanical properties
  - FRP will deteriorate at high temperatures.
  - FRP is flammable and emits toxic fumes and smoke while burning.

FRP should not be left exposed in a structure. It should be protected by a coating that will provide suitable fire protection. If FRP cannot be properly protected against accidental exposure to fire, Bakis et al. (2002) recommend the degree of strengthening (i.e., the ultimate capacity of the strengthened element divided by that of the unstrengthened element) should be increased to provide a factor of safety. While the cost of FRP materials tends to be high, the potential benefits of its use, when compared to traditional strengthening techniques, will generally outweigh that cost. GFRP is the least expensive FRP (Capozucca, 2001; Bastidas et al., 2003).

### **1.3 FIBRE CEMENT MATRIX (FCM)**

Another type of external surface lay-up (ESLU) reinforcement uses woven fibre meshes, once again made of either carbon (CFCM) or glass (GFCM), embedded in a polymer modified cement matrix. This has the benefit of being more compatible with the

masonry substrate in terms of bond, moisture permeability and thermal coefficient (Kolsch, 1998). In addition to protecting the fibres from the environment, the cement matrix is also naturally noncombustible and, therefore, fire resistant. Unlike the epoxy used to apply FRP, the cement matrix contains no toxic materials so no special safety equipment is required and no special health regulations must be satisfied. Furthermore, the cement matrix is applied to the wall like a traditional mortar parging. For these reasons, this form of construction is much more worker friendly.

#### **1.4 CODES AND STANDARDS**

Reinforcing bars made from FRP can be used similar to traditional steel reinforcement to reinforce masonry beams and walls for shear and flexural loads. The design will be based on many of the same principles and assumption. However, the designer must take into account the different material and mechanical properties, and the linear elastic stress-strain behaviour of FRP. A FRP-reinforced design must allow for less ductility than a conventional steel-reinforced design. A good example of this is the flexural design of a masonry beam. With a steel-reinforced beam, it is desirable for the section to be under-reinforced so that the steel yields before the masonry crushes. This is the basis for ductile failure. This is not the case if FRP reinforcing bars are used. In an under-reinforced masonry beam, the FRP bars will rupture before the masonry crushes, rather than gradually yielding. This is a brittle failure. It is best that the section is over-reinforced so that the masonry will crush before the FRP ruptures. It will allow for more energy absorption and deformation before ultimate failure (Bakis et al., 2002).



Due to its different physical and material properties compared to other, more traditional, civil engineering materials (i.e., steel, concrete, wood, masonry), FRP warrants separate treatment in codes and standards. Codes for FRP design have been in development since the 1980s and their proper use will allow structures containing FRP to be designed, built, operated and maintained with safety and confidence (Bakis et al., 2002). Canada (CSA S806, 2002), the United States (ACI 440 Committee, 2001), Japan and Europe have all developed their own FRP design guidelines.

## **1.5 RESEARCH OBJECTIVES**

Research using full scale wall tests to evaluate the effectiveness of FRP reinforcing to resist shear slip would be limited by time and cost considerations. In addition, full scale tests do not create pure shear conditions so that interpretation of the results is complicated by consideration of more complex stress conditions. It was desirable to be able to conduct a sufficient number of tests to evaluate various FRP reinforcing alternatives and it was desirable to isolate the influence of bed joint shear to facilitate interpretation of the test data. Therefore, a necessary first step in this research was to evaluate various test specimen configurations and to choose the most satisfactory one. In addition, this reported first phase of the research should provide some initial insight into the effectiveness of the retrofit method.

The main objective of the experimental work is to investigate the effects of different glass fibre reinforcing schemes on the strength, failure modes and post-peak response of masonry under direct shear loading. Another objective is to demonstrate that,

with the proper selection of the fibreglass laminate (FGL) reinforcement, shear failure, which is common in URM walls with low aspect ratios, can be mitigated.

## **1.6 LITERATURE REVIEW**

This section contains a review of past experimental investigations pertaining to the two main topics addressed in this study: the in-plane behaviour and corresponding analysis of URM walls, and the use of fibre reinforced polymer (FRP) for the retrofit of structural systems.

### **1.6.1 SHEAR SLIP FAILURE OF URM**

In addition to limits on the capacity of a masonry wall due to tension or compression failure, the possibility of shear failure should be considered. Various experimental investigations have been conducted to understand the shear-slip failure of URM.

Hegemier et al. (1978) conducted shear-slip tests on three-block stacked concrete masonry assemblages using Type-S mortar. The specimens were tested under an applied constant normal stress. It was observed that the fracture strength of the bed joints increased monotonically with precompression, up to the point of block failure. In the absence of precompression, joint behaviour was brittle. It was concluded that, for ungrouted masonry, the Mohr-Coulomb failure criteria is sufficient for engineering purposes. Based on their research, and a review of other work done, Hegemier et al. (1978) concluded that the coefficient of friction,  $\mu$ , has great variability. In this case it was reported to vary from 0.61 to 0.88.

Drysdale et al. (1979) conducted 74 shear tests of clay brick masonry assemblages. The four-brick specimens were designed to transmit pure shear along the bed joints without inducing bending moments. Constant levels of precompression, applied normal to the bed joints, ranging from 0% to 30% of the compressive strengths of the corresponding prisms, were used in the tests. The influence of using mortar of varying strength and using bricks with different initial rates of absorption (IRA) was also included. The mode of failure was consistently shear-slip along two of the bed joints. It was concluded that the shear bond strength was not proportional to the compressive strength of the mortar. Extreme values of initial rate of absorption (IRA) did have an influence on reducing the shear strength of the specimens. If a masonry unit had a low IRA, it may not have drawn in enough mortar to form intimate contact. Conversely, if a masonry unit had a high IRA, it may have tended to dry out the mortar at the brick-mortar interface and produce low bond along the dry layer. A nearly linear relationship between the increased shear strength and the precompression stress was discovered. However, at higher levels of precompression, the relationship became nonlinear. This suggested that the Mohr-Coulomb theory of internal friction cannot be used for the full range of compression stresses normal to the bed joint.

Atkinson et al. (1989) tested fifty-six shear slip specimens with up to four cycles of displacement controlled shear reversal. The aim was to examine the horizontal bed joint shear failure mode and shear load-displacement behaviour under static and cyclic loading. The influence of different levels of normal stress, ranging from 0.4 MPa to 4.2 MPa, was also included. The shear-slip stresses were applied over a longer two-block bed

joint length (past investigations had slip plane lengths of one unit or less). This was done to better represent an actual wall, and to produce more uniform stresses and deformations along the slip plane. A finite element analysis confirmed that the shear stress along the slip plane was essentially uniform. An interesting finding was that the post-peak slope of the load-displacement curve was not constant but decreased with increasing displacement. Atkinson et al. (1989) concluded that this was an indication that there was a softening of the bed joint as the displacement increases to the peak load value. This experimental research also confirmed satisfactorily modeling of shear strength using the Mohr-Coulomb criterion. The value of the cohesion component was found to be dependent on the physical condition of the bed joint and, obviously, varied depending on the specimen.

Van der Pluijm (1993) conducted 54 deformation controlled tests on stacked two-unit shear specimens. The specimens were constructed from three different types of brick, and each was used in combination with two types of mortar. The specimens were tested in pure shear with an applied normal compressive stress ranging from 0.1 MPa to 1.0 MPa. Using a linear FEM calculation, it was shown that the resulting stress distribution was nearly constant along the bed joint slip plane. When the shear strength versus the applied normal compressive stress was plotted, it yielded a linear pattern which was best described using the Mohr-Coulomb relationship. As usual, the amount of cohesion depended on the unit type and the mortar used. Stronger mortar produced higher cohesion. Results of the tests indicated that, after the peak load was reached, any residual strength was only due to friction along the bed joint. The coefficient of friction was determined to be 0.75.

## **1.6.2 MASONRY SUB-ASSEMBLAGES STRENGTHENED WITH FRP**

In order to investigate the influence of FRP on the potential failure modes of URM walls subjected to in-plane loading, experimental investigations have been carried out on smaller sub-assemblages, as described below. In this way, the failure modes (sliding shear, diagonal tension, compression) could be isolated and studied independently. Again, one of the main advantages of using assemblages, rather than full scale walls, is that a large number of tests can be conducted relatively quickly and inexpensively. For this literature review, the focus is on the influence of FRP on sliding shear failure.

Ehsani et al. (1997) conducted thirty-seven direct shear tests on specimens constructed with three standard clay bricks in a “triplet” type specimen. These specimens were retrofitted with FRP laminates of varying length, density (strength) and fibre orientation ( $0^\circ/90^\circ$ ,  $\pm 45^\circ$ ). A sheet of lubricated plywood was placed between the bricks instead of mortar so that the contribution of the mortar to the shear resistance could be removed. This was also done to try to simulate the detrimental effect on the shear strength of an existing initial gap between the bricks. The specimens were tested under displacement controlled, monotonically increasing loading.

The two failure modes reported were influenced by the strength and development length of the fabric. The first failure mode was shear failure along one of the bed joints and the second failure mode was delamination of the fabric in the middle brick region or along fabric edges (bond failure). For higher fibre density fabrics, the latter debonding failure predominated. Shorter laminates showed combined shear failure as well as

delamination. In most cases, the ultimate load of the  $\pm 45^\circ$  orientated fabric was slightly greater than its  $0^\circ/90^\circ$  counterpart at the same fabric density. Conversely, the displacement at the ultimate load for the  $\pm 45^\circ$  orientation was only 20% to 30% of that for the  $0^\circ/90^\circ$  orientation. An almost constant stiffness was observed for the  $\pm 45^\circ$  FRP throughout the entire loading range. For the  $0^\circ/90^\circ$  FRP, the stiffness was initially constant but decreased gradually. It was concluded that orienting the fibres at  $\pm 45^\circ$  allows the wall to resist larger forces within a smaller amount of deformation, whereas using  $0^\circ/90^\circ$  oriented FRP will produce a more ductile failure but with slightly lower capacity.

El-Dakhkhni et al. (2004) tested fifty-seven assemblages constructed out of full-scale concrete masonry blocks. Out of these, twenty-four were loaded under direct shear. The four-block shear specimens were configured so as to eliminate any bending moment along the bed joints. Three different glass FRP retrofitting schemes were used, which varied by thickness, number of layers and fibre orientation (i.e., unidirectional or bidirectional:  $\pm 45^\circ$  or  $0^\circ/90^\circ$ ). At very low levels of load and displacement, a brittle debonding mode of failure of the unretrofitted specimens occurred at the interface between the block and the mortar. The first failure mode of the retrofitted specimens was tearing of the GFRP along the bed joint slip planes in a 'Z' pattern. This failure mode is associated with the thinner laminate that has a lower strength than the bond between the GFRP and the masonry. This failure mode is more ductile than for the bare specimens because the fibres tear gradually and can sustain some post-peak loads. At ultimate failure, these specimens withstood an average post-peak load of 68% of the maximum load.



The second observed failure mode was delamination of the laminate. This failure mode is associated with the thicker laminates where their strength is greater than the bond between the GFRP and the masonry. This failure mode is the most ductile because delamination occurs more gradually than tearing. The final observed failure mode was crushing of the top and/or lower blocks, leaving the GFRP undamaged. This failure mode is associated with strong laminates with good adhesion strength to the masonry. Shear-slip failures were not achieved prior to the premature compression failure of the specimens. Depending on the type of GFRP used, shear capacities increased by five to fourteen times that of the bare specimens.

Hamid et al. (2005) conducted an investigation to study the influence of FRP on the in-plane behaviour of URM. Forty-two URM assemblages were constructed using one-third-scale “true-model” (Harris and Sabnis, 1999) blocks. The specimens were tested under different stress combinations representing the range of stress conditions encountered in masonry shear and infill walls. Of these 42 assemblages, six were 4-block joint shear, or direct shear, specimens. Three of the direct shear specimens were strengthened with a bidirectional  $0^{\circ}/90^{\circ}$ , 0.25 mm thick Glass-FRP (GFRP) sheet with  $2.55 \text{ g/cm}^3$  of E-glass fibres bonded to both faces. The joint shear strength of the retrofitted specimens was found to be 8.2 times that of the unretrofitted counterparts. Also, the average slip displacement at peak load of the retrofitted specimens was over 34 times that of the unretrofitted counterparts. The FRP prevented sudden brittle failure associated with shear slip-failure and allowed a more gradual ductile failure to occur.

### **1.6.3 FULL-SCALE MASONRY WALLS STRENGTHENED WITH FRP**

Various experimental investigations have been conducted to understand in-plane behaviour of full scale URM cantilever walls retrofitted with FRP.

Fam et al. (2002) performed two tests on one full-scale masonry wall (1.22 m long  $\times$  2.13 m high) subjected to in-plane reversed cyclic load using a hydraulic actuator. The double wythe wall was constructed with standard clay units in running bond using Type-S mortar. A 70 mm cavity was left between the wythes. The cavity was reinforced with 13 No. 6 (19mm) vertical steel bars at 75 mm o.c. and 7 No. 4 (12.7 mm) horizontal steel bars. The cavity was grouted solid. The wall's "toes" were confined with 3.2 mm thick, 380 mm long steel plates. During Test 1, the wall was loaded to a maximum of 334 kN, which corresponded to a lateral displacement of 23 mm. At failure, a maximum lateral displacement of 46 mm was reached, which corresponded to a load of 324 kN. Typical damage consisted of horizontal flexural cracks along the lower bed joints in the early loading stages, followed by 45° diagonal tension cracks. Severe toe crushing and spalling occurred in the late loading stages. For Test 2, the wall was repaired and retrofitted with GFRP. The GFRP was applied on only one side of the wall to simulate a practical and realistic repairing scenario for an existing structure. The GFRP retrofit consisted of 305 mm wide unidirectional strips, placed 25 mm apart horizontally and 150 mm apart vertically. The interface between the wall and concrete support beam was also reinforced with  $\pm 45^\circ$  bidirectional GFRP. The wall endured three full cycles of 76 mm displacement, and a maximum displacement of 203 mm was reached. The maximum capacities were 11% and 38% greater than the unreinforced specimen in the push and pull



directions, respectively. Near the corners of the wall, vertical splitting and delamination (outward local bucking of the laminate) occurred as well as unit crushing. The test was terminated when the wall was essentially ripped out of the footing. A close inspection revealed that the old cracks did not open and a new crack pattern had formed.

Zhao et al. (2003) tested three squat walls (1.4 m wide  $\times$  1.0 m high  $\times$  0.190 m thick) constructed in running bond using 20 cm concrete block. *Wall 1* was the unretrofitted control specimen. *Wall 2* was retrofitted with bidirectional CFRP, and *Wall 3* was retrofitted with the same scheme as *Wall 2* but after cracking to simulate a repair scenario. Cracking was observed in *Wall 3* at a 0.7 mm displacement, corresponding to the application of a 140 kN lateral load. The retrofit scheme consisted of 200 mm wide strips of CFRP applied as cross-braces (i.e., corner-to-corner) and anchored at the ends using steel plates and anchor bolts. The strips were applied to both sides of the wall. An in-plane load was applied using a hydraulic actuator while a constant axial stress of 1.2 MPa was maintained for all tests.

*Wall 1* cracked at a lateral load of 132 kN, which corresponded to a horizontal displacement of 0.7 mm. A sudden vertical crack appeared near the centre of the specimen and was followed by diagonal cracking. The average ultimate lateral load was 166 kN with a corresponding average horizontal displacement of 3.1 mm. *Wall 2* cracked at a lateral load of 140 kN (6.1% increase) with a corresponding horizontal displacement of 0.9 mm (28.6% increase). The average ultimate lateral load was 256 kN (54.2% increase) with a corresponding horizontal displacement of 6.7 mm (116.1% increase). At failure, diagonal cracks had formed in the bottom corner of the compression area. In

addition, some CFRP in the compression zones had delaminated and some units were crushed. The repaired *Wall 3* cracked at a lateral load of 150 kN (13.6% increase) with a corresponding horizontal displacement of 0.9 mm (28.6% increase). The average ultimate lateral load was 195 kN (17.5% increase) with a corresponding horizontal displacement of 3.6 mm (16.1% increase). At failure, a slip of 7 mm suddenly occurred along the bed joint between the 2<sup>nd</sup> and 3<sup>rd</sup> courses from the bottom. For all of the tests, the ultimate displacement was recorded at the point where the post-peak load had decreased to 85% of the ultimate (maximum) value. The GFRP increased the stiffness of the walls in the later stages of loading by delaying the development of diagonal cracks. All of the specimens failed in either diagonal tension or sliding shear failure.

El-Gawady et al. (2004) performed two tests on one half-scale squat masonry wall (710 mm height × 1570 mm length × 75 mm width). The wall was constructed in running bond using weak mortar (3.2 MPa ± 0.35 MPa). It was tested using in-plane static cyclic loading with a constant normal stress of 0.35 MPa. The first test was the control specimen, with no FRP applied. In the second test, the wall was repaired with GFRP, on one side only, and retested. The GFRP increased the cracking load by approximately 3 times. The ultimate lateral load resistance increased by approximately 1.5 times and the drift was increased by approximately 2.8 times. After the GFRP ruptured, the retrofitted specimen behaved similarly to the unretrofitted specimen. During both tests, the specimens developed flexural cracks along the lower bed joints, followed by sliding concentrated along the base and, finally, by a rocking failure mode.

Further work of a similar nature was also carried out by Vandergrift et al. (2002), Elgwady et al. (2002), and Capozucca (2001). This is by no means an exhaustive list but is sufficient to indicate the state of knowledge at the time that the research in this report was carried out.

#### **1.6.4 FULL-SCALE MASONRY IN-FILL WALLS STRENGTHENED WITH FRP**

In low-rise masonry buildings, it is not necessarily the best strategy to completely prevent sliding shear failure mode from occurring. During a seismic event, slip along the joint planes can provide a stable source of energy absorption and damping (Hegemier et al., 1978; Hall et al., 2002). This is not the case with URM infill walls. A common method of multi-storey building construction involves infilling the steel or reinforced concrete frame with unreinforced masonry walls. In some cases, the infill walls may not have been included in the analysis and design because they are considered architectural nonstructural elements (Bastidas et al., 2003; El-Dakhakhni et al., 2003). This is not necessarily a conservative approach if the walls are built in tight to the frame. During a seismic event, such infill walls will interact with the frame and influence its strength, stiffness, ductility, and the load distribution. Since infill walls not isolated by movement joints will interact with the frame, it makes economic sense to include them in the analysis of the building's dynamic response to seismic loads. The problem is that under high seismic loads, the building may exhibit poor performance as the infill panels are progressively damaged during each cycle which equates to degradation of the building's stiffness, strength and energy dissipation capacity (El-Dakhakhni, 2003).

The main failure modes of an infill masonry wall are:

- Corner crushing (i.e., compression failure of the diagonal strut)
- Sliding shear (i.e., knee brace)
- Out-of-plane collapse

Sliding shear is the most common failure in URM infill walls and the most undesirable (El-Dakhkhni, 2003). Not only does it tend to occur suddenly, but it prevents utilization of the full strength of the wall. Sliding shear can also cause severe damage to the frame columns at their midheight and can lead to overstressing of adjacent members (Drysdale et al., 1999; Belarbi et al., 2003). Corner crushing is the most desirable because it allows the full strength of the wall to be utilized while avoiding overstressing the frame.

Bastidas et al. (2003) tested a full scale wall (2.2 m high  $\times$  3 m long  $\times$  9 cm thick) surrounded by a reinforced concrete frame in in-plane cyclic lateral loading at drifts ranging from 0.01% to 1.5%. The wall was constructed using 9 cm wide  $\times$  23 cm high  $\times$  33 cm long nonstructural hollow clay units typical for South America. It was reinforced with 2.5 cm wide unidirectional GFRP strips diagonally placed, but not corner-to-corner, on both sides of the wall to promote a symmetrical response. The masonry maintained its integrity up to 1% drift. Most damage occurred in the top corners which were not reinforced with GFRP.

El-Dakhkhni et al. (2003) tested six 3.6 x 3.0 m single storey steel frames infilled with URM panels (both with and without openings) under cyclic in-plane loading. No shear connection was provided between the wall and the frame. Some of the specimens were unreinforced and others were reinforced with GFRP laminate on both sides of the wall. The GFRP was cut to exact wall dimension and not anchored to the

steel frame. The fibres were oriented perpendicular to the bed joints. The bare frame was able to resist a maximum load of approximately 200 kN at 100 mm max displacement. The unretrofitted infilled frame was able to resist an ultimate load of approximately 400 kN at 50 mm max displacement. The retrofitted infilled frame was able to resist a maximum load of approximately 600 kN at 50 mm displacement, and a post-peak load of approximately 300 kN at 100 mm max displacement. The GFRP provided the required shear slip resistance and maintained the integrity of the wall by preventing out-of-plane buckling and spalling. Thus, the diagonal compression strut remained intact for maximum strength, stiffness and beneficial post-peak behaviour. The undesirable failure modes, namely sliding shear and diagonal cracking, were prevented.

### **1.6.5 OTHER RESEARCH**

The experimental investigation of the potential benefits of FRP has not been limited to masonry walls subjected to in-plane loading. Numerous studies have been done on each of the following:

1. Out-of-Plane Loading
2. Blast Loading
3. Arches and Vaults
4. Anchorage
5. Columns
6. Beams

### **1.7 CONCLUSION**

In earthquake prone areas, failure of URM walls result in the most property damage, injuries and loss of life. Traditional strengthening techniques have several undesirable properties. Past research has shown that FRP reinforcement is an effective method of increasing both the strength and ductility of URM. Masonry reinforced with

FRP is truly the coming together of the old and new worlds. However, past research has not fully documented the influence of amount, orientation, or bonding material for FRP reinforcing applied to enhance shear-slip behaviour of unreinforced concrete block masonry. The research reported in the following chapters deals specifically with the effectiveness of using FRP reinforcement to modify shear-slip behaviour of originally unreinforced concrete block masonry.



## **CHAPTER 2: DESIGN AND CONSTRUCTION OF TEST SPECIMENS**

### **2.1 INTRODUCTION**

This chapter contains information on design and construction of the test specimens and on the materials used. The tests were organized into the three phases described below.

Phase One was designed mainly to evaluate the suitability of various test specimen configurations for determining shear-slip strength and behaviour along bed joints. The intent was to evaluate the behaviour for both unreinforced hollow concrete block specimens (URM) and similar masonry specimens reinforced with surface bonded glass fibre laminates (GFRM). As a result, the only test variables included were the geometry of the test specimen and whether or not glass fibre was applied to improve performance. For GFRM modified specimens, it was anticipated that post-cracking and post-peak behaviour might be important for strength, stiffness, and energy dissipation considerations. In addition to the main purpose of choosing the best test specimen, it was anticipated that data from these tests would provide valuable documentation of basic properties of URM and the specific effect of retrofitting with one type of glass fibre reinforced polymer (GFRP).

The second test phase was designed to evaluate the potential to obtain two sets of data from each specimen and to provide insight into the relative merits of using fibreglass mesh compared to fibreglass cloth.

Finally, Phase Three was planned to provide data on the effects of weight (or cross sectional area) of fibreglass and orientation of the fibres relative to the slip plane.



## **2.2 PHASE ONE**

### **2.2.1 SPECIMEN TYPES AND DESIGNATION**

**Choice of Test Specimen.** Phase One of the experimental program consisted of testing the five different geometries of masonry assemblages shown in Figure 2.1. These specimens are simply modifications of the “triplet” and “modified triplet” used in past studies (Drysdale et al., 1999) to simulate shear loading along mortar bed joints to determine the shear-slip resistance.

The triplet shaped specimen has support points applied as close as possible to the shear plane along the bed joint in order to minimize the magnitude of bending stresses introduced perpendicular to the bed joint along the shear planes. In addition, the intent was to provide loading on the central block so that load was applied as nearly as possible to those bed joints. Variations of the triplet specimen involved increasing the length of the shear-slip plane. There were three reasons for considering possible benefits of longer shear-slip planes. They are:

1. The increase in shear resistance should only increase in proportion to the length of the shear slip plane and thus bending moments would similarly only increase proportionally. The advantage is then that resistance to bending (section modulus) increases in proportion to the square of the length of the shear plane so that the magnitude of the bending stresses would be less significant:

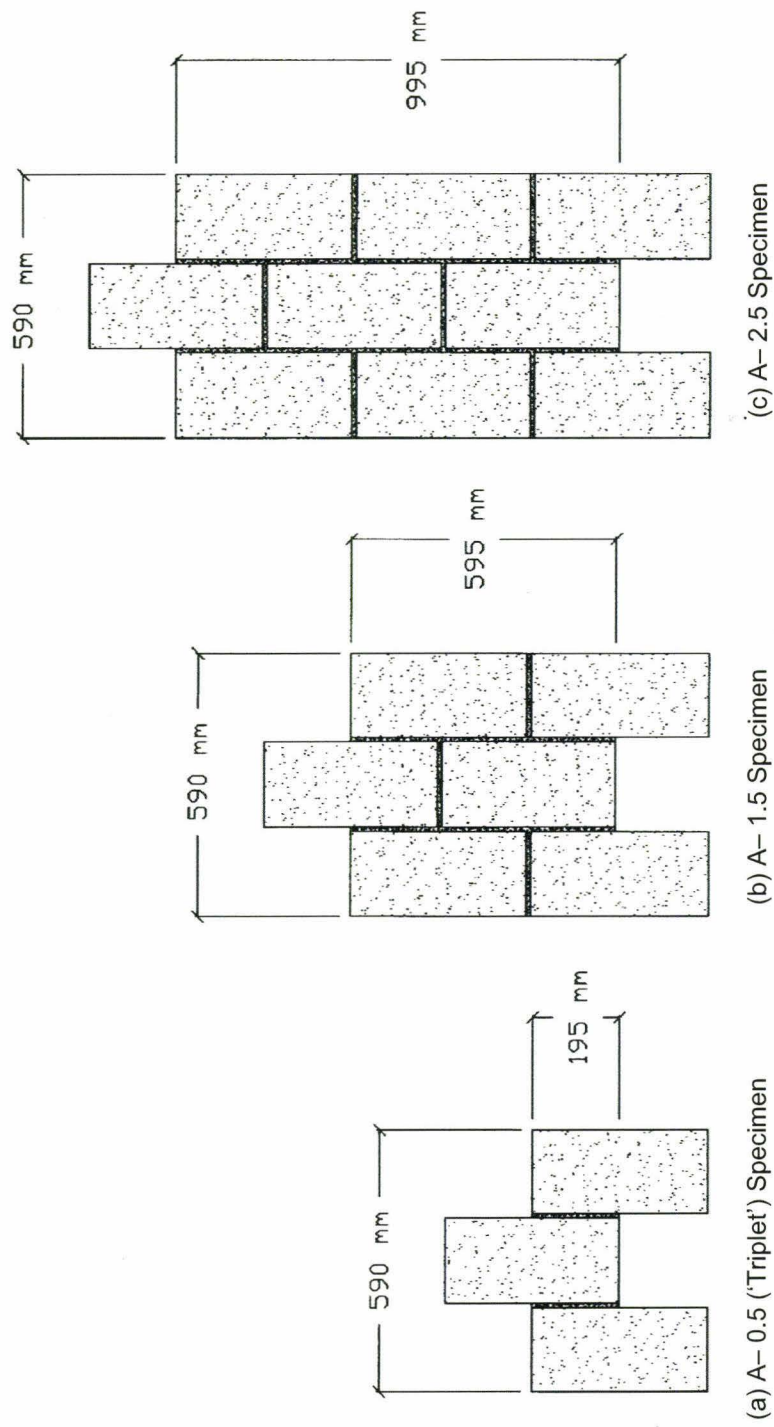


Figure 2.1 – Phase One Test Specimens (Full Stretcher Units Used)

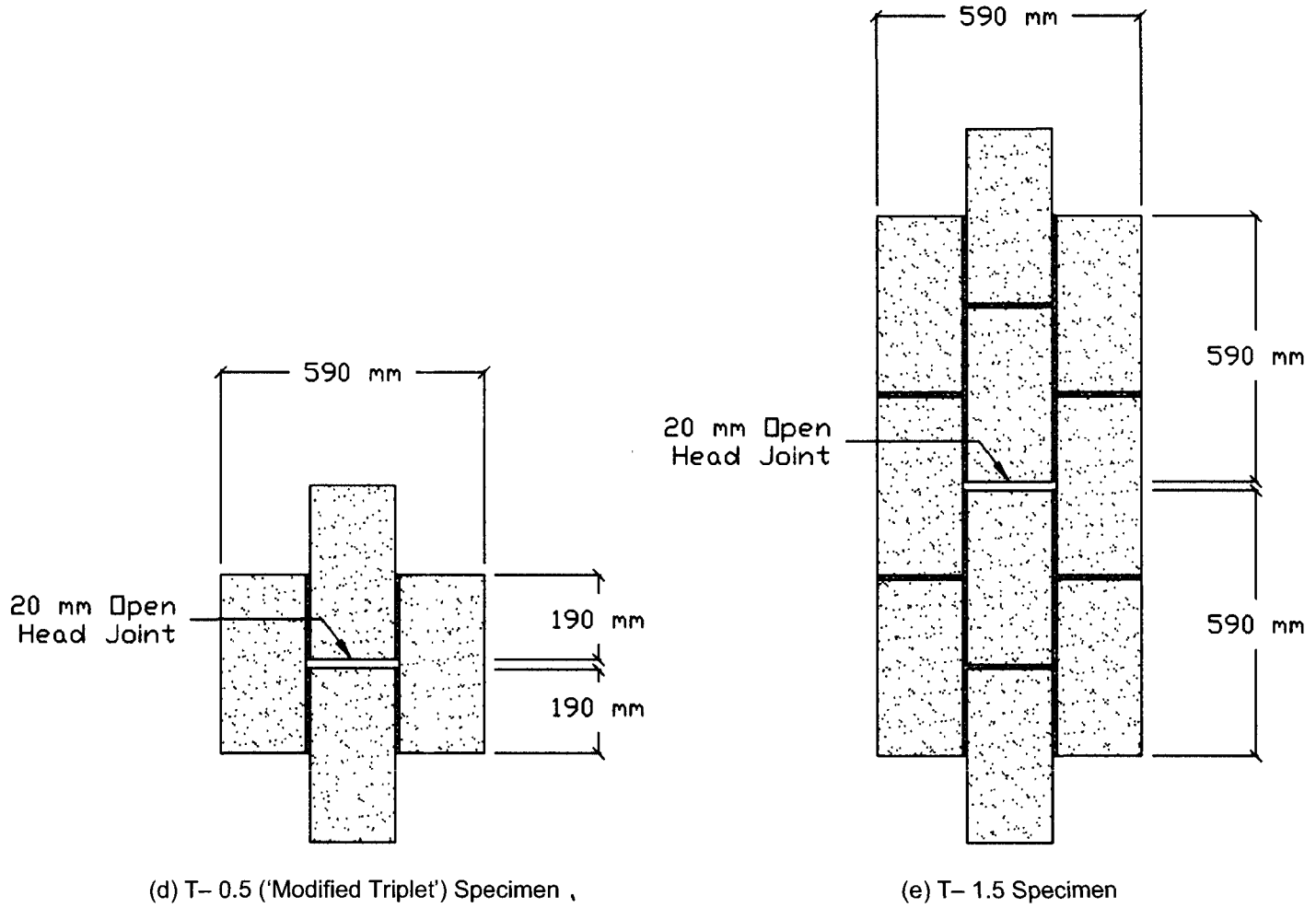


Figure 2.1 (continued) – Phase One Test Specimens (Full Stretcher Units Used)

$$\text{Section modulus, } S = \frac{I}{c} = \frac{\frac{1}{12}bh^3}{h/2} = \frac{1}{6}bh^2 \quad (2.1)$$

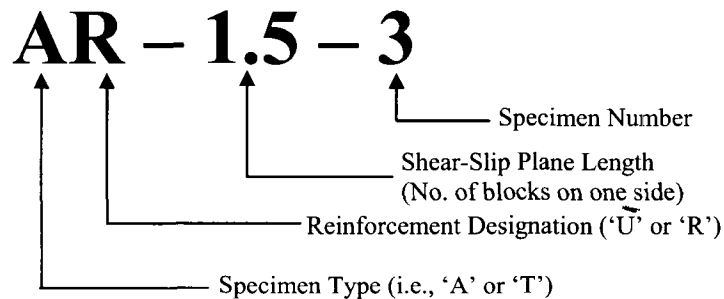
where  $I$  = moment of inertia,  $c$  = distance from neutral axis to the extreme fibre,  $b$  = combined average width of the two mortared face shell bed joints, and  $h$  = length of the shear-slip plane.

2. Finite element studies (Atkinson et al., 1989) showed that, near the ends of the slip plane, shear stresses were not uniform, whereas they were reasonably uniform over regions away from the ends. Therefore, it is reasoned that a longer shear-slip length should reduce the importance of nonuniform distribution of shear stress.
3. Contrary to normal material science theory wherein larger test specimens tend to exhibit lower strengths due to greater probability of a critical combination of flaws (Batdorf, 1986), materials that may have very large random weaknesses show less influence of flaws on strength and variability where the weak zone is a smaller fraction of the potential failure path (Bazant, 1997). Thus, a longer length should give more representative results with decreased variability.

The modified triplet shape specimen provided symmetry about the midheight above and below a gap, which was provided to permit slip to occur. The symmetry of the loading and lack of support points along the exterior courses of the test specimen were intended to reduce the magnitude of bending stresses. A longer shear-slip plane potentially has the same advantages as described above. However, for both the triplet and

modified triplet specimens, potential for local cracking and high axial deformation created limits on the possible length of the shear-slip failure plane.

**Specimen Identification.** For later reference, note that the designation for each specimen in Phase One begins with the letter ‘A’ or ‘T’. The letter ‘A’ indicates that the specimen is a ‘triplet’ (an A-shape) or a variation of it, and the letter ‘T’ indicates that the specimen is a ‘modified triplet’ (a T-shape) or a variation of it. The next letter in the designation is ‘U’ or ‘R’ which stand for unreinforced or reinforced, respectively. The next number in the designation indicates the length of the shear slip plane on each side of the specimen as a multiple of the number of blocks. The last number is simply the specimen number. A labelling sample can be found in Figure 2.2.



**Figure 2.2 – Phase One Specimen Labelling Sample**

### **2.2.2 CONSTRUCTION AND PREPARATION OF PHASE ONE TEST SPECIMENS**

**Construction.** Forty specimens, consisting of eight of each of the five configurations shown in Figure 2.1, were constructed. Of these forty specimens, fifteen (consisting of three of each of the five configurations) were retrofitted on both faces with GFRP. Specimens were reinforced with 295 g/m<sup>2</sup> (8.7 oz./yd.<sup>2</sup>)(dry weight) Tyfo® WEB Composite, which is a bidirectional (0°/90° fibre orientation) and isotropic fibreglass

cloth. [Additional manufacturer’s information on this fibreglass cloth is provided in Appendix A.] The type of GFRP reinforcement was kept constant so that the performance of each shape could be directly compared. The fibres were oriented at 0°/90° to the bed joints. Unfortunately, three specimens (one TU-0.5 and two AU-0.5) were damaged in the laboratory and, therefore, were not tested. A summary of the test matrix and specimen dimensions is provided in Table 2.1

**Table 2.1 – Phase One Test Matrix and Specimen Dimensions**

<b>Specimen Type</b>	<b>Unreinforced</b>	<b>Reinforced</b>	<b>Slip Plane Length (mm)</b>	<b>Total Width (mm)</b>
A-0.5	3 × AU-0.5	3 × AR-0.5	195	590
A-1.5	5 × AU-1.5	3 × AR-1.5	495	590
A-2.5	5 × AU-2.5	3 × AR-2.5	995	590
T-0.5	4 × TU-0.5	3 × TR-0.5	190	590
T-1.5	5 × TU-1.5	3 × TR-1.5	590	590

NOTE: Specimens reinforced with Tyfo® WEB Composite bidirectional 0°/90° GFRP on both faces.

The specimens were constructed using standard 20 cm hollow concrete masonry block stretcher units and face shell bedding with Type-S mortar to represent normal construction practice. In order to minimize the statistical variability of the block strength, all the blocks in this study were taken from the same batch. The blocks had an average compressive strength of 25.0 MPa, based on the average cross-sectional area. The assembled masonry had an average measured compressive strength ( $f'_m$ ) of 15 MPa based on the average of three compression tests of 4-block high face shell mortared prisms. In order to minimize the effect of varying workmanship on the properties of the assemblages, the same experienced mason constructed all the specimens using actual field techniques and mortar flow. In order to assist the mason, the specimens were constructed using running bond in long wythes (shown in Figure 2.3(b)), which simulated

standard practice for constructing a wall. In order to easily separate the specimens later on, 10 mm (3/8 inch) plywood strips were used as spacers between specimens instead of mortar.

Due to the presence of a drain, the floor where the specimens were constructed was not entirely level. The mason suggested a simple, but effective, solution which deserves mention. Before the mason laid the first course of blocks, he sandwiched a generous amount of mortar between two layers of plastic sheet. He could then set the first course of blocks on this adjustable foundation and level it as required.

As is standard practice, the fresh mortar joints were tooled to a concave profile when they become “thumbprint hard.” Tooling the joints compacted the mortar and forced it into tight contact with the concrete masonry units, which is thought to improve the bond. A photographic illustration of construction of the specimens is provided in Figure 2.3.

**Specimen Surface Preparation.** The head joints between the two middle blocks of the ‘T’ specimens were intentionally left unfilled to allow these specimens to fail in shear-slip. For equilibrium, the load applied to the central block had to be transferred to the edge blocks by shear. If the centre head joint had been mortared, the specimen would not fail in shear-slip. The centre course would act essentially as a compression column with an increased cross section over part of the height. All of the specimens were allowed to air cure for at least 28 days before they were prepared for application of the GFRP.

As can be see in Figure 2.4, any excess mortar in the open head joints of the ‘T’ specimens was carefully removed to prevent interference with the slip of the blocks along





(a) Leveling the First Course



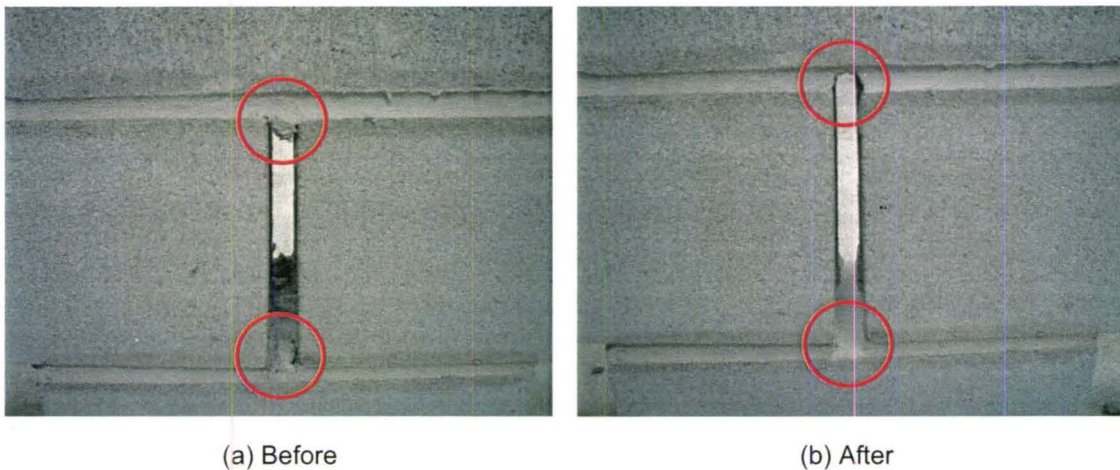
(b) Construction of Specimens in Running Bond



(c) 10 mm Plywood Strips Used as Spacers to Separate the Specimens

**Figure 2.3** – Construction of Phase One Specimens

the bed joints. This excess mortar in the open head joints was not removed until after the specimens had cured. It was carefully drilled out with a 1/8 inch masonry drill bit. Fortunately none of the specimens were damaged during this process. [It was recognized that this method was not ideal. During the construction of specimens for the later test phases, the excess mortar in the open head joints was removed while the mortar was still fresh.]



**Figure 2.4 – Excess Mortar Removed from Open Head Joints**

The surfaces of all the specimens were cleaned with a wire brush to remove any visible deposits of mortar. Dust was removed using an air hose. This was done to ensure maximum adhesion between the block and the GFRP. Surface preparation is very important to the success of FRP application because any irregularities or barriers to bond of the epoxy can result in premature delamination from the masonry (Abdel-Wahed, 2004).

**Application of GFRP.** The glass fibre fabric was cut to cover an area equal to the length of the mortared bed joint times 590 mm (three block heights plus two mortar bed

joints). Similar to El-Dakhakhni et al. (2004), for the ‘T’ specimens a gap in the fabric at the location of the open head joint was not cut out since it would provide minimal resistance. The glass fibre cloth was bonded to the specimens using a two-part epoxy; the Tyfo® S Epoxy, which was recommended and provided by the manufacturer. The fabric and the epoxy were donated by Fyfe Co. The epoxy was applied to the surface of the specimens using a paint roller. The pre-cut sheets of glass fabric were then saturated with epoxy and placed on the specimens with the fibres oriented at 0°/90° to the bed joints. Several passes of the paint roller were used to remove excess epoxy and any air voids. The removal of the air voids ensured full contact between the masonry and the GFRP. A photographic illustration of the GFRP application process is provided in Figure 2.5.

### **2.2.3 MATERIAL PROPERTIES**

**Mortar.** To simulate actual construction practices, Type-S mortar was used to construct the assemblages. The mix proportions by weight were 1 part Portland cement, 0.21 parts type-N hydrated lime and 3.53 parts masonry sand. This corresponded approximately to 1:0.5:3.3 parts by volume, based on the assumed density of the Portland cement equal to 1505 kg/m<sup>3</sup>, the type-N hydrated lime equal to 640 kg/m<sup>3</sup> and the masonry sand equal to 1608 kg/m<sup>3</sup> (Essawy, 1986). Twelve batches of Type-S mortar were mixed over the two days of specimen construction. Three [51 × 51 × 51 mm (2 × 2 × 2 inch)] mortar cube specimens were taken from each batch of mixed mortar to test for compressive strength as per ASTM C-109. The average compressive strength of the thirty-six mortar cubes was 25.1 MPa with a 5.6 % coefficient of variation (C.O.V.). The full results are provided in Table 2.2.

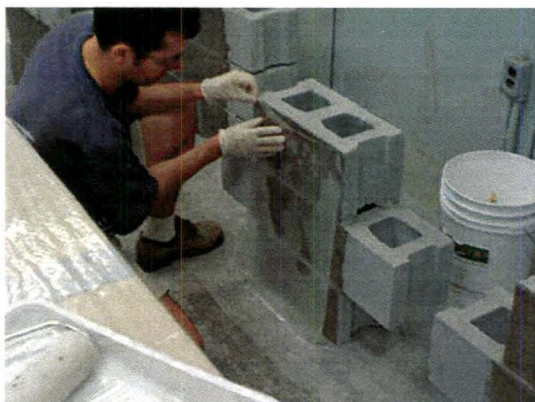




(a) Applying Epoxy to the Specimen



(b) Saturating the Fibreglass Fabric with Epoxy



(c) Applying the Fabric to the Specimen

**Figure 2.5 – Process of Applying GFRP to Phase One Specimens**

**Table 2.2 – Phase One Mortar Properties**

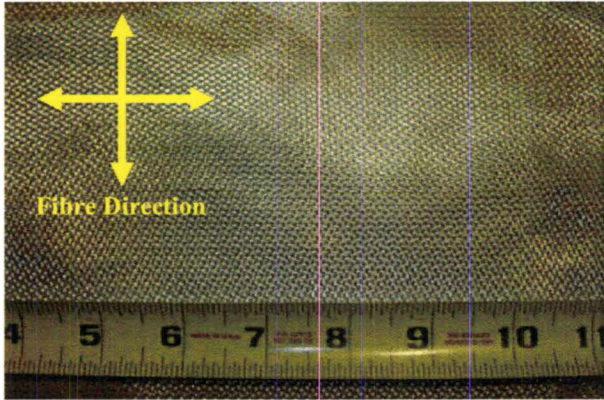
<b>Batch #</b>	<b>Cube #</b>	<b>Failure Load (kN)</b>	<b>Strength (MPa)</b>	<b>Flow (%)</b>
1	1.1	64.2	24.7	105
	1.2	65.6	25.2	
	1.3	68.8	26.5	
2	2.1	70.7	27.2	116
	2.2	72.5	27.9	
	2.3	71.1	27.3	
3	3.1	61.0	23.5	122
	3.2	63.4	24.4	
	3.3	67.1	25.8	
4	4.1	62.2	23.9	116
	4.2	66.1	25.4	
	4.3	68.3	26.3	
5	5.1	64.0	24.6	119
	5.2	64.4	24.8	
	5.3	64.5	24.8	
6	6.1	52.2	20.1	132
	6.2	56.2	21.6	
	6.3	61.7	23.7	
7	7.1	63.5	24.4	124
	7.2	64.8	24.9	
	7.3	63.7	24.5	
8	8.1	64.9	25.0	120
	8.2	63.0	24.2	
	8.3	63.5	24.4	
9	9.1	67.0	25.8	120
	9.2	68.8	26.5	
	9.3	69.4	26.7	
10	10.1	61.9	23.8	123
	10.2	62.3	24.0	
	10.3	60.0	23.1	
11	11.1	69.3	26.6	119
	11.2	67.2	25.8	
	11.3	72.6	27.9	
12	12.1	64.2	24.7	126
	12.2	64.0	24.6	
	12.3	62.2	23.9	
<b>Average =</b>		<b>65.3</b>	<b>25.1</b>	<b>120.4</b>
<b>C.O.V. (%) =</b>		<b>5.6</b>	<b>5.6</b>	<b>5.5</b>

Good mortar workability was essential for efficient and proper construction of the specimens. In the laboratory, a measure of the mortar’s workability is attained using the

flow test. In this test, the flow of the mortar is measured by the increase in diameter of a standardized 100 mm diameter cone of mortar after twenty-five drops on a flow table. Values of up to 130% are usually required to satisfy the mason’s requirements. Photographs of the mortar cube sampling and workability test are provided in Figure 2.6. While mortar strength is important as a measure of quality control, it is often less important than the bond (Drysdale et al., 1999). In general, as the workability of the mortar improves, so does the bond. The mortar had an average flow of 120.4 % for the 12 batches with a 5.5 % C.O.V. The full results are listed in Table 2.2.

**GFRP Composite.** The properties of the GFRP composite, which were determined according to ASTM D-3039, were provided by the manufacturer (Fyfe Co., 2004) and are reproduced in Table 2.3. No independent tests were conducted. Further information on both Tyfo® WEB Composite and Tyfo® S Epoxy are provided in Appendix A. A photograph of the Tyfo® WEB Composite fabric is also provided in Table 2.3.

**Table 2.3 - Tyfo® WEB Composite GFRP Properties**

<b>Composite Gross Laminate Properties</b>	<b>Value</b>	<b>Dry Fabric Photograph</b>
Ultimate tensile strength in primary fibre direction (MPa)	309	
Elongation at break (%)	1.6	
Tensile Modulus (GPa)	19.3	
Ultimate tensile strength 90° to primary fibre direction (MPa)	309	
Laminate thickness (mm)	0.25	
<b>Typical Dry Fibre Properties</b>		
Tensile Strength (GPa)	3.24	
Tensile Modulus (GPa)	72.4	
Ultimate Elongation (%)	4.5	
Density (g/cm <sup>3</sup> )	2.55	
Weight (oz./yd. <sup>2</sup> )	8.7	





(a) Mortar Cubes for Strength



(b) Flow Test for Workability (before test)



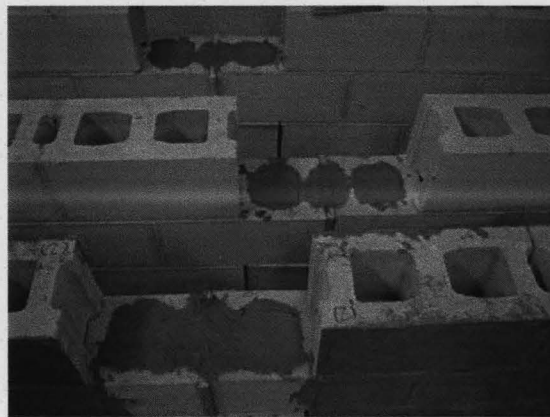
(c) Flow Test for Workability (after test)

**Figure 2.6 – Tests to Determine Mortar Properties**



## **2.2.4 TEST SETUP AND INSTRUMENTATION**

Since the specimens were not grouted, there was concern that they might fail in compression at the supports and points of application of the load rather than by shear-slip along the bed joints. This would result in a lower bound strength and diminish the value of the test. Therefore, to help ensure reaching a shear-slip failure along the bed joints, the end cells and fogged ends of blocks at the extreme top and bottom of each specimen were grouted (Figure 2.7) and subsequently wrapped with GFRP. Before the specimens were tested, the epoxy was allowed to cure for at least five days. [The manufacturer, Fyfe Co. (2004), recommends a minimum curing time of 48 hours.] Prior to testing, the top and bottom of each specimen was capped with a thin layer of Hydrostone to ensure full contact with the 12.7 mm ( $\frac{1}{2}$  inch) thick steel loading plates.



**Figure 2.7 – Grouted End Cells**

**Smaller Specimens.** The smaller specimens (i.e., A-0.5, A-1.5, T-0.5) were tested vertically under monotonically increasing loading in a Tinius Olsen testing machine, as seen in Figure 2.8.

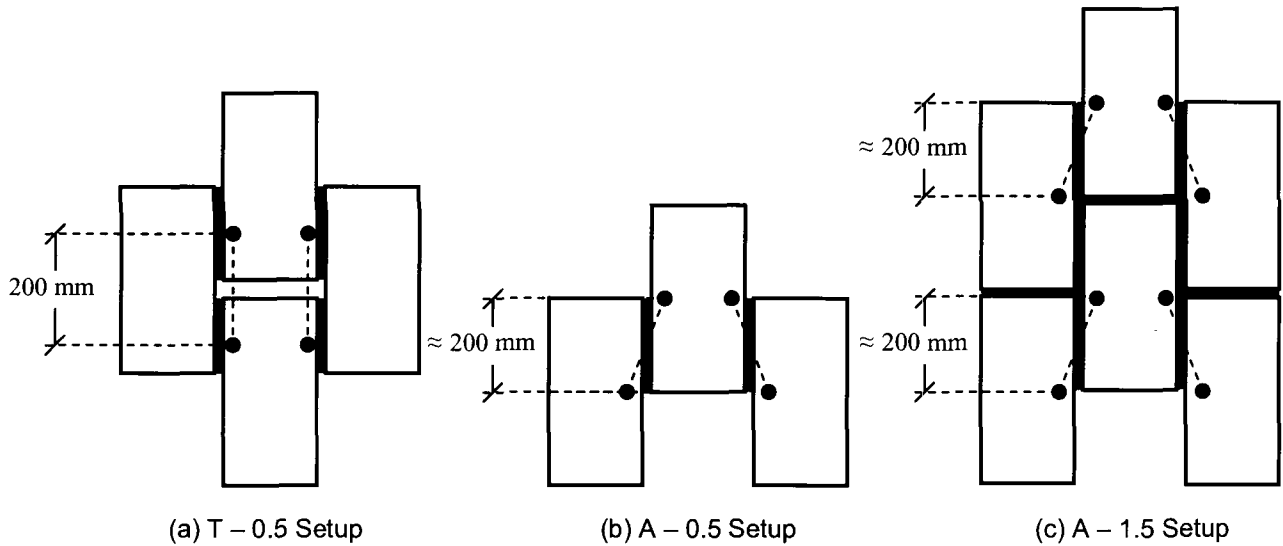


Specimen in Testing Machine

**Figure 2.8** – Tinius Olsen Testing Machine

The specimens were loading at a rate ranging between 0.005 and 0.01 inch/minute (0.12 – 0.25 mm/min). The relative movement across the bed joint slip planes was measured using a mechanical gauge. For the T-0.5 specimens, the mechanical gauge points were oriented vertically, parallel to the bed joints, and spanned the middle gap, as shown in Figure 2.9(a). Displacement measurements during testing were taken along both bed joints. For the A-0.5 and A-1.5 specimens, the mechanical gauge points were oriented at an angle across the bed joint, as shown in Figure 2.9(b) and (c), respectively. The angle across the bed joint is exaggerated in the figure, but in reality was so small that any measured displacement was assumed to equal displacement parallel to the bed joint. Displacement measurements during testing were taken along both bed joints. For the A-1.5 specimens, two pairs of mechanical gauge points were placed along both bed joints. This was done to gain a more representative displacement measurement along the longer bed joint. In the analysis, the gauge points on the left were averaged and the gauge points on the right were averaged. The nominal gauge length between the points was 200 mm.

For all of the aforementioned specimens, displacement readings were only taken along one face. The load was recorded manually from the gauge on the test machine.



**Figure 2.9** – Phase One Mechanical Displacement Gauge Setup for Smaller Specimens

**Larger Specimens.** For the larger specimens (i.e., A-2.5, T-1.5), it was necessary to construct a customized testing apparatus, as shown in Figure 2.10. The apparatus consisted essentially of two steel columns prestressed down onto the 600 mm (2 ft.) thick strong floor of the laboratory, a spreader beam, and a 51 mm (2 inch) thick steel top bearing plate. The load was applied using a hydraulic cylinder, with 1779 kN (400,000 lbs.) maximum capacity. The applied load was monitored using a commercial load cell with a spherical head.

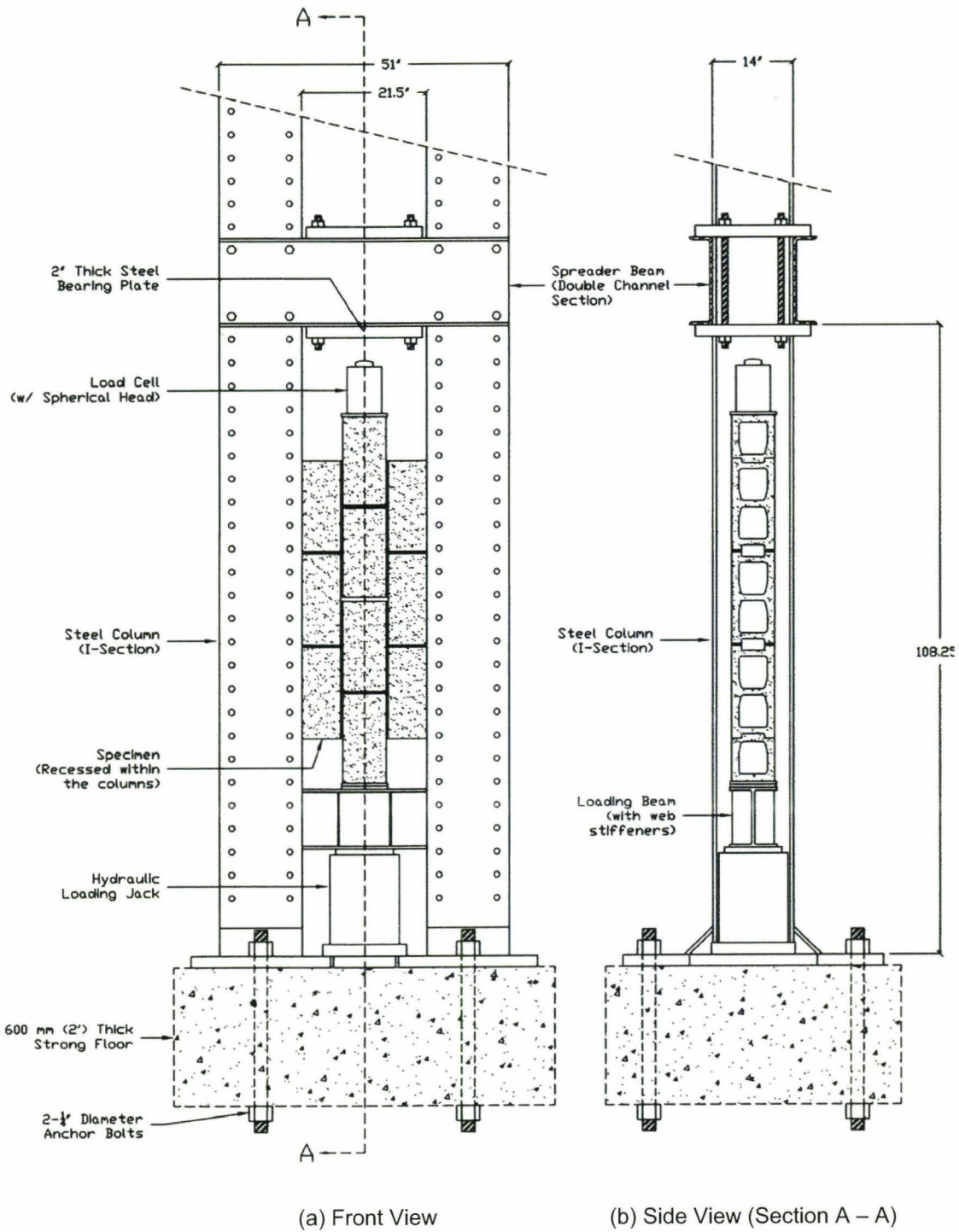
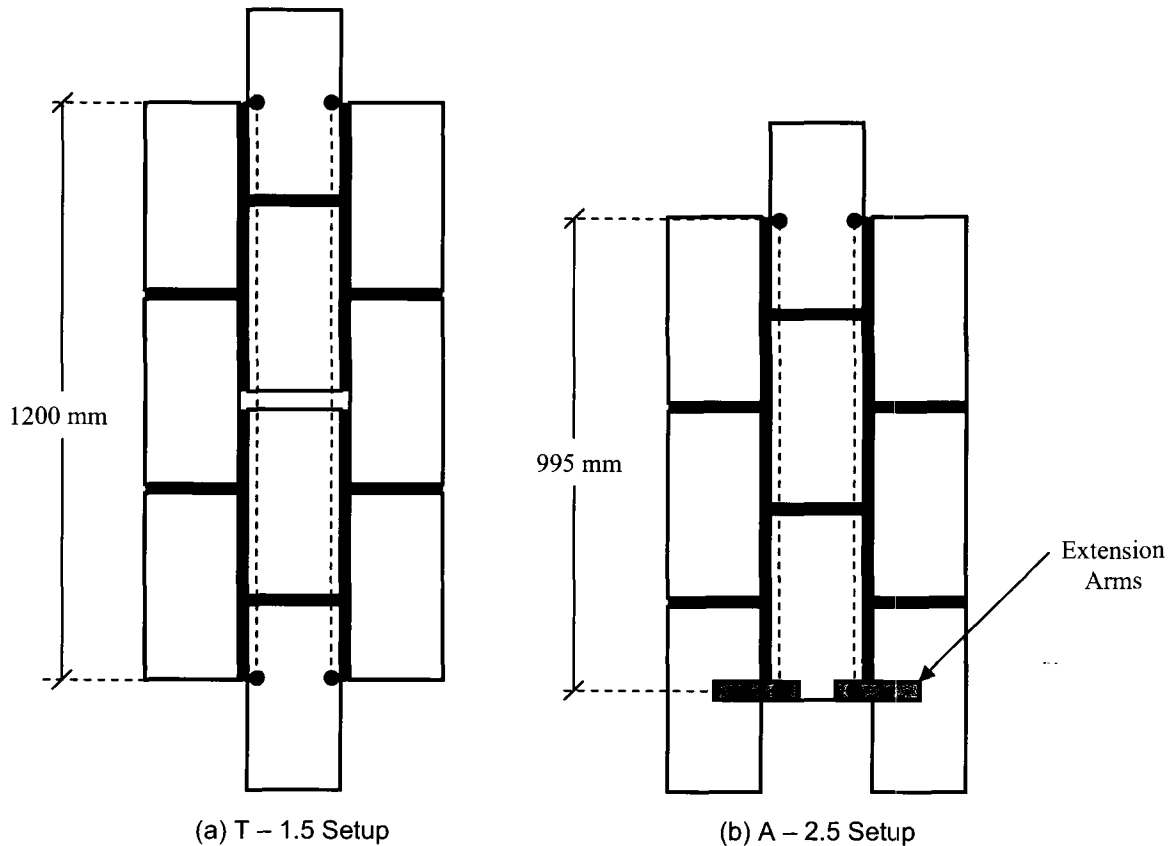


Figure 2.10 – Customized Testing Apparatus

The relative movement between the blocks along the slip plane was measured using linear potentiometric displacement transducers (LPDTs), with 25 mm stroke, connected to a PC data acquisition system. For the T-1.5 specimens, four LPDTs (two per face) were placed vertically to be parallel to the bed joints and spanned the middle gap, as shown in Figure 2.11(a). For the A-2.5 specimens, using extension arms to cross the bed joint, four LPDTs (two per face) were placed vertically and parallel to the bed joints, as shown in Figure 2.11(b). The extension arms were necessary to allow the LPDTs to be placed vertically. Otherwise they would have been oriented at an angle and not measured the actual slip. For the T-1.5 and A-2.5 specimens, the nominal gauge lengths were 1200 mm and 995 mm, respectively.



**Figure 2.11 – Phase One LPDT Setup for Larger Specimens**



For the A-2.5 and T-3.0 specimens, the load was recorded using a commercial load cell, which was also connected to the data acquisition system. For the specimens retrofitted with GFRP, a 445 kN (100,000 lbs.) load cell was used to accommodate the higher failure loads. Since the specimens not retrofitted with GFRP would undoubtedly fail at much lower loads, a 111 kN (25,000 lbs.) load cell was used for improved resolution.

Specimens placed in either testing apparatus were positioned and centred as exactly as possible to limit any rotation of the blocks in the direction perpendicular to the plane of the laminate. Before the ‘A’ specimens were tested, the bases were set on two steel rollers. The centrelines of the rollers were placed 5 mm away from the inside face of the bottom blocks. This was done to minimize the eccentricity between the top and bottom loading, which minimized the induced bending moment along the bed joints. The bases of the ‘T’ specimens were set directly on the base of the test machine or jack.

### **2.3 PHASE TWO PRIMER**

The second test phase was conducted to evaluate the merits of obtaining two sets of data from each specimen. The details of this phase are presented in Section 2.5. It was thought that this information would make more sense once the details of Phase Three in Section 2.4 were presented.

### **2.4 PHASE THREE**

#### **2.4.1 SPECIMEN TYPES AND DESIGNATION**

In Phase Three, twenty-one T-1.5 type specimens (see Figure 2.1(e)) were constructed. [A discussion regarding the analysis and justification of specimen selection

is provided in Chapter 3.] Again, the T-1.5 specimen is a variation of the “modified triplet” specimen, which provided double symmetry about the gap. All twenty-one specimens were retrofitted with a proprietary surface-bonded fibreglass mesh. This fibreglass mesh is different from the fibreglass cloth used in Phase One, which was more of a traditional fabric. It is an open mesh glass fibre laminate coated with polymer. Photos illustrating the difference between all the meshes used are provided in Figure 2.12. The fibreglass mesh was chosen because it was more readily available and came in a variety of lower density weights. It was important for the specimens to fail in shear slip. Using lower density laminates helped ensure that the laminate fails before the blocks at the supports fail. The fibreglass cloth used in Phase One was adhered to the specimens with an epoxy resin, whereas the fibreglass mesh used in Phase Three was adhered via a modified mortar parging. The modified parging provides a finish that could be part of the final finish whereas the epoxy is not an attractive finish.

Three different dry weights of mesh were used:  $131 \text{ g/m}^2$  ( $3.9 \text{ oz./yd.}^2$ ),  $163 \text{ g/m}^2$  ( $4.8 \text{ oz./yd.}^2$ ) and  $359 \text{ g/m}^2$  ( $10.6 \text{ oz./yd.}^2$ ). For a fourth weight the  $131 \text{ g/m}^2$  ( $3.9 \text{ oz./yd.}^2$ ) mesh was applied in a double layer. Each mesh was applied to three T-1.5 specimens at both,  $0^\circ/90^\circ$  and  $\pm 45^\circ$  to the bed joint. In total, nine specimens had mesh at  $\pm 45^\circ$  to the bed joint and twelve specimens had mesh at  $0^\circ/90^\circ$  to the bed joint. The full test matrix for Phase Two is shown in Table 2.4.

Unlike Phase One, where the properties of the fibreglass cloth fabric were identical in both directions (Fyfe Co., 2004), the mesh used in Phase Three was nonisotropic. The strength in the warp direction was not equal to the strength in the weft



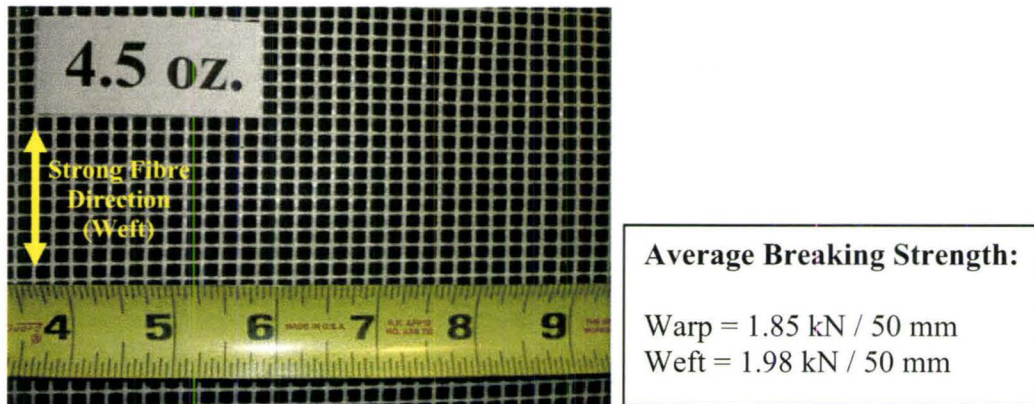
direction. The warp refers to the fibres that run lengthwise along the mesh and the weft refers to the fibres orientated at 90° to the warp. The average breaking strength of the meshes were provided by the manufacturer and are reproduced in Figure 2.12. No independent tests were conducted.

**Table 2.4 – Phase Three Testing Schedule**

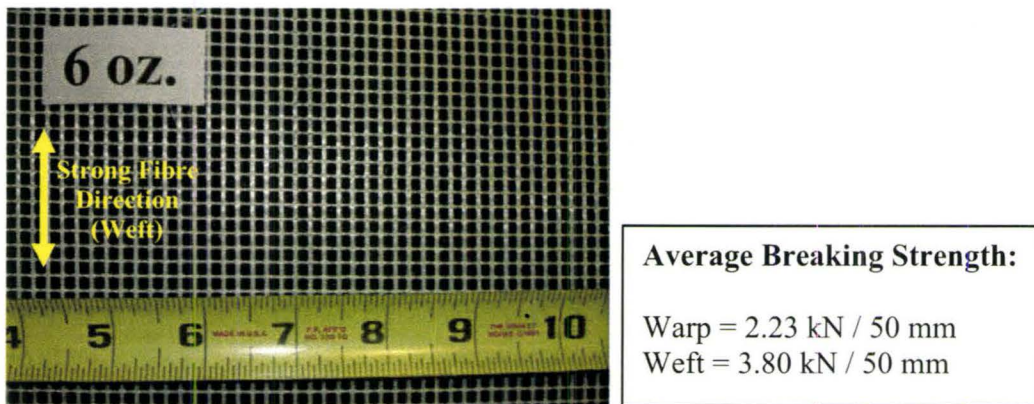
<b># of Specimens</b>	<b>Mesh Weight (Dry)</b>	<b>Mesh Weight (Finish/Parged)</b>	<b>Orientation to Bed Joint</b>
3	131 g/m <sup>2</sup> (3.9 oz./yd. <sup>2</sup> )	153 g/m <sup>2</sup> (4.5 oz./yd. <sup>2</sup> )	0°/90°
3			±45°
3	163 g/m <sup>2</sup> (4.8 oz./yd. <sup>2</sup> )	200 g/m <sup>2</sup> (6 oz./yd. <sup>2</sup> )	0°/90°
3			±45°
3	262 g/m <sup>2</sup> (7.8 oz./yd. <sup>2</sup> )	306 g/m <sup>2</sup> (9 oz./yd. <sup>2</sup> )	0°/90°
3			±45°
3	359 g/m <sup>2</sup> (10.6 oz./yd. <sup>2</sup> )	418 g/m <sup>2</sup> (12.3 oz./yd. <sup>2</sup> )	0°/90°

#### **2.4.2 CONSTRUCTION AND PREPARATION OF THE TEST SPECIMENS**

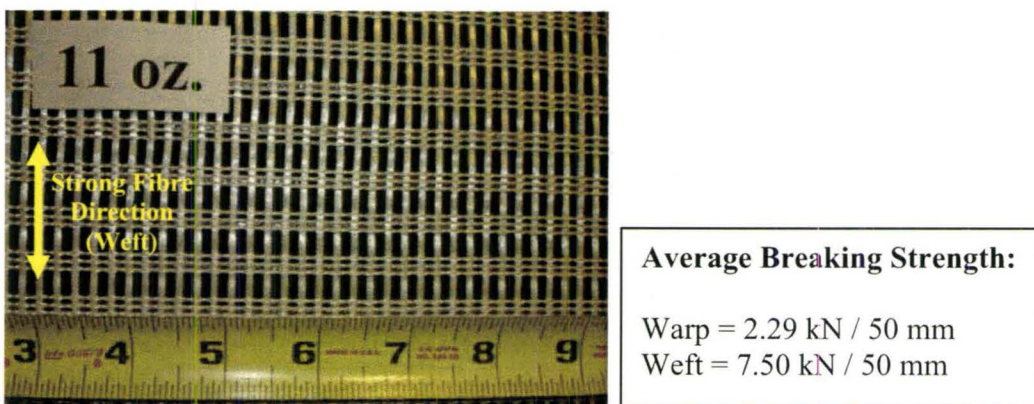
The twenty-one T-1.5 specimens used in Phase Two were constructed by the same experienced mason, with concrete blocks from the same batch; using the same techniques as for the specimens in Phase One (see Section 2.2.2). Once again, the head joints between the two middle blocks of the specimens were left unfilled to allow these specimens to fail in shear-slip. For Phase Three, the excess mortar in the open head joint was removed while it was still fresh. This eliminated the need for drilling and light chiselling later on (as was required for Phase One), which could have damaged the specimens. All of the specimens were allowed to air cure for at least 28 days before they were prepared for application of the mesh. The specimens were prepared for the application of the mesh using the same techniques of Phase One (see Section 2.2.2).



(a) Dry Mesh Weight: 3.9 oz./yd.<sup>2</sup> (4.5 oz./yd.<sup>2</sup> Finish Weight)



(b) Dry Mesh Weight: 4.8 oz./yd.<sup>2</sup> (6.0 oz./yd.<sup>2</sup> Finish Weight)



(c) Dry Mesh Weight: 10.6 oz./yd.<sup>2</sup> (12.3 oz./yd.<sup>2</sup> Finish Weight)

Figure 2.12 – Phase Three Fibreglass Mesh

As before, mesh was applied to both faces of the specimen. Proper cutting and placement of the mesh was critical in Phase Three. Since the mesh was nonisotropic, the effectiveness of the retrofit was dependent on the fibre orientation. Typically, externally bonded laminates are applied so that the fibres mainly resist forces in tension (Kolsch, 1998).

For the  $0^\circ/90^\circ$  mesh specimens, the mesh was cut to cover an area equal to the length of the mortared bed joint (length of slip planes) times 590 mm (three block heights plus two mortar bed joints). The mesh was cut so that, when applied to the specimens, the fibres in the strong direction (the weft) were perpendicular to the bed joint. In this configuration, the fibres would provide a shear friction type resistance. A gap in the mesh was cut out at the location of the open head joint to allow shear slip to occur.

For the  $\pm 45^\circ$  mesh specimens to achieve the maximum possible strength, it was necessary for the fibres in the strong direction to be in tension during the test. This configuration is most effective for resisting shear forces (Vandergrift, 2002). Figure 2.13(a) shows the shear deformation along the bed joints and the associated diagonal tension fields (Figure 2.13(b)), as reported by El-Dakhkhni (2002). Since the mesh was not isotropic, in order for the fibres in the strong direction to be in tension, the mesh had to be cut and applied in four quadrants. Based on the shear deformation of the bed joints, orienting the mesh in each quadrant such that the fibres in the strong direction pointed towards the gap ensured they would be in tension (Figure 2.14). A cardboard template and a  $45^\circ$  set-square were used to expedite the cutting of the ninety-six pieces of mesh



required. The mesh was cut so that adjacent pieces would overlap by 100 mm. The minimum recommended overlap is 50 mm (DuRock, 2005).

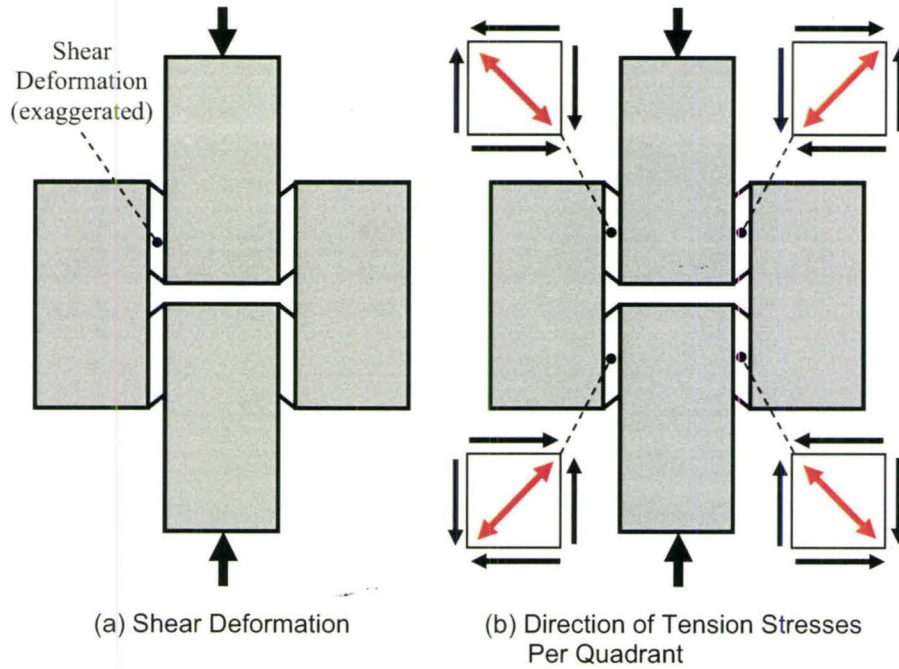


Figure 2.13 – Shear Deformation and Tension Stresses Along the Bed Joints During Testing

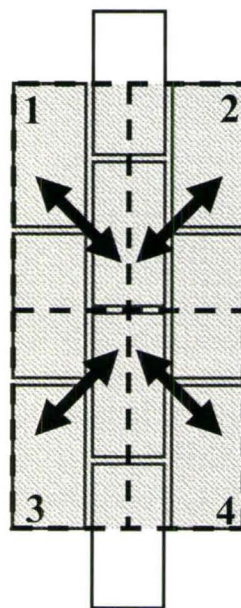


Figure 2.14 – Strong Fibre Direction Per Quadrant

Unlike the Tyfo® WEB Composite used in Phase One, which is designed to be saturated with epoxy before application, the fibreglass mesh was adhered to the specimens using an acrylic modified mortar, or parging. The parging is ideal for adhering fibreglass mesh because it is both strong and flexible. The proprietary water-based acrylic *Prep-Coat* product, sold in 30 kg buckets, was mixed with Type 10 Portland cement at a ratio of 3:2 by weight (i.e. three parts Pre-Coat to two parts Type 10 Portland cement) as per the manufacturer's recommendations. The parging was mixed in batches of 10 kg (6 kg water-based acrylic to 4 kg Type 10 Portland cement) which was enough for one specimen. Using an electric drill with a mixing paddle, the two components were gradually blended together until the mixture was homogenous. A few drops of water were added to improve the workability of the mix. Good workability is important because it prevents excess drying when the parging is applied to large surfaces, and allows the parging to properly penetrate the openings of the mesh for maximum embedment. (Kolsch, 1998). Based on the supplier's information (DuRock, 2005), it was acceptable to add up to 90 millilitres of water to a 10 kg batch of parging to improve the workability.

The parging was applied to the face of the specimens using an unnotched rectangular trowel. While holding the trowel at approximately 30°, a 2 to 3 mm thick layer of the parging was applied. To prevent the blocks from absorbing too much water and drying out the parging before applying the mesh, only one face of the specimen was coated at a time. The reinforcing mesh was immediately imbedded into the parging. With the open mesh, air voids were not an issue, but it was important that the mesh was properly oriented and did not have any wrinkles, ripples or waves. Once the mesh was

embedded, the trowel was passed over it to push the parging through the openings to ensure full contact. Another layer of parging, approximately 1 mm thick, was applied to completely cover the mesh, if necessary. Any parging that penetrated the gap in the centre course was cleaned out to prevent interference with slippage of the blocks during testing. The parging was allowed to cure for at least 7 days, as per the manufacturer's recommendation, before testing. A photographic record of the glass mesh application process is provided in Figure 2.15 (page 57).

As in Phase One, the specimens were not grouted. Once again to ensure shear-slip failure along the bed joints, rather than compression failure at the supports, the extreme top and bottom of each specimen were grouted (Figure 2.7).

### **2.4.3 MATERIAL PROPERTIES**

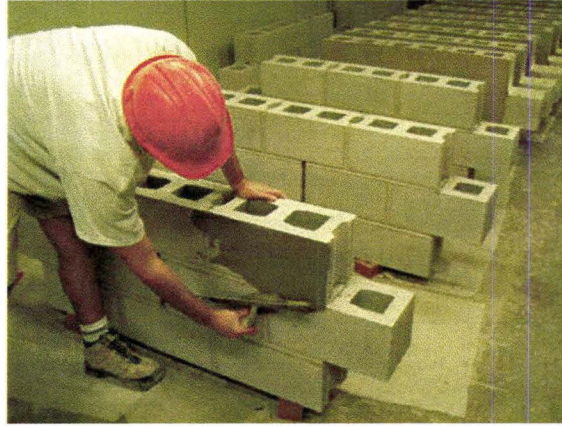
**Mortar and Parging.** To simulate actual construction practices, Type-S mortar was used to construct the assemblages. The mix proportions by weight were 1 part Portland cement, 0.21 parts lime and 3.53 parts masonry sand. Twelve batches of Type-S mortar were mixed over the two days of specimen construction. Three [51 × 51 × 51 mm (2 × 2 × 2 inch)] mortar cube specimens were taken from each batch of mixed mortar to test for compressive strength as per ASTM C-109. The average 28-day compressive strength of the thirty-six mortar cubes was 21.1 MPa with a 10.4% COV. The mortar had an average flow of 113.3% for the 12 batches with a 5.2% COV.

As a comparison, six cube specimens were taken from one batch of the parging to test its 7-day and 28-day strength. The 7-day and 28-day compressive strengths of the parging were 20.3 MPa (10.6% COV) and 28.6 MPa (8.9% COV), respectively. Thus, in





(a) Mixing the Parging



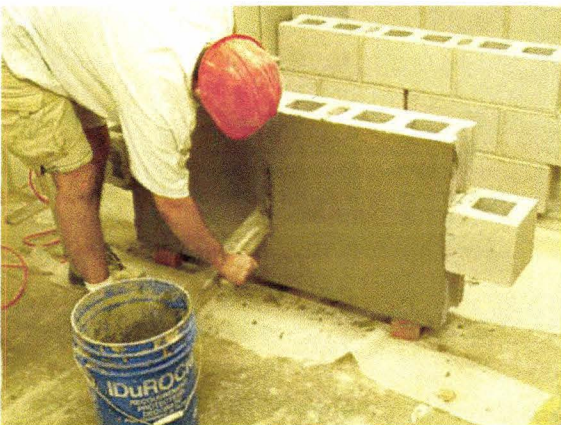
(b) Applying a Thin Layer of Parging



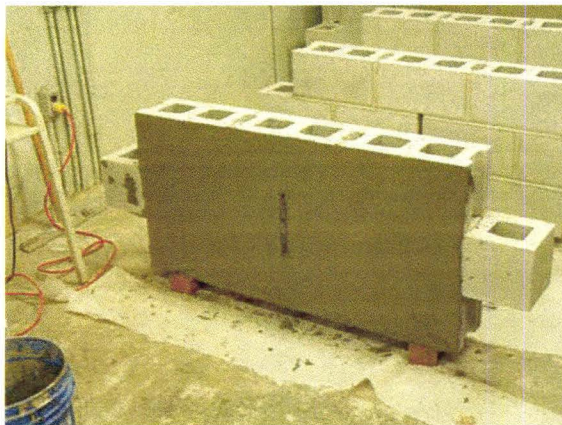
(c) Setting the Mesh into the Parging Layer



(d) Applying a Layer of Parging Over the Mesh



(e) Removing Excess Parging from the Open Head Joint



(f) Finished Specimen

**Figure 2.15** – Application of Glass Mesh Using Modified Parging

general, the strengths of the mortar and the parging are comparable. No further independent tests were conducted on the parging. As per ASTM D1623C the bond strength of the parging was greater than 0.3 MPa after 7 days of curing (DuRock, 2005). Further information on the parging can be found in Appendix A. A summary of the results are presented in Table 2.5 (page 59).

**Fibreglass Mesh.** The properties of the fibreglass meshes used, which were provided by the supplier, have been reproduced in Table 2.6 (page 60). No independent tests on the meshes were conducted. Further information can be found in Appendix A.

#### **2.4.4 TEST SETUP AND INSTRUMENTATION**

The twenty-one glass mesh reinforced T-1.5 specimens were tested with the same testing apparatus as in Phase One, as was shown in Figure 2.10. Prior to testing, the top and bottom of each specimen was capped with a thin layer of Hydrostone to ensure full contact with the 12.7 mm ( $\frac{1}{2}$  inch) thick steel loading plates.

For Phase Three, the setup for monitoring the relative movement between the blocks along the slip plane was refined. The four 25 mm stroke LPDTs from Phase One were replaced with eight 12.5 mm stroke LPDTs connected to a PC data acquisition system. The LPDTs were still placed vertically and parallel to the bed joints, but this time they did not span the middle gap. Each LPDT (four on the front and four on the back of the specimen) monitored displacements along its own slip plane. The extension arms were once again utilized to permit the vertical LPDTs to measure slip across the bed joint. An illustration of the instrumentation is shown in Figure 2.16. The average gauge length for each LPDT was 563.4 mm.

**Table 2.5 – Phase Three Mortar Properties**

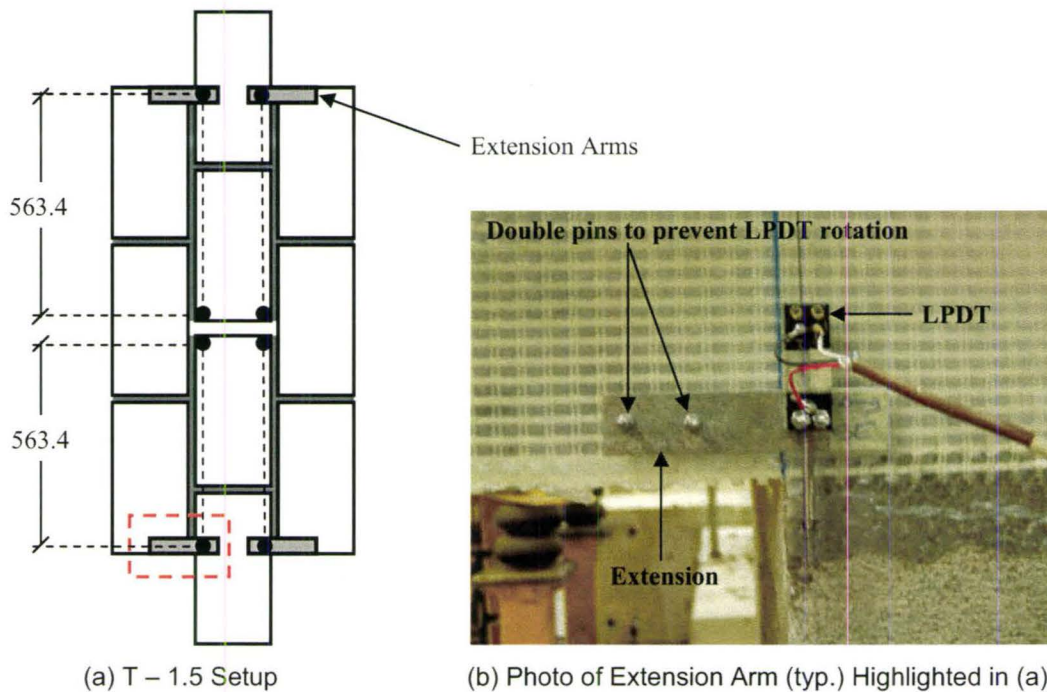
<b>Batch #</b>	<b>Cube #</b>	<b>Failure Load (kN)</b>	<b>Strength (MPa)</b>	<b>Flow (%)</b>
1	1.1	46.6	17.9	106
	1.2	50.7	19.5	
	1.3	47.4	18.2	
2	2.1	48.4	18.6	107
	2.2	50.7	19.5	
	2.3	51.0	19.6	
3	3.1	55.7	21.4	119
	3.2	56.7	21.8	
	3.3	59.3	22.8	
4	4.1	47.0	18.1	117
	4.2	48.7	18.7	
	4.3	47.3	18.2	
5	5.1	56.6	21.8	118
	5.2	60.4	23.2	
	5.3	61.2	23.5	
6	6.1	55.1	21.2	107
	6.2	57.1	22.0	
	6.3	51.2	19.7	
7	7.1	52.8	20.3	113
	7.2	54.2	20.8	
	7.3	53.7	20.6	
8	8.1	66.3	25.5	104
	8.2	66.9	25.7	
	8.3	60.5	23.3	
9	9.1	57.8	22.2	114
	9.2	65.3	25.1	
	9.3	62.9	24.2	
10	10.1	52.6	20.2	122
	10.2	53.8	20.7	
	10.3	59.5	22.9	
11	11.1	57.7	22.2	115
	11.2	57.1	22.0	
	11.3	53.8	20.7	
12	12.1	52.4	20.1	118
	12.2	46.1	17.7	
	12.3	49.0	18.8	
<b>Average =</b>		<b>54.8</b>	<b>21.1</b>	<b>113.3</b>
<b>C.O.V. (%) =</b>		<b>10.4</b>	<b>10.4</b>	<b>5.2</b>



**Table 2.6 – Fibreglass Mesh Properties**

Approx. Mesh Weight, g/m <sup>2</sup> (oz./yd. <sup>2</sup> )		Average Breaking Strength (N per 5cm wide strip)		Dry Elongation (%)	
Dry	Finished	Warp	Weft	Warp	Weft
131 (3.9)	153 (4.5)	185	198	4.2	3.4
163 (4.8)	200 (5.9)	223	380	3.8	2.9
359 (10.6)	418 (12.3)	229	750	3.7	4.3

Specimens placed in the test apparatus were positioned and centred as accurately as possible to limit any rotation of the blocks in the direction perpendicular to the plane of the laminate. Another refinement added to the placement of the specimens in the apparatus was to centre and set them on a 1 mm thick, 15 mm wide strip of metal. The strip acted like a point load, ensuring the reaction load acted along the centre of the specimen, within the 15 mm width. With the strip at the bottom and the spherical head of the load cell at the top, the line of action was guaranteed to act close to the centreline of the specimen.

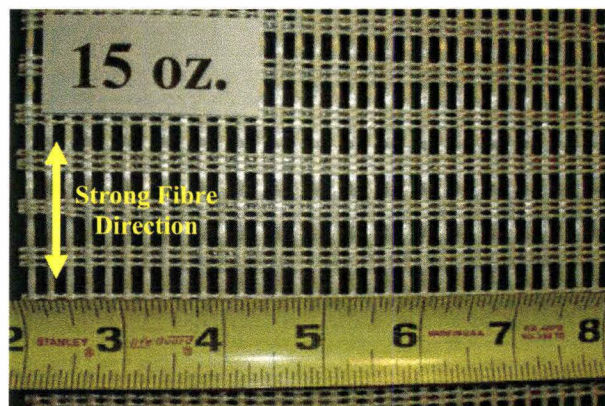


**Figure 2.16 – Phase Three LPDT Setup for All Specimens**

## 2.5 PHASE TWO

The second test phase was designed to (1) evaluate the potential to obtain two sets of data from each specimen, (2) to provide insight into the relative merits of using fibreglass mesh compared to fibreglass cloth, and (3) to provide insight into the relative merits of applying fibreglass mesh with epoxy versus modified mortared parging. The epoxy used was the same as that used for adhering the fibreglass fabric in Phase One testing.

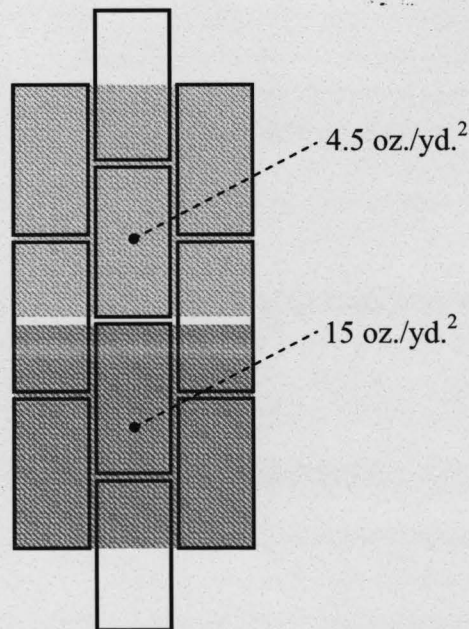
The T-1.5 specimens were selected for this phase and were tested using the same equipment as used for the larger specimens of Phase One. In order to obtain two sets of data from one specimen, it was decided to apply two different weights of mesh on the same specimen. Half of each specimen would be reinforced with a light weight mesh and the other half would be reinforced with a heavier mesh. As described earlier for the other phases, the reinforcement was placed on both the front and back of the specimen. The mesh weights (finished) selected were: 4.5 oz./yd.<sup>2</sup> and 15 oz./yd.<sup>2</sup>. A photograph of each mesh can be found in Figures 2.12(a) and 2.17, respectively. The meshes were oriented at 0°/90° to the bed joint. The reinforcement scheme is illustrated in Figure 2.18.



**Figure 2.17** – 15 oz./yd.<sup>2</sup> (Finished Weight) Mesh



The concept was that the slip planes reinforced with the 15 oz./yd.<sup>2</sup> mesh would be stronger and hence not fail before the slip planes reinforced with 4.5 oz./yd.<sup>2</sup> mesh failed. To monitor the displacements along all the slip planes, the same LPDT instrumentation scheme illustrated previously in Figure 2.16 was used. It was assumed that only the slip planes reinforced with the 4.5 oz./yd.<sup>2</sup> mesh would fail, and that insignificant displacements would occur along the slip planes reinforced with the 15 oz./yd.<sup>2</sup> mesh. The specimen would then be repaired, by dry packing the cells along the damaged slip planes with stiff grout, and retested. The cured grout would then ensure failure along the 15 oz. mesh reinforced slip planes.



**Figure 2.18 – Phase Two Mesh Reinforcement Scheme**

## 2.6 SUMMARY

- The test method, apparatus and specimens were selected to simulate shear slip, following the rationale from Kolodziejski (1982) and Eshani (1997),

- The research was conducted in three phases with the scope ranging from analyzing the influence of specimen shape, assessing the feasibility of obtaining two sets of data from each specimen, to determining the influence of fibre weight and orientation on the shear-slip performance.
- Construction of the specimens followed standard practices in order to better reflect actual wall construction practices.
- As is discussed in Chapter 3, the Phase One test program was successful in defining the best shape and size of test specimen to use. The data itself was also of direct use as an evaluation of strength and behaviour of fibreglass reinforced masonry subjected to shear-slip failure.
- As is discussed in Chapter 3, the Phase Two test program showed that it was neither practical nor reliable to attempt to obtain two sets of data from one test specimen. Data from first failure of the specimen is of some direct use.
- As is discussed in Chapter 4, the Phase Three test program provides good documentation of strength and behaviour of originally unreinforced concrete block masonry retrofitted, to improve shear-slip capacity, with surface-bonded fibreglass mesh using a modified paring as the bonding material.

## **CHAPTER 3: PHASE ONE AND TWO EXPERIMENTAL RESULTS**

### **3.1 INTRODUCTION**

This chapter contains the results from Phases One and Two of the experimental investigation. The purposes of these phases were described in Chapter 2.

The data plots presented in this chapter contain the load per metre (kN/m) versus average displacement of each test conducted in Phase One of this experimental investigation. This allows for a more direct comparison of the results for each specimen shape when the test load (plotted along the y-axis) was divided by the length of the specimen's respective slip plane. All the displacements recorded along the slip planes were averaged and plotted along the x-axis. Data plots of all the raw data are reproduced in Appendix C.

To assist with the analysis, an average curve for each set of test specimens was also calculated. An average curve was calculated by first dividing each kN/m value along the y-axis by its respective maximum (ultimate) load; a process known as normalizing. At this stage, the y-axis of each plot ranges from a dimensionless 0 to 1. For each set of data, a best-fit curve was determined using *Microsoft Excel*. Then, at each point along the y-axis from 0 to 1, the corresponding displacement values, along the x-axis were averaged. The best-fit curve was used for this step. [This also could have been done another way, where, at selected displacements along the x-axis, the corresponding dimensionless y-axis values could be averaged.] This averaging of the normalized curves results in a single curve, but the y-axis still ranges from a dimensionless 0 to 1. The final step is to multiply the y-axis by the average maximum load/metre of the specimen set.

## **PHASE ONE**

The designations for each type of specimen were presented in Chapter 2 on pages 28 and 29.

### **3.2 A – 0.5 SPECIMENS**

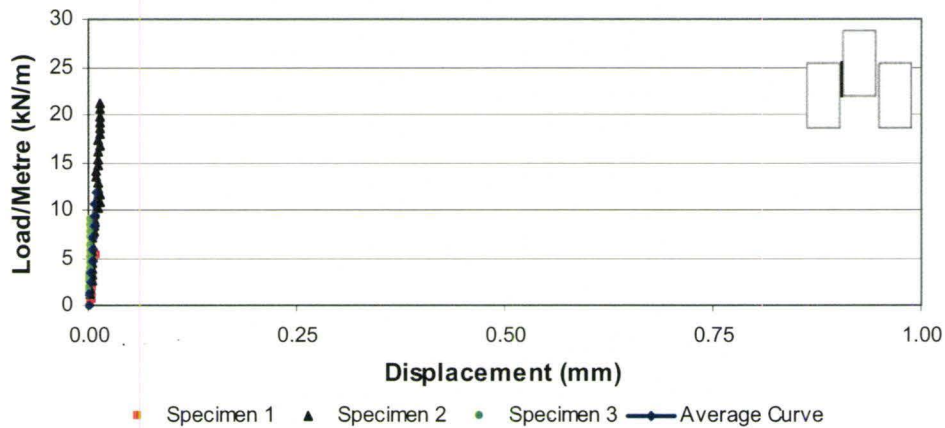
#### **3.2.1 UNREINFORCED (AU – 0.5)**

Of all the specimens tested in Phase One, these unreinforced A-shaped specimens with a half-block shear slip length were by far the most fragile. To avoid damaging the specimens while they were being transported to the testing machine and during set-up for testing, it was necessary to apply precompression force normal to the bed joint slip plane. This was accomplished with the use of two 190 mm × 190 mm × 3/4 inch thick plywood boards and a 1/2 inch (12.7 mm) diameter threaded rod with washers and nuts. All of this apparatus was removed prior to testing. Even with all these precautions, two out of the five specimens were damaged prior to testing. The extreme fragile nature of this specimen configuration is the first comment against its use in any further experimental investigations.

It was expected that these specimens would not be able to support much load prior to failure; thus mechanical Demec displacement readings were taken at 0.125 kN load increments for the first specimen and 0.250 kN load increments for the remaining two specimens. Once the ultimate load was reached, which occurred at very low displacement, the specimen failed suddenly along one of the bed joints. The failure was debonding of the mortar at the interface between the mortar and the block. At this point, the specimen had zero capacity. The average failure load was 4.9 kN at an average



displacement of 0.0087 mm. The amount of scatter of the failure load is evident by the high coefficient of variation (C.O.V.) of 71.9%. The Load/Metre versus Average Displacement plot is provided in Figure 3.1.



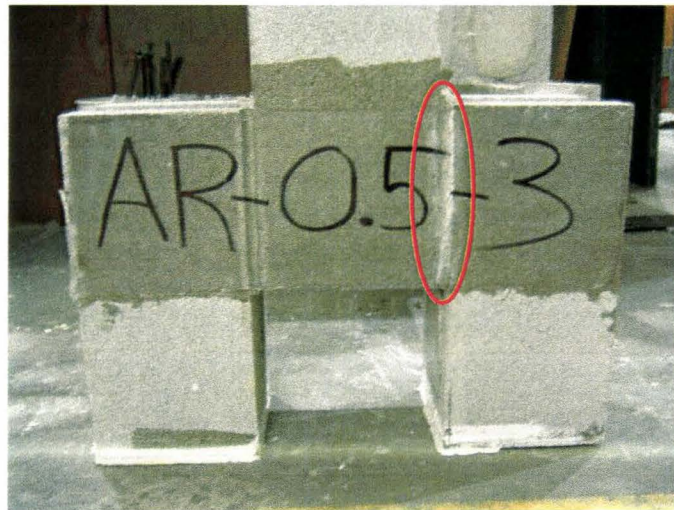
**Figure 3.1 – Specimen AU – 0.5: Load/Metre versus Displacement**

### **3.2.2 REINFORCED (AR – 0.5)**

With the GFRP laminate applied, the A-shaped specimens with half-block overlap were far easier to handle. Precompression force was not required to assist with their transportation and test set up. Nonetheless, care was taken so as not to damage the specimens. It was expected that these specimens would be able to support much higher loads prior to failure. Thus mechanical Demec displacement readings were taken at 1.0 kN load intervals. As the load reached the maximum, fine cracks and white discoloration, as shown in Figure 3.2, were observed in the epoxy along one of the bed joint slip planes. The white discoloration is analogous to that observed when a piece of coloured plastic is bent to an extreme angle causing permanent deformation.



During post-cracking, the glass fibres suspended in the epoxy are being deformed but are still intact. After the maximum load was reached, the specimen did not lose all capacity. It continued to support some, albeit decreasing, load, which was accompanied by further cracking and discolouration of the failed bed joint slip plane, as the displacement increased. The post peak response was recorded by stopping the test machine at various levels of displacement and recording the load at that displacement. Eventually, the displacement reached a large enough value where the fibres began to tear.



**Figure 3.2** – Typical Damage Along Slip Plane of Reinforced A-0.5 Specimens

Loading in the post-peak region could continue up to the complete tearing of the glass fibres. This was achieved for the first specimen only. For the remaining two specimens their respective tests were halted once the displacements reached the maximum value that the Demec gauge could read. These specimens still had residual capacity. The average maximum load was 31.7 kN at an average displacement of 0.12 mm. Use of GFRP greatly deduced the scatter of the results, compared to the

unreinforced specimens, as is evident by the much lower C.O.V. of 18.0%. The Load/Metre versus Average Displacement plot is presented in Figure 3.3.

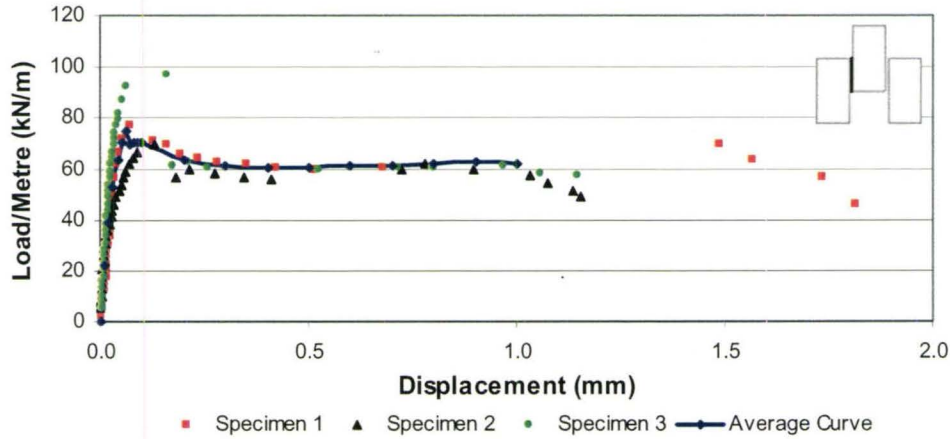


Figure 3.3 – Specimen AR – 0.5: Load/Metre versus Displacement

### 3.3 A – 1.5 SPECIMENS

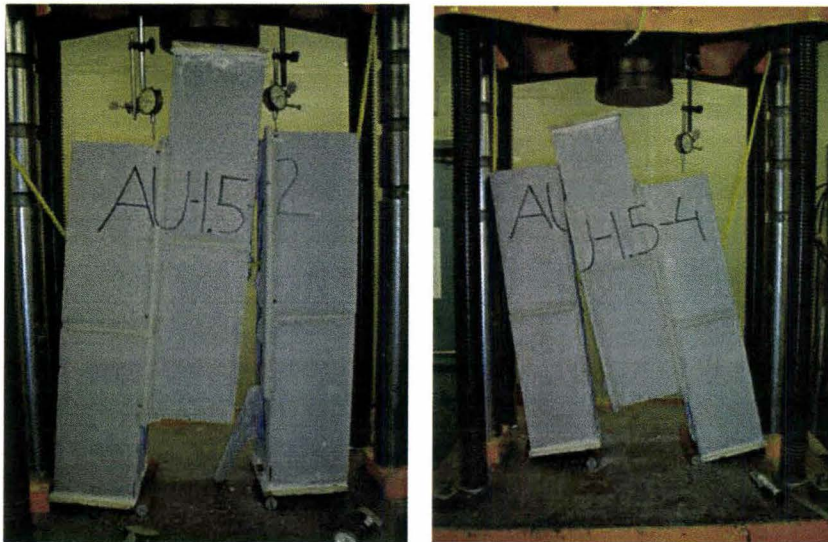
#### 3.3.1 UNREINFORCED (AU – 1.5)

Due to the greater robustness of these larger specimens, all five specimens remained undamaged during transport to the testing machine and test set-up. No precompression was used. This was the first set of unreinforced specimens tested for Phase One of this experimental investigation. During testing, Demec displacement readings were taken at 1.0 kN intervals. When the ultimate (maximum) load was reached, which occurred at very low displacement, the specimen failed suddenly along one of the bed joints. The failure was debonding of the mortar at the interface between the mortar and the block, as shown in Figure 3.4.

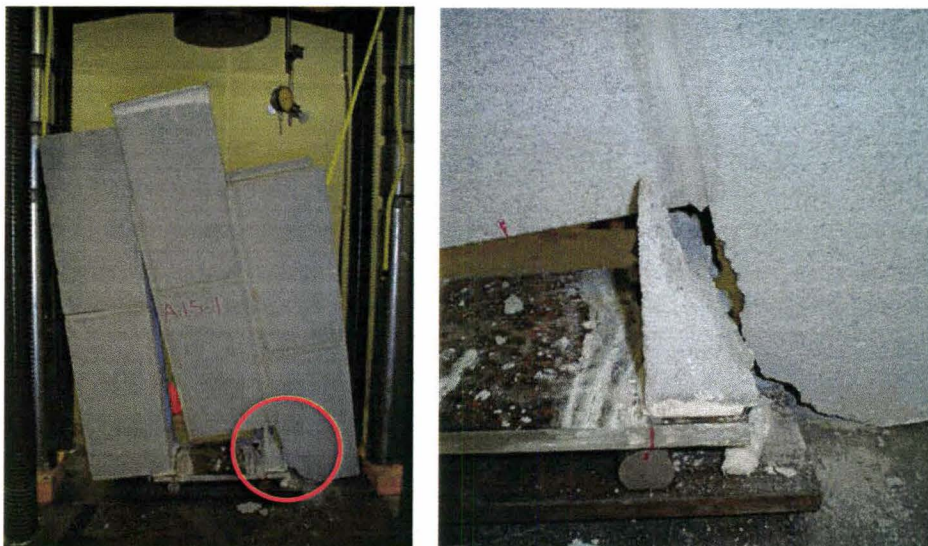
Following failure at the ultimate load, the specimen had zero capacity. The average failure load was 22.9 kN at an average displacement of 0.023 mm. The amount



of scatter of the failure load is evident by the C.O.V. of 24.6%. Only the failure of the first specimen was accompanied by crushing of one block at the lower support points, as shown in Figure 3.5. This toe crushing seemed to happen simultaneously with shear slip failure and did not occur in any of the other specimens. The Load/Metre versus Average Displacement plot is provided in Figure 3.6.



**Figure 3.4 – Typical Failure Mode of AU – 1.5 Specimens**



**Figure 3.5 – Block Crushing at Lower Support Point of Specimen AU – 1.5 – 1**

If the test results from specimen AU – 1.5 – 1 is omitted as not indicative of shear-slip capacity, the average maximum load changes to 21.2 kN/m (with a low C.O.V. of 11.2 %) at 0.023 mm average displacement.

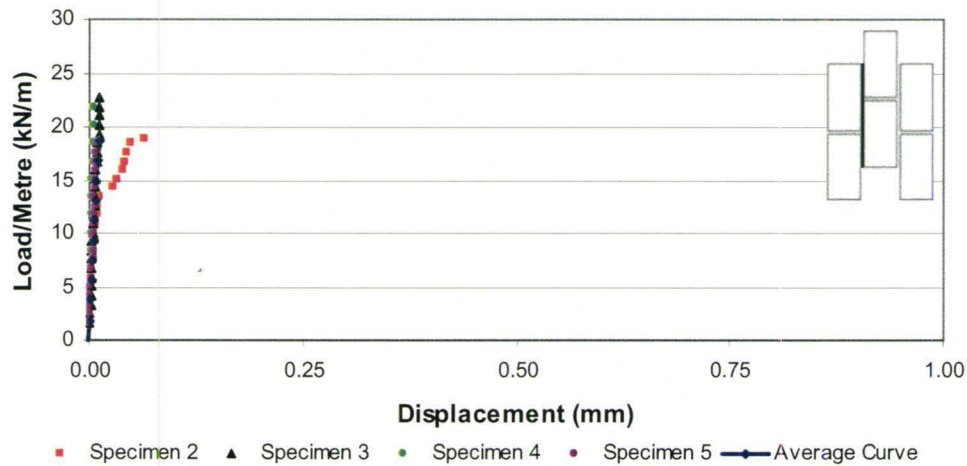


Figure 3.6 – Specimen AU – 1.5: Load/Metre versus Displacement

### 3.3.2 REINFORCED (AR – 1.5)

This was the first set of reinforced specimens tested for Phase One of this experimental investigation. It was expected that they would have a much larger failure load than their unreinforced counterparts. Since the Demec displacement readings were taken manually, there was the potential for an excessive number of data points if the load interval between readings was too small. Demec displacement readings were taken at 2.0 kN intervals and 5.0 kN intervals for approximately the first and second half of loading, respectively. For each specimen, Demec displacement readings were only taken up to the maximum load. However, all specimens were tested up their complete failure to observe their final failure mode.



The first specimen (AR – 1.5 – 1) failed by crushing of one block at the lower support points, as shown in Figure 3.7, prior to reaching maximum shear-slip resistance. Very limited displacements were recorded up to this point. This also was confirmed by visual observations. The typical near-failure occurrence of fine cracks and white discolouration of the epoxy were not observed along any of the bed joints. Therefore, this test was a lower bound indication of the strength of the specimen. As can be seen in Figure 3.7, the support “feet” of this very first test specimen were not filled with grout and subsequently wrapped with GFRP. This is the reason for the premature failure of this specimen.



**Figure 3.7** – Block Crushing at Lower Support Point of Specimen AR – 1.5 – 1

For the remaining specimens, in order to prevent premature failure, the support “feet” were filled with grout and wrapped with GFRP. For the second specimen (AR – 1.5 – 2), the increase in displacement following the initial slip resulted in incomplete tearing of the GFRP along the right bed joint slip plane, as shown in Figure 3.8. The load



registered on the Tinius Olsen machine steadily decreased as the GFRP continued to tear. Final post-peak failure was caused by crushing of one block at the lower support points, as shown in Figure 3.9. The block crushing was not as severe as for the first specimen, shown in Figure 3.7 and did not limit the maximum load. The failure of the third specimen (AR – 1.5 – 3) was complete tearing of the GFRP along the left bed joint, as shown in Figure 3.10.

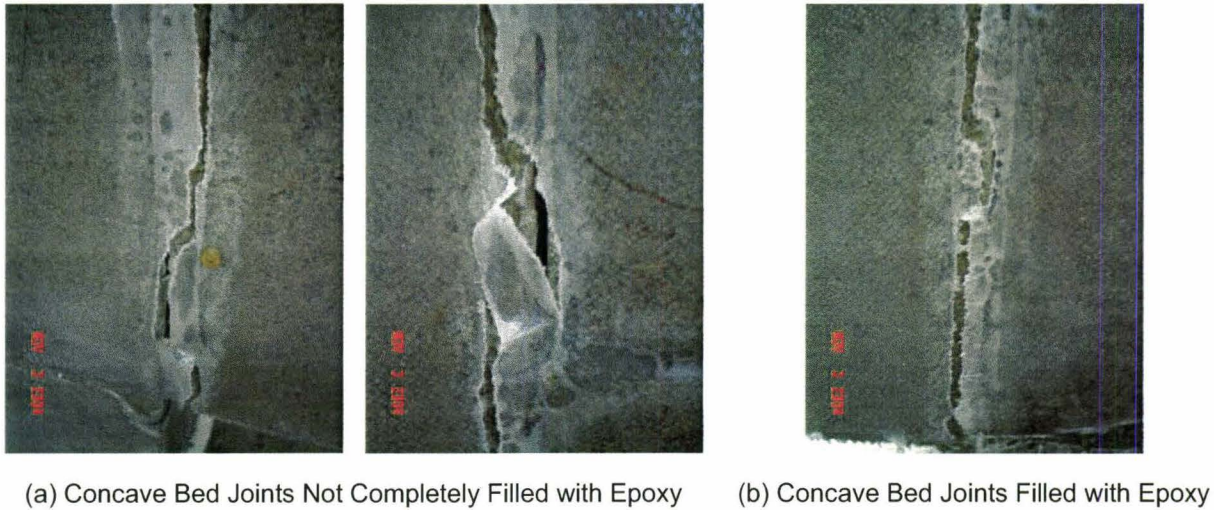


(a) Concave Bed Joints Not Completely Filled with Epoxy      (b) Concave Bed Joints Filled with Epoxy

**Figure 3.8 – Damaged GFRP for Specimen AR – 1.5 – 2**



**Figure 3.9 – Block Crushing at Lower Support Point of Specimen AR – 1.5 – 2**



**Figure 3.10** – Damaged GFRP for Specimen AR – 1.5 – 3

The somewhat different appearance of the tearing shown in Figures 3.8(a) and 3.10(a) was found to coincide with the concave profile of the mortar joints being not completely filled with epoxy.

Once the GFRP had completely torn, the specimen had zero capacity. No post-fibre-tearing block crushing occurred at the lower supports. With the type of GFRP used for this experimental phase, it appears that a slip plane length of 1.5 block lengths is on the cusp between shear slip failure and premature block crushing. This seems to be the case if the support points are not reinforced.

The average ultimate load was 117.3 kN at an average displacement of 0.21 mm. The significant amount of scatter of the failure load is evident by the C.O.V. of 27.6%. However, since the toe crushing failure mode of the first specimen is different from that of the other two (which themselves had similar failure modes) it makes sense to remove its results from the calculations. Considering only AR – 1.5 – 2 and AR – 1.5 – 3, the



average ultimate load and the corresponding average displacement increased to 136.0 kN and 0.29 mm, respectively. The Load/Metre versus Average Displacement plot for these latter two specimens is presented in Figure 3.11.

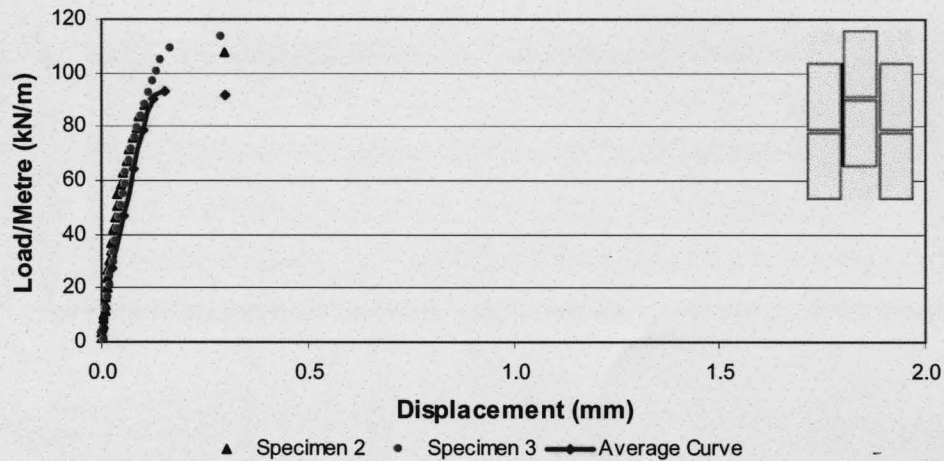


Figure 3.11 – Specimen AR – 1.5: Load/Metre versus Displacement

### 3.4 A – 2.5 SPECIMENS

#### 3.4.1 UNREINFORCED (AU – 2.5)

The load and displacement data for these specimens were recorded using the data acquisition system described in Chapter 2. It was expected that these specimens would not be able to support much load prior to failure. Once the ultimate load was reached, which occurred at very low amounts of displacement, the specimen failed suddenly along one of the bed joints. The failure mode was debonding of the mortar at the interface between the mortar and the block; this was similar to the unreinforced AU–1.5 specimens as shown in Figure 3.4. At this point, the specimen had zero capacity. The average failure load was 44.9 kN at an average displacement of 0.072 mm. The amount of scatter of the

failure load is evident by the coefficient of variation (C.O.V.) of 20.6%. The Load/Metre versus Average Displacement plot is provided in Figure 3.12.

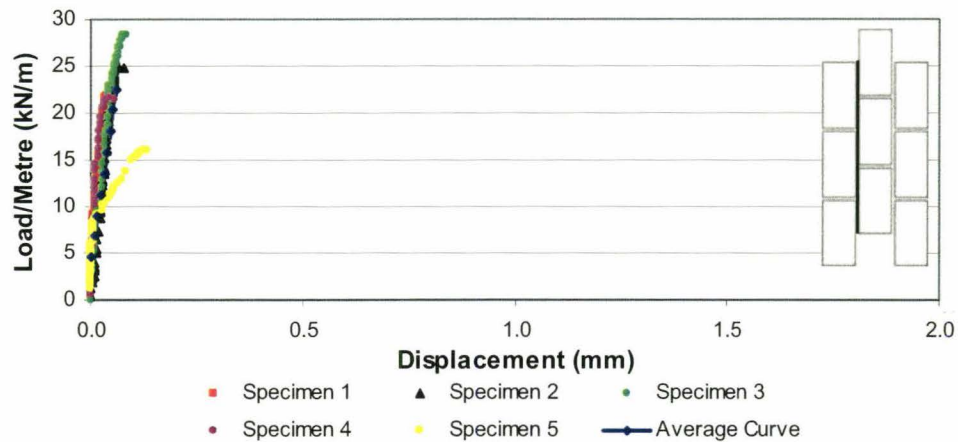


Figure 3.12 – Specimen AU – 2.5: Load/Metre versus Displacement

### 3.4.2 REINFORCED (AR – 2.5)

The load and displacement data for these specimens were recorded using the data acquisition system described in Chapter 2. All three specimens failed by crushing of one block at the lower support points, as shown in Figure 3.13. This occurred prior to any observable failure in the GFRP. Very limited, or negligible, displacements were recorded up to this point.



Figure 3.13 – Typical Block Crushing at Lower Support Point of Specimen AR-2.5

By visual observations, no fine cracks or white discolouration of the epoxy were visible along any of the bed joints. The GFRP was essentially undamaged. Therefore, these results are a lower bound indication of the strength of these specimens. The GFRP provided such high resistance along the bed joint slip planes that the blocks at the lower supports failed first. These results might have been expected based on similar results from the AR – 1.5 specimens. With the type of GFRP used for this experimental phase, a slip plane length of 2.5 block lengths is beyond the threshold of shear slip failure. The average failure load was 199.1 kN at an average displacement of 0.41 mm. The amount of scatter of the failure load is evident by the C.O.V. of 16.1%. The Load/Metre versus Average Displacement plot is presented in Figure 3.14. Again, it should be emphasised that shear-slip did not occur. Prior to premature toe crushing of Specimen 2, essentially zero displacement was recorded by the LPDT (possibly due to a faulty wire connection). This resulted in a vertical load/metre versus displacement curve. This curve is present in Figure 3.14 for completeness, but was not used to calculate the average curve.

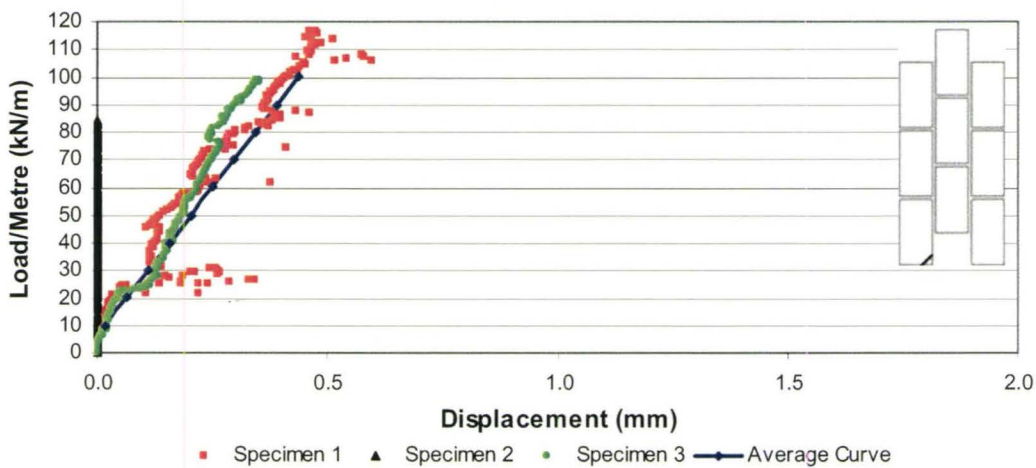


Figure 3.14 – Specimen AR – 2.5: Load/Metre versus Displacement



### 3.5 T – 0.5 SPECIMENS

#### 3.5.1 UNREINFORCED (TU – 0.5)

Although these specimens were potentially as fragile as the AU – 0.5 specimens, their symmetry made them much easier to transport to the testing machine and set up for testing. No precompression apparatus was necessary during the set-up phase. Unfortunately, one specimen was accidentally dropped and destroyed. It was expected that these specimens would not be able to support much load prior to failure, but their symmetry would allow them to resist more load than the AU – 0.5 specimens. Thus mechanical Demec displacement readings were taken at increments of 0.5 kN for the first specimen and at 1.0 kN for the remaining specimens. Once the ultimate load was reached, which occurred at low displacement, the specimen failed along slip planes in a characteristic ‘Z’ pattern, as shown in Figure 3.15. This was the case for all specimens. The failure was debonding of the mortar at the interface between the mortar and the block. At this point the specimen had zero capacity.

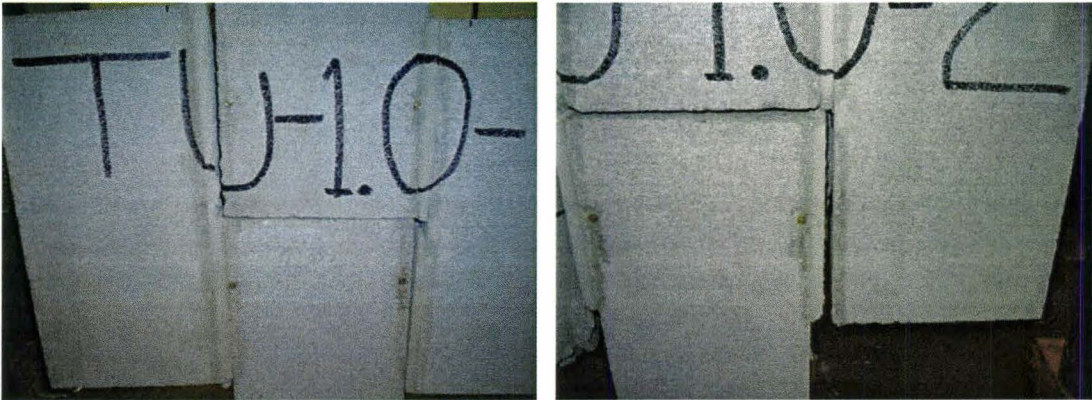


Figure 3.15 – Typical Failure Mode of TU – 0.5 Specimens

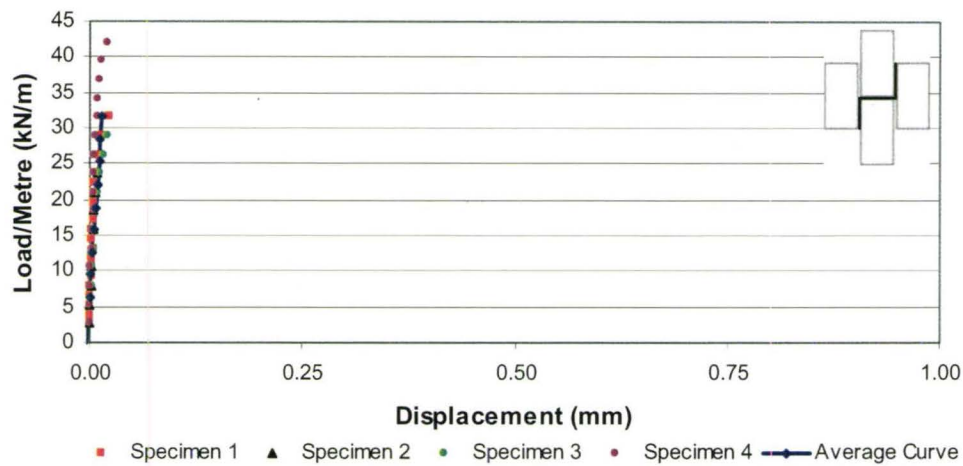
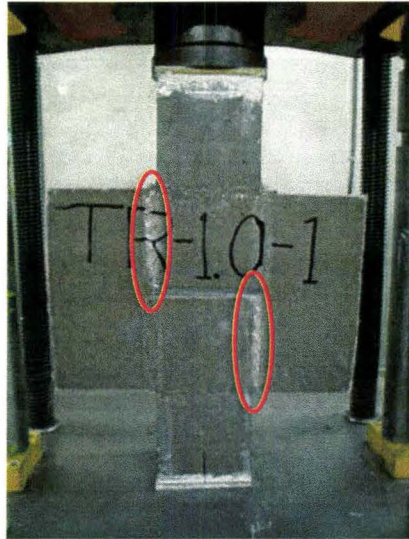


Figure 3.16 – Specimen TU – 0.5: Load/Metre versus Displacement

The average failure load was 12.6 kN at an average displacement of 0.018 mm. The variability of the failure load is evident by the C.O.V. of 21.8%. The Load/Metre versus Average Displacement plot is provided in Figure 3.16.

### 3.5.2 REINFORCED (TR – 0.5)

It was expected that the reinforced specimens would be able to support much higher loads than the unretrofitted counterparts prior to failure. Thus, mechanical Demec displacement readings were taken at 2.0 kN intervals. As the load reached the ultimate, fine cracks and white discoloration were observed in the epoxy along the bed joint slip planes, again in the characteristic 'Z' pattern. During this stage, it seemed that the glass fibres suspended in the epoxy were being deformed but were still intact. After the maximum load was reached, the specimens did not lose all capacity. They continued to resist increasing displacement, albeit at steadily decreasing load, which was accompanied by further cracking and discolouration along the failed bed joint slip planes, as shown in Figure 3.17.



**Figure 3.17** – Typical Damage Along Slip Plane of Reinforced TR-0.5 Specimens

The post-peak response was recorded by stopping the testing machine at various levels of load and recording the displacements. Eventually, the displacement reached a high enough value where the fibres began to tear, as shown in Figure 3.18. Each test was halted once the displacements reached the maximum that the Demec gauge could read. The GFRP was only partially torn. Therefore, these specimens still had some remaining capacity.



(a) Concave Bed Joints Not Completely Filled with Epoxy

(b) Concave Bed Joints Filled with Epoxy

**Figure 3.18** – Damaged GFRP for TR – 0.5 Specimens



The somewhat different appearance of the tearing shown in Figures 3.18(a) was found to coincide with the concave profile of the mortar joints being not completely filled with epoxy.

The average ultimate load was 39.9 kN at an average displacement of 0.147 mm. The use of GFRP greatly reduced the amount of scatter of the results, as is evident by the much lower C.O.V. of 6.4%. The Load/Metre versus Average Displacement plot is presented in Figure 3.19.

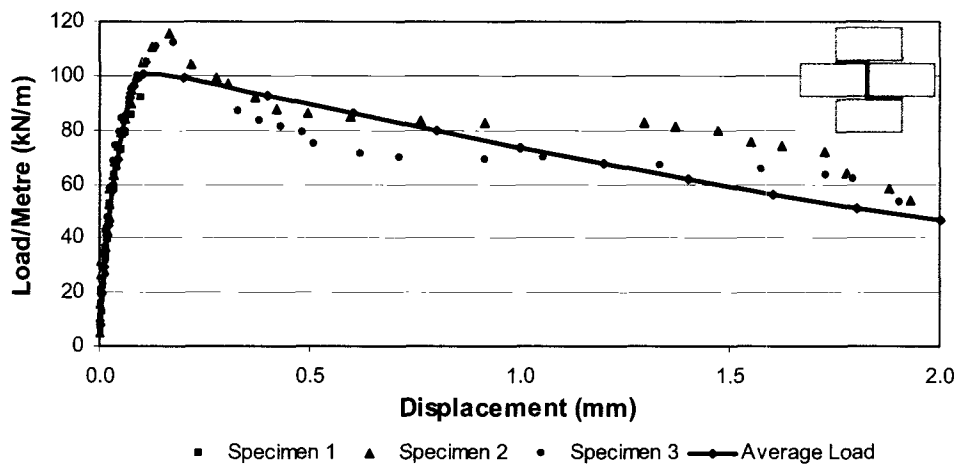


Figure 3.19 – Specimen TR – 0.5: Load/Metre versus Displacement

### 3.6 T – 1.5 SPECIMENS

#### 3.6.1 UNREINFORCED (TU – 1.5)

The load and displacement data for these specimens were recorded using the data acquisition system described in Chapter 2. It was expected that these specimens would not be able to support much load prior to failure. Once the ultimate loads were reached, which occurred at very small displacements, the specimens failed along the slip planes in a characteristic ‘Z’ pattern. This was the case for all specimens. The failure mode was



debonding of the mortar at the interface between the mortar and the block, as shown in Figure 3.20. At this point, the specimen had zero capacity. The average ultimate load was 26.4 kN at an average displacement of 0.047 mm. The variability of the capacity is evident by the C.O.V. of 15.3%. The Load/Metre versus Average Displacement plot is provided in Figure 3.21.

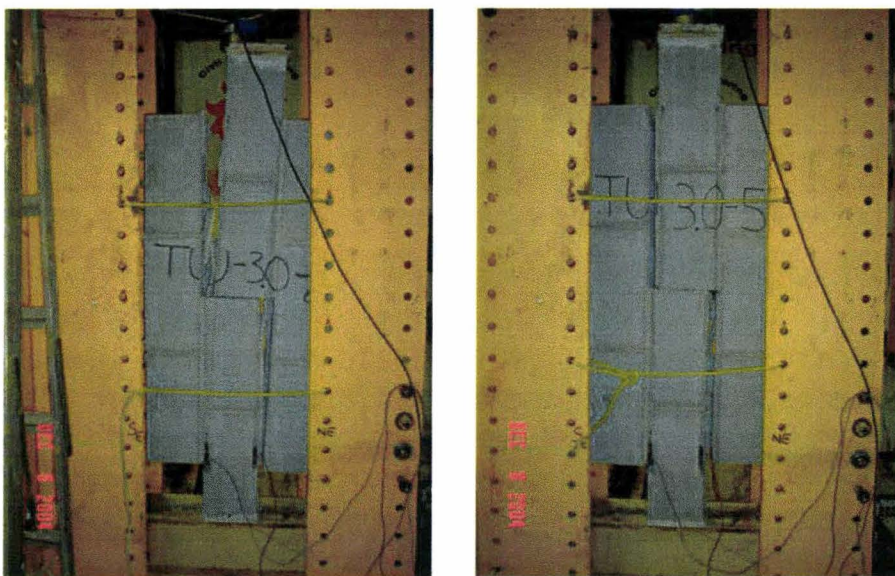


Figure 3.20 – Typical Failure Mode of TU – 1.5 Specimens

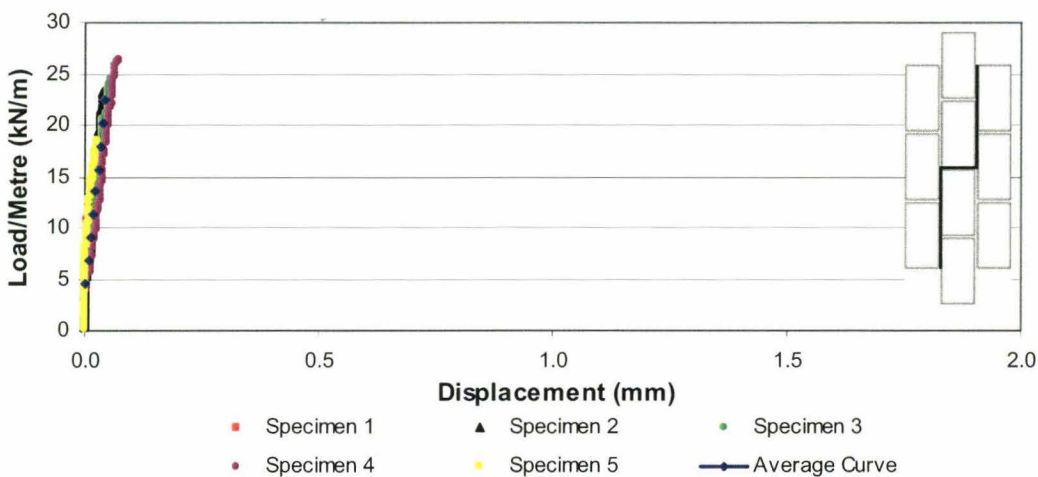


Figure 3.21 – TU – 1.5: Load/Metre versus Displacement

### **3.6.2 REINFORCED (TR – 1.5)**

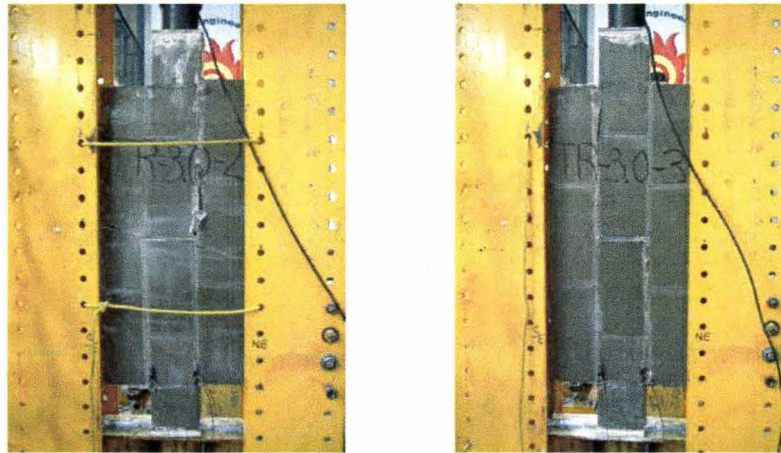
The load and displacement data for these specimens were recorded using the data acquisition system described in Chapter 2. As the load reached the maximum value, fine cracks and white discoloration were observed in the epoxy along the bed joint slip planes, as shown in Figure 3.22.



**Figure 3.22** – Minor Damage to GFRP Along Bed Joint (Prior to Full Fabric Tearing)

During this increasing resistance stage, the GFRP continued to deform but was still intact. After the maximum load was reached, the specimens did not lose all capacity. They continued to resist increasing displacement, albeit at decreasing load. The increasing displacement was accompanied by further cracking and discolouration of the failed bed joint slip planes. Eventually the displacement reached a value where the fibres began to tear. Loading in the post-peak region continued up to the complete tearing of the glass fibres. For the third specimen (AR – 1.5 – 3), the slip plane and GFRP damage was localized to the characteristic ‘Z’ pattern only, as shown in Figure 3.23(b). For the other

two specimens, the ‘Z’ pattern damage was accompanied by an induced rotation which resulted in middle block splitting, as shown in Figure 3.23(a).

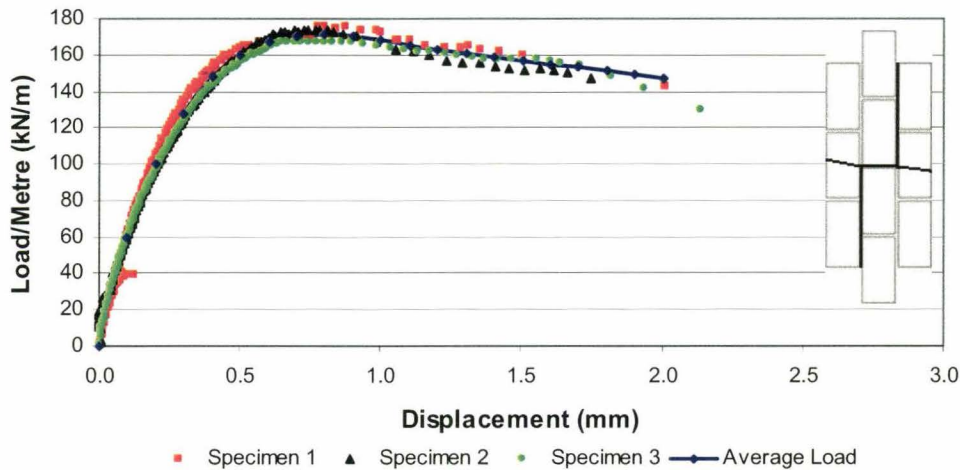


(a) ‘Z’ Crack Plus Middle Block Splitting

(b) ‘Z’ Crack

**Figure 3.23** – Typical Failure Modes of TR – 1.5 Specimens

Up to middle block cracking, the damaged along the slip planes was fairly uniform. The average maximum load was 203.5 kN at an average displacement of 0.772 mm. The use of GFRP greatly reduced the scatter of the results, as is evident by the much lower C.O.V. of 2.5%. The Load/Metre versus Average Displacement plot is presented in Figure 3.24.



**Figure 3.24** – Specimen TR – 1.5: Load/Metre versus Displacement



### **3.7 DISCUSSION OF PHASE ONE EXPERIMENTAL RESULTS**

The typical failure of the unreinforced specimens was a brittle shear-slip debonding mode which occurred at low levels of both load and displacement. The debonding occurred at the interface between the block and the mortar. This failure mode is to be expected considering the weak shear bond strength of the mortar and the absence of compressive stresses normal to the mortar bed joints for these tests. Previous investigations (Drysdale et al., 1979; Atkinson et al., 1998) have documented the strengthening and deformational benefits of axial compression normal to the bed joints. The observed brittle failure mode was described by Hamid et al. (2005) as having very little displacement or load change between initiation of cracking at the block-mortar interface and total debonding.

All of the glass fibre reinforced specimens, with one exception, failed in shear slip along the bed joints but at much higher loads than the comparable unreinforced specimens. As shown in Table 3.1, they reached shear slip strengths ranging from 3.2 to 7.7 times that of their unretrofitted counterparts. Upon examining the failed reinforced specimens, it was confirmed that the mortar joints had indeed debonded, most likely early during the test, and thus the laminates provided the resistance to the applied load. For most of the retrofitted specimens, at large displacements, the laminate began to tear. Where complete tearing did not occur, the test was terminated when the displacement measurements reached the limit of the instrumentation. Failure by delamination did not occur with any of the specimens. For specimen type AR-2.5, which consistently failed by crushing of one block at the lower support points, the laminate was undamaged and,



therefore, the recorded strength is only a lower bound estimate of shear slip capacity. The load carried by externally bonded FRP at the ultimate shear state is difficult to quantify (Bakis et al., 2002).

The complete summary of the Phase One experimental results is presented in Table 3.1 (page 87). As can be seen, the unreinforced specimens exhibited high variability as measured by the coefficient of variation (C.O.V.). For all of the specimens, the application of the GFRP greatly reduced the variability. An average face shell thickness of 34 mm was used in calculating shear stress for both reinforced and unreinforced specimens. As is indicated in Table 3.1, two distinct failure modes were observed. For the triplet type of specimen, only one side of the specimen failed whereas, for the modified triplet type of specimens, cracks and failure occurred above and below the empty head joint on opposite sides of the specimen (i.e., ‘Z’ crack failure). For the modified triplet type of specimen, it was not possible to have only one side fail because any “softening” of the response on one side of the specimen results in a shifting of load to the other side.

Typical load per metre versus displacement data was presented earlier in this chapter for the unreinforced specimens. These specimens exhibited sudden brittle loss of capacity at their maximum load at small displacements. In comparison, after the reinforced specimens reached their maximum load, a gradual decrease in load resistance occurred with increasing displacement. This greatly increased deformability and ended with the eventual tearing of the GFRP laminate. The experimental and analytical work conducted by Ehsani et al. (1997) revealed that when FRP fibres were oriented at  $0^{\circ}/90^{\circ}$

to the applied load, the resulting shear-deformation relationship was nonlinear. This was shown to be the case in the data presented here.

### 3.8 SELECTION OF SPECIMEN CONFIGURATION

In evaluating the various shapes of the test specimens, several factors have been considered. A schematic diagram of idealized Type ‘A’ and Type ‘T’ specimens is presented in Figure 3.25. The modified triplet (Type ‘T’) specimen (Figure 3.25(a)), was originally developed to minimize bending stresses (normal stresses) along the bed joint slip planes. In general, the single triplet (Type ‘A’) shape of specimens (Figure 3.25(b)) introduces more bending stresses over the length of the bed joint due to unavoidable eccentricity of the positions of the applied load and reaction points.

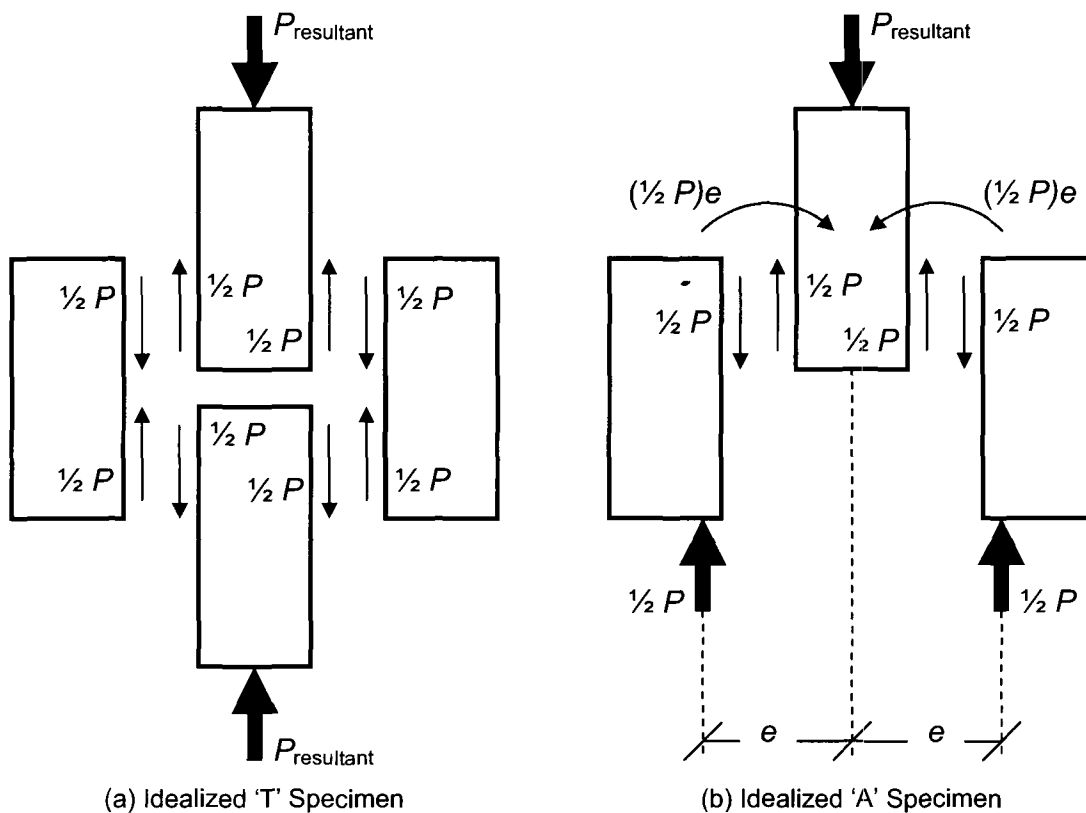


Figure 3.25 – Schematic Diagram of Shear Force Distribution

Table 3.1 – Phase One Experimental Results

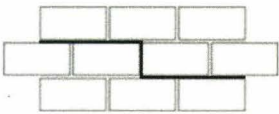
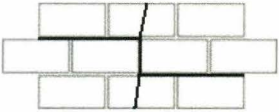
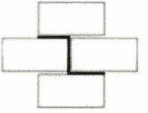
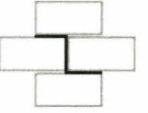
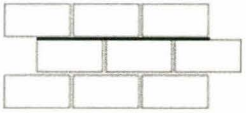

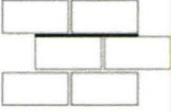
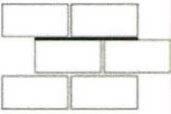
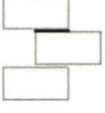
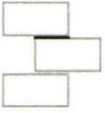
Typical Failure Mode	Specimen #	Failure Load, $P_{max}$ (kN) <sup>†</sup>	Load/Metre (kN/m) <sup>*</sup>	Shear Strength (MPa) <sup>‡</sup>	Load C.O.V. (%)	$\Delta$ at $P_{max}$ (mm) <sup>**</sup>
<b>TU – 1.5 (Unreinforced)</b>						
<b>Slip Plane Properties: Length = 0.59 m; Width = 0.068 m; Area = 0.04012 m<sup>2</sup></b>						
'Z' crack 	1	22.8	19.3	0.28	15.3	0.0393
	2	27.9	23.6	0.35		0.0466
	3	28.8	24.4	0.36		0.0542
	4	31.0	26.3	0.39		0.0705
	5	21.6	18.3	0.27		0.0261
	Average	<b>26.4</b>	<b>22.4</b>	<b>0.33</b>		<b>0.047</b>
<b>TR – 1.5 (Reinforced)</b>						
'Z' crack or 'Z' crack w/ middle block splitting 	1	207.5	175.8	2.59	2.5	0.7739
	2	205.2	173.9	2.56		0.7446
	3	197.7	167.5	2.46		0.7983
	Average	<b>203.5</b>	<b>172.4</b>	<b>2.54</b>		<b>0.7722</b>
<b>TU – 0.5 (Unreinforced)</b>						
<b>Slip Plane Properties: Length = 0.19 m; Width = 0.068 m; Area = 0.01292 m<sup>2</sup></b>						
'Z' crack 	1	12.4	32.6	0.48	21.8	0.0229
	2	9.8	25.8	0.38		0.0087
	3	11.7	30.8	0.45		0.0201
	4	16.3	42.9	0.63		0.0213
	Average	<b>12.6</b>	<b>33.0</b>	<b>0.49</b>		<b>0.0183</b>
<b>TR – 0.5 (Reinforced)</b>						
'Z' crack 	1	37.5	98.7	1.45	6.4	0.0980
	2	39.6	104.2	1.53		0.1651
	3	42.6	112.1	1.65		0.1778
	Average	<b>39.9</b>	<b>105.0</b>	<b>1.54</b>		<b>0.1470</b>
<b>AU – 2.5 (Unreinforced)</b>						
<b>Slip Plane Properties: Length = 0.995 m; Width = 0.068 m; Area = 0.0677 m<sup>2</sup></b>						
Cracking along slip plane 	1	43.4	21.8	0.32	20.6	0.0379
	2	49.9	25.1	0.37		0.0653
	3	56.6	28.4	0.42		0.0825
	4	42.7	21.5	0.32		0.0409
	5	31.8	16.0	0.23		0.1344
	Average	<b>44.9</b>	<b>22.6</b>	<b>0.33</b>		<b>0.0722</b>



Table 3.2 (continued) – Phase One Experimental Results						
<b>AR – 2.5 (Reinforced)</b>						
Toe crushing 	1	232.2	116.7	1.72	16.1	0.4723
	2	168.2	84.5	1.24		Negligible
	3	197.0	99.0	1.46		0.3508
	<b>Average</b>	<b>199.1</b>	<b>100.1</b>	<b>1.47</b>		<b>0.4115</b>
<b>AU – 1.5 (Unreinforced)</b>						
<b>Slip Plane Properties:</b> Length = 0.595 m; Width = 0.068 m; Area = 0.0405 m <sup>2</sup>						
Cracking along slip plane 	1	13.8	11.6	0.17	24.6	N/A
	2	22.5	18.9	0.28		0.0648
	3	27.6	23.2	0.34		0.0119
	4	27.6	23.2	0.34		0.0047
	5	23.0	19.3	0.28		0.0095
	<b>Average</b>	<b>22.9</b>	<b>19.2</b>	<b>0.28</b>		<b>0.0227</b>
<b>AR – 1.5 (Reinforced)</b>						
Cracking along slip plane 	1	80.0	67.2	0.99	27.6	0.0403
	2	137.0	115.1	1.69		0.2963
	3	135.0	113.4	1.67		0.2864
	<b>Average</b>	<b>117.3</b>	<b>98.6</b>	<b>1.45</b>		<b>0.2076</b>
<b>AU – 0.5 (Unreinforced)</b>						
<b>Slip Plane Properties:</b> Length = 0.195 m; Width = 0.068 m; Area = 0.01326 m <sup>2</sup>						
Cracking along slip plane 	1	2.1	5.4	0.08	71.9	0.0095
	2	8.8	22.6	0.33		0.0134
	3	3.7	9.5	0.14		0.0032
	<b>Average</b>	<b>4.9</b>	<b>12.5</b>	<b>0.18</b>		<b>0.0087</b>
<b>AR – 0.5 (Reinforced)</b>						
Cracking along slip plane 	1	30.0	76.9	1.13	18.0	0.0711
	2	27.0	69.2	1.02		0.1327
	3	38.0	97.4	1.43		0.1596
	<b>Average</b>	<b>31.7</b>	<b>81.2</b>	<b>1.19</b>		<b>0.1211</b>

† Maximum load as recorded by the commercial load cell or Tinius Olsen machine.

\* Maximum load equally distributed along both bed joints and divided by the length of the bed joint slip plane.

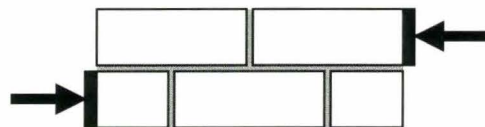
‡ Maximum load equally distributed along both bed joints and divided by the area of the bed joint slip plane.

\*\* From displacement instrumentation.



Although this bending can be substantially reduced by applying the loads close to the bed joints, some bending always remains. Furthermore, with the load applied close to the edge, there is a chance that the corner (toe) can crush during testing. For Type ‘A’ specimens with longer slip planes, compression failure of the blocks at the lower supports due to concentrated reaction forces at these points, made such specimens less suitable for the study.

In terms of the distribution of shear stress along the bed joint, a finite element analysis by Atkinson et al. (1998) showed that nearly uniform shear stress exists except near the ends of the shear transfer zone. Therefore, it was expected that use of a longer shear transfer zone should reduce the impact of this region of nonuniform stress. However, the shear-slip specimens analyzed by Atkinson et al. (1998) were of the configuration shown in Figure 3.26. This configuration is different from the ones used in this study; therefore an independent finite element analysis was required.



**Figure 3.26** – Atkinson et al. (1998) Shear Slip Specimens

A finite element analysis was performed on the five specimen configurations used in Phase One of this experimental investigation. The full details of the analysis, performed by Dr. Wael El-Dakhakhni, Assistant Professor of Civil Engineering at McMaster University, are provided in Appendix B. For the T-1.5 specimen, the finite element analysis indicated that, along most of the length of the shear slip plane, the

normal stress was uniform and relatively low, which inherently produces nearly pure shear conditions along the bed joint slip plane. The longer shear transfer length would reduce the significance of the compression stress concentration. As shown in Table 3.1, this shape of specimen also, typically, had less variability of results. Therefore, the T-type specimen was preferred. Considering both the need to minimize bending stress normal to the bed joint and the desire to have nearly uniform shear stresses prior to initial bed joint cracking, the T-1.5 type of specimen was chosen for further shear-slip research.

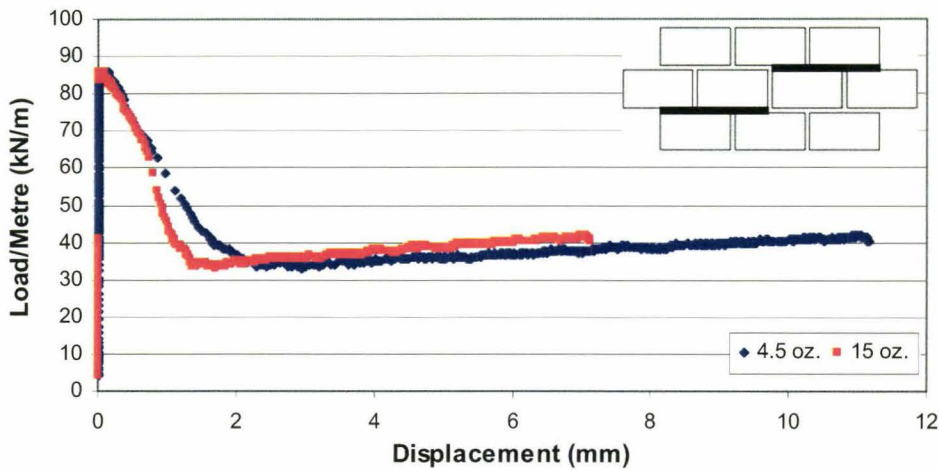
## **PHASE TWO**

### **3.9 PHASE TWO EXPERIMENTAL RESULTS**

As described in Chapter 2, the T-1.5 type specimen was used throughout this phase. The justification for the use of this specimen configuration for further shear-slip research was discussed in Section 3.8.

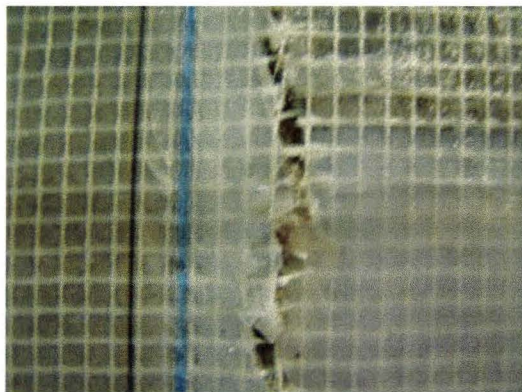
#### **3.9.1 SPECIMEN 1: TEST 1 –EPOXY APPLIED 4.5 oz./yd.<sup>2</sup> and 15 oz./yd.<sup>2</sup> MESH AT 0°/90° (No applied clamping force)**

The load and displacement data for these specimens were recorded using the data acquisition system described in Chapter 2. During the test, the load continued to increase up to the onset of cracking, at which point the load began to decrease. The maximum recorded failure load was 101.2 kN (85.8 kN/m). Before cracking occurred virtually no displacements were recorded by the LPTDs. Immediately after cracking, the displacements began to increase and this was accompanied by decreasing capacity. The Load/Metre versus Average Displacement for both slip planes is shown in Figure 3.27.

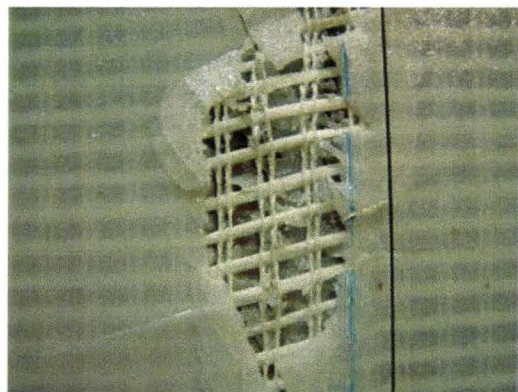


**Figure 3.27** – Load/Metre vs. Average Displacement of Epoxy Applied 4.5 oz./yd.<sup>2</sup> and 15 oz./yd.<sup>2</sup> Mesh at 0°/90° (No applied clamping force)

This test did not go according to plan. Failure occurred along the lower-right and upper-left slip planes in the ‘Z’ crack pattern (i.e., both the 4.5 oz./yd.<sup>2</sup> and 15 oz./yd.<sup>2</sup> mesh failed). The failure of the 4.5 oz./yd.<sup>2</sup> mesh was by tearing (Figure 3.28(a)) whereas the failure of the 15 oz./yd.<sup>2</sup> mesh was delamination (Figure 3.28(b)). During the testing, the thicker epoxy cracked and flaked off leaving the 15 oz./yd.<sup>2</sup> mesh deformed, but undamaged.



(a) Tearing of 4.5 oz./yd.<sup>2</sup> Mesh



(b) Delamination of 15 oz./yd.<sup>2</sup> Mesh

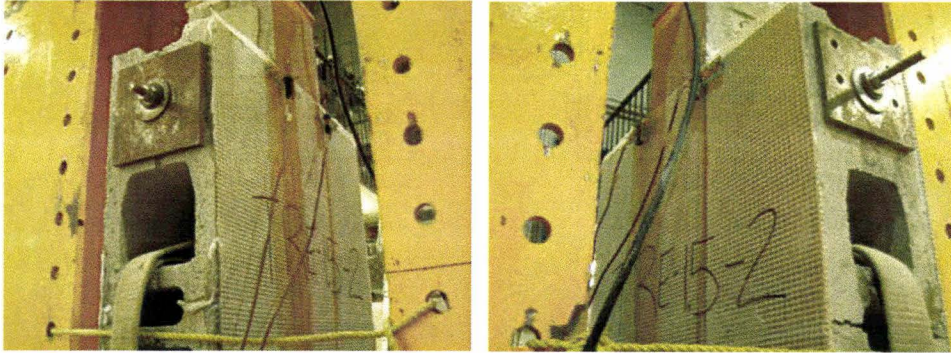
**Figure 3.28** – Damage of Epoxied Mesh Applied at 0°/90°

Failure of the 4.5 oz./yd.<sup>2</sup> mesh involved the eventual complete tearing of the mesh. It was observed that initially the mesh deformed but gradually, as the displacements increased, it began to tear. It is the tearing of the fibres that resulted in the loss of capacity. After the specimen had lost about half of its capacity, the load gradually began increasing under larger displacement. It is hypothesised that this may have been the result of the 15 oz./yd.<sup>2</sup> mesh along the other failure plane deforming and providing limited clamping force normal to the bed joint while it was delaminating. The explanation for this behaviour will be reviewed again in Chapter 4. The test was terminated once the centre gap was closed. It was hoped that only the two upper slip planes reinforced with the 4.5 oz./yd.<sup>2</sup> mesh would have failed. Then it would have been possible to repair the specimen and test the 15 oz./yd.<sup>2</sup> mesh. No further tests were performed on this specimen.

### **3.9.2 SPECIMEN 2: TEST 1 –EPOXY APPLIED 4.5 oz./yd.<sup>2</sup> and 15 oz./yd.<sup>2</sup> MESH AT 0°/90° (15 oz./yd.<sup>2</sup> mesh reinforced slip planes clamped)**

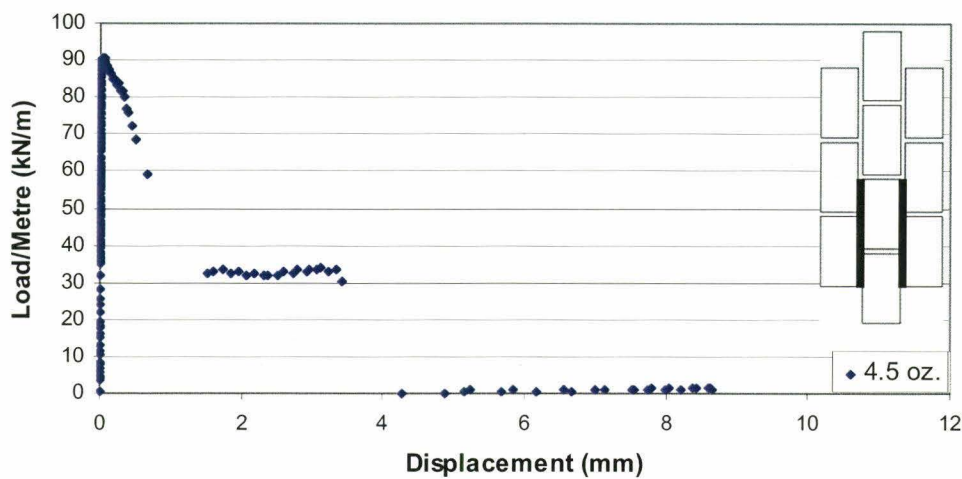
To ensure that the 4.5 oz./yd.<sup>2</sup> mesh failed before the 15 oz./yd.<sup>2</sup> mesh, a compression force was applied to the slip planes reinforced with the 15 oz./yd.<sup>2</sup> mesh. In order to minimize the potential influence of the compression force on the region reinforced with the 4.5 oz./yd.<sup>2</sup> mesh, the compression force was applied to the cells farthest from the centre gap. It was applied using a ½ inch (12.7 mm) diameter threaded rod and a two ½ inch (12.7 mm) thick steel plates, as shown in Figure 3.29.





**Figure 3.29** – Clamping Apparatus

During the test, the load continued to increase up to the onset of cracking, at which point the load began to drop. Before cracking was visible, virtually no displacements were recorded by the LPTDs. Immediately after cracking, the displacements began to increase and this was accompanied by a rapid decrease in the load. Failure of the 4.5 oz./yd.<sup>2</sup> mesh involved the eventual complete tearing of the mesh. Only the two slip planes reinforced with the 4.5 oz./yd.<sup>2</sup> mesh failed, thus the clamping strategy worked. The Load/Metre versus Average Displacement plot is shown in Figure 3.30.

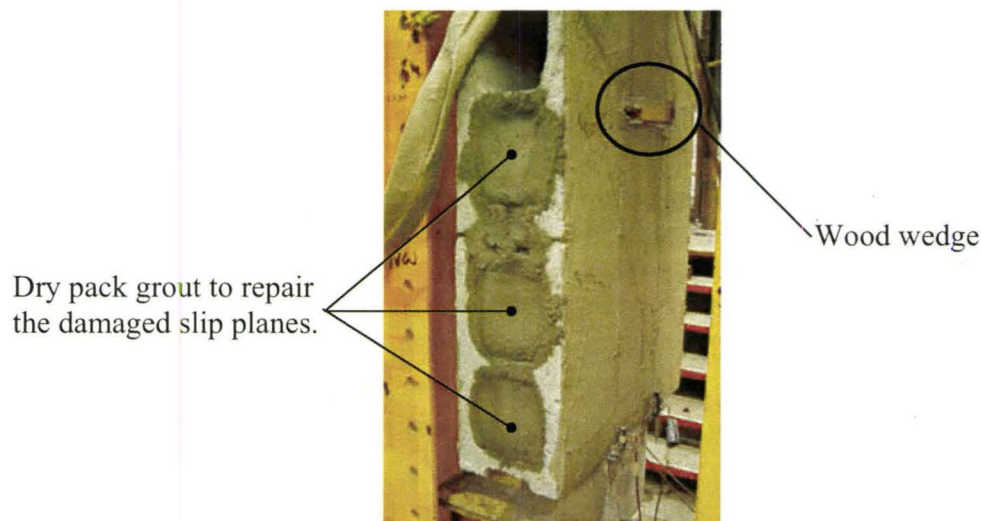


**Figure 3.30** – Load/Metre vs. Average Displacement of Epoxy Applied 4.5 oz./yd.<sup>2</sup> and 15 oz./yd.<sup>2</sup> Mesh at 0/90° (15 oz./yd.<sup>2</sup> mesh reinforced slip planes clamped)

At the termination of the test, the slip plane still had capacity due to friction. The maximum recorded failure load was 106.7 kN (90.4 kN/m). As will be seen in Chapter 4, on average, this was twice that of specimens reinforced with 4.5 oz./yd.<sup>2</sup> mesh applied using the modified parging, but without any form of compression. It is clear that the use of epoxy greatly increased the capacity of the 4.5 oz./yd.<sup>2</sup> mesh, but it was uncertain what influence, if any, the compression force had provided.

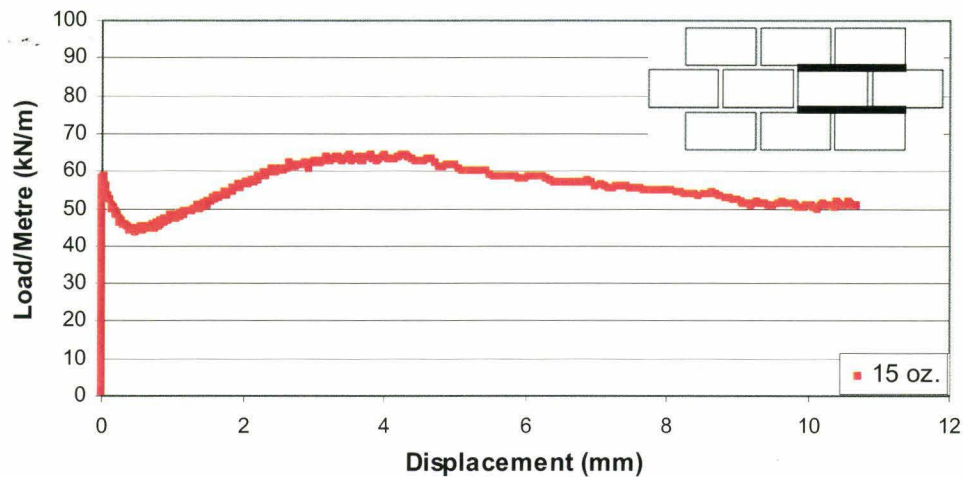
**3.9.3 SPECIMEN 2: TEST 2 – EPOXY APPLIED 4.5 oz./yd.<sup>2</sup> and 15 oz./yd.<sup>2</sup> MESH AT 0°/90° (Damaged 4.5 oz./yd.<sup>2</sup> mesh reinforced slip planes repaired)**

The specimen described in the previous section was repaired so the joints with the 15 oz./yd.<sup>2</sup> mesh could be tested. To repair the specimen, two wood wedges were forced into the then fully closed centre gap to widen it in order to allow as much slip as possible. This process was fairly difficult to perform and not without danger of causing other damage. Stiff grout was then dry packed into the block cells at the location of the damaged slip planes and allowed to cure for approximately 16 hours before testing. A photograph of the repaired specimen is reproduced in Figure 3.31



**Figure 3.31 – Repaired Specimen**

During the test, the load continued to increase up to the onset of cracking, at which point the load began to drop. Before cracking occurred, virtually no displacements were recorded by the LPTDs. The Load/Metre versus Average Displacement plot is available in Figure 3.32. There was concern as to what influence the repair process might have had on the outcome of this test. It was thought that friction along the slip planes could be enhanced by the grouted zone holding the slipping joints together similar to the precompression force applied in the first part of testing of this specimen.

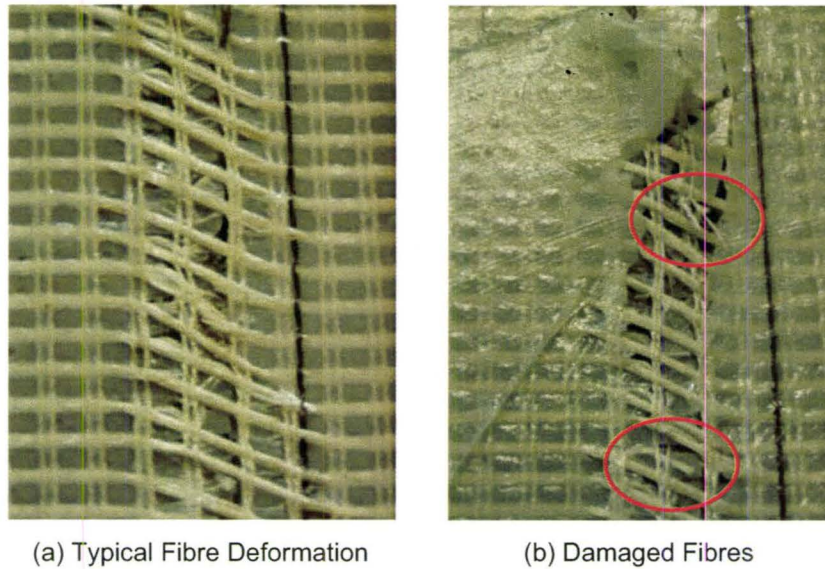


**Figure 3.32** – Load/Metre vs. Average Displacement of Epoxy Applied 4.5 oz./yd.<sup>2</sup> and 15 oz./yd.<sup>2</sup> Mesh at 0/90° (Damaged 4.5 oz./yd.<sup>2</sup> mesh reinforced slip planes repaired)

As illustrated in Figure 3.32, it was actually during the post-cracking stage that the load reached its maximum level. This phenomenon was unique to this test. It was observed that once cracking of the epoxy used to bond the mesh to the concrete block specimens occurred, it began peeling away leaving the mesh underneath deformed, but undamaged under increasing displacement. This initial slip was accompanied by an early drop in the load but, after a displacement of about 0.5 mm, the load again began to



increase. It is hypothesized that enough displacement had occurred to cause the fibres to go into tension which applied a clamping force along the bed joint slip planes. As the displacement increased, so did the clamping force which resulted in the observed load increase. Photographs of the deformed mesh are provided in Figure 3.33(a).



**Figure 3.33** – Damaged Epoxyed 15 oz./yd.<sup>2</sup> Mesh Applied at 0°/90°

After a displacement of approximately 4.0 mm, the load began to drop. The test was terminated once the centre gap was fully closed. Upon closer inspection of the mesh, it was observed that some of the fibres had ruptured (Figure 3.33(b)). It is hypothesized that this coincided with the second decrease in load. As indicated by the ductile failure, the primary failure mode was delamination. However, after sufficient initial slip, it appeared that the epoxy could adequately secure some of the fibres so that their maximum strength could be developed. The maximum recorded failure load was 77.1 kN (65.3 kN/m).



### 3.9.4 SPECIMEN 3: TEST 1 – MORTAR PARGING APPLIED 4.5 oz./yd.<sup>2</sup> and 15 oz./yd.<sup>2</sup> MESH AT 0°/90° (No applied clamping force)

As a comparison to Test 1 of Specimen 1, a similar test was conducted only this time the meshes were applied using the modified mortar parging described in Chapter 2. Once again, no clamping force was applied to the slip planes.

During the test, the load continued to increase up to the onset of cracking, at which point the load began to drop. Before cracking occurred, virtually no displacements were recorded by the LPTDs. Immediately after cracking, the displacements began to increase and this was accompanied by a decreased resistance to loading. The Load/Metre versus Average Displacement data was plotted in Figure 3.34.

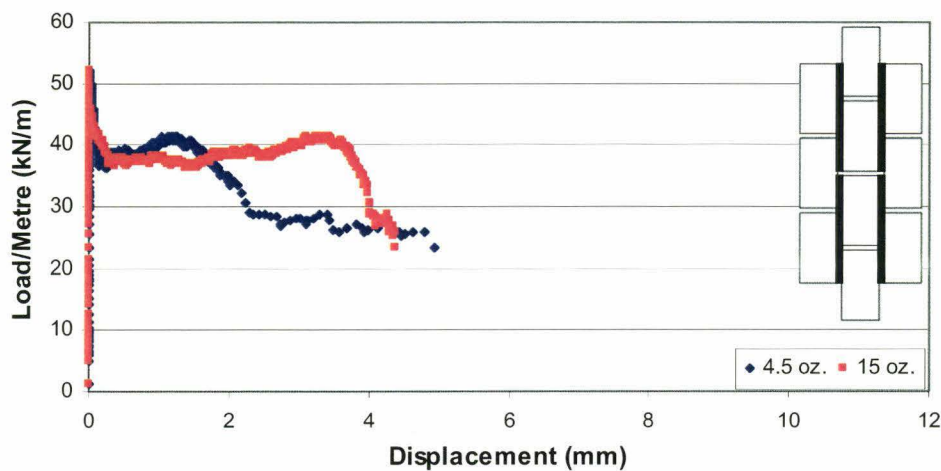
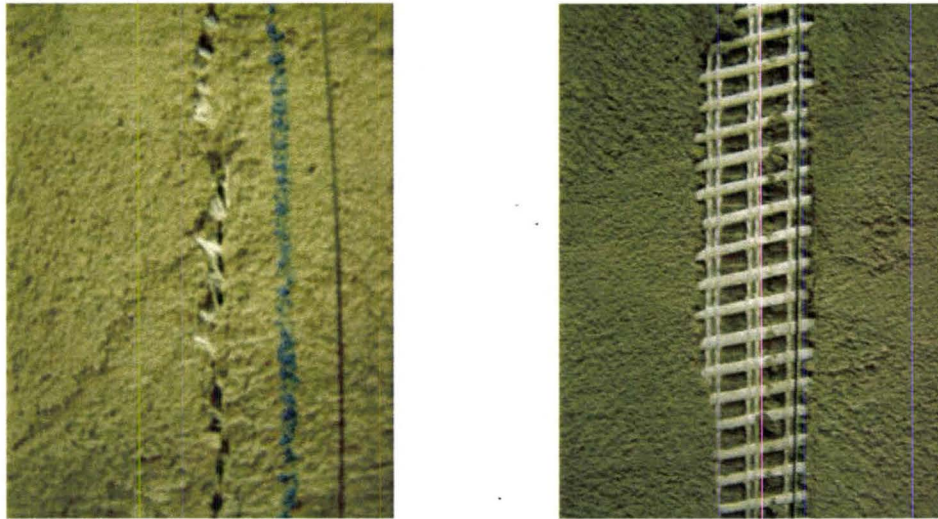


Figure 3.34 – Load/Metre vs. Average Displacement of Mortar Parging Applied 4.5 oz./yd.<sup>2</sup> and 15 oz./yd.<sup>2</sup> Mesh at 0/90° (No applied clamping force)

Cracking occurred along all four bed joint slip planes. Failure of the 4.5 oz./yd.<sup>2</sup> mesh was by the eventual rupturing of the mesh fibres. Failure of the 15 oz./yd.<sup>2</sup> mesh was by delamination. The mortar parging cracked and peeled away leaving the mesh

underneath deformed, but undamaged. Photographs of the damaged slip planes are reproduced in Figure 3.35.



(a) Typical 4.5 oz./yd.<sup>2</sup> Mesh Fibre Damage (b) Typical 15 oz./yd.<sup>2</sup> Mesh Fibre Delamination

**Figure 3.35** – Damage to Mortar Applied Mesh at 0°/90° for Specimen 3, Test 1

The test was terminated once the centre gap was closed. As illustrated previously in Figure 3.34, cracking of the 15 oz./yd.<sup>2</sup> mesh reinforced slip planes was more ductile than the 4.5 oz./yd.<sup>2</sup> mesh reinforced slip planes. As will be shown in Chapter 4, this is consistent with fibre delamination. At test termination, the 4.5 oz./yd.<sup>2</sup> mesh reinforced slip planes had a residual capacity of approximately 25 kN/m. It is hypothesized that not all the fibres had ruptured because, as was shown previously in Figure 3.30 (and in the next section in Figure 3.36), residual capacity from shear friction alone was less than 10 kN/m. The maximum recorded failure load was 61.3 kN (51.5 kN/m). This load resistance was the lowest out of all the tests in Phase 2.

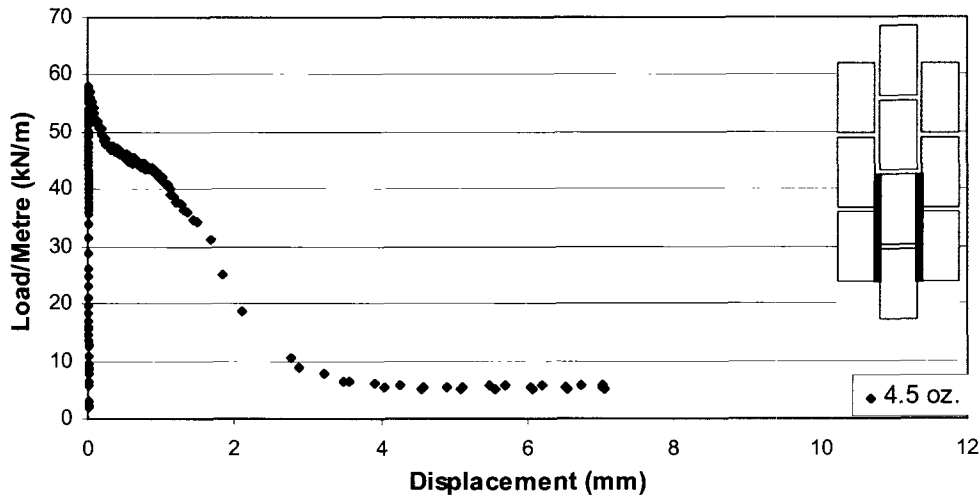
### **3.9.5 SPECIMEN 4: TEST 1 – MORTAR PARGING APPLIED 4.5 oz./yd.<sup>2</sup> and 15 oz./yd.<sup>2</sup> MESH AT 0°/90° (15 oz./yd.<sup>2</sup> mesh reinforced slip planes clamped)**

As a comparison to Test 1 of Specimen 2, a similar test was conducted only this time the meshes were applied using the modified mortar parging described in Chapter 2. Once again, in order to ensure that the 4.5 oz./yd.<sup>2</sup> mesh failed before the 15 oz./yd.<sup>2</sup> mesh, a clamping force was applied to the slip planes reinforced with the 15 oz./yd.<sup>2</sup> mesh. In order to minimize the potential influence of the compression force on the 4.5 oz./yd.<sup>2</sup> mesh, the compression force was applied to the cells furthest from the centre gap. A clamping process, similar to that shown in Figure 3.29, was used.

During the test, the load continued to increase up to the onset of cracking, at which point the load began to drop. Before cracking occurred, virtually no displacements were recorded by the LPTDs. Immediately after cracking, the displacements began to increase and this was accompanied by decreased resistance to load. Failure of the 4.5 oz./yd.<sup>2</sup> mesh was by the eventual complete tearing of the mesh. Only the two slip planes reinforced with the 4.5 oz./yd.<sup>2</sup> mesh failed. Thus once again the clamping strategy worked in that it prevented cracking through the joints reinforced with 15 oz./yd.<sup>2</sup> mesh. The Load/Metre versus Average Displacement data is plotted in Figure 3.34. The residual capacity observed is the result of shear friction along the damaged bed joints.

As will be seen in Chapter 4, the shape of the Load/Metre versus Average Displacement curve is similar to that of specimens reinforced with 4.5 oz./yd.<sup>2</sup> mesh oriented at 0°/90° to the bed joints using modified parging, and no form of precompression. The maximum load resisted by the specimen was 68.5 kN (58.0 kN/m). This on average, as will also be seen in Chapter 4, was 17 kN (14 kN/m) more than the

maximum load resisted by similar specimens with no form of precompression. It appears that the precompression force had a significant influence on the performance of the specimen. Thus the failed joints were not repaired and the remaining uncracked joints reinforced with 15 oz./yd.<sup>2</sup> mesh were not tested.



**Figure 3.36** – Load/Metre vs. Average Displacement of Mortar Parging Applied 4.5 oz./yd.<sup>2</sup> and 15 oz./yd.<sup>2</sup> Mesh at 0/90° (15 oz./yd.<sup>2</sup> mesh reinforced slip planes clamped)

A summary of all the Phase Two experimental results, along with a physical description of the specimens tests is provided in Table 3.2 (page 101).

### 3.9.6 PHASE TWO CONCLUSIONS

Specimens with mesh applied using epoxy had higher strengths than those where the mesh was applied with parging. Therefore, when using the same fibre mesh, preliminary tests indicate better utilization of the fibre strength is achieved when it is bonded to the masonry substrate using epoxy.

Based on the difficulty with testing, the possible additional damaged associated with the method of repairing the specimens, plus the apparent influence of the clamping



action, it was concluded that it was not feasible to obtain two sets of data from each specimen.

**Table 3.2 – Phase Two Experimental Results**

Specimen #	Test #	Description	Maximum Load, $P_{max}$ (kN) <sup>†</sup>	Load/Metre (kN/m) <sup>*</sup>	Shear Strength (MPa) <sup>‡</sup>
<b>Slip Plane Properties: Length = 0.59 m; Width = 0.068 m; Area = 0.04012 m<sup>2</sup></b>					
1	1	Epoxy applied 4.5 oz./yd. <sup>2</sup> and 15 oz./yd. <sup>2</sup> mesh at 0°/90° (No clamping force applied)	101.2	85.8	1.26
2	1	Epoxy applied 4.5 oz./yd. <sup>2</sup> and 15 oz./yd. <sup>2</sup> mesh at 0°/90° (15 oz./yd. <sup>2</sup> mesh reinforced slip planes clamped)	106.7	90.4	1.33
	2	Epoxy applied 4.5 oz./yd. <sup>2</sup> and 15 oz./yd. <sup>2</sup> mesh at 0°/90° (Damaged 4.5 oz./yd. <sup>2</sup> mesh reinforced slip planes repaired)	77.1	65.3	0.96
3	1	Mortar parging applied 4.5 oz./yd. <sup>2</sup> and 15 oz./yd. <sup>2</sup> mesh at 0°/90° (No clamping force applied)	61.3	51.5	0.76
4	1	Mortar parging applied 4.5 oz./yd. <sup>2</sup> and 15 oz./yd. <sup>2</sup> mesh at 0°/90° (15 oz./yd. <sup>2</sup> mesh reinforced slip planes clamped)	68.5	58.1	0.85

<sup>†</sup> Maximum load as recorded by the commercial load cell.

<sup>\*</sup> Maximum load equally distributed along both bed joints and divided by the length of the bed joint slip plane.

<sup>‡</sup> Maximum load equally distributed along both bed joints and divided by the area of the bed joint slip plane.

### 3.10 SUMMARY

- In Phase One, a total of 37 shear slip specimens were tested to failure, and of these 15 were reinforced with GFRP
- For all the specimen types, the GFRP increased the strength and ductility of the specimens and reduced the variability of the results, compared to the unretrofitted counterparts.

- For the T-1.5, T-0.5, A-2.5, A-1.5 and A-0.5 specimens the average increase in shear strength was 7.7, 3.1, 4.5, 5.2 and 6.6 times that, respectively, of the unretrofitted counterparts.
- For the T-1.5, T-0.5, A-2.5, A-1.5 and A-0.5 specimens the average increase in displacement at the maximum applied load was 16.4, 8.0, 5.7, 9.1 and 13.9 times that, respectively, of the unretrofitted counterparts.
- The T-1.5 specimen was chosen for further research based mainly on its ability to reduce bending induced tensile stresses, thus producing the most nearly pure shear stress conditions of all the specimen configurations.
- In Phase Two, a total of five shear slip tests were conducted and it was concluded that it was not feasible to obtain two sets of data from each specimen.
- Furthermore, when using the same fibre mesh, the Phase Two test results indicate better utilization of the fibre strength is achieved when it is bonded to the masonry substrate using epoxy rather than mortar parging.

## **CHAPTER 4: PHASE THREE EXPERIMENTAL RESULTS**

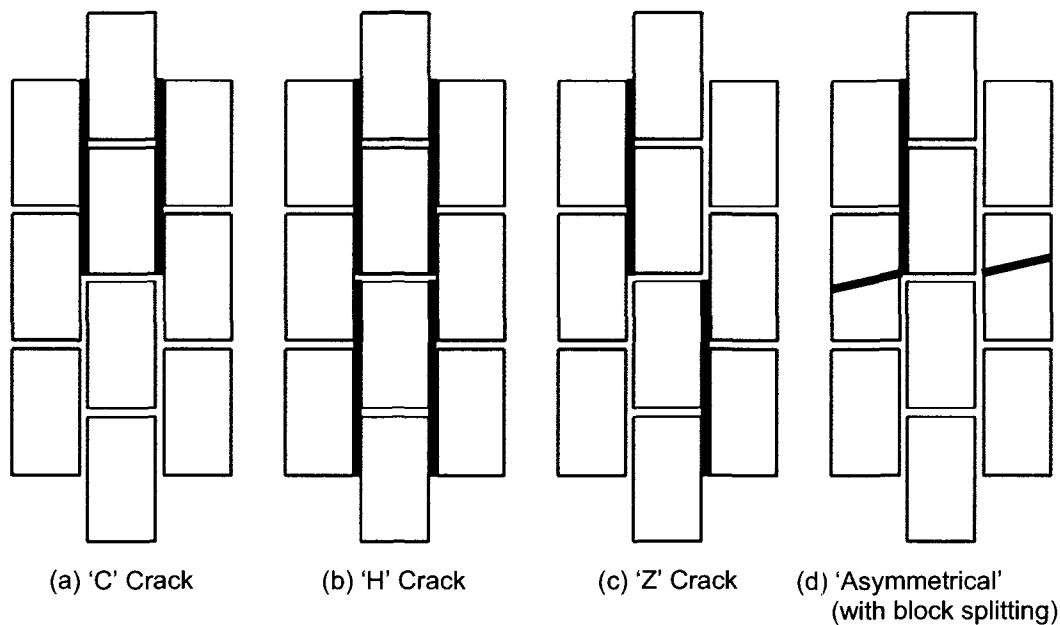
### **4.1 INTRODUCTION**

This chapter contains the results from Phase Three of the experimental investigation. In this phase, twenty-one T-1.5 specimens were tested with four different weights of fibreglass mesh, with a finished weight of 4.5 oz./yd.<sup>2</sup>, 6.0 oz./yd.<sup>2</sup>, 9.0 oz./yd.<sup>2</sup> and 12 oz./yd.<sup>2</sup> applied with modified mortar parging at two different orientations to the bed joint slip plane (0°/90°, ±45°).

Similar to Chapter 3, to allow for a more direct comparison, the data plots presented in this chapter contain the load per metre (kN/m) versus average displacement for each test. [Data plots of all the raw data can be found in Appendix C.] To assist with the analysis, an average curve for each set of test specimens was also obtained, using the same method as described in Chapter 3.

### **4.2 INTRODUCTION TO TYPICAL PHASE THREE SPECIMEN CRACK PATTERNS**

During testing of the twenty-one specimens in Phase Three of the experimental investigation, it was observed that the specimens failed in one of four distinct crack patterns. These patterns have been named the ‘C’ crack, ‘H’ crack, ‘Z’ crack, and Asymmetrical. Each pattern is illustrated in Figure 4.1. The applied load is transferred from the centre block to the side blocks along the bed joint slip planes. Once the slip plane on one side of specimen fails, the load is transferred to the other side. Therefore, no two in-line slip planes can fail. Throughout this chapter, these figures will be referred to in order to help the reader visualize and interpret the results.

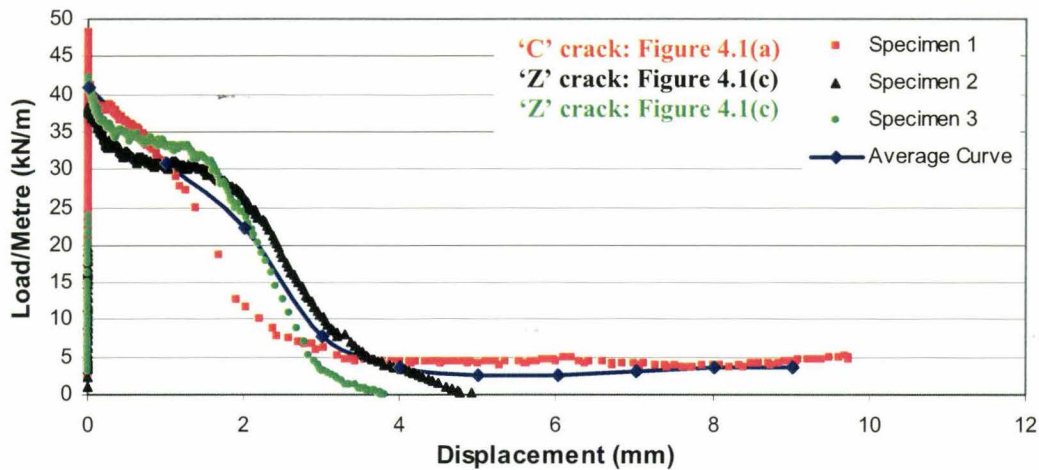


**Figure 4.1 – Typical Phase Three Specimen Crack Patterns**

#### **4.3 SPECIMENS RETROFITTED WITH 4.5 oz. MESH ORIENTED AT 0° AND 90° TO THE BED JOINTS**

Specimens 1, 2 and 3 all displayed similar load-displacement behaviour. During each test, the load continued to increase up to the onset of cracking, at which point it began to drop. Before cracking occurred, virtually no displacements were recorded by the LPTDs. Immediately after cracking, the displacements began to increase and this was accompanied by a gradual drop in the applied load. For specimens 2 and 3, at a post-peak residual capacity of about 50% of the maximum load, the rate of loss of capacity began to increase. For Specimen 1, this increased rate of loss of capacity occurred at a higher residual capacity and a lower average displacement. The Load/Metre versus Average Displacement data for the aforementioned specimens was plotted in Figure 4.2.





**Figure 4.2** – Load/Metre vs. Average Displacement (4.5 oz./yd.<sup>2</sup> mesh at 0°/90°)

Complete failure of the specimens and loss of capacity was caused by the eventual complete tearing of the mesh. Based on the results from the other tests in this phase, to be discussed later, it is hypothesised that initially the mesh was being deformed but, gradually, as the displacements increased, it began to tear. It is the tearing of the fibres that resulted in the increased rate of loss of capacity. The tests were terminated once the fibres were completely torn, at which point the capacity had decreased to zero. For Specimen 1, major cracks formed along the two lower bed joints (i.e., ‘C’ crack pattern shown in Figure 4.1(a)), both on the front face and the rear face. Hairline cracks also formed along the two upper bed joints. For both Specimens 2 and 3, major cracks formed along the lower-left and upper-right bed joints (i.e., ‘Z’ crack pattern shown in Figure 4.1(c)), both on the front face and the rear face. A typical photograph of a damaged bed joint is reproduced in Figure 4.3.

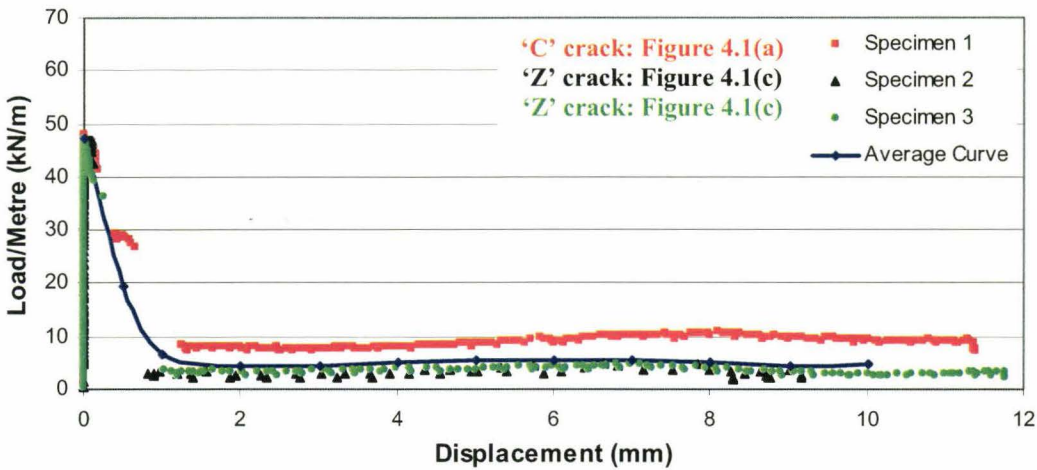


**Figure 4.3** – Typical Fibre Damage (Tearing) of Bed Joints Reinforced with 4.5 oz. Mesh at  $0^{\circ}/90^{\circ}$

#### **4.4 SPECIMENS RETROFITTED WITH 4.5 oz. MESH ORIENTED AT $\pm 45^{\circ}$ TO THE BED JOINTS**

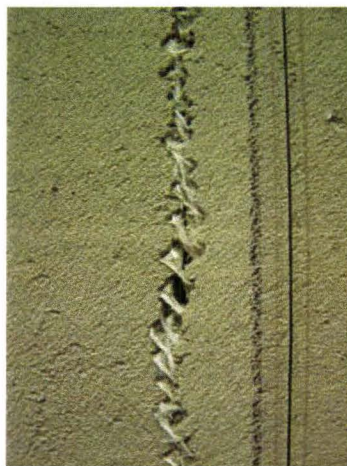
Specimens 1, 2 and 3 displayed similar load-displacement behaviour; during each test, the load continued to increase up to the onset of cracking, at which point there was a sudden dramatic drop in resistance to load. Before cracking occurred, virtually no displacements were recorded by the LPTDs. The average maximum resistance of these three specimens was greater than that of their  $0^{\circ}/90^{\circ}$  reinforced counterparts. The Load/Metre versus Average Displacement data for these specimens are plotted in Figure 4.4.

The fibres oriented to resist load in uniaxial tension began to rupture once the ultimate load of the test specimen was reached. The sudden drop in capacity is clearly noticeable in the load-displacement figures, but it does not decrease to zero. The mesh did not completely tear and was able to provide some limited residual capacity. Nonetheless, this type of failure is much more brittle with more rapid loss of capacity than the  $0^{\circ}/90^{\circ}$  reinforced counterparts. Each test was terminated once the centre 20 mm gap was closed.



**Figure 4.4** – Load/Metre vs. Average Displacement (4.5 oz./yd.<sup>2</sup> mesh at  $\pm 45^\circ$ )

For Specimen 1, major cracks formed along the two upper bed joints (i.e., ‘C’ crack pattern shown in Figure 4.1(a)), both on the front face and the rear face. Hairline cracks also formed along the two lower bed joints. For Specimens 2 and 3, major cracks formed along the upper-left and lower-right bed joints (‘Z’ crack pattern shown in Figure 4.1(c)), both on the front face and the rear face. A typical photograph of a damaged bed joint is provided in Figure 4.5.



**Figure 4.5** – Typical Fibre Damage (Tearing) of Bed Joints Reinforced with 4.5 oz. Mesh at  $\pm 45^\circ$



#### 4.5 SPECIMENS RETROFITTED WITH 6 oz. MESH ORIENTED AT 0° AND 90° TO THE BED JOINTS

Specimens 1, 2 and 3 displayed similar load-displacement behaviour during their respective tests. The load continued to increase up to the onset of cracking, at which point the load began to drop with increasing displacement (slip). However the decrease in capacity was relatively small. Before cracking occurred, virtually no displacements were recorded by the LPTDs. The Load/Metre versus Average Displacement data for these specimens are plotted in Figure 4.6.

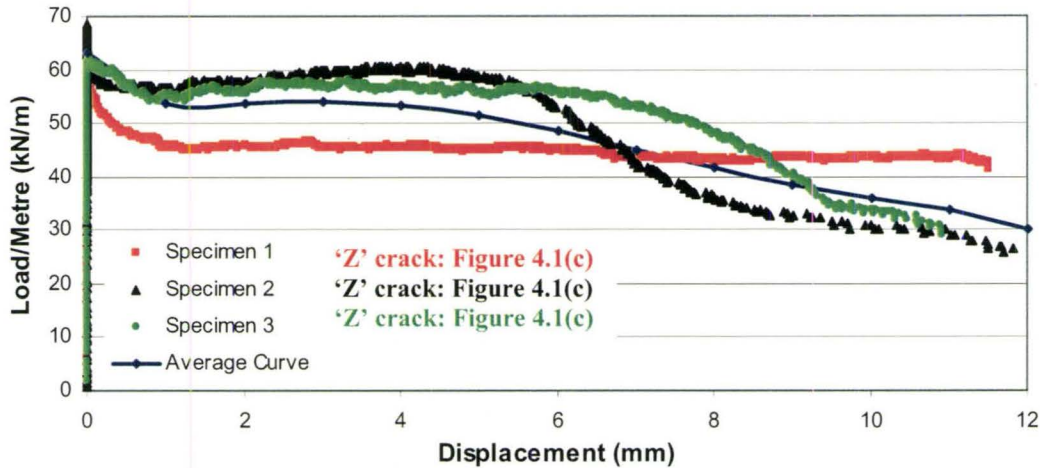
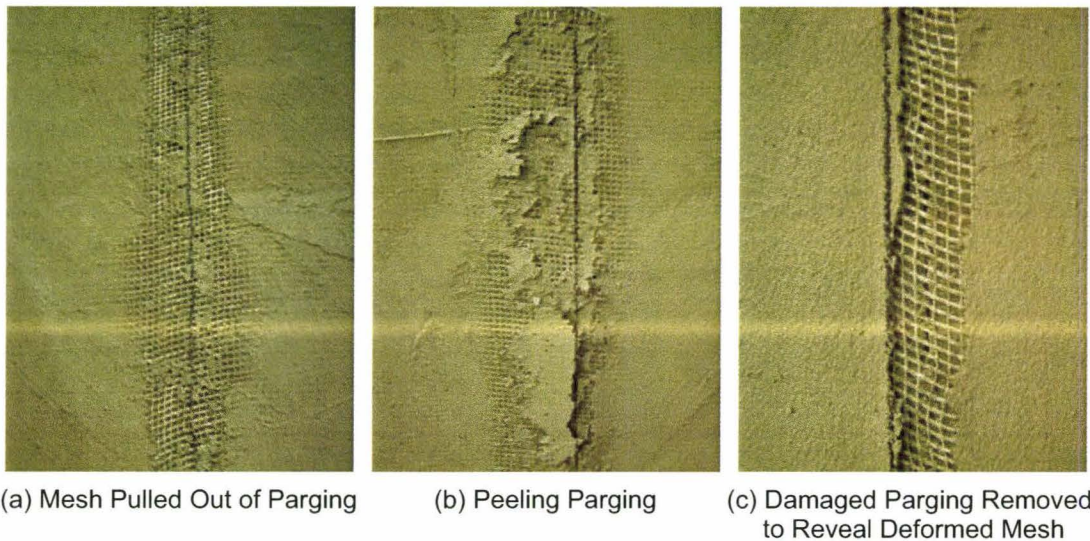


Figure 4.6 – Load/Metre vs. Average Displacement ( 6 oz./yd.<sup>2</sup> mesh at 0°/90°)

Up to approximately midway through the testing range of displacements, the capacity remained essentially constant as the displacements increased. During this stage of testing, it was noticed that the cement parging, used to adhere the mesh to the concrete block specimens, began to crack and peel away, leaving the mesh underneath undamaged. This type of failure is known as delamination. It is a much more ductile failure mode than tearing. As can be seen in Figure 4.6, at very large slip displacements, the capacity did again begin to decrease. After the test was terminated, upon closer inspection of the



failure planes, it was observed that a small percentage of the fibres had torn. For Specimen 1, tearing of the fibres did not occur at all and after a larger than average initial drop in capacity, the load remained essentially constant. Thus, it was concluded that partial tearing of the mesh resulted in the decreases in load resistance for Specimens 2 and 3 at approximately midway through testing. All of the tests were terminated once the centre gap in each specimen was closed. For all three specimens, the major slip cracks formed along the upper-left and lower-right bed joints (i.e., ‘Z’ crack pattern shown in Figure 4.1(c)), both on the front face and the rear face. Photographs of damaged bed joints are presented in Figure 4.7.



**Figure 4.7** – Typical Damage of Bed Joints Reinforced with 6.0 oz. Mesh at  $0^{\circ}/90^{\circ}$

#### **4.6 SPECIMENS RETROFITTED WITH 6 oz. MESH ORIENTED AT $\pm 45^{\circ}$ TO THE BED JOINTS**

Specimens 1, 2 and 3 all displayed similar Load/Metre versus Average Displacement behaviour, as shown in Figure 4.8. During each test, the load continued to

increase up to the onset of cracking. Before cracking occurred, virtually no displacements were recorded by the LPTDs.

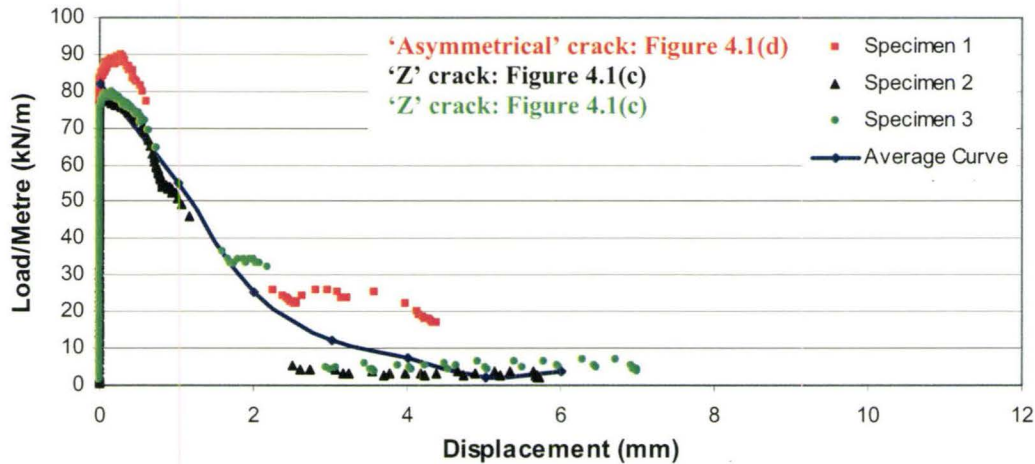
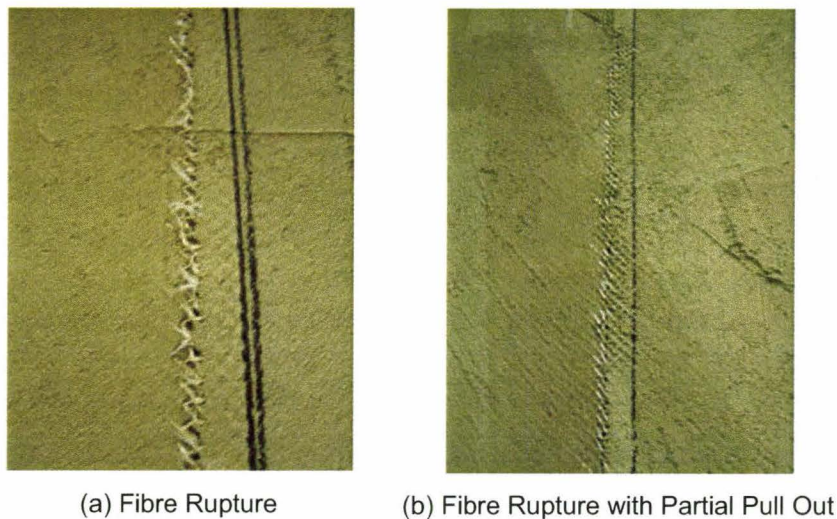


Figure 4.8 – Load/Metre vs. Average Displacement ( 6 oz./yd.<sup>2</sup> mesh at  $\pm 45^\circ$ )

During the initial cracking, there was a very limited increase in load with corresponding small displacements before the dramatic decrease in capacity began. With fully developed cracking, the load decreased continuously with no sudden decreases as the displacements increased. The fibres assisting in resisting load are in uniaxial tension and, once their individual ultimate load resistance was reached, they ruptured. The rapid decrease in load with increasing displacements coincides with the sequential rupturing of individual fibres. The average maximum capacity of these three specimens was greater than that of their  $0^\circ/90^\circ$  reinforced counterparts. The rapid decrease in capacity is clearly noticeable in the load-displacement figures but, because it did not decrease to zero, the incompletely torn mesh was able to provide a small residual capacity. Clearly, this type of failure is much more brittle than observed for the  $0^\circ/90^\circ$  reinforced counterparts. Each test was terminated once the centre gap was closed. For Specimen 1, a major crack only

formed along the upper-left bed joint. A hairline fracture did form along the upper-right bed joint but this was insufficient to prevent the induced rotation which resulted in splitting of the centre blocks (see Figure 4.1(d)). Specimens 2 and 3 failed in the more typical manner. Major cracks formed along the lower-left and upper-right bed joints (i.e., ‘Z’ crack pattern shown in Figure 4.1(c)), both on the front face and the rear face. Photographs of the damaged bed joints are provided in Figure 4.9.



**Figure 4.9** – Typical Torn Fibre Damage of Bed Joints Reinforced with 6.0 oz. Mesh at  $\pm 45^\circ$

#### **4.7 SPECIMENS RETROFITTED WITH 9 oz. MESH ORIENTED AT $0^\circ$ AND $90^\circ$ TO THE BED JOINTS**

Specimens 1, 2 and 3 all displayed similar Load/Metre versus Average Displacement behaviour during their respective tests, as shown in Figure 4.10. During each test, the load continued to increase up to the visible onset of cracking, at which point the load decreased slightly. Before cracking occurred, virtually no displacements were recorded by the LPTDs. After cracking, large increases in displacements were



accompanied by constant high residual capacities which, in the case of Specimen 2, later began to decrease.

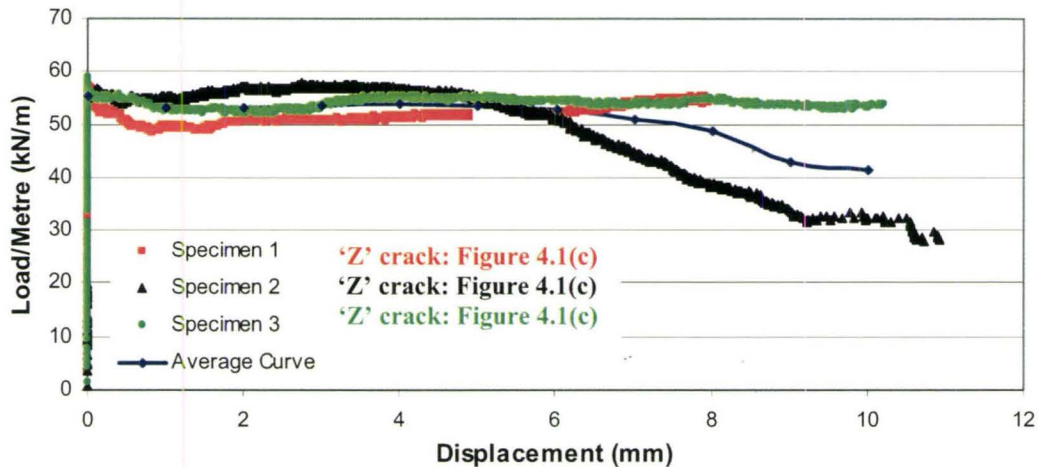
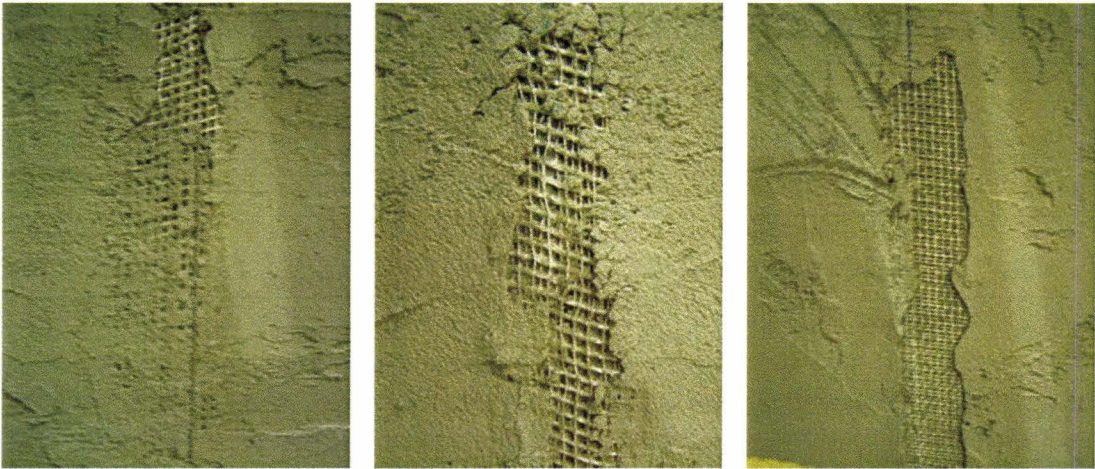


Figure 4.10 – Load/Metre vs. Average Displacement ( 9 oz./yd.<sup>2</sup> mesh at 0°/90°)

For Specimens 1 and 3, the load reached a plateau and remained essentially constant for the duration of the test. During this stage of the testing, it was noticed that the cement parging, used to bond the mesh to the concrete block specimens, was cracking and peeling away, leaving the mesh underneath undamaged. This is the same ductile delamination failure noticed in previous tests for fibres oriented at 0°/90° to the bed joints. The failure mode of Specimen 2 was slightly different. Up to approximately midway through the test, the capacity remained essentially constant (delamination failure) as the displacements increased, at which point the load began to decrease. After the test was terminated, closer inspection of the failure planes showed that a small percentage of the fibres had torn. No tearing of the mesh was observed with Specimens 1 or 3. Thus it was concluded that partial tearing of the mesh resulted in the decreased load resistance in Specimen 2. All of the tests were terminated once the centre gap in each specimen was



closed. For Specimens 1 and 2, the major cracks formed along the lower-left and upper-right bed joints (i.e., ‘Z’ crack pattern shown in Figure 4.1(c)), both on the front face and the rear face. For Specimen 3, the major cracks formed along the upper-left and lower-right bed joints (‘Z’ crack pattern shown in Figure 4.1(c)), both on the front face and the rear face. Photographs of the damaged bed joints are reproduced in Figure 4.11.



(a) Mesh Pulled Out of Parging (b) Damaged Parging Removed to Reveal Deformed Mesh

**Figure 4.11** – Typical Damage of Bed Joints Reinforced with 9.0 oz. Mesh at  $0^{\circ}/90^{\circ}$

**4.8 SPECIMENS RETROFITTED WITH 9 oz. MESH ORIENTED AT  $\pm 45^{\circ}$  TO THE BED JOINTS**

Specimens 1, 2 and 3 all displayed similar Load/Metre versus Average Displacement behaviour during their respective tests, as shown in Figure 4.12. The load continued to increase up to the onset of cracking. Before cracking occurred, virtually no displacements were recorded by the LPTDs. There was very limited measurable displacement before the sudden dramatic decrease in capacity occurred. At about 1 mm displacement, a stable state was reached and, for larger displacements, the capacity continued to decrease but with no sudden decreases. Once again, the fibres assisting in

resisting load are in uniaxial tension and, once their individual ultimate loads were reached, they ruptured. The initial rupture of some fibres coincides with the initial sudden decrease in load and sudden increase in the displacements. The average maximum load of these three specimens was greater than that of their  $0^{\circ}/90^{\circ}$  reinforced counterparts. The initial sudden decrease in capacity is clearly noticeable in Figure 4.12, but it does not drop to zero. The mesh did not completely tear and was able to provide limited residual capacity.

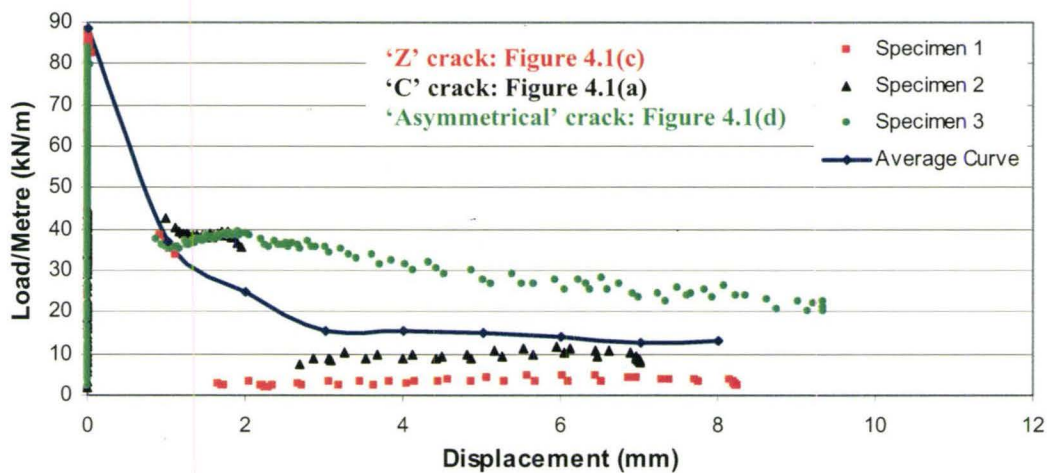


Figure 4.12 – Load/Metre vs. Average Displacement ( 9 oz./yd.<sup>2</sup> mesh at  $\pm 45^{\circ}$ )

This type of failure is much more brittle than observed for the  $0^{\circ}/90^{\circ}$  reinforced counterparts. Each test was terminated once the centre gap was closed. For Specimen 1, the major cracks formed along the upper-left and lower-right bed joints (i.e., ‘Z’ crack pattern shown in Figure 4.1(c)). For Specimen 2, the major cracks formed along the lower-left and lower-right bed joints (i.e., ‘C’ crack pattern shown in Figure 4.1(a)). For Specimen 3, a major crack only formed along the upper-left bed joints. A hairline crack did form along the upper-right bed joint but this was insufficient to prevent the induced



rotation which resulted in splitting of the centre blocks (see Figure 4.1(d)). A photograph of a typical damaged bed joint is provided in Figure 4.13.



**Figure 4.13** – Typical Fibre Damage (Tearing) of a Bed Joint Reinforced with 9.0 oz. Mesh at  $\pm 45^\circ$

#### **4.9 SPECIMENS RETROFITTED WITH 12 oz. MESH ORIENTED AT $0^\circ$ AND $90^\circ$ TO THE BED JOINTS**

Specimens 1, 2 and 3 all displayed similar Load/Metre versus Average Displacement behaviour during their respective tests, as shown in Figure 4.14. The load continued to increase up to the onset of cracking, at which point the load began to drop. Before cracking occurred, virtually no displacements were recorded by the LPTDs. Immediately after cracking, the increasing displacement was accompanied by a rapid decrease in the capacity. With all three specimens, the load eventually reached a plateau and essentially remained constant for the duration of the test. Over this constant load displacement, it was noticed that the cement parging, used to adhere the mesh to the concrete block specimens, cracked and peeled away, leaving the mesh underneath undamaged. This is the same ductile delamination failure noticed in previous tests. No tearing of the mesh was observed with any of the specimens. All of the tests were terminated once the centre gap was closed. For Specimens 1 and 3, the major cracks

formed along all four of the bed joints (i.e., ‘H’ crack pattern shown in Figure 4.1(b)), both on the front face and the rear face. For Specimen 2, the major cracks formed along the lower-left and upper-right bed joints (i.e., ‘Z’ crack pattern shown in Figure 4.1(c)), both on the front face and the rear face. The ‘C’ or ‘Z’ crack patterns are much more typical than the ‘H’ crack pattern. Photographs of the damaged bed joints are provided in Figure 4.15.

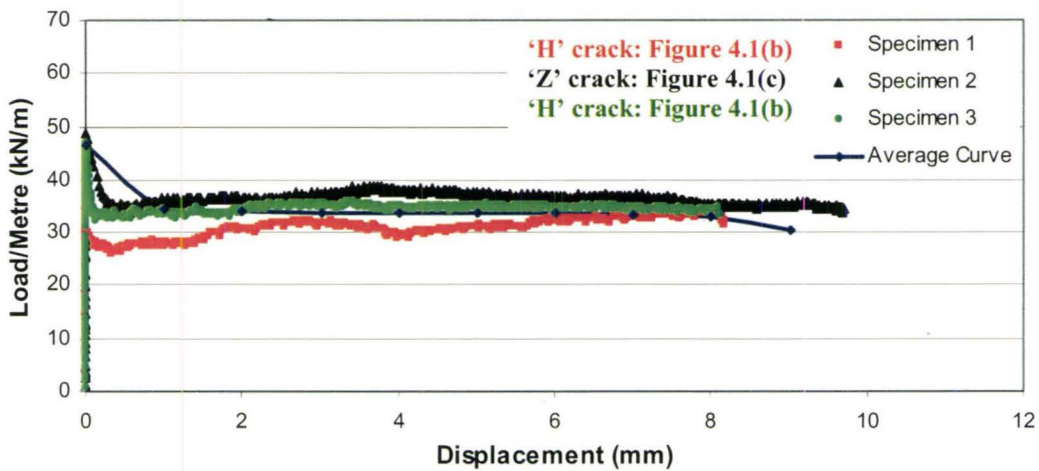
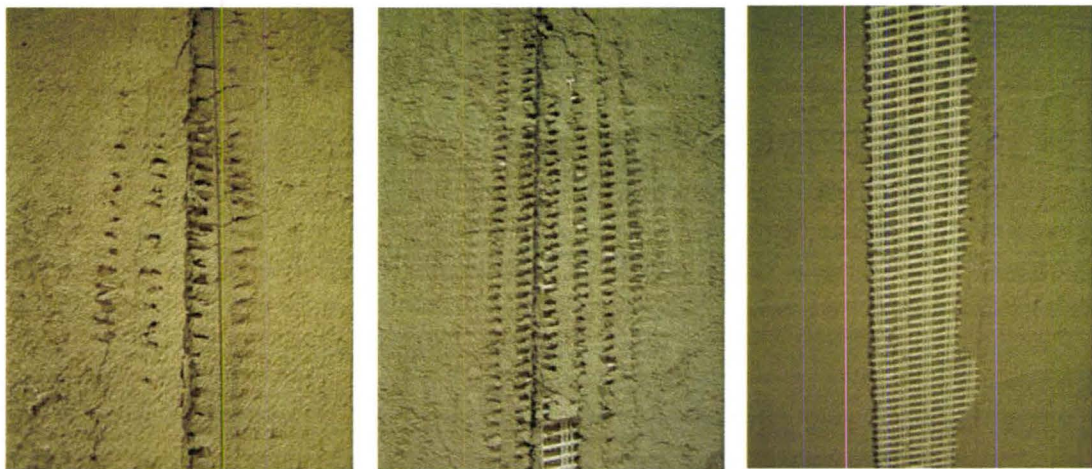


Figure 4.14 – Load/Metre vs. Average Displacement ( 12 oz./yd.<sup>2</sup> mesh at 0°/90°)



(a) Mesh Pulled Out of Parging (Progressive Damage) (b) Damaged Parging Removed to Reveal Deformed Mesh

Figure 4.15 – Typical Damage of Bed Joints Reinforced with 12 oz. Mesh at 0°/90°



#### **4.10 FAILURE MODES OF THE STRENGTHENED SPECIMENS**

As stated previously, the configuration of the specimens was originally selected because it would allow the specimens to fail in pure shear. Aside from the weight of the mesh being used, the major variable being assessed was the orientation of the mesh fibres to the bed joint slip planes (either  $0^{\circ}/90^{\circ}$  or  $\pm 45^{\circ}$ ). From the discussion and Load/Metre versus Average Displacement plots presented in Sections 4.3 to 4.9, it can be concluded that for any given mesh weight, the specimens with the  $0^{\circ}/90^{\circ}$  fibre orientation failed in a much more ductile fashion than with the  $\pm 45^{\circ}$  orientation. The ductility for the  $0^{\circ}/90^{\circ}$  fibre orientation is characterized, typically, by extensive deformation while still maintaining a fairly constant load once the maximum load is exceeded.

Except for the 4.5 oz. mesh, for the other mesh weights at  $0^{\circ}/90^{\circ}$  fibre orientation, by the end of each test the fibres were deformed but undamaged. Thus the system could have withstood further deformation. This ductile failure is very different from the comparatively brittle failure observed with all the  $\pm 45^{\circ}$  oriented meshes. Once the maximum load was reached, which occurred at a very small displacement, there was a sudden and significant loss in capacity as the fibres began to rupture. However, specimens with the  $\pm 45^{\circ}$  fibre orientation were able to reach higher loads than their  $0^{\circ}/90^{\circ}$  counterparts. The aforementioned observations are consistent with the conclusions made by Eshani et al. (1997).

For convenience to the reader, the average Load/Metre versus Average Displacement plots for the specimens with the  $0^{\circ}/90^{\circ}$  and  $\pm 45^{\circ}$  mesh orientations are reproduced in Figure 4.16 and Figure 4.17, respectively. The area under the Load/Metre

versus Average Displacement plots reflects the energy absorbing capacity of the mesh system. For any mesh weight, the area under the  $0^{\circ}/90^{\circ}$  plot is much larger than that for the  $\pm 45^{\circ}$  orientation and is thus a measure of ability to absorb much more energy. This property is very advantageous in seismic regions where energy absorption is an important requirement for constructing earthquake resistant structures.

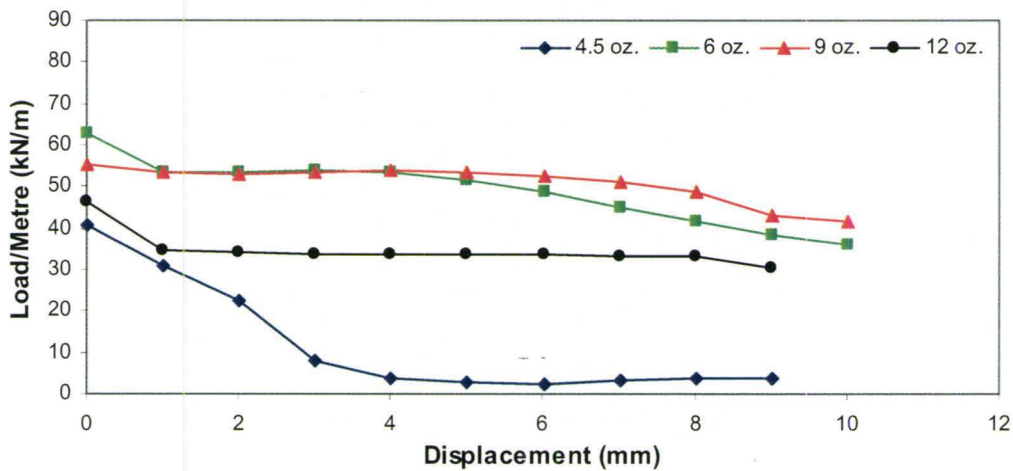


Figure 4.16 – Average Load/Metre vs. Average Displacement Curves for  $0^{\circ}/90^{\circ}$  Mesh

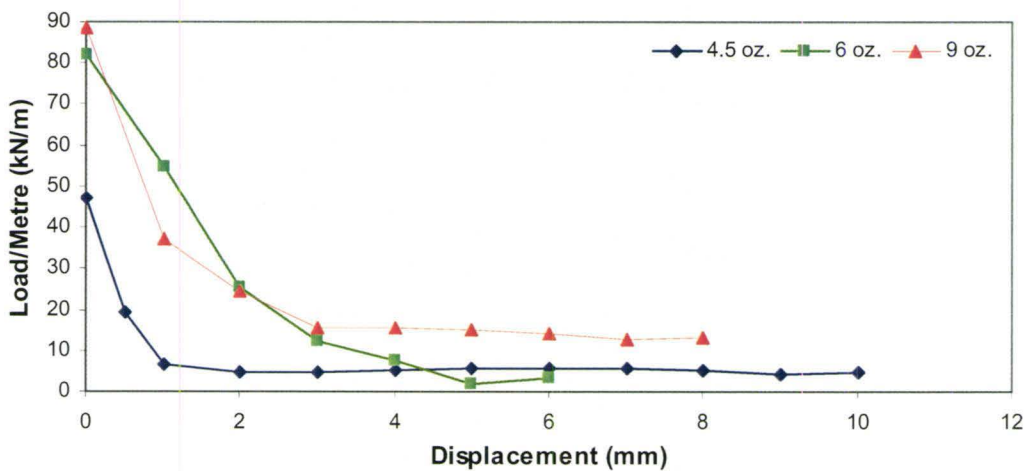


Figure 4.17 – Average Load/Metre vs. Average Displacement Curves for  $\pm 45^{\circ}$  Mesh

A summary of the experimental results of all the Phase Three specimens, and the unreinforced TU – 1.5 specimens from Phase One, are presented in Table 4.1. For the specimens retrofitted with mesh at  $\pm 45^\circ$  orientation, failure was caused by the tearing/rupture of the fibres along the mortared bed joints. This failure mode is associated with the strength of the laminate being less than the strength of the bond between the laminate and the masonry. [As will be discussed later, this does not imply that all fibres were able to share equally in resisting load.] Due to the orientation of the fibres and the direction of the principal tension, the fibres are in uniaxial tension and fail once their individual capacities are reached. As previously stated, rupture of the fibres occurred at very small displacements. For every mesh weight, except the 4.5 oz. weight, partial rupture of the fibres occurred. Some of the fibres along the slip plane were still intact, which accounts for the residual, albeit greatly reduced, capacities.

For the specimens retrofitted with mesh at the  $0^\circ/90^\circ$  orientation, failure was caused by delamination of the fibre mesh along the reinforced mortared bed joints. This failure mode is associated with the strength of the laminate being greater than the strength of the bond between the laminate and the masonry. Due to their orientation, the fibres in the strong direction of the mesh were perpendicular to the direction of the load (i.e., perpendicular to the bed joint slip plane). In essence they acted as tension ties. As slip along the plane occurred, the fibres deformed in tension and began creating a clamping action along the bed joint to provide a shear-friction resistance to slip. At this stage, instead of rupturing, the fibres were torn out of the mortar parging. At the end of each test, it took very little effort to brush away the damaged parging to reveal the undamaged

fibres beneath. The first layer of parging was still bonded to the masonry. The only exception was the 4.5 oz. mesh at  $0^{\circ}/90^{\circ}$  orientation which did tear.

During testing, the initial behaviour of all the specimens was very similar. The load continued to increase until a crack formed along one of the four bed joints slip planes. At this point, the load began to decrease as the displacements increased. (Up to formation of the first crack no significant displacements were recorded by the 12.5 mm stroke LPDTs. [It is suspected that the LPDTs used did not have sufficient resolution to adequately capture the displacement up to the formation of the first crack.] The weakened slip plane resulted in more of the load being transferred to the adjacent bed joint. Most often, the failure along one of the slip planes was followed by failure along the slip plane diagonal to it in the ‘Z’ crack pattern (Figure 4.1(c)). Occasionally, the initial slip plane failure was followed by cracking along the slip plane next to it to form the ‘C’ crack pattern (Figure 4.1(a)). As expected, the ‘Z’ crack was by far the most common pattern. The two most rare failure patterns were the ‘H’ crack (Figure 4.1(b)), in which cracks formed along all four slip planes, and the ‘asymmetrical’ crack (Figure 4.1(d)), in which failure occurred along only one slip plane which induced a rotation resulting in middle block splitting. For the  $\pm 45^{\circ}$  fibre orientation, the failure was initiated by tearing of the mesh along one of the four slip planes. This was followed by tearing of the mesh along the slip plane diagonal to the original tear.

A full summary of the Phase Three experimental results is provided in Table 4.1.



**Table 4.1 – Phase Three Experimental Results**

<b>Slip Plane Properties: Length = 0.59 m; Width = 0.068 m</b>						
<b>Specimen</b>	<b>Typical Failure Mode</b>	<b>Mesh Failure Description</b>	<b>Maximum Load, <math>P_{max}</math> (kN)<sup>†</sup></b>	<b>Load/Metre (kN/m)<sup>*</sup></b>	<b>Shear Strength (MPa)<sup>‡</sup></b>	<b>C.O.V. (%)</b>
<b>Unreinforced (Phase One TU – 1.5 Results)</b>						
1	'Z' crack Figure 4.1(c)	N/A	22.8	19.3	0.28	15.3
2	'Z' crack Figure 4.1(c)	N/A	27.9	23.6	0.35	
3	'Z' crack Figure 4.1(c)	N/A	28.8	24.4	0.36	
4	'Z' crack Figure 4.1(c)	N/A	31.0	26.3	0.39	
5	'Z' crack Figure 4.1(c)	N/A	21.6	18.3	0.27	
<b>Average</b>	N/A	N/A	<b>26.4</b>	<b>22.4</b>	<b>0.33</b>	
<b>4.5 oz./yd.<sup>2</sup> at 0°/90°</b>						
1	'C' crack Figure 4.1(a)	Tearing (complete)	57.3	48.5	0.71	10.3
2	'Z' crack Figure 4.1(c)	Tearing (complete)	46.9	39.7	0.58	
3	'Z' crack Figure 4.1(c)	Tearing (complete)	50.4	42.7	0.63	
<b>Average</b>	N/A	N/A	<b>51.5</b>	<b>43.6</b>	<b>0.64</b>	
<b>4.5 oz./yd.<sup>2</sup> at ±45°</b>						
1	'C' crack Figure 4.1(a)	Tearing (incomplete)	55.6	47.1	0.69	0.3
2	'Z' crack Figure 4.1(c)	Tearing (incomplete)	55.2	46.8	0.69	
3	'Z' crack Figure 4.1(c)	Tearing (incomplete)	55.3	46.9	0.69	
<b>Average</b>	N/A	N/A	<b>55.4</b>	<b>46.9</b>	<b>0.69</b>	
<b>6 oz./yd.<sup>2</sup> at 0°/90°</b>						
1	'Z' crack Figure 4.1(c)	Delamination	68.5	58.1	0.85	8.4
2	'Z' crack Figure 4.1(c)	Delamination w/ Partial Tearing	80.7	68.4	1.01	
3	'Z' crack Figure 4.1(c)	Delamination w/ Partial Tearing	72.9	61.8	0.91	
<b>Average</b>	N/A	N/A	<b>74.0</b>	<b>62.7</b>	<b>0.92</b>	
<b>6 oz./yd.<sup>2</sup> at ±45°</b>						
1	'Asymmetrical' Figure 4.1(d)	Tearing (incomplete)	105.7	89.6	1.32	7.5
2	'Z' crack Figure 4.1(c)	Tearing (incomplete)	92.4	78.3	1.15	
3	'Z' crack Figure 4.1(c)	Tearing (incomplete)	93.9	79.6	1.17	
<b>Average</b>	N/A	N/A	<b>97.3</b>	<b>82.5</b>	<b>1.21</b>	

<b>Table 4.1 (continued) – Summary of Phase Three Results</b>						
<b>9 oz./yd.<sup>2</sup> at 0°/90°</b>						
1	'Z' crack Figure 4.1(c)	Delamination	67.0	56.8	0.83	3.9
2	'Z' crack Figure 4.1(c)	Delamination w/ Partial Tearing	72.4	61.3	0.90	
3	'Z' crack Figure 4.1(c)	Delamination	69.3	58.7	0.86	
<b>Average</b>	<b>N/A</b>	<b>N/A</b>	<b>69.6</b>	<b>58.9</b>	<b>0.87</b>	
<b>9 oz./yd.<sup>2</sup> at ±45°</b>						
1	'Z' crack Figure 4.1(c)	Tearing (incomplete)	103.6	87.8	1.29	5.4
2	'C' crack Figure 4.1(a)	Tearing (incomplete)	110.1	93.3	1.37	
3	'Asymmetrical' Figure 4.1(d)	Tearing (incomplete)	98.8	83.7	1.23	
<b>Average</b>	<b>N/A</b>	<b>N/A</b>	<b>104.2</b>	<b>88.3</b>	<b>1.30</b>	
<b>12 oz./yd.<sup>2</sup> at 0°/90°</b>						
1	'H' crack Figure 4.1(d)	Delamination	48.6	41.2	0.61	10.9
2	'Z' crack Figure 4.1(c)	Delamination	60.5	51.3	0.75	
3	'H' crack Figure 4.1(d)	Delamination	54.8	46.5	0.68	
<b>Average</b>	<b>N/A</b>	<b>N/A</b>	<b>54.6</b>	<b>46.3</b>	<b>0.68</b>	

† Maximum load as recorded by the commercial load cell.

\* Maximum load equally distributed along both bed joints and divided by the length of the bed joint slip plane consisting of two face shells.

‡ Maximum load equally distributed along both bed joints and divided by the area of the bed joint slip plane.

By examining Table 4.1, it is observed that the crack pattern had an influence on the maximum failure load of each specimen, particularly the 'C' crack versus the 'Z' crack. When the 'Z' crack (Figure 4.1(c)) failure pattern occurred, the specimen split into two separate components that had a tendency to move away from each other, which greatly reduced the friction along the failed slip planes. When the 'C' crack (Figure 4.1(a)) failure pattern occurred, the contact between the failed slip planes, and therefore also the friction, was maintained. Thus, it was expected that specimens which failed in the 'C' crack pattern would have a higher failure load and higher residual post-peak capacity.

This is confirmed by examining Table 4.1 and the Load/Metre versus Average Displacement graphs presented in Sections 4.2 to 4.9.

#### 4.11 INFLUENCE OF FIBRE WEIGHT WITH ORIENTATION

As previously discussed, for any given weight of mesh the maximum load/metre strength along the slip plane was greater for the  $\pm 45^\circ$  orientation than the  $0^\circ/90^\circ$  orientation. At  $\pm 45^\circ$ , the tensioned fibres were able to directly resist the shear force prior to rupturing. The discussion will now focus on the influence of fibre weight on the average load/metre capacity. It is natural human instinct to expect that doubling the fibre weight will result in double the capacity. This proportional strength concept is examined in the following sections

##### 4.11.1 FIBRES AT $\pm 45^\circ$ ORIENTATION

For mesh fibres oriented at  $\pm 45^\circ$  to the slip plane, the average load/metre strengths of the unreinforced specimen, and the 4.5 oz., 6 oz. and 9 oz. reinforced specimens, were 22.4 kN/m, 46.9 kN/m, 82.5 kN/m and 88.3 kN/m, respectively. These values have been plotted below in Figure 4.18.

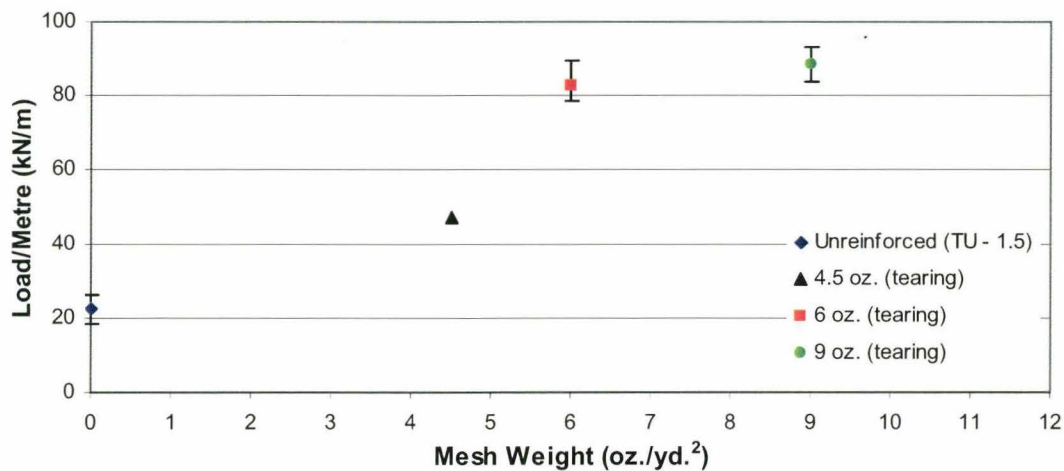


Figure 4.18 – Average Load/Metre vs. Mesh Weight for  $\pm 45^\circ$  Fibre Orientation



Every increase in the weight of the mesh was accompanied by an increase in the average strength of the slip plane. The use of 4.5 oz. mesh more than doubled the capacity compared to the unreinforced specimen, which is a great improvement. Recalling that the 9 oz. mesh was created by applying two layers of the 4.5 oz. mesh, it is interesting to note that the average load/metre strength of the 9 oz. mesh was nearly double that of the 4.5 oz. mesh (88.3 kN/m versus 46.9 kN/m). However, the performance of the 6 oz., single layer, mesh was just slightly below that of the 9 oz. mesh.

A comparison of the performance of each mesh, based on weight, is valid if they all have the same basic strength. As presented in Chapter 2, the 4.5 oz. and 6 oz. meshes had an average breaking strength along the strong (weft) direction of 1.98 kN/50 mm and 3.80 kN/50 mm, respectively. Therefore, the 9 oz. mesh had an average breaking strength of 3.96 kN/ 50 mm, which is not much larger than the strength of the 6 oz. mesh. Since the fibres resisting the tension force were oriented at  $45^\circ$  to the bed joint, a component of the force acted parallel to the bed joints, and the other component acted normal to the bed joints (providing a normal tensile force), as illustrated in Figure 4.19. The normal tensile force, in turn, created shear friction resistance through equal compression clamping action along the bed joints.

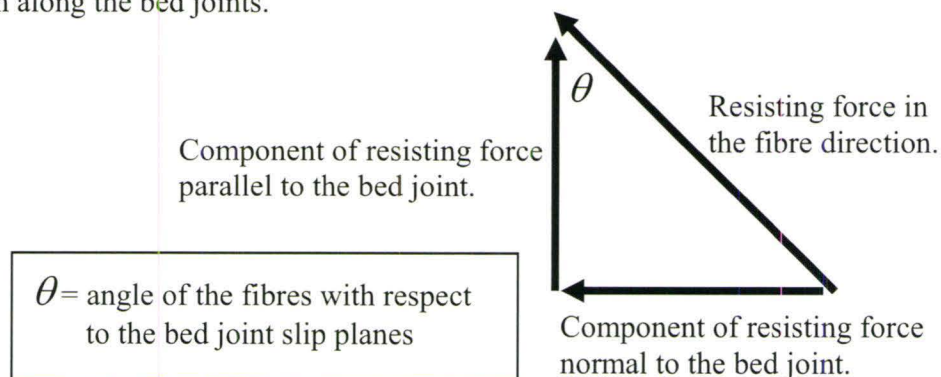


Figure 4.19 – Resolved Force Components



Using the average maximum load ( $P_{\max}$ ) from Table 4.1 for the 4.5 oz., 6 oz., and 9 oz. meshes oriented at  $\pm 45^\circ$ , the following analysis can be performed:

**(1) 4.5 oz. Mesh:**

$$\sin \theta (P_{\text{parallel}} + \mu P_{\text{normal}}) = P_{\text{theoretical}}, \quad \theta = 45^\circ \quad (4.1)$$

$$\sin 45^\circ \left\{ \begin{array}{l} \left[ \left( \frac{1.98 \text{ kN}}{50 \text{ mm}} \right) \times \left( \frac{590 \text{ mm}}{\text{slip plane}} \right) \times (4 \text{ slip plane}) \times \cos 45^\circ \right] + \\ \left[ \mu \left( \frac{1.98 \text{ kN}}{50 \text{ mm}} \right) \times \left( \frac{590 \text{ mm}}{\text{slip plane}} \right) \times (4 \text{ slip plane}) \times \sin 45^\circ \right] \end{array} \right\} = P_{\text{theoretical}}$$

$$0.707[(93.46 \text{ kN})(0.707) + (1.0)(93.46 \text{ kN})(0.707)] = 93.43 \text{ kN}$$

$$\frac{P_{\text{max, experimental}}}{P_{\text{theoretical}}} = \frac{55.40 \text{ kN}}{93.43 \text{ kN}} = 0.59$$

**(2) 6 oz. Mesh:**

$$\sin \theta (P_{\text{parallel}} + \mu P_{\text{normal}}) = P_{\text{theoretical}}, \quad \theta = 45^\circ \quad (4.2)$$

$$\sin 45^\circ \left\{ \begin{array}{l} \left[ \left( \frac{3.80 \text{ kN}}{50 \text{ mm}} \right) \times \left( \frac{590 \text{ mm}}{\text{slip plane}} \right) \times (4 \text{ slip plane}) \times \cos 45^\circ \right] + \\ \left[ \mu \left( \frac{3.80 \text{ kN}}{50 \text{ mm}} \right) \times \left( \frac{590 \text{ mm}}{\text{slip plane}} \right) \times (4 \text{ slip plane}) \times \sin 45^\circ \right] \end{array} \right\} = P_{\text{theoretical}}$$

$$0.707[(179.36 \text{ kN})(0.707) + (1.0)(179.36 \text{ kN})(0.707)] = 179.31 \text{ kN}$$

$$\frac{P_{\text{max, experimental}}}{P_{\text{theoretical}}} = \frac{97.30 \text{ kN}}{179.31 \text{ kN}} = 0.54$$

**(3) 9 oz. Mesh:**

$$\sin \theta (P_{\text{parallel}} + \mu P_{\text{normal}}) = P_{\text{theoretical}}, \quad \theta = 45^\circ \quad (4.3)$$

$$\sin 45^\circ \left\{ \begin{array}{l} \left[ \left( \frac{3.96 \text{ kN}}{50 \text{ mm}} \right) \times \left( \frac{590 \text{ mm}}{\text{slip plane}} \right) \times (4 \text{ slip plane}) \times \cos 45^\circ \right] + \\ \left[ \mu \left( \frac{3.96 \text{ kN}}{50 \text{ mm}} \right) \times \left( \frac{590 \text{ mm}}{\text{slip plane}} \right) \times (4 \text{ slip plane}) \times \sin 45^\circ \right] \end{array} \right\} = P_{\text{theoretical}}$$

$$0.707[(186.92 \text{ kN})(0.707) + (1.0)(186.92 \text{ kN})(0.707)] = 186.85 \text{ kN}$$

$$\frac{P_{\text{max, experimental}}}{P_{\text{theoretical}}} = \frac{104.2 \text{ kN}}{186.85 \text{ kN}} = 0.56$$

The  $\sin \theta$  term in Equations 4.1, 4.2 and 4.3 is required to account for the reduced amount of tension fibres per unit length of bed joint crossing the bed joint slip plane as the angle  $\theta$  becomes shallower. Referring to Figure 4.19, when the angle  $\theta$  equals  $90^\circ$ , the maximum amount of tension fibres cross the slip plane (i.e.,  $\sin 90^\circ = 1$ ). When the angle  $\theta$  equals  $0^\circ$ , no tension fibres cross the slip plane (i.e.,  $\sin 0^\circ = 0$ ).

Assuming the coefficient of friction ( $\mu$ ) was 1.0, as per CSA S304.1 (2004), the mesh applied using parging was about 56% efficient based on the theoretical capacity. As reported in Chapter 1, the coefficient of friction ( $\mu$ ) could be as low as 0.3. Although friction is unlikely to be so low, in this case, the efficiency for the 4.5 oz., 6 oz., and 9 oz. meshes would be 0.91, 0.83 and 0.86, respectively (for an average of 87%). In any case, it is clear that the full strengths of the meshes are not developed and that the efficiency ratios as a fraction of the basic strength of all the meshes are essentially equal. Therefore,

at  $\pm 45^\circ$  the strengthening effect of the reinforcement is proportional to the weight of the mesh.

#### 4.11.2 FIBRES AT $0^\circ/90^\circ$ ORIENTATION

For mesh fibres oriented at  $0^\circ/90^\circ$  to the slip plane, the average load/metre strengths of the unreinforced, and the 4.5 oz., 6 oz., 9 oz. and 12 oz. reinforced specimens were 22.4 kN/m, 43.6 kN/m, 62.7 kN/m, 58.9 kN/m and 46.3, respectively. These values have been plotted below in Figure 4.20.

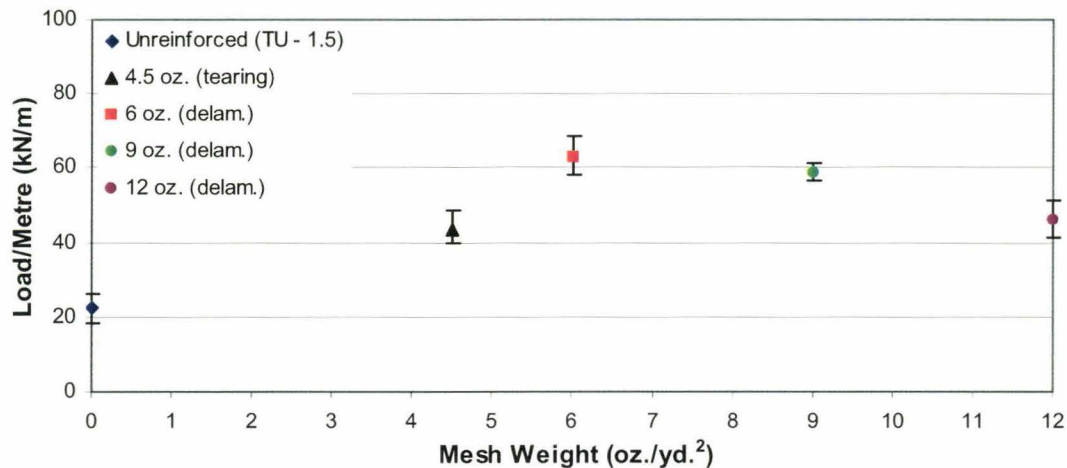


Figure 4.20 – Average Load/Metre vs. Mesh Weight for  $0^\circ/90^\circ$  Fibre Orientation

Considering that the fibre mesh layers delaminated, it is not surprising that each mesh weight was not able to develop its full strength. In general, increasing the weight of the mesh was accompanied by some increase in the average strength of the slip plane but not in a consistent pattern. The maximum was achieved with the 6 oz. mesh above which, the slip plane strength actually decreased with increased mesh weight.

It is clear that for maximum capacity, the strength of the fibres must be developed. This can only happen when the fibres tear. By re-examining the “Mesh Failure

Description” column in Table 4.1, for the 6 oz. mesh at  $0^{\circ}/90^{\circ}$ , it can be seen that partial tearing of the fibres did occur for most of the specimens. In this experimental investigation, the 6 oz. mesh oriented at  $0^{\circ}/90^{\circ}$  to the slip planes appears to be on the cusp between tearing and delamination. In many cases, the actual failure mechanism is a combination of both delamination and fibre tearing (Bakis et al., 2002). The delamination which occurred with the mortar embedded glass mesh was not characteristic of that observed with epoxy embedded fibres.

Typically, delamination of FRP occurs when the masonry substrate fails (cracks) and the entire laminate peels away on one or both sides of the crack, with a thin layer of the masonry attached to it (La Mendola et al., 2001). With the mesh, delamination consisted of the fibres being pulled out of the mortar. Again, a layer of parging was still present on the specimen. Therefore, bond failure at the block-parging interface did not occur (i.e., the applied surface had adequate strength). For the higher weight meshes, delamination at lower loads may be associated with effectiveness of embedment of the mesh in the modified cement parging. The larger area of mesh may make it easier to pull the mesh out of the parging because of the reduced connection (bond area) between the layers of parging. Generally, the bond condition determines whether delamination or fibre tearing will occur. This phenomenon can be explained by examining the weaves of the mesh fibres. Close-up photos of the various meshes are reproduced in Figure 4.21 (page 130).

Since there is limited bond between the parging and mesh fibres, the bond is based on physical interlock achieved during the application process (i.e., penetration of

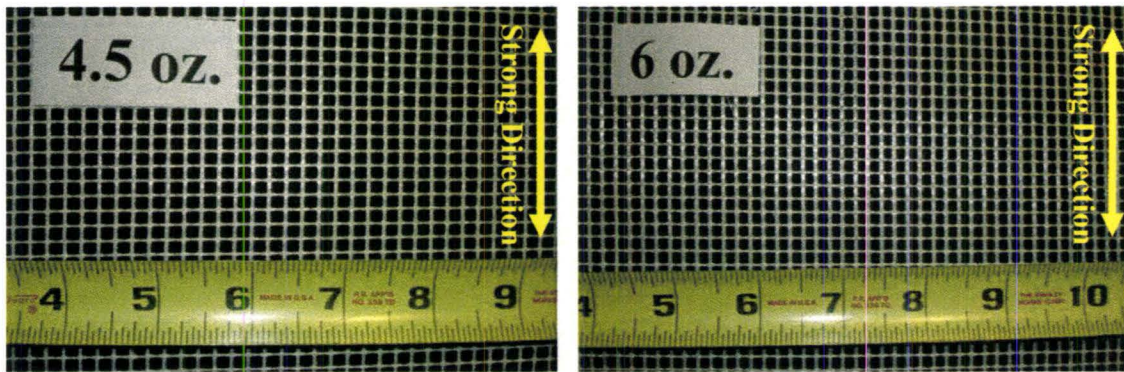


matrix through fibre) (Kolsch, 1998). Therefore, after applying the mesh to the specimens, it was necessary to force the second layer of mortar parging in between the fibre strands to ensure contact with the first layer. The maximum amount of contact would be reduced by the surface area occupied by the mesh. The task of creating good contact between the mortar layers was much easier for the 4.5 oz. and 6 oz. meshes which have fairly evenly spaced strands and large enough gaps between the strands for the mortar to pass through. This was not the case for the remaining mesh weights. Doubling up of the 4.5 oz. mesh to create 9 oz. mesh resulted in much smaller gaps between the fibres as it was impossible to line the strands of mesh perfectly. This made the task of forcing the mortar through the gaps much more difficult. Also, the net area of contact between the parging layers would be reduced by the larger area of mesh. For the 12 oz. mesh, there are very small gaps between the fibres oriented in the weak direction. It was difficult to confirm the mortar had passed through these small openings. Once again it is possible there was incomplete penetration of the mortar parging through the mesh. Incomplete penetration of the mortar through the mesh would result in limited embedment and could result in premature delamination before the mesh was able to develop high tensile stresses. Even with full penetration, the contact area (minimum area) of parging would be substantially reduced by the larger mesh area.

#### **4.12 SUMMARY**

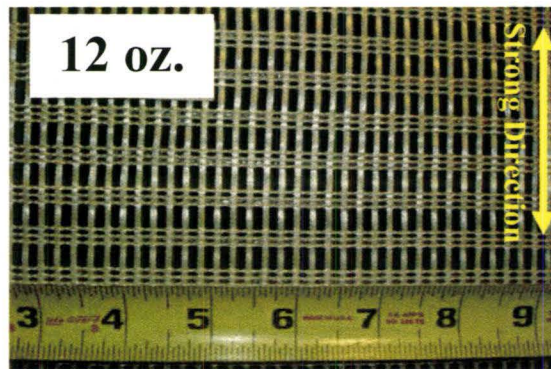
In Phase Three of this experimental investigation, twenty-one T-1.5 specimens were tested with fibreglass meshes having finished weights of 4.5 oz./yd.<sup>2</sup>, 6.0 oz./yd.<sup>2</sup>, 9.0 oz./yd.<sup>2</sup>, and 12 oz./yd.<sup>2</sup> applied with modified mortar parging at two different

orientations to the bed joint slip plane ( $0^{\circ}/90^{\circ}$ ,  $\pm 45^{\circ}$ ). These results compare favourably with the test results from the unretrofitted specimens, which failed in a brittle debonding mode at low levels of both load and displacement. This was due to the relative weak adhesion between the mortar and the unit, and the lack of friction resistance due to the absence of compressive stresses normal to the bed joints.



(a) 4.5 oz./yd.<sup>2</sup> (Finished Weight)

(b) 6 oz./yd.<sup>2</sup> (Finished Weight)



(c) 12 oz./yd.<sup>2</sup> (Finished Weight)

**Figure 4.21 – Fibreglass Mesh Weaves**

The retrofitted specimens described in this chapter failed at much higher levels of both load and displacement compared to the unretrofitted specimens. Typically, for any given mesh weight, orienting the fibres at  $\pm 45^{\circ}$  resulted in failure characterized by higher strength and less ductility compared to tests with fibres oriented at  $0^{\circ}/90^{\circ}$  to the bed joints.

At  $\pm 45^\circ$  orientation, the fibres ruptured at failure. When the mesh was oriented at  $0^\circ/90^\circ$ , the fibres pulled out of the cement parging, which limited the strength, but enabled specimens to undergo large deformations while maintaining fairly constant load. For the specimens reinforced with 4.5, 6.0 and 9 oz. mesh oriented at  $\pm 45^\circ$ , the increase in shear strength was 2.1, 3.7, and 3.9 times that, respectively, of the unretrofitted counterparts. For the specimens reinforced with 4.5, 6.0, 9 and 12 oz. mesh oriented at  $0^\circ/90^\circ$ , the increase in shear strength was 1.95, 2.8, 2.6, and 2.1 times that, respectively, of the unretrofitted counterparts.

It is clear that for surface bonded laminates, the effectiveness of the retrofit is limited not only by the bond strength between the laminate and the substrate (Bakis et al., 2002) but also by the bond strength between the layers of cement parging and the strength of the parging to resist pull-out of the fibres. Delamination limits the strengthening capacity of the fibres in tension. This result is similar to that observed by La Mendola et al. (2001) and Kolsch (1998).

## **CHAPTER 5: CONCLUSIONS AND RECOMMENDATIONS**

### **5.1 FINAL SUMMARY**

In earthquake prone areas, failure of URM walls result in the most property damage, injuries and loss of life compared to other forms of construction. As discussed earlier, traditional strengthening techniques have several undesirable properties, including being labour intensive and adding weight to the structure. Past research has shown that FRP reinforcement is an effective method of increasing both the strength and ductility of URM.

The experimental investigation presented in this report was conducted in three phases with the scope ranging from analyzing the influence of specimen shape, assessing the feasibility of obtaining two sets to data from each specimen, to determining the influence of fibre weight and orientation on the shear-slip performance. The test method, apparatus and specimens were selected to simulate shear slip along bed joints, following the rationale from Kolodziejcki (1982) and Eshani (1997). Construction of the specimens followed standard practices in order to better reflect actual wall construction techniques.

As discussed in Chapter 3, the Phase One test program was successful in defining the best shape and size of test specimen to use. The data itself was also of direct use as an evaluation of strength and behaviour of GFRP reinforced masonry subjected to shear-slip failure. Thirty-seven shear slip specimens were tested to failure, and of these 15 were reinforced with GFRP. For the T-1.5, T-0.5, A-2.5, A-1.5 and A-0.5 specimens, the average increase in shear strength was 7.7, 3.1, 4.5, 5.2 and 6.6 times that, respectively, of the unretrofitted counterparts. For the T-1.5, T-0.5, A-2.5, A-1.5 and A-0.5 specimens



the average increase in displacement at the maximum applied load was 16.4, 8.0, 5.7, 9.1 and 13.9 times that, respectively, of the unretrofitted counterparts. The Phase Two test program showed that it was neither practical nor reliable to attempt to obtain two sets of data from one test specimen. The data from this test phase was of some direct use. Specimens with mesh applied using epoxy had higher strengths than those where the mesh was applied with parging. Therefore, when using the same fibre mesh, preliminary tests indicate better utilization of the fibre strength is achieved when it is bonded to the masonry substrate using epoxy.

As discussed in Chapter 4, the Phase Three test program provided a good documentation of the strength and behaviour of concrete block masonry reinforced to improve shear-slip capacity with fibreglass mesh adhered using a modified parging. Twenty-one T-1.5 specimens were tested with four different weights of fibreglass mesh (finished weights of 4.5 oz./yd.<sup>2</sup>, 6.0 oz./yd.<sup>2</sup>, 9.0 oz./yd.<sup>2</sup> and 12 oz./yd.<sup>2</sup>) applied with modified mortar parging at two different orientations to the bed joint slip plane (0°/90°, ±45°). The retrofitted specimens failed at much higher levels of both load and displacement compared to the unretrofitted specimens. Typically, for any given mesh weight, orienting the fibres at ±45° resulted in failure characterized by higher strength and less ductility compared to tests with fibres oriented at 0°/90° to the bed joints. For the specimens reinforced with 4.5, 6.0 and 9 oz. mesh oriented at ±45°, the increase in shear strength was 2.1, 3.7, and 3.9 times that, respectively, of the unretrofitted counterparts. For the specimens reinforced with 4.5, 6.0, 9 and 12 oz. mesh oriented at 0°/90°, the increase in shear strength was 1.95, 2.8, 2.6, and 2.1 times that, respectively, of the

unretrofitted counterparts. At  $\pm 45^\circ$  orientation, the fibres ruptured at failure. When the mesh was oriented at  $0^\circ/90^\circ$ , the fibres pulled out of the cement parging, which limited the strength, but enabled specimens to undergo large deformations while maintaining fairly constant residual capacity.

## 5.2 COMPARISON OF EXPERIMENTAL RESULTS WITH CODE EQUATIONS

The shear strengthening of components with surface-bonded FRP is treated in both the latest (2002) Canadian standard (*CSA S806-02: Design and Construction of Building Components with Fibre Reinforced Polymers*) and the latest (2001) American guide (*ACI 440.2 R-01: Guide for the Design and Construction of Externally Bonded FRP Systems for Strengthening Concrete Structures*). The Canadian standard includes components constructed from concrete and masonry, whereas the American guide deals specifically with concrete. Furthermore, the shear provisions in the American guide specifically relate to beams and columns, whereas the shear provisions in the Canadian document also include walls.

For concrete block masonry walls reinforced with FRP, the shear resistance,  $V_r$ , given by CSA S806-02, Clause 11.5.2, *Shear Strength Enhancement*, is:

$$V_r = V_m + V_{ms} + V_F \leq V_m + 0.40\phi_m \sqrt{f'_m} A_e \quad (5.1)$$

where the three components are specified as follows:

1.  $V_m$  = shear resistance provided by the masonry

$$= 0.20\phi_m \sqrt{f'_m} A_e \quad (5.2)$$

where  $\phi_m$  = resistance factor of masonry

= 0.55

**Note:** In the 2004 edition of *CSA S304.1: Masonry Design for Buildings*, the resistance factor of masonry,  $\phi_s = 0.60$ .

$f'_m$  = specified compressive strength of masonry

$A_e$  = effective shear transfer area of a wall

**Note:** This is generally the mortared face shell area.

2.  $V_{ms}$  = shear resistance provided by steel in the masonry

$$= \frac{\phi_s (0.6 A_h f_{yh} d)}{s} \quad (5.3)$$

where  $\phi_s$  = resistance factor of reinforcing steel  
= 0.8

$A_h$  = area of one leg of the transverse reinforcement

$f_{yh}$  = specified yield strength of the transverse reinforcement

$d$  = distance from extreme compression fibre to centroid of tension reinforcement

$s$  = spacing of transverse reinforcement of a wall

**Note:** Since the specimens used in this experimental investigation did not contain any steel reinforcement,  $V_{ms}$  is equal to zero. For shear slip failure, it is not obvious that transverse reinforcement, if present, would have any influence since it does not cross the slip plane. Therefore, this term probably should not be applied to shear-slip capacity calculations. In this form, this term appears to apply more to diagonal tension failure as opposed to shear-slip failure.

3.  $V_F$  = shear resistance provided by FRP reinforcement

$$= m\phi_F t_F f_F D' \quad (5.4)$$

where  $m = 1$  or  $2$ , depending on the number of wall faces reinforced

$$\begin{aligned} \phi_F &= \text{resistance factor of FRP composites} \\ &= 0.75 \end{aligned}$$

$t_F$  = thickness of the FRP jacket

$f_F$  = stress in FRP composites

$$= 0.004E_F \leq \phi_F f_{Fu} \quad (5.5)$$

where  $E_F$  = modulus of elasticity of FRP composite

$f_{Fu}$  = ultimate tensile strength of FRP composite

$D'$  = core dimensions from centre-to-centre of the peripheral hoops of a column.

**Note:** The strain limit of 0.004 in Equation 5.5 is an empirical number based on committee consensus, and was chosen to account for possible delamination. It is believed by most that at this strain, which is double the yield strain of 400 MPa yield steel, delamination will commence; it is a conservative value. Using Equation 5.5, based on the GFRP material data sheet (Appendix A, pg. 144), the maximum usable stress in the FRP composite,  $f_F$ , is the lesser of:

$$0.004 \times 19.3 \text{ GPa} = 77.2 \text{ MPa} \text{ and } 0.75 \times 309 \text{ MPa} = 231.75 \text{ MPa}, \therefore 77.2 \text{ MPa} \text{ governs.}$$

Based on the aforementioned definitions, the shear resistance capacity defined by Equation 5.1 becomes:



$$\begin{aligned} V_r &= V_m + V_{ms} + V_F \leq V_m + 0.40\phi_m\sqrt{f'_m}A_e \\ &= V_m + 0 + V_F \leq 0.20\phi_m\sqrt{f'_m}A_e + 0.40\phi_m\sqrt{f'_m}A_e \\ &= \dot{V}_m + V_F \leq V_{r,\max} = 0.60\phi_m\sqrt{f'_m}A_e = 0.60(0.55)\sqrt{15}A_e \end{aligned} \quad (5.6)$$

**Note:** In both the 1994 and 2004 editions of CSA S304.1, the basic value for  $V_m$  is  $0.16\phi_m\sqrt{f'_m}A_e$ .

The official code definition of  $D'$  in Equation 5.4 was the cause of some confusion since it refers to columns. Through email correspondence with Dr. Ghani Razaqpur, Professor of Civil Engineering at McMaster University and a member of the CSA S806-02 technical committee, the author was informed that when dealing with an unreinforced masonry wall strengthened with a continuous FRP sheet, it can be assumed that  $D'$  is equal to  $0.8l_w$ ; where  $l_w$  is the length of the wall (Razaqpur, 2006). With regard to the shear slip specimens,  $l_w$  would be the length of the shear slip plane. Therefore, the FRP contribution to shear slip strength, defined by Equation 5.4, simply becomes the ultimate tensile strength of the FRP multiplied by its cross-sectional area across the slip plane.

CSA S806-02 does not explicitly take into consideration the orientation of the fibres with respect to the shear-slip planes. It is implied that the fibres are oriented at  $90^\circ$  to the slip plane. For other orientations, only the component normal to the slip plane must be considered (Razaqpur, 2006). As was shown by Eshani et al. (1997) and as was demonstrated in the Chapter 4, fibre orientation does have an influence on the shear strength enhancement.

Presented in Table 5.1, the average maximum experimental load for each specimen configuration used in Phase One is compared to the GFRP contribution to shear slip capacity,  $P_{\text{theoretical } 1}$ , calculated using the minimum value of  $f_F$  in CSA S806-02, Clause 11.5.2. For comparison, the shear slip capacity,  $P_{\text{theoretical } 2}$ , was also calculated using the full fibre strength. No reduction factors of any type were used in the analysis. The contribution of the masonry to the shear strength enhancement,  $V_m$ , was ignored because, based on the amount of deformation required to rupture the GFRP fibres, by the time the fibres rupture, the interface between the block and the mortar would have debonded (i.e.,  $V_m = 0$ ).

**Table 5.1 – Comparison of Phase One GFRP Reinforced Specimen Results with CSA S806-02**

<b>GFRP Material Properties:</b>						
$m = 4$ (one per mortared face shell)						
$t_f = 0.00025$ m						
$f_F = 77.2$ MPa (see page 133), $f_{Fu} = 309$ MPa						
			$V_{F1} = P_{\text{theoretical } 1} = m \times t_f \times l_w \times f_F$			
			$V_{F2} = P_{\text{theoretical } 2} = m \times t_f \times l_w \times f_{Fu}$			
Specimen	Slip Plane Length, $l_w$ (m)	$P_{\text{max, experimental}}^{\ddagger}$ (kN)	$P_{\text{theoretical}}$ (kN)		Efficiency (%) <sup>*</sup>	
			$f_F$	$f_{Fu}$	$f_F$	$f_{Fu}$
TR – 1.5	0.59	203.5	45.5	182.3	447.3	111.6
TR – 0.5	0.19	39.9	14.7	58.7	271.4	68.0
AR – 0.5	0.195	31.7	15.1	60.3	209.9	52.6
AR – 1.5	0.595	117.3	45.9	183.9	255.6	63.8
AR – 2.5	0.995	199.1	76.8	307.5	259.2	64.7

<sup>‡</sup> Total failure load as recorded by the Tinius Olsen testing machine or commercial load cell

<sup>\*</sup> Efficiency =  $(P_{\text{max, experimental}}) \div (P_{\text{theoretical}}) \times 100\%$

As illustrated in Table 5.1, the test data shows well above 100% efficiency when the stress in the GFRP is limited to 77.2 MPa (i.e.,  $0.004E_F$ ). This is a very conservative method of estimating the maximum load. It is not surprising that it most poorly estimates the maximum experimental load of the GFRP reinforced T-1.5 specimen. As was explained in Section 3.8 and Appendix B, one of the main reasons why the T-1.5 specimen was selected for further research was because the finite element analysis

indicated that along most of the length of the shear slip plane, the normal stress induced by the load was mostly uniform and relatively low. This produced as close to pure shear conditions along the slip plane as was possible under the testing conditions. For the other specimens, the estimation of the theoretical capacity was closer to the experimental results because the stress distributions were not as ideal as the T-1.5. The experimental results were influenced by induced bending stresses along the slip planes. An improved but unconservative estimation of the experimental load for the T-1.5 specimen is achieved when the full strength of the GFRP (i.e., 309 MPa) is used. As expected, for the other specimens the estimation of the theoretical capacity is not as close to the experimental results because, once again, the stress distributions were not as ideal as the T-1.5. The experimental results were influenced by induced bending stresses along the slip planes. Clearly, while the full strength of the fibres cannot be developed, the strain limited method of defining fibre stress is quite conservative. This research may help affect future changes to this limitation.

CSA S806 provides a factor of safety against undesirable/unknown conditions and general variability in materials and workmanship by introducing material resistance factors (i.e.,  $\phi_F = 0.75$ ), limiting the maximum usable stress in the FRP composite, and employing other techniques, such as limiting the shear transfer length to  $0.8l_w$ .

### **5.3 CONCLUSIONS AND RECOMMENDATIONS**

The T-1.5 specimen configuration proved to be the most effective for conducting the experiments. This specimen configuration had the least variability of the results and limited the normal stresses caused by bending along the bed joint slip planes.

The use of surface bonded fibreglass mesh laminates is an effective method of increasing the shear slip strength and ductility of unreinforced concrete masonry. Orienting the fibres at  $\pm 45^\circ$  to the bed joints results in failure characterized by higher strength and lower ductility compared to when the fibres are oriented at  $0^\circ/90^\circ$ .

This fibre reinforced strengthening technique can be customized to suit the structural requirements of the building by altering the weight of the fibres, the orientation to the bed joints and the bonding agent. Where extra strength is required, epoxy can be used as the bonding agent. Where pseudo-ductility is required, the modified parging can be used as the bonding agent. The modified parging also has the added benefits of providing fire protection for the fibres, and possibly being the final finished surface. Since behaviour is influenced by the weakest component, it is not advantageous to use high strength fibres if adequate bonding techniques are not used (La Mendola, 2001). The fibres will tend to pull out of the bonding agent before the maximum strength is reached.

#### **5.4 SUGGESTIONS FOR FUTURE RESEARCH**

A possible next step in this research would be to study the influence of surface bonded glass fibre mesh on the in-plane behaviour of full scale, low-aspect-ratio ( $l/w < 1$ ) shear walls subjected to displacement controlled in-plane cyclic loading. The cyclic loading will give an indication of the energy absorption capability and strength degradation of the walls under multiple cycles of loading. The variables to be examined would once again include the weight of the fibreglass mesh and its orientation to the bed joints (i.e.,  $0^\circ/90^\circ$ ,  $\pm 45^\circ$ ). The comparative study should also include mesh applied using the modified mortar parging versus mesh applied using the epoxy. Using full scale walls also



would allow the influence of aspect ratio to be included as one of the variables. Also, in actual structural retrofits it is not always possible to apply fibreglass laminate to both faces of a wall. The investigation should also include the influence of single-sided application versus double-sided application to the performance of the reinforcement. Since the inclusion of all these variables could lead to a large number of tests, with prohibitive time and cost requirements, a parametric study should first be required to determine the most critical combination of variables.

## **REFERENCES**

- Abdel-Wahed, O. H. (2004) “Application and Rehabilitation of FRP in Masonry Wall.” Research Submitted for the Requirement of the Degree of Full Professor in Structural Engineering. Ain Shams University, Cairo, Egypt. 2004.
- ACI Committee 440. (2001). “ACI 440.1 R-01: Guide for the Design and Construction of Concrete Reinforced with FRP Bars.” American Concrete Institute, Farmington Hills, Michigan.
- ACI Committee 440. (2001). “ACI 440.2 R-01: Guide for the Design and Construction of Externally Bonded FRP Systems for Strengthening Concrete Structures.” American Concrete Institute, Farmington Hills, Michigan.
- Applied Technology Council (ATC-33 Project). (1997). “NEHRP Commentary on the Guidelines for the Seismic Rehabilitation of Buildings.” *FEMA Publication 274*. Washington, D.C.
- American Society for Testing and Materials (ASTM). (2003). “*ASTM D-1623C: Standard Test Method for Tensile and Tensile Adhesion of Rigid Cellular Plastics.*” ASTM, West Conshohocken, PA.
- American Society for Testing and Materials (ASTM). (2005). “*ASTM C-109: Standard Test Method for Compressive Strength of Hydraulic Cement Mortars (Using 2-in. or [50 mm] Cube Specimens.*” ASTM, West Conshohocken, PA.
- American Society for Testing and Materials (ASTM). (2006). “*ASTM D-3039: Standard Test Method for Tensile Properties of Polymer Matrix Composite Materials.*” ASTM, West Conshohocken, PA.
- Atkinson, R. H., Amadei, B. P., Saeb, S., Sture, S. (1998). “Response of Masonry Bed Joints in Direct Shear.” *ASCE Journal of Structural Engineering*. Vol. 115, No. 9, 2276–2296.
- Bajpai, Kunwar., Duthinh, Dat. (2003). “Bending Performance of Masonry Walls Strengthened with Near-Surface Mounted FRP Bars.” Proceedings of the 9<sup>th</sup> *North American Masonry Conference*, Clemson, South Carolina, USA, pp. 1052-1063.
- Bakis, C.E., Bank, L.C., Brown, V.L., Cosenza, E., Davalos, J.F. Lesko, J.J., Machida, A., Rizkalla, S.H., Triantafillou, T.C. (2002). “Fiber-Reinforced Polymer Composites for Construction – State-of-the-Art Review.” *ASCE Journal of Composites for Construction*, Vol. 6, No. 2, pp. 73-87.

Bastidas, E.D., Molina, L.F., Yamin, L., Sarria, A., Ortega, J.P., Tumialan, J.G. (2003). “Non-Structural Masonry Walls Strengthened with GFRP Laminates.” Proceedings of the 9<sup>th</sup> North American Masonry Conference, Clemson, South Carolina, USA, June 1-4, pp. 168-179.

Batdorf, S. B. (1986). “Fracture: Statistical Theories.” In *Encyclopedia of Materials Science and Engineering, Volume 3*, ed. M. B. Bever, The M.I.T. Press, Cambridge, MA. pp. 1858-1864.

Bazant, Z. P., Chen, E-P. (1997). “Scaling of Structural Failure.” *Applied Mechanics Review*, Vol. 50, No. 10 (October). pp. 593-627.

Beigay, Mike., Young, Davit T., Gergely, Janos. (2002). “An Improved Composite Anchoring System.” Proceedings of the 3<sup>rd</sup> International Conference on Composites in Infrastructure (ICCI), San Francisco, California, U.S.A.

Belarbi, Abdeldjelil., Silva, Pedro F., Li, Tong. (2003). “An Experimental Evaluation of In-Plane URM Walls Strengthened with FRP Composites.” Proceedings of the 9<sup>th</sup> North American Masonry Conference, Clemson, South Carolina, USA, June 1-4, pp. 1101-1112.

Bosiljkov, V., Page, A., Bokan-Bosiljkov, V., Zarnic., R. (2003). “Performance Based Studies of In-Plane Loaded Unreinforced Masonry Walls.” *Masonry International: Journal of the British Masonry Society*, Vol. 16, No. 2. pp. 39-50.

Campanaro, F., Drysdale, R., Hamid, A. (2005). “Use of Fibre Reinforced Polymer to Enhance the Sliding Shear Resistance of Unreinforced Concrete Masonry.” Proceedings of the 10<sup>th</sup> Canadian Masonry Symposium, Banff, Alberta, Canada, June 8-12.

Canadian Standards Association International (CSA). (2002). “CSA S806: Design and Construction of Building Components with Fibre Reinforced Polymers.” CSA, Mississauga, Ontario, Canada.

Canadian Standards Association (CSA). (2004). “CSA S304.1 – Masonry Design for Buildings.” CSA, Mississauga, Ontario.

Capozucca, Roberto. (2001). “Brickwork Masonry Walls Reinforced By CFRP.” Proceedings of the 9<sup>th</sup> Canadian Masonry Symposium, University of New Brunswick, Fredericton, New Brunswick, Canada, June 4-6.

Drysdale, R. G., Hamid, A. A., Baker, L. R. (1999). *Masonry Structures: Behavior and Design* (2<sup>nd</sup> ed.). The Masonry Society, Boulder, Colorado.

Drysdale, Robert G., Hamid, Ahmad A., Heidebrecht, Arthur C. (1979). “Tensile Strength of Concrete Masonry.” *ASCE Journal of the Structural Division*, Vol. 105, No. ST7, July. pp. 1261-1275.

Drysdale, R. G., Vanderkyle, R., Hamid, A. (1979) “Shear Strength of Brick Masonry Joints.” Proceedings of the *Fifth International Brick Masonry Conference*, Washington, D.C.

DuRock Alfacing International Ltd. (2005, online): Available: [www.durock.com](http://www.durock.com)

Ehsani, M. R., Saadatmanesh, H., Al-Saidy, A. (1997). “Shear Behavior of URM Retrofitted with FRP Overlays.” *ASCE Journal of Composites for Construction*. Vol. 1, No. 1, pp. 17-25.

Ehsani, M. R., Saadatmanesh, H., Velazquez-Dimas, J. I. (1999). “Behavior of Retrofitted URM Walls Under Simulated Earthquake Loading.” *ASCE Journal of Composites for Construction*, Vol. 3, No. 3, pp. 134-142.

El-Dakhkhni, W. W., (2002) “*Experimental and Analytical Seismic Evaluation of Concrete Masonry-Infilled Steel Frames Retrofitted using GFRP Laminates.*” Ph.D. Thesis, Drexel University, Philadelphia, Pennsylvania.

El-Dakhkhni, Wael W., Hamid, Ahmad A., Elgaaly, Mohammed. (2003) “Design and Retrofit of Concrete Masonry Infilled Steel Frames Using GFRP Laminates” Proceedings of the *9<sup>th</sup> North American Masonry Conference*, Clemson, South Carolina, USA. June 1-4, pp. 1076-1088.

El-Dakhkhni, Wael W., Hamid, Ahmad A., Elgaaly, Mohamed. (2004) “In-Plane Strengthening of URM Infill Wall Assemblages Using GFRP Laminates.” *TMS Journal*, September, Boulder, Colorado. pp. 13-24.

El-Gawady, M., Hegner, J., Lestuzzi, P., Badoux, M. (2004). “Static Cyclic Tests on URM Wall Before and After Retrofitting with Composites.” Proceedings of the *13<sup>th</sup> International Brick and Block Masonry Conference*, Amsterdam, July 4-7.

Elgwady, Mohamed A., Lestuzzi, Pierino., Badoux, Marc. (2002). “Dynamic In-Plane Behaviour of URM Wall Upgraded with Composites.” Proceedings of the *3<sup>rd</sup> International Conference on Composites in Infrastructure (ICCI)*, San Francisco, California, U.S.A.

Essawy, A. S. (1986). “*Strength of Hollow Concrete Masonry Walls Subjected to Lateral (Out-of-Plane) Loading.*” Ph.D. thesis, McMaster University, Hamilton, Ontario.

Fam, Amir., Musiker, Daniel., Kowalsky, Mervyn., Rizkalla, Sami. (2002). “In-Plane Testing of Damaged Masonry Wall Repaired with FRP.” *Advanced Composite Letters*, Vol. 11, No. 6, pp. 275-281.



Fyfe Co. LLC (2004, online): Available: [www.fyfeco.com](http://www.fyfeco.com)

Hall., J. D., Schuman, P. M., Hamilton III, H. R. (2002). “Ductile Anchorage for Connecting FRP Strengthening of Under-Reinforced Masonry Buildings.” *ASCE Journal of Composites for Construction*, Vol. 6, No. 1, pp. 3-10.

Hamid, A. A., El-Dakhakhni, W. W., Hakam, Z. H. R. (2005) “Behavior of Composite Unreinforced Masonry – Fiber-Reinforced Polymer Wall Assemblages Under In-Plane Loading.” *ASCE Journal of Composites for Construction*. Vol. 9, No. 1.

Hamilton III, H. R., Dolan, C. W. (2001). “Flexural Capacity of Glass FRP Strengthened Concrete Masonry Walls.” *ASCE Journal of Composites for Construction*, Vol. 5, No. 3, pp. 170-178.

Hamoush, Sameer A., McGinley, Mark W., Mlakar, Paul., Scott, David., Murray, Kenneth. (2001). “Out-of-Plane Strengthening of Masonry Walls with Reinforced Composites.” *ASCE Journal of Composites for Construction*, Vol. 5, No. 3, pp.139-145.

Harris, H. G., Sabnis, G. M. *Structural Modeling and Experimental Techniques (2<sup>nd</sup> ed.)*. CRC Press, New York. 1999.

Hegemier, S. K., Arya, S. K., Krishnamoorthy, G., Nachbar, W., Furgerson, R. (1978). “On the Behavior of Joints in Concrete Masonry.” *Proceedings of the North American Masonry Conference*, Boulder, CO. pp. 4-1 to 4-21.

Kolodziejcki, Edward A. (1982). “*Shear Strength of Intersecting Masonry Walls.*” Master of Engineering (M.Eng.) thesis, McMaster University, Hamilton, Ontario, Canada.

Kolsch, Holger. (1998). “Carbon Fiber Cement Matrix (CFCM) Overlay System for Masonry Strengthening.” *ASCE Journal of Composites for Construction*, Vol. 2, No. 2, pp. 105-109.

Kurtis, K. E., Dharan, C. K. H. (1997). “Composite Fibers for External Reinforcement of Natural Stone.” *ASCE Journal of Composites for Construction*, Vol., 2, No. 3, pp. 116-119.

Kuzik, Marc D., Elwi, Alaa E., Cheng, J. J. Roger. (2003). “Cyclic Flexural Tests of Masonry Walls Reinforced with Glass Fiber Reinforced Polymer Sheets.” *ASCE Journal of Composites for Construction*, Vol. 7, No. 1, pp. 20-30.

La Mendola, L., Campione, G., Mascari, C., Zingone, G. (2001). “Experimental Investigation on Delamination Phenomena Between Fiber Reinforced Plastic (FRP) and Masonry.” *Proceedings of the 9<sup>th</sup> Canadian Masonry Symposium*, University of New Brunswick, Fredericton, New Brunswick, Canada, June 4-6.

Mangenes, G., Calvi, G. M. (1997). “In-plane Response of Brick Masonry Walls.” *Earthquake Engineering Structural Dynamics*, 26, pp. 1091-1112.

Paulay, T., Priestley, M. J. N. (1992). *Seismic Design of Reinforced Concrete and Masonry Buildings*. John Wiley & Sons, Inc., New York.

Razaqpur, A. Ghani. (2006). Email, August 21, <razaqpur@mcmaster.ca>

Tan, Kiang Hwee., Patoary, M. K. H. (2004) “Strengthening of Masonry Walls Against Out-of-Plane Loads Using Fiber-Reinforced Polymer Reinforcement.” *ASCE Journal of Composites for Construction*, Vol. 8, No. 1, pp. 79-87.

Razaqpur, A. Ghani. (2006). Email, August 21, <razaqpur@mcmaster.ca>

Triantafillou, T. C. (1998) “Strengthening of Masonry Structures Using Epoxy-Bonded FRP Laminates.” *ASCE Journal of Composites for Construction*. Vol. 2, No. 2, pp. 96-104.

Textilglas Canada Limited, Etobicoke, Ontario. (April, 2005). Fax: 416-626-7377

Tumialan, J. Gustavo., Galati, Nestore., Nanni, Antonio. (2003). “Field Assessment of Unreinforced Masonry Walls Strengthened with Fiber Reinforced Polymer Laminates.” *ASCE Journal of Structural Engineering*, Vol. 129, No. 8, pp. 1047-1056.

Vandergrift, Jon., Gergely, Janos., Young, David T. (2002). “CFRP Retrofit of Masonry Walls.” Proceedings of the 3<sup>rd</sup> *International Conference on Composites in Infrastructure (ICCI)*, San Francisco, California, U.S.A.

van der Pluijm, Rob. (1993). “Shear Behaviour of Bed Joints.” Proceedings of the *Sixth North American Masonry Conference*, Philadelphia, Pennsylvania, June 6-9. pp. 125-136.

Velazquez-Dimas, J. I., Ehsani, M. R. (2000) “Modeling Out-of-Plane Behavior of URM Walls Retrofitted with Fiber Composites.” *ASCE Journal of Composites for Construction*, Vol. 4, No. 4, pp. 172-181.

Zhao, Tong., Xie, Jian., Li, Haoju. (2003) “Strengthening of Cracked Concrete Block Masonry Walls Using Continuous Carbon Fiber Sheet.” Proceedings of the 9<sup>th</sup> *North American Masonry Conference*. Clemson, South Carolina, USA, June 1-4, pp. 156-167.

## APPENDIX A: MATERIAL DATA SHEETS

### Tyfo® WEB Composite using Tyfo® S Epoxy

#### DESCRIPTION

The Tyfo® WEB Composite is an ICBO ER-5282 listed material comprised of Tyfo® S Epoxy and Tyfo® WEB reinforcing fabric. Tyfo® WEB is a custom 0°/90° bi-directional weave glass fabric used in the Tyfo® Fibwrap System. The glass material is orientated in both the 0° and 90° direction in optimum configuration. The Tyfo® S Epoxy is a two-component epoxy matrix material for bonding applications.

#### USE

Tyfo® WEB Fabric is combined with Tyfo® epoxy material for lightweight reinforcement for masonry, as a reinforced coating, and finish fabric application for bridges, buildings, and other structures.

#### ADVANTAGES

- ICBO ER-5282 listed material
- Good high & low temperature properties
- Long working time
- High elongation
- Ambient cure
- 100% solvent-free
- Rolls can be cut to desired widths prior to shipping

#### COVERAGE

Approximately 1,564 sq. ft. surface area with 3 to 4 units of Tyfo® S Epoxy and 1 roll of Tyfo® WEB Fabric when used with the Tyfo® Saturator.

#### PACKAGING

Order Tyfo® S Epoxy in 55-gallon (208L) drums or pre-measured units in 5-gallon (19L) containers. Tyfo® WEB Fabric typically ships in 50" x 375 lineal foot (1.3m x 114.3m) rolls. Typically ships in 12" x 13" x 64" (305mm x 330mm x 1626mm) boxes.

#### EPOXY MIX RATIO

100.0 component A to 42.0 component B by volume. (100 component A to 34.5 component B by weight.)

#### SHELF LIFE

Epoxy - two years in original, unopened and properly stored containers.  
Fabric - ten years in proper storage conditions.

#### STORAGE CONDITIONS

Store at 40° to 90° F (4° to 35° C).  
Avoid freezing. Store rolls flat, not on ends, at temperatures below 100° F (38° C). Avoid moisture and water contamination.

#### CERTIFICATE OF COMPLIANCE

- Will be supplied upon request, complete with state and federal packaging laws with copy of labels used.
- Material safety data sheets will be supplied upon request.
- Possesses 0% V.O.C. level.

TYPICAL DRY FIBER PROPERTIES	
Tensile Strength	470,000 psi (3.24 GPa)
Tensile Modulus	10.5 x 10 <sup>6</sup> psi (72.4 GPa)
Ultimate Elongation	4.5%
Density	0.092 lbs./in. <sup>3</sup> (2.55 g/cm <sup>3</sup> )
Weight per sq. yd.	8.7 oz. (295 g/m <sup>2</sup> )

COMPOSITE GROSS LAMINATE PROPERTIES			
PROPERTY	ASTM METHOD	TYPICAL TEST VALUE	DESIGN VALUE*
Ultimate tensile strength in primary fiber direction, psi	D-3039	44,800 psi (309 MPa) (0.45 kip/in. width)	35,840 psi (247 MPa) (0.36 kip/in. width)
Elongation at break	D-3039	1.6%	1.6%
Tensile Modulus, psi	D-3039	2.8 x 10 <sup>6</sup> psi (19.3 GPa)	2.24 x 10 <sup>6</sup> psi (15.4 GPa)
Ultimate tensile strength 90 degrees to primary fiber, psi	D-3039	44,800 psi (309 MPa) (0.45 kip/in. width)	35,840 psi (247 MPa) (0.36 kip/in. width)
Laminate Thickness		0.01 in. (0.25 mm)	0.01 in. (0.25 mm)

\* Design and specification values will vary based on individual project requirements and applicable safety factors. Contact Fyfe Co. LLC engineers to determine appropriate specification values.

EPOXY MATERIAL PROPERTIES		
Curing Schedule 72 hours post cure at 140° F (60° C).		
PROPERTY	ASTM METHOD	TYPICAL TEST VALUE*
Tg 140° F (60° C) Post Cure (24 hours)	ASTM D-4065	180° F (82° C)
Tensile Strength <sup>1</sup> , psi	ASTM D-638 Type 1	10,500 psi (72.4 MPa)
Tensile Modulus, psi	ASTM D-638 Type 1	461,000 psi (3.18 GPa)
Elongation Percent	ASTM D-638 Type 1	5.0%
Flexural Strength, psi	ASTM D-790	17,900 psi (123.4 MPa)
Flexural Modulus, psi	ASTM D-790	452,000 psi (3.12 GPa)

<sup>1</sup> Testing temperature: 70° F (21° C) Crosshead speed: 0.5 in. (13mm)/min. Grips Instron 2716-0055 - 30 kips  
\* Specification values can be provided upon request.

Figure A.1 – Fibreglass Cloth [reproduced from Fyfe Co., 2004]

**HOW TO USE  
THE TYFO® S COMPOSITE SYSTEM**

**DESIGN**

The Tyfo® System shall be designed to meet specific design criteria. The criteria for each project is dictated by the engineer of record and any relevant building codes and/or guidelines. The design should be based on the allowable strain for each type of application and the design modulus of the material. The Fyfe Co. LLC engineering staff will provide preliminary design at no obligation.

**INSTALLATION**

Tyfo® System to be installed by Fyfe Co. LLC trained and certified applicators. Installation shall be in strict compliance with the Fyfe Co. LLC Quality Control Manual.

**SURFACE PREPARATION**

The required surface preparation is largely dependent on the type of element being strengthened. In general, the surface must be clean, dry and free of protrusions or cavities, which may cause voids behind the Tyfo® composite. Column surfaces that will receive continuous wraps typically require only a broom cleaning. Discontinuous wrapping surfaces (walls, beams, slabs, etc.) typically require a light sandblast, grinding or other approved methods to prepare for bonding. Tyfo® FibrAnchors™ are incorporated in some designs. The Fyfe Co. LLC engineering staff will provide the proper specifications and details based on the project requirements.

**MIXING**

For pre-measured units in 5-gallon (19L) containers, pour the contents of component B into the pail of component A. For drums, premix each component: 100.0 parts of component A to 42.0 parts of component B by volume (100 parts of component A to 34.5 parts of component B by weight). Mix thoroughly for five minutes with a Tyfo® low speed mixer at 400-600 RPM until uniformly blended.

**APPLICATION**

Feed fabric through the Tyfo® Saturator and apply using the Tyfo® wrapping equipment or approved hand methods. See data sheet on this equipment. Hand saturation is allowable, provided the epoxy is applied uniformly and meets the specifications.

**LIMITATIONS**

Minimum application temperature of the epoxy is 40°F (4°C). **DO NOT THIN**, solvents will prevent proper cure.

**CAUTION!**

**COMPONENT A - Irritant**

Prolonged contact to the skin may cause irritation. Avoid eye contact.

**COMPONENT B - Irritant**

Contact with skin may cause severe burns. Avoid eye contact. Product is a strong sensitizer. Use of safety goggles and chemical resistant gloves recommended. Remove contaminated clothing. Avoid breathing vapors. Use adequate ventilation. Use of an organic vapor respirator recommended.

**SAFETY PRECAUTIONS**

Use of an approved particle mask is recommended for possible airborne particles. Gloves are recommended when handling fabrics to avoid skin irritation. Safety glasses are recommended to prevent eye irritation.

**FIRST AID**

In case of skin contact, wash thoroughly with soap and water. For eye contact, flush immediately. For respiratory problems, remove to fresh air. Wash clothing before reuse.

**CLEANUP**

Collect with absorbent material, flush with water. Dispose of in accordance with local disposal regulations. Uncured material can be removed with approved solvent. Cured materials can only be removed mechanically.

**TYFO® S COMPOSITE SAMPLES**

Please note that field samples are to be cured for 48-hours at 140°F (60°C) before testing. Testing shall be in accordance with ASTM D-3038 and the Fyfe Co. LLC sample preparation and testing procedures.

**SHIPPING LABELS CONTAIN**

- State specification number with modifications, if applicable
- Component designation
- Type, if applicable
- Manufacturer's name
- Date of manufacture
- Batch name
- State lot number, if applicable
- Directions for use
- Warnings or precautions by law

**KEEP CONTAINER TIGHTLY CLOSED.  
NOT FOR INTERNAL CONSUMPTION.  
CONSULT MATERIAL SAFETY DATA SHEET  
(MSDS) FOR MORE INFORMATION.  
KEEP OUT OF REACH OF CHILDREN.  
FOR INDUSTRIAL USE ONLY.**

Figure A.1 (continued) – Fibreglass Cloth [reproduced from Fyfe Co., 2004]



# Tyfo® S Saturant Epoxy

## DESCRIPTION

The Tyfo® S Epoxy is a two-component epoxy matrix material for bonding applications. It is a high elongation material which gives optimum properties as a matrix for the Tyfo® Fibrwrap System. It provides a long working time for application, with no offensive odor. Tyfo® S Epoxy may also be thickened and used as a prime or finish coat depending upon the project requirements.

## USE

The Tyfo® S Epoxy matrix material is combined with the Tyfo® fabrics to provide a wet-layup composite system for strengthening structural members.

## ADVANTAGES

- Good high temperature properties
- Good low temperature properties
- Long working time
- High elongation
- Ambient cure
- 100% solvent-free

## COVERAGE

Approximately 0.8 pounds of epoxy per 1.0 pound of fabric when our Tyfo® Saturator is used. When used as a prime coat the coverage is highly dependent upon the existing surface.

## PACKAGING

Order in 55-gallon drums or pre-measured units in 5-gallon containers.

## MIX RATIO

100.0 parts of component A to 42.0 parts of component B by volume. (100 parts of component A to 34.5 parts of component B by weight.)

## SHELF LIFE

Two years in original, unopened and properly stored containers.

## STORAGE CONDITIONS

Store at 40° to 90° F (4° to 32° C). Avoid freezing.

## CERTIFICATE OF COMPLIANCE

- Will be supplied upon request, complete with state and federal packaging laws with copy of labels used.
- Material safety data sheets will be supplied upon request.
- Possesses 0% V.O.C. level, per ASTM D-2389.

## HOW TO USE

### THE TYFO® S EPOXY

## INSTALLATION

Tyfo® System to be installed by Fyfe Co. LLC trained and certified applicators. Installation shall be in strict compliance with the Fyfe Co. LLC Quality Control Manual.

## SURFACE PREPARATION

The required surface preparation is largely dependent on the type of element being strengthened. In general, the surface must be clean, dry and free of protrusions or cavities, which may cause voids behind the Tyfo® composite. Column surfaces that will receive continuous wraps typically require only a broom cleaning. Discontinuous wrapping surfaces (walls, beams, slabs, etc.) typically require a light sandblast, grinding or other approved methods to prepare for bonding. Mechanical anchors are incorporated in some designs. The Fyfe Co. LLC engineering staff will provide the proper specifications and details based on the project requirements.

## MIXING

For pre-measured units in 5-gallon containers, pour the contents of component B into the pail of component A. For drums, premix each component: 100.0 parts of component A to 42.0 parts of component B by volume (100 parts of component A to 34.5 parts of component B by weight). If material is too thick, drum heaters may be used on metal containers, or heat unmixed components by placing containers in 130° F (54° C) tap water or sunlight, if available, until the desired viscosity is achieved. Do not thin; solvents will prevent proper cure. Mix thoroughly for five minutes with a low speed mixer at 400-600 RPM until uniformly blended. When using as a prime coat or finish coat, Tyfo® S Epoxy may be thickened in the field to the desired consistency.

## APPLICATION

Tyfo® S Epoxy is applied to a variety of Tyfo® fabrics using the Tyfo® Saturator or by approved hand-applied methods. See data sheet on this equipment. Hand saturation is allowable, provided the epoxy is applied uniformly and meets the specifications. Tyfo® S Epoxy can also be applied as a prime coat by brush or roller.

## LIMITATIONS

Minimum application temperature of the epoxy is 40° F (4° C). **DO NOT THIN**; solvents will prevent proper cure.

EPOXY COMPONENT PROPERTIES	
Color	Component A is clear to pale yellow Component B is clear
Viscosity	Component A at 77° F (25° C) is 11,000-13,000 cps ASTM D-2392-80. Component B at 77° F (25° C) is 11 cps ASTM D-2393-80.
Pot Life	3 to 6 hours at 68° F (20° C).
Viscosity of Mixed Product	600-700 cps.
Density at 68° F (20° C) (Pound/Gallon)	Component A = 9.7 (4.4kg/3.79L) Component B = 7.9 (3.6kg/3.79L) Mixed product = 9.17 (4.2kg/3.79L)

Figure A.2 – Epoxy [reproduced from Fyfe Co., 2004]

EPOXY MATERIAL PROPERTIES		
Curing Schedule 72 hours post cure at 140° F (60° C).		
PROPERTY	ASTM METHOD	TYPICAL TEST VALUE <sup>a</sup>
Tg 140° F (60° C) Post Cure (24 hours)		180° F (82° C)
Tensile Strength <sup>1</sup> , psi	ASTM D-638 Type 1	10,500 (72.4 MPa)
Tensile Modulus, psi		461,000 (3.18 GPa)
Elongation Percent	ASTM D-638 Type 1	5.0%
Flexural Strength, psi	ASTM D-790	17,900 (123.4 MPa)
Flexural Modulus, psi	ASTM D-790	452,000 (3.12 GPa)

<sup>1</sup> Testing temperature: 70° F (21° C) Crosshead speed: 0.5 in. (13mm)/min. Grips Instron 2716-0055 - 30 kips  
<sup>a</sup> Specification values can be provided upon request.

**CAUTION:**

**COMPONENT A - Irritant:**  
 Prolonged contact to the skin may cause irritation. Avoid eye contact.

**COMPONENT B - Irritant:**  
 Contact with skin may cause severe burns. Avoid eye contact. Product is a strong sensitizer. Use of safety goggles and chemical resistant gloves recommended. Remove contaminated clothing. Avoid breathing vapors. Use adequate ventilation. Use of an organic vapor respirator recommended.

**FIRST AID**

In case of skin contact, wash thoroughly with soap and water. For eye contact, flush immediately with plenty of water; contact physician immediately. For respiratory problems, remove to fresh air. Wash clothing before reuse.

**CLEANUP**

Collect with absorbent material, flush with water. Dispose of in accordance with local disposal regulations. Uncured material can be removed with approved solvent. Cured materials can only be removed mechanically.

**SHIPPING LABELS CONTAIN**

- State specification number with modifications, if applicable
- Component designation
- Type, if applicable
- Manufacturer's name
- Date of manufacture
- Batch name
- State lot number, if applicable
- Directions for use
- Warnings or precautions required by law

**KEEP CONTAINER TIGHTLY CLOSED. NOT FOR INTERNAL CONSUMPTION. CONSULT MATERIAL SAFETY DATA SHEET (MSDS) FOR MORE INFORMATION. KEEP OUT OF REACH OF CHILDREN. FOR INDUSTRIAL USE ONLY.**

Figure A.2 (continued) – Epoxy [reproduced from Fyfe Co., 2004]

## MESH SPECIFICATIONS

<b>IN ACCORDANCE WITH:</b>	ASTM D-76; D-579; D-5035; MIL-Y-1140
<b>TYPE</b>	<b>STANDARD</b>
<b>COUNT</b>	Warp-ends/in 12 Fill - picks/in 6
<b>WEAVE</b>	Leno 6 X 6
<b>STANDARD WIDTH</b>	38 inches
<b>STANDARD LENGTH</b>	50 yards
<b>AREA COVERED</b>	475 sq.ft.
<b>MESH DESCRIPTION</b>	
Dry Weight	131 g/sq.m (3.9 oz./sq.yd.)
Coating Weight	22 g/sq.m (0.6 oz./sq.yd.) 14%
Finished Weight (+/- 10%)	153 g/sq.m (4.5 oz./sq.yd.)
<b>GLASS COMPOSITION</b>	
Warp	ECG 37 - 1/0
Fill	1800 yds/lb Roving
<b>AVERAGE BREAKING STRENGTH</b>	
dN/ 5cm (lbf / 2 in.) (12 picks & 12 ends tested)	Warp 185 (422) Fill 198 (452)
Alkali resistance after conditioning according to EIMA standard 105.01	Warp 129 (294) 70 % Fill 182 (415) 92 %
<b>ELONGATION (Dry)</b>	Warp 4.2 % Fill 3.4 %
<b>FINISH</b>	Soft, alkali resistant, self-extinguishing. Compatible with other materials of EIFS.

Figure A.3 – 4.5 oz./yd.<sup>2</sup> (Finished Weight) Fibreglass Mesh [reproduced from Textilglas, 2005]

## MESH SPECIFICATIONS

<b>IN ACCORDANCE WITH:</b>	<b>ASTM D-76; D-579; D-5035; MIL-Y-1140</b>
<b>TYPE</b>	<b>4446 HIGH STANDARD</b>
<b>COUNT</b>	Warp-ends / in <b>12</b> Fill-picks / in <b>6</b>
<b>WEAVE</b>	<b>Leno            6 X 6</b>
<b>STANDARD WIDTH</b>	<b>38 inches</b>
<b>STANDARD LENGTH</b>	<b>50 yards</b>
<b>AREA COVERED</b>	<b>475 sq.ft.</b>
<b>MESH DESCRIPTION:</b>	
Dry Weight	<b>163 g/ sq. m ( 4.8 oz./ sq.yd.)</b>
Coating Weight	<b>37 g/ sq. m ( 1.1 oz./ sq.yd.) 18.5%</b>
Finished Weight (+/- 10%)	<b>200 g/ sq. m ( 5.9 oz./ sq.yd.)</b>
<b>GLASS COMPOSITION</b>	Warp <b>ECG 37 1/0</b> Fill <b>1200 yds/lb Roving</b>
<b>AVERAGE BREAKING STRENGTH</b>	
dN / 5 cm    ( lbf / 2 in.)	Warp <b>223 ( 492 )</b>
(12 picks & 12 ends tested)	Fill <b>380 ( 838.)</b>
Alkali Resistancy after conditioning to EIMA Standard 105.01	Warp <b>122 ( 265 ) 55%</b> Fill <b>247 ( 545 ) 65%</b>
<b>ELONGATION    ( Dry )</b>	Warp <b>3.8</b> Fill <b>2.9</b>

Figure A.4 – 6 oz./yd.<sup>2</sup> (Finished Weight) Fibreglass Mesh [reproduced from Textilglas, 2005]



## MESH SPECIFICATIONS

<b>IN ACCORDANCE WITH:</b>	<b>ASTM D-76; D-579 D-5033; MIL-Y-1140</b>
<b>TYPE</b>	<b>4612 INTERMEDIATE PLUS (SD.4520M/40)</b>
<b>COUNT</b>	Warp-ends / in    12 Fill-picks / in    5
<b>WEAVE</b>	Leno            2 X 2
<b>STANDARD WIDTH</b>	38 inches
<b>STANDARD LENGTH</b>	25 yards
<b>AREA COVERED</b>	238 sq.ft.
<b>MESH DESCRIPTION:</b>	
Dry Weight	359 g/ sq. m ( 10.6 oz./ sq.yd.)
Coating Weight	59 g/ sq. m ( 1.7 oz./ sq.yd.) 16 %
Finished Weight ( +/- 10% )	418 g/ sq. m ( 12.3 oz./ sq.yd.)
<b>GLASS COMPOSITION</b>	Warp    ECK 18 - 1/0 Fill     450 yds/lb Roving
<b>AVERAGE BREAKING STRENGTH</b>	
dN / 5 cm ( lbf / 2 in.) (5 picks & 12 ends tested)	Warp    229 ( 523 ) Fill     750 ( 1715 )
Alkali Resistance after conditioning according to EIMA Standard 105.01	Warp    205 ( 470 ) 89% Fill     580 ( 1325 ) 77%
<b>ELONGATION</b> ( Dry )	Warp    3.7 % Fill     4.3 %
<b>FINISH</b>	Soft, alkali resistant, self-extinguishing. Compatible with other materials of EIFS

Figure A.5 – 12 oz./yd.<sup>2</sup> (Finished Weight) Fibreglass Mesh [reproduced from Textilglas, 2005]



Afacing International Limited

**PREP-COAT**  
EIFS Base Coat  
& Adhesive

**PRODUCT DESCRIPTION**

*Prep-Coat* serves two distinct functions: as an adhesive for expanded polystyrene (EPS), and as the base coat into which reinforcing fibre glass mesh is embedded. *Prep-Coat* is a water-based acrylic product, that once applied, forms a strong yet flexible base coat as well as a high-strength adhesive. *Prep-Coat* can be applied in coats ranging from  $\frac{1}{16}$  to  $\frac{1}{8}$  in. (1.6 to 3.2 mm). *Prep-Coat* is available in three aggregate sizes: fine; regular; or coarse. One 5 gal US (19 ltr) pail covers approximately 165 sq ft (15.5 sq m) when mixed with Portland Cement. This applies to either a 2 mm (1/12 in) base coat applied over EPS, or an adhesive applied with a  $\frac{1}{2}$  inch notched trowel held at a minimum 30° angle. Apply the adhesive so that the notches align vertically on the wall. Refer to system specifications for application procedure and substrate suitability.

**MIXING INSTRUCTIONS**

Gradually add 22 pounds (10 kg) of Type 10 Portland Cement to one half pail (33 pounds (15 kg)) of *Prep-Coat* being continually mixed until a workable consistency is obtained. Let the mixture stand for five minutes, then remix and use. Pot life is two hours. Up to 8 ounces (225 ml) of water may be added to enhance workability only. Discard any material that has begun to stiffen. **Under no circumstances shall the weight of the Portland Cement exceed that of the *Prep-Coat*.**

**PRECAUTIONS**

Store *Prep-Coat* at temperatures above 5°C (41°F) and below 40°C (104°F), and off the ground in a dry place away from direct sunlight. **Under no circumstances shall *Prep-Coat* be permitted to freeze.**

Make sure the substrate is free of efflorescence, releasing agents, paraffin, pollution buildup, oil, frost, moisture, loose material, paint, or any other foreign matter. Make sure the surface and ambient temperatures are 5°C (41°F) or greater when applying *Prep-Coat* and remain so until it has fully set and dried (minimum of 24 hours). Protect *Prep-Coat* from winds exceeding 25 km/hr (15 mph), from rain, hail, snow, and all other possible damage until it has fully set and dried (minimum of 24 hours).

**PERFORMANCE TESTS AND PRODUCT PROPERTIES**

Water Absorption: 15.2 % of dry weight (UEAtc Article 3.3.1.2)  
Water Vapour Permeance: 297 ng/Pa.s.m<sup>2</sup> (ASTM E96-95)  
Impermeability to Water: passed 2 hours (UEAtc Article 3.3.1.1)  
Bond Strength exceeds cohesive strength of Expanded Polystyrene and Cement Board (ASTM D1623C)  
Bond Strength to Finish Coat or Bear Coat: >100 kPa after 2 hours drying and  
>300 kPa after 7 days drying (ASTM D1623C)  
Non-Combustible when mixed 1:1 by weight with Type 10 Portland Cement (CAN/ULC-S114M)  
Density: 1.64 g/ml. PH: 8.5 Viscosity: 33,600 cps (spindle 7 @ 10 rpm)

Figure A.6 – Modified Mortar Parging [reproduced from DuRock, 2005]



## **APPENDIX B: FINITE ELEMENT ANALYSIS**

### **B.1 INTRODUCTION**

This appendix contains the results of a finite element analysis performed, on the five specimen configurations used in Phase One of this experimental investigation, by Dr. Wael El-Dakhakhni, Assistant Professor of Civil Engineering at McMaster University. The data is discussed by the author as background to the discussion of the average shear stress along bed joints of concrete block masonry subjected to shear-slip failure. The analysis was performed on bare specimens, without any FRP reinforcement. For post-peak slip of fibre reinforced joints, the distribution of shear is expected to be relatively uniform.

### **B.2 FINITE ELEMENT ANALYSIS DETAILS**

The following are the details of the finite element analysis:

- **Computer Program Used:** LS-DYNA
- **Analysis:** Linear elastic with an assumed load of 20 kN.
- **Sign Convention:** Tension is negative (-) and Compression is positive (+).
- **Assumed Material Properties:**
  - **Block:** Young's Modulus of Elasticity ( $E_b$ ) = 25 GPa  
Poisson's Ratio ( $\nu$ ) = 0.2
  - **Mortar:** Young's Modulus of Elasticity ( $E_m$ ) = 12 GPa  
Poisson's Ratio ( $\nu$ ) = 0.2
- **Geometry:**
  - **Specimens:** As described in Chapter 2.
  - **Face Shells:** Thickness = 36 mm

• **Finite Elements:**

- Solid with no rotational degrees of freedom.
- **Block Elements/Mesh Size:** 19.5 mm × 18 mm
- **Mortar Bed Joints Elements/Mesh Size:** 19.5 mm × 10 mm

**B.3 SHEAR STRESS ALONG SLIP PLANES**

For each specimen, the analytical results were used to plot the shear and normal stress distributions along the slip planes. Since the finite element analysis were linear elastic, the stresses caused by the actual experimental failure loads was obtained by multiplying the results by the appropriate scaling factor. Based on the test results from the unretrofitted Phase One specimens (Table 3.1), the applicable multiplication factors are provided in Table B.1.

**Table B.1 – Multiplication Factors for Scaling Finite Element Analysis**

<b>Specimen</b>	<b>Average <math>P_{max}</math> (kN)<sup>†</sup></b>	<b>Applied FE Load (kN)<sup>‡</sup></b>	<b>Scaling Factor</b>
AU – 0.5	4.9	20	0.245
AU – 1.5	22.9	20	1.145
AU – 2.5	44.9	20	2.245
TU – 0.5	12.6	20	0.63
TU – 1.5	26.4	20	1.32

<sup>†</sup> Maximum failure load as recorded by the Tinius Olsen machine or commercial load cell.

<sup>‡</sup> Load applied at the top of the specimen.

For each specimen, the plots of shear stress distribution along the slip planes are presented in Figures B.1 to B.5. The figures contain the distribution based on the finite element analysis' load and the scaled distribution based on the actual average failure load of the specimen. The figures also contain the shear stress contours, which illustrate the presence of stress concentrations. The plots are “wavy” because a relatively coarse finite



element mesh was used. This is acceptable for the purpose of this investigation because the plots are only needed to determine the general trend of the shear stress distribution.

To confirm the validity of the finite element analysis, the average experimental shear stresses are also plotted in Figures B.1 to B.5. Furthermore, Table B.2 contains a comparison between the experimental and finite element analysis results. Scaling the finite element analysis results equated to an 89% to 98% prediction of the experimental results.

**Table B.2 – Correlation Between Experimental and Finite Element Analysis Results**

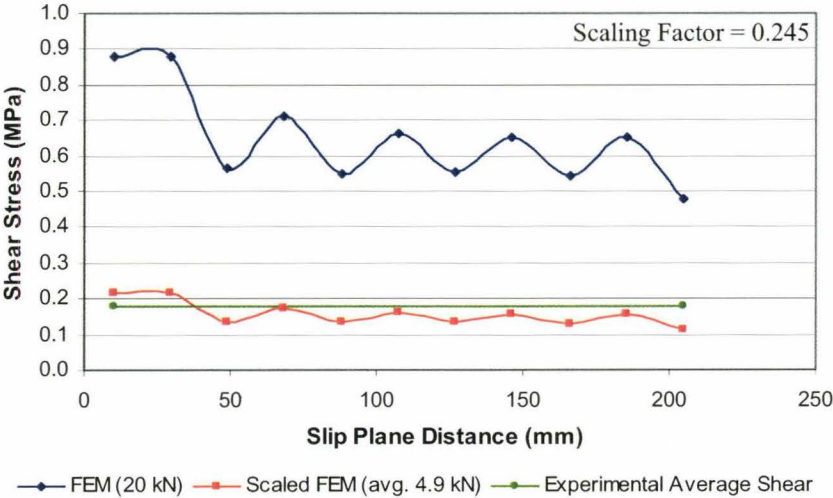
Specimen	Experimental		Scale Factor	Finite Element Analysis			%*
	Avg. P <sub>max</sub> (kN) <sup>†</sup>	Avg. Shear Stress (MPa)		Applied FE Load (kN) <sup>‡</sup>	Avg. Shear Stress (MPa)	Scaled Shear Stress (MPa)**	
AU – 0.5	4.9	0.18	0.245	20	0.65	0.16	89
AU – 1.5	22.9	0.28	1.145	20	0.23	0.26	93
AU – 2.5	44.9	0.33	2.245	20	0.14	0.32	97
TU – 0.5	12.6	0.49	0.63	20	0.75	0.47	96
TU – 1.5	26.4	0.33	1.32	20	0.24	0.32	97

<sup>†</sup> Maximum failure load as recorded by the Tinius Olsen machine or commercial load cell.

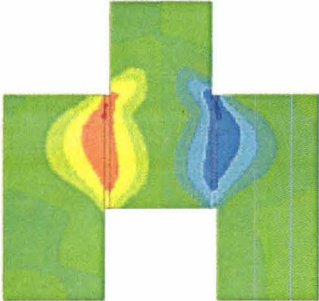
<sup>‡</sup> Load applied at the top of the specimen.

\*\* (Finite Element Analysis Average Shear Stress) × (Multiplication Factor)

\* (Finite Element Analysis Scaled Avg. Shear Stress) ÷ (Experimental Avg. Shear Stress) × 100%



**Shear Stress Contours**  
(From LS-DYNA Finite Element Analysis)



**Figure B.1 – Specimen A-0.5: Shear Stress Distribution Along Slip Planes**

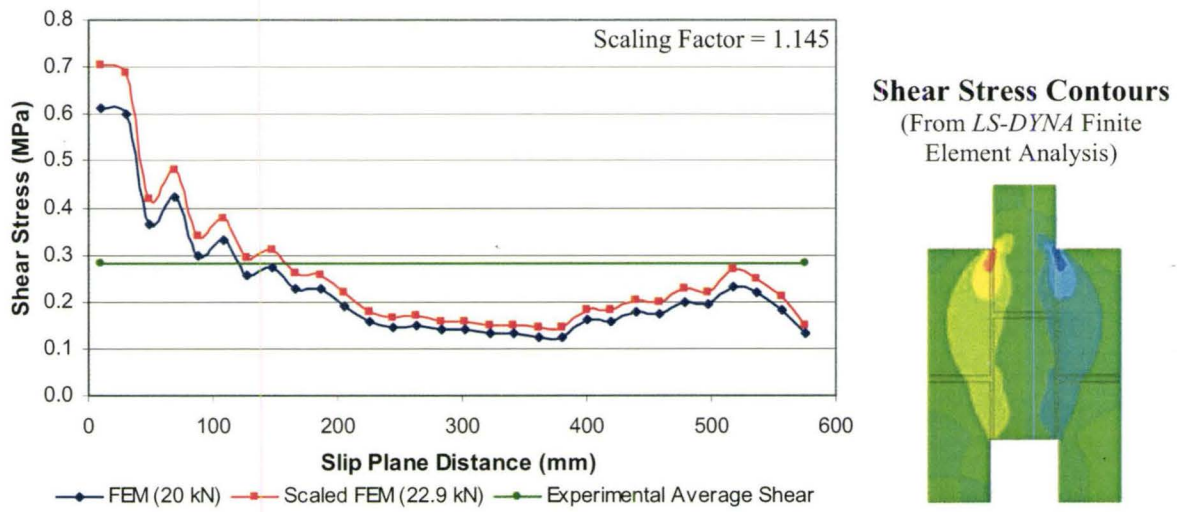


Figure B.2 – Specimen A-1.5: Shear Stress Distribution Along Slip Planes

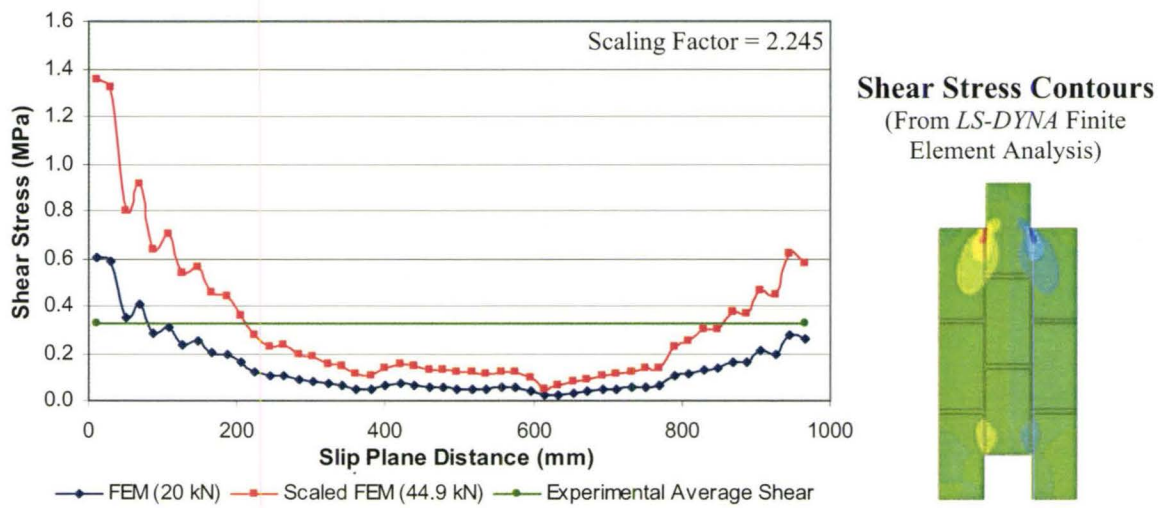


Figure B.3 – Specimen A-2.5: Shear Stress Distribution Along Slip Planes

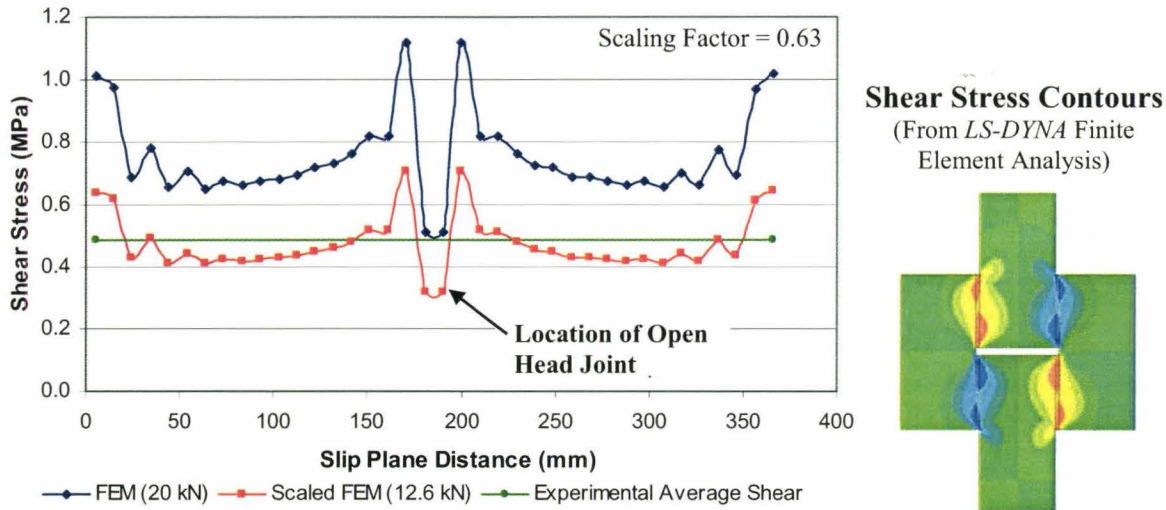


Figure B.4 – Specimen T-0.5: Shear Stress Distribution Along Slip Planes

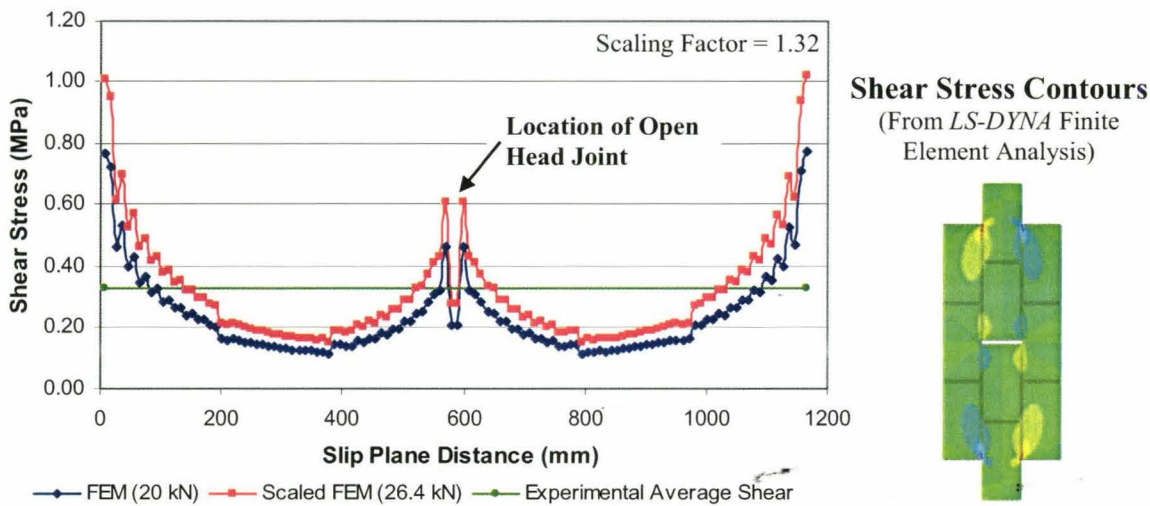


Figure B.5 – Specimen T-1.5: Shear Stress Distribution Along Slip Planes

The shear stress distribution plots in Figures B.1 to B.5 show that, for the ‘A’ specimens, there is a stress concentration at the start of the shear transfer zone, whereas for the ‘T’ specimens, there are stress concentrations at both the start and end of each of the four shear transfer zones. Note that at the ends of the slip planes, the shear stress



values are the average for the element and not located at the free surface. Thus, the shear stress is not zero..

#### B.4 NORMAL STRESS ALONG SLIP PLANES

The results of the finite analysis were also used to plot the normal stress distribution along the slip plane. So that a direct comparison could be easily made, the normal stress distribution for all of the specimens was plotted in Figures B.7 to B.10. For a specimen to undergo as close to pure shear-slip failure as possible, it was necessary for low, ideally no, normal stress to be induced. Normal tensile stress will tend to pull the bed joints apart which would cause premature failure, while normal compression stress will increase shear friction which will increase the specimen's strength.

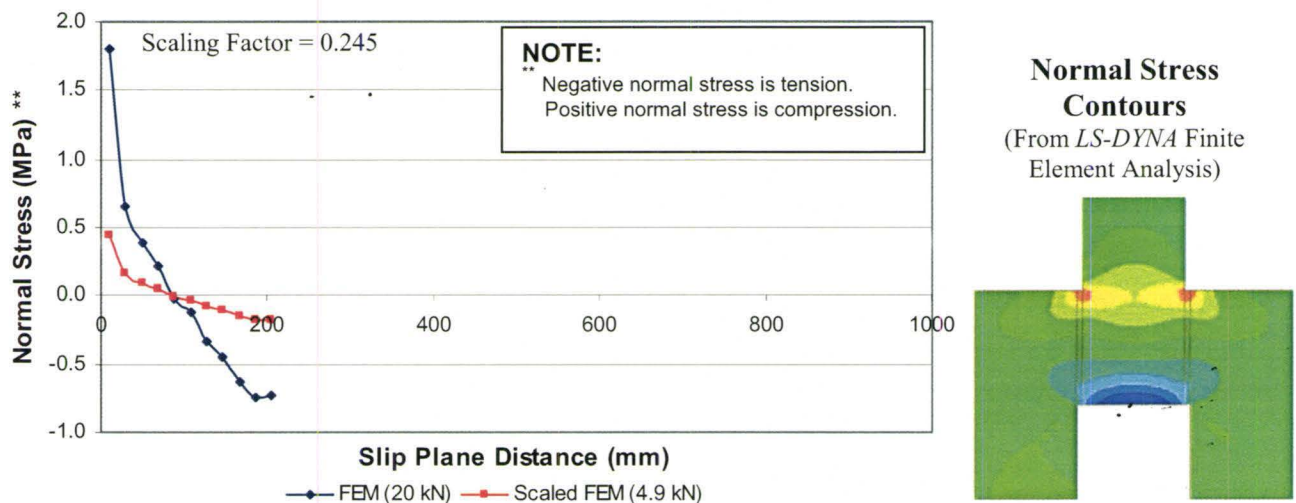


Figure B.6 – Specimen A-0.5: Normal Stress Distribution Along Slip Planes

Limiting the amount of induced tension stress normal to the bed joint slip planes is necessary because according to S304.1 (2004), the specified tensile strength of ungrouted concrete block masonry (bonded using Type-S mortar) is only 0.4 MPa.



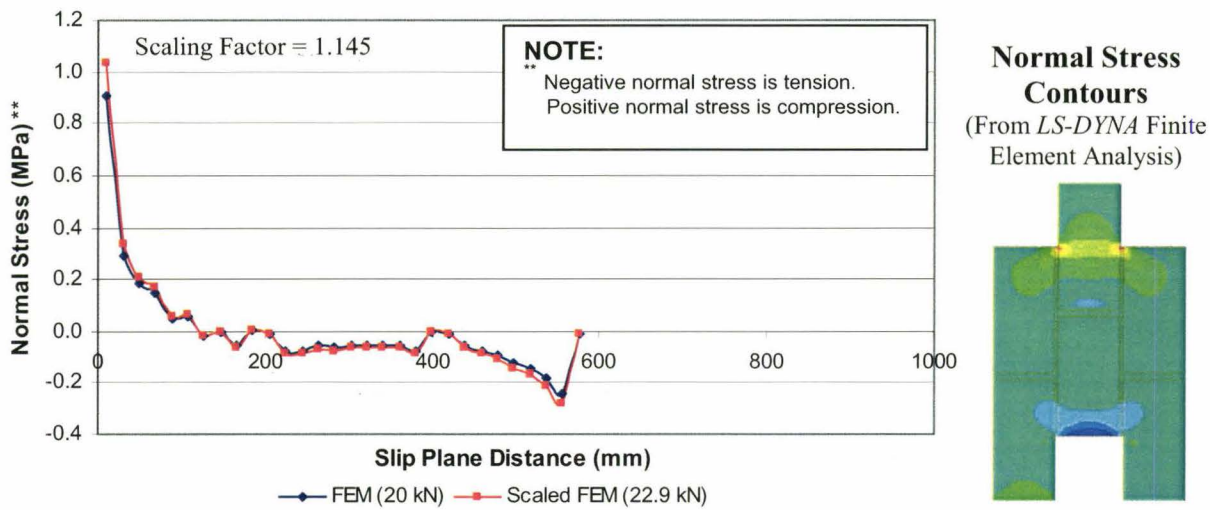


Figure B.7 – Specimen A-1.5: Normal Stress Distribution Along Slip Planes

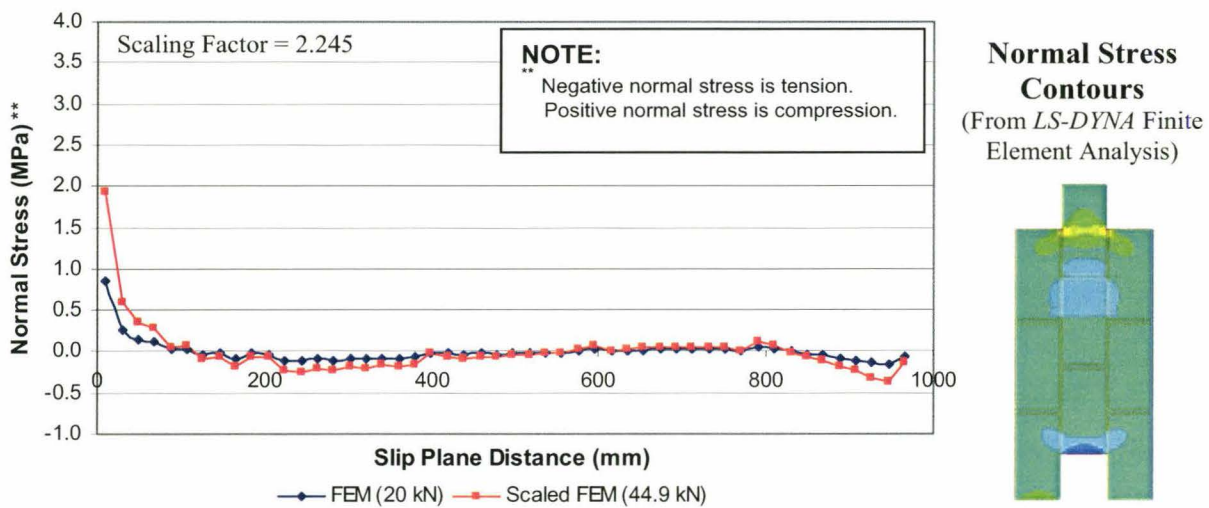


Figure B.8 – Specimen A-2.5: Normal Stress Distribution Along Slip Planes

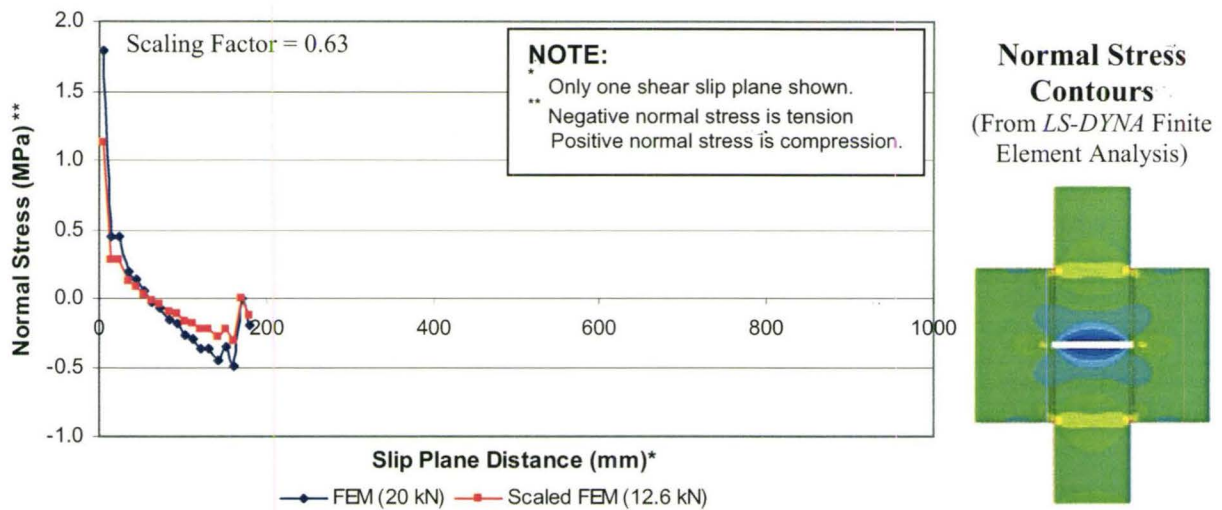


Figure B.9 – Specimen T-0.5: Normal Stress Distribution Along Slip Planes

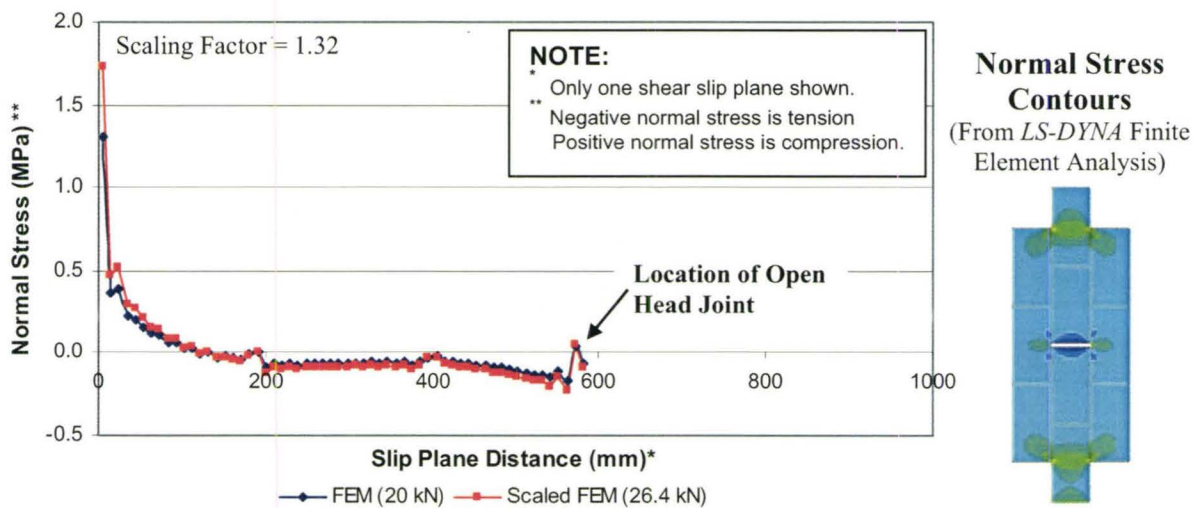


Figure B.10 – Specimen T-1.5: Normal Stress Distribution Along Slip Planes

Based on the scaled finite element analysis curves, all of the specimens had normal stress concentrations at the beginning and end of the slip planes. The arching action experienced by specimen A-0.5 tended to pull the specimen apart which resulted in high variability of the results, as shown in Table 3.1. Therefore this specimen was not

ideal for further shear slip research. Specimen T-0.5 performed better than specimen A-0.5 by reducing the normal tension force at the end of the slip plane. However, the shorter shear transfer length would increase the significance of the stress concentrations so it also was also not ideal for further shear slip research. Both the A-1.5 and especially the A-2.5 specimens had relatively low normal stress along most of their respective slip planes with a tensile concentration of approximately 0.2 MPa at the end of the slip plane. However, as discussed in Chapter 3, the lower blocks of these specimens had a tendency to crush due to the reaction forces, making them unsuitable for further study. For the T-1.5 specimen, the finite element analysis indicated that along most of the length of the shear slip plane, the normal stress was uniform and relatively low, which produced nearly pure shear conditions along the bed joint slip plane. Also, the longer shear transfer length would reduce the significance of the compression stress concentration. As shown in Table 3.1, this shape of specimen also, typically, had less variability of results. Therefore, the T-type specimen was preferable.

## **B.5 REVISED FINITE ELEMENT ANALYSIS**

The results of the finite element analysis are influenced by the assumed material properties. The original analysis assumed that the stiffness of the mortar,  $E_m$ , was half the stiffness of the block,  $E_b$ , ( $E_m = 12$  GPa versus  $E_b = 25$  GPa). In reality, the stiffness of the mortar is anywhere from 10% to 20% the stiffness of the block.

For the T-1.5, the finite element analysis was performed again. All of the details described in Section B.2 were kept constant except for the stiffness of the mortar,  $E_m$ .  $E_m$  was assumed to be 10% the stiffness of the block, or 2.5 GPa.

As illustrated in Figure B.11, the reduced mortar stiffness resulted in lower shear stress concentrations near the ends and more uniform shear stress distribution along the middle of the slip planes when compared to Figure B.5.

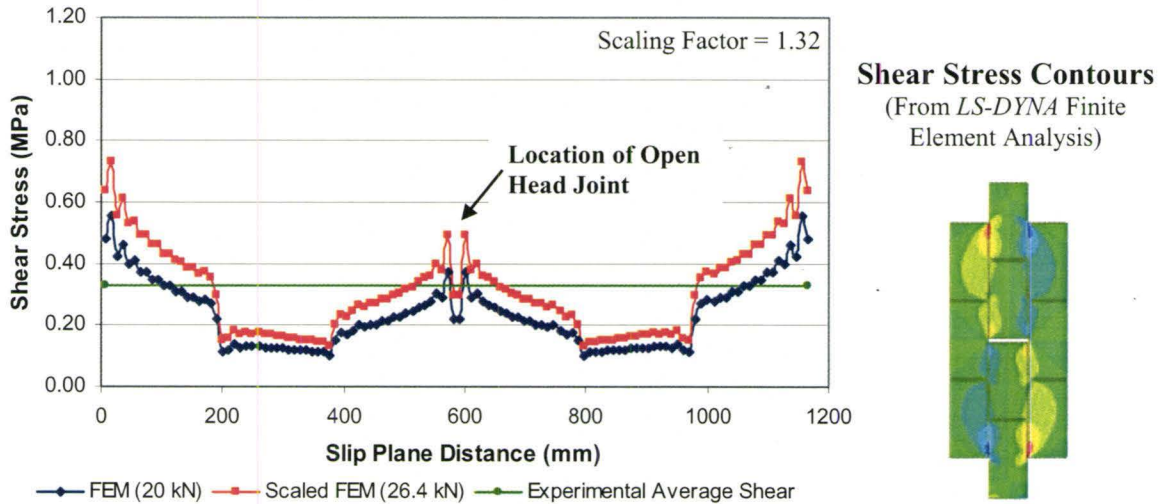


Figure B.11 – Specimen T-1.5: Revised Shear Stress Distribution Along Slip Planes

As illustrated in Figure B.12, the reduced mortar stiffness resulted in lower normal stress concentrations near the ends of the slip planes when compared to Figure B.10.

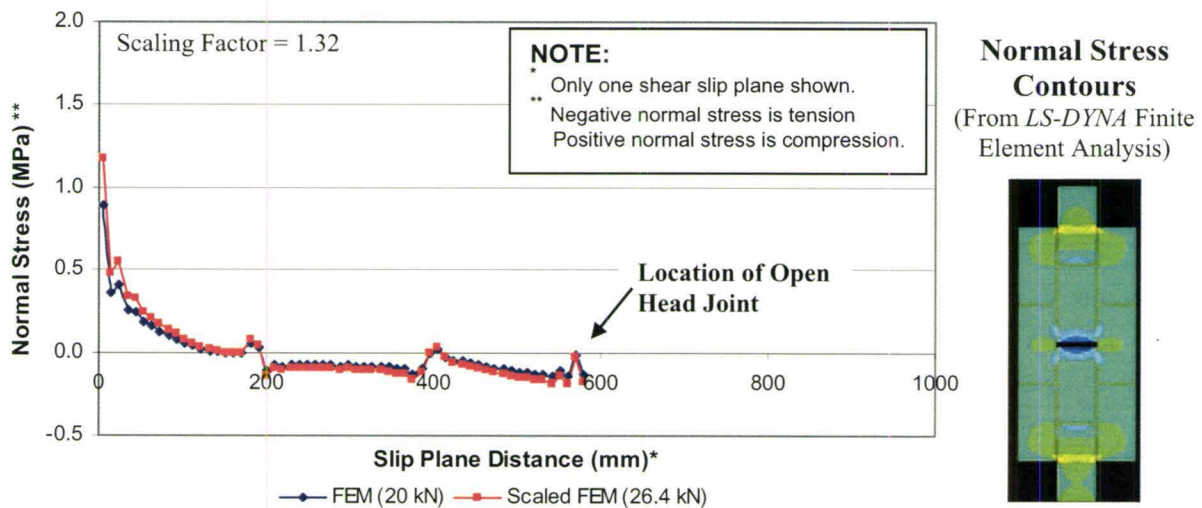


Figure B.12 – Specimen T-1.5: Revised Normal Stress Distribution Along Slip Planes



Therefore, reducing the stiffness of the mortar to a more realistic value resulted in more favourable shear and normal stress distributions along the slip planes. Although the revised analysis was only performed on the T-1.5 specimen, the same should hold true for the remaining specimen configurations.

## **B.6 CONCLUSION**

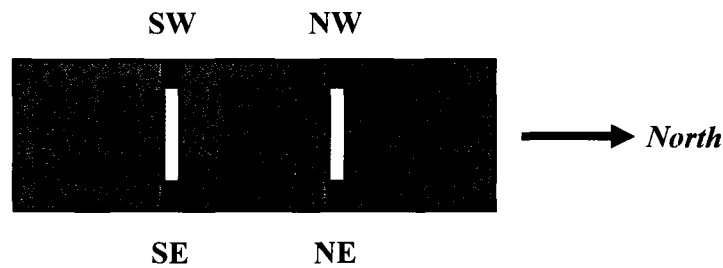
The results of the finite element analysis are influenced by the assumed material properties of the block and mortar. Reducing the stiffness of the mortar to a more realistic value resulted in more uniform shear and normal stress distributions along the slip plane.

Considering the need to minimize bending stress normal to the bed joint and the desire to have nearly uniform shear stresses prior to initial bed joint cracking, the T-1.5 type of specimen was chosen for further shear slip research.

## **APPENDIX C: RAW EXPERIMENTAL DATA**

### **C.1 INTRODUCTION**

This appendix contains the raw experimental data from Phase One and Three. The plotted loads and displacements are as recorded by the commercial load cell (or Tinius Olsen machine) and LPDTs (or mechanical gauge), respectively. The designations for each type of specimen were presented in Chapter 2 on pages 28 and 29. For the A–2.5 and T–1.5 specimens, the orientation of the slip planes in the custom-made testing apparatus is defined in Figure C.1.

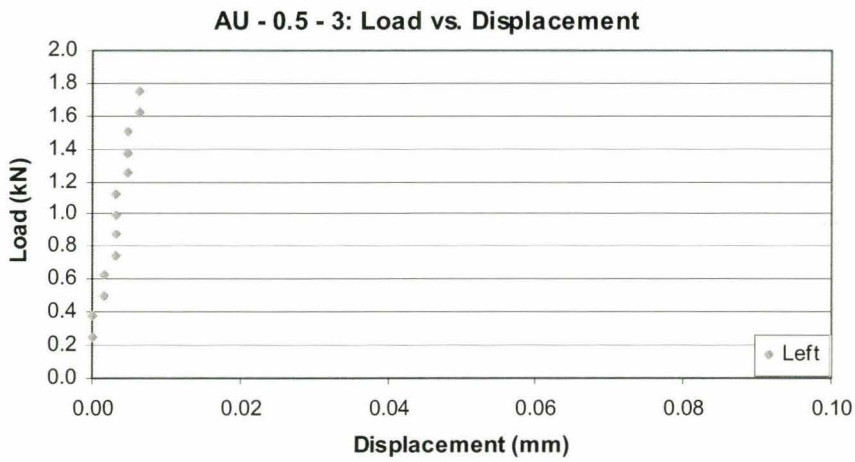
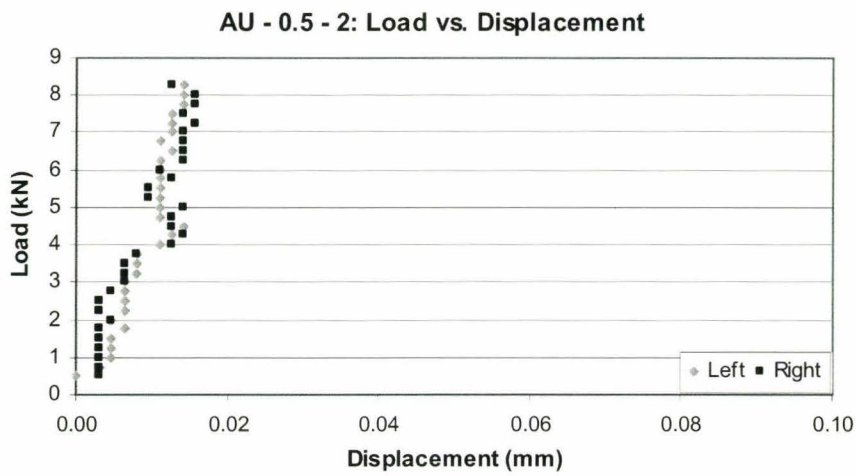
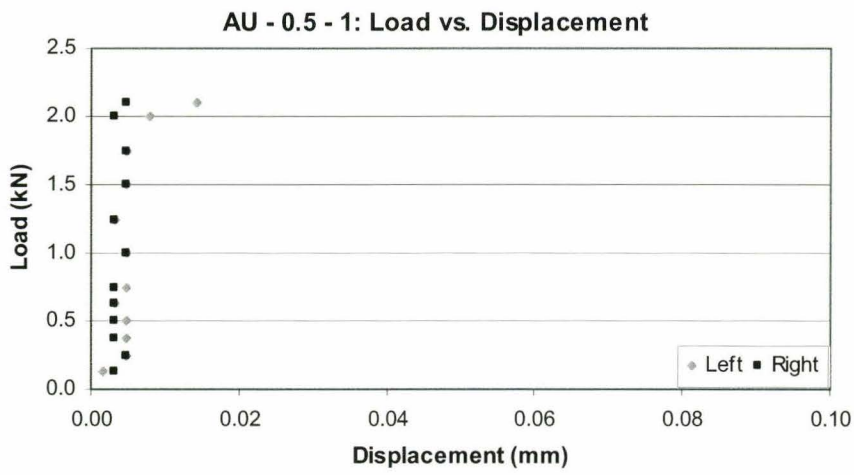


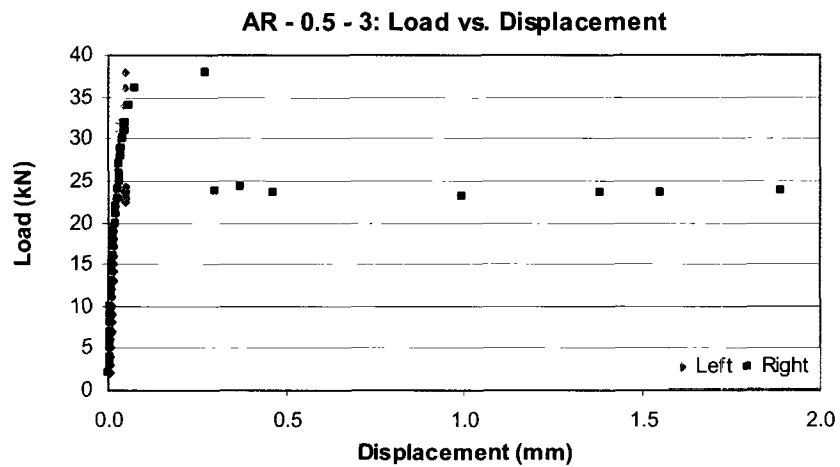
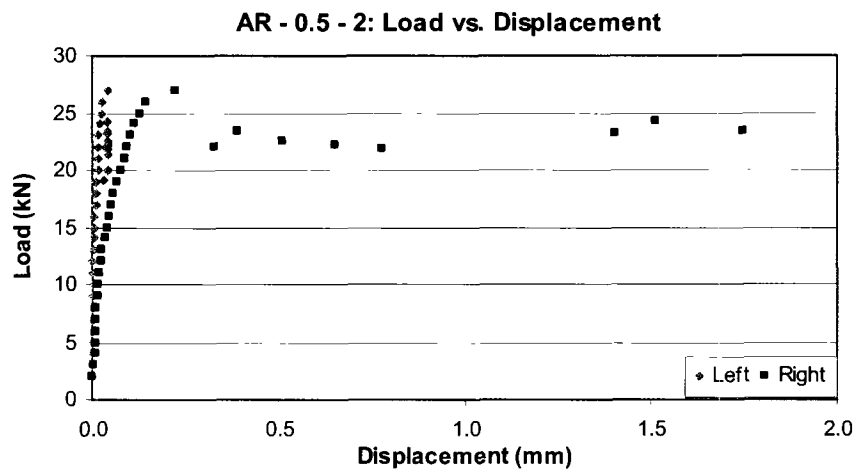
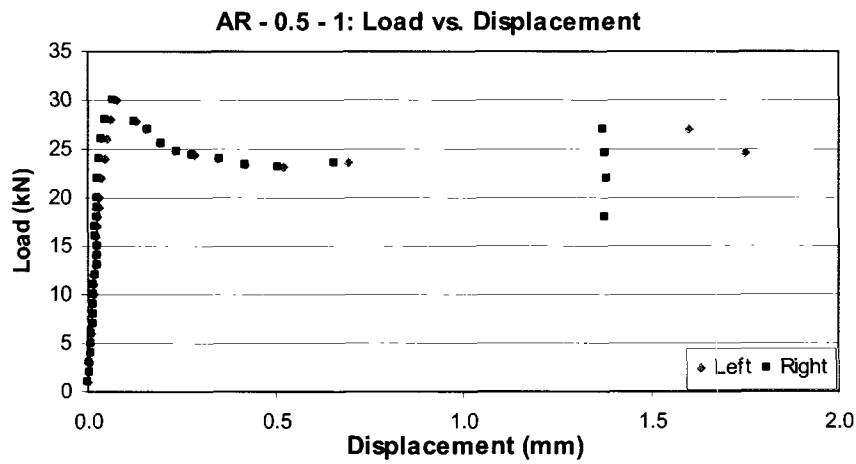
**Figure C.1** – Orientation of Slip Planes in the Custom-Made Testing Apparatus  
(Used For Specimens A–2.5 and T–1.5)

### **C.2 PHASE ONE RAW DATA**

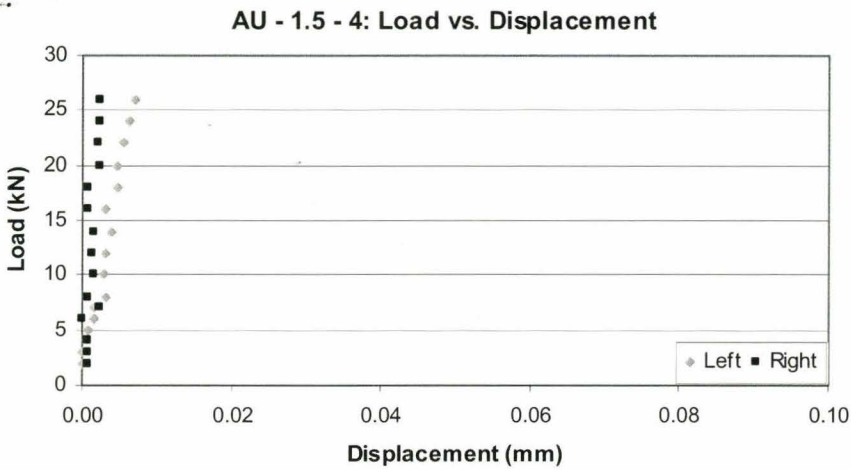
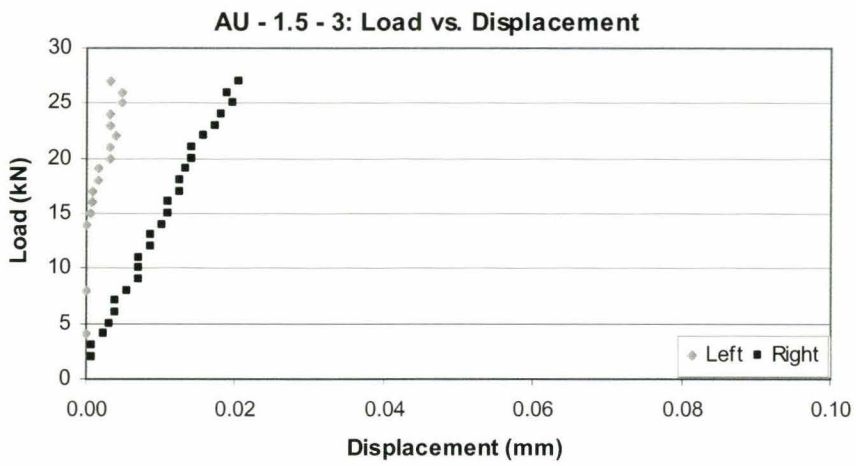
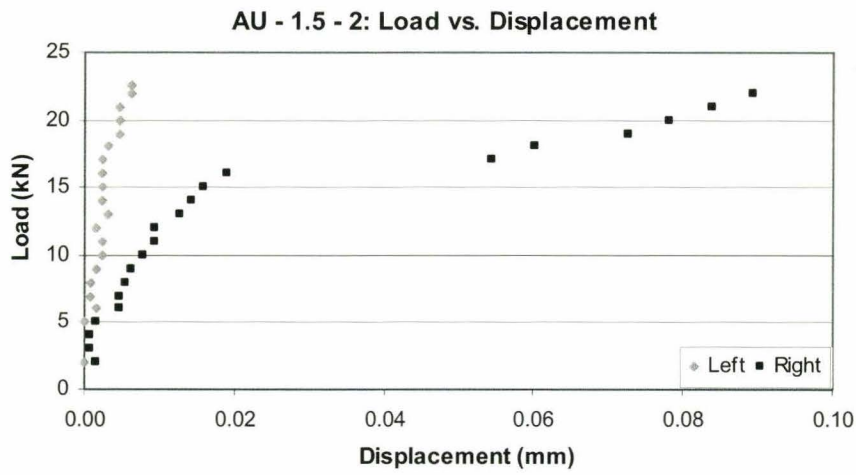
**Table C.1** – Phase One Table of Contents

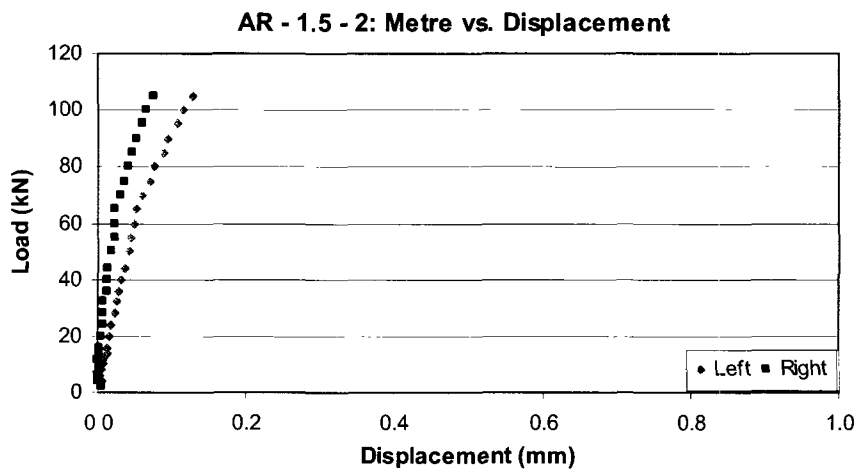
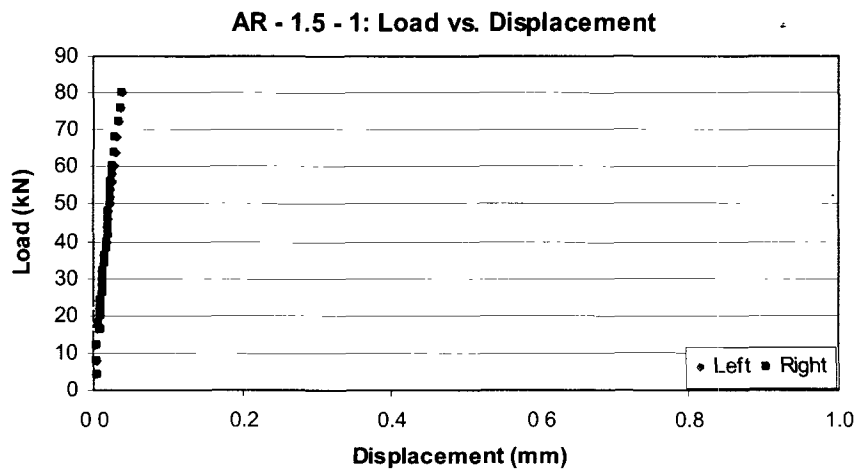
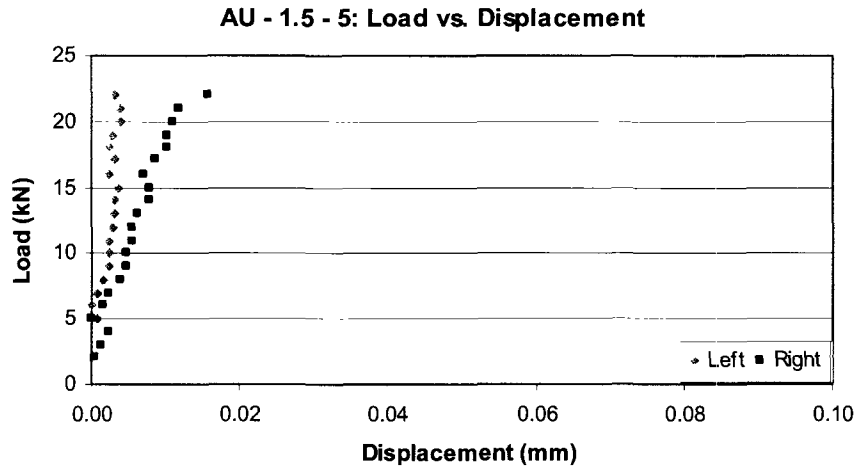
<b>Specimen</b>	<b>Page</b>	<b>Specimen</b>	<b>Page</b>	<b>Specimen</b>	<b>Page</b>
AU–0.5–1	164	AR–1.5–3	168	TR–0.5–1	172
AU–0.5–2	164	AU–2.5–1	168	TR–0.5–2	172
AU–0.5–3	164	AU–2.5–2	168	TR–0.5–3	172
AR–0.5–1	165	AU–2.5–3	169	TU–1.5–1	173
AR–0.5–2	165	AU–2.5–4	169	TU–1.5–2	173
AR–0.5–3	165	AU–2.5–5	169	TU–1.5–3	173
AU–1.5–2	166	AR–2.5–1	170	TU–1.5–4	174
AU–1.5–3	166	AR–2.5–3	170	TU–1.5–5	174
AU–1.5–4	166	TU–0.5–1	170	TR–1.5–1	174
AU–1.5–5	167	TU–0.5–2	171	TR–1.5–2	175
AR–1.5–1	167	TU–0.5–3	171	TR–1.5–3	175
AR–1.5–2	167	TU–0.5–4	171		

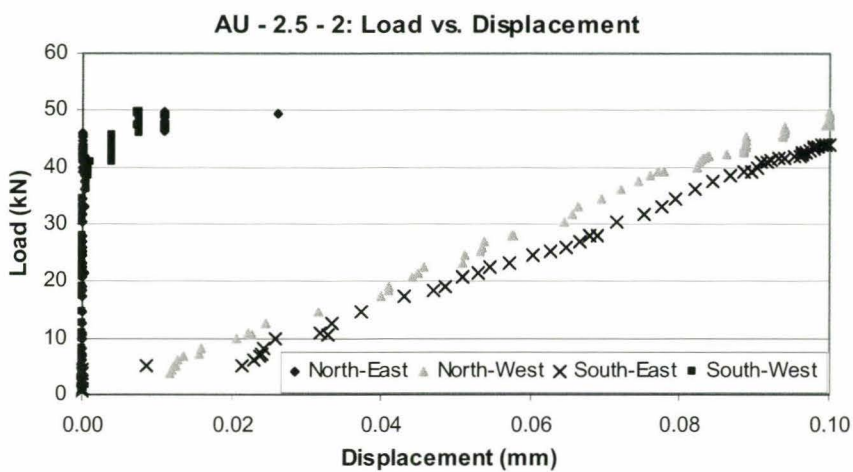
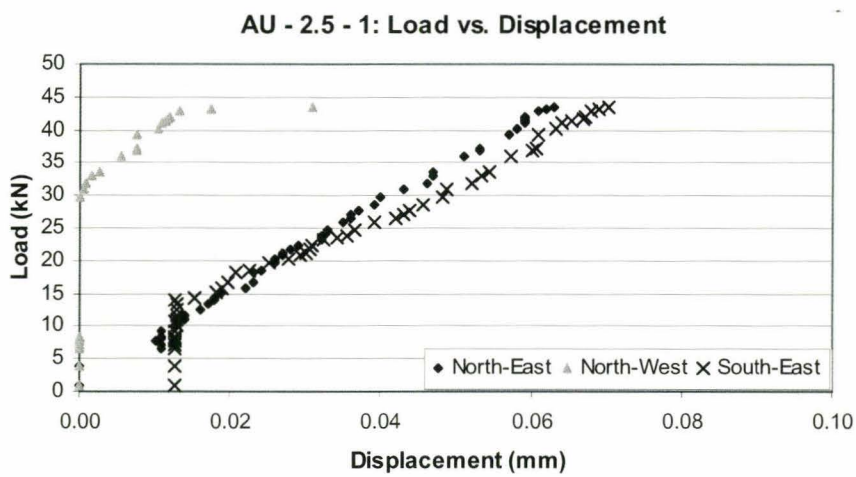
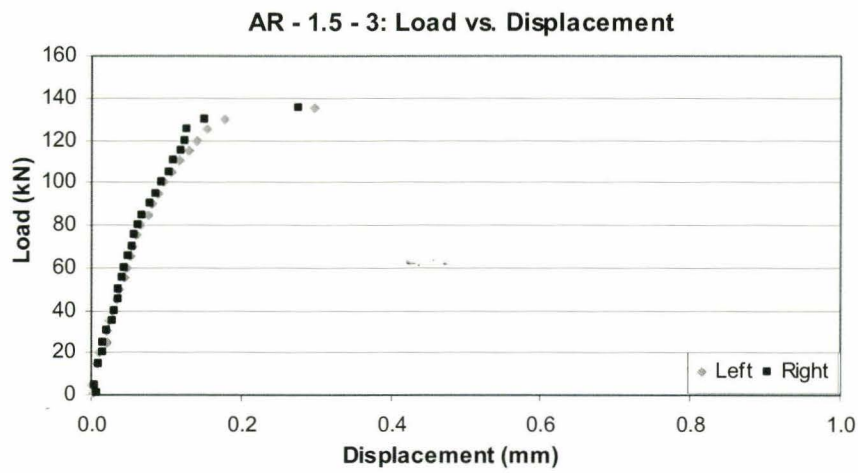


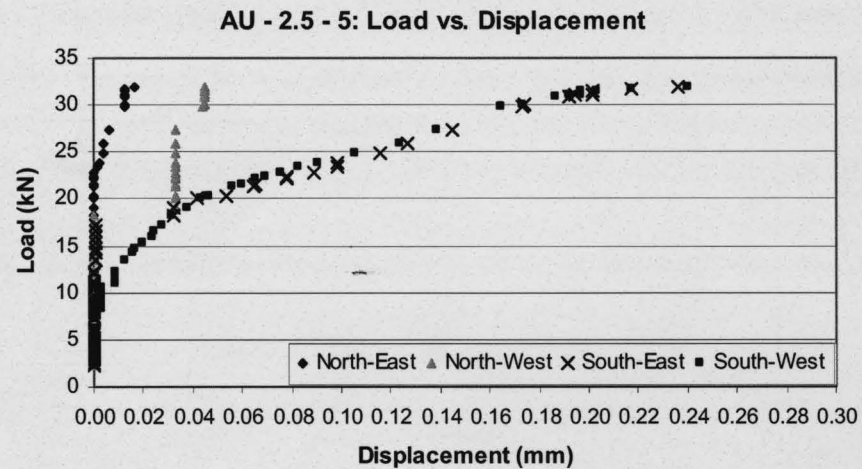
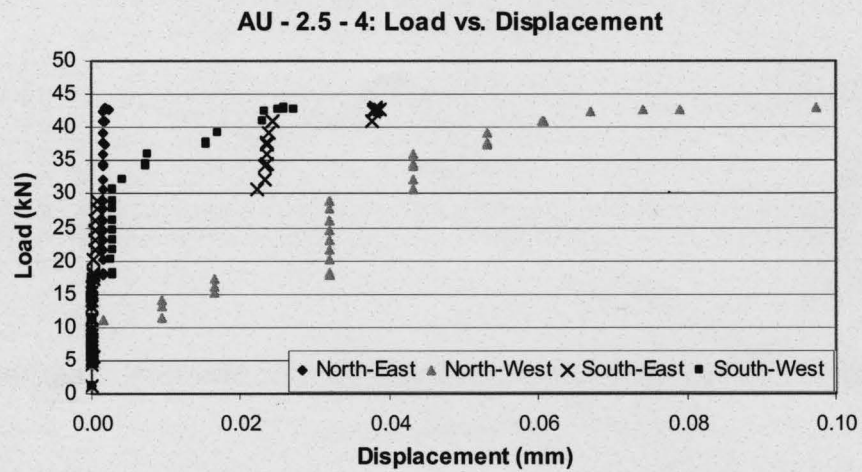
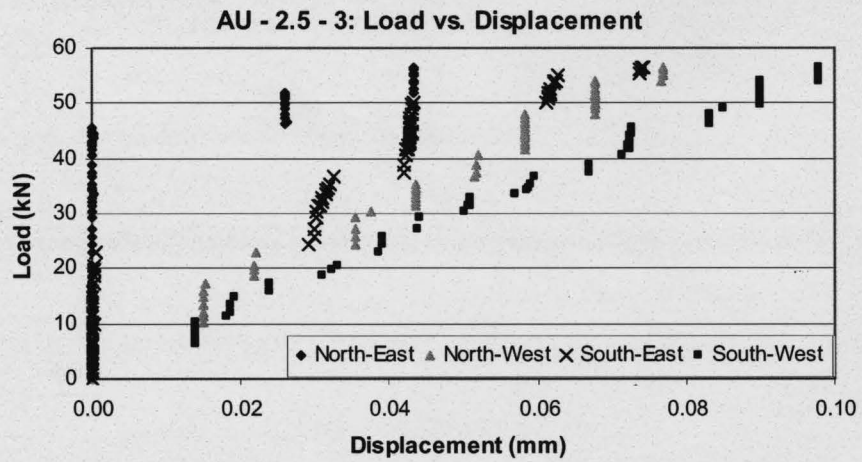




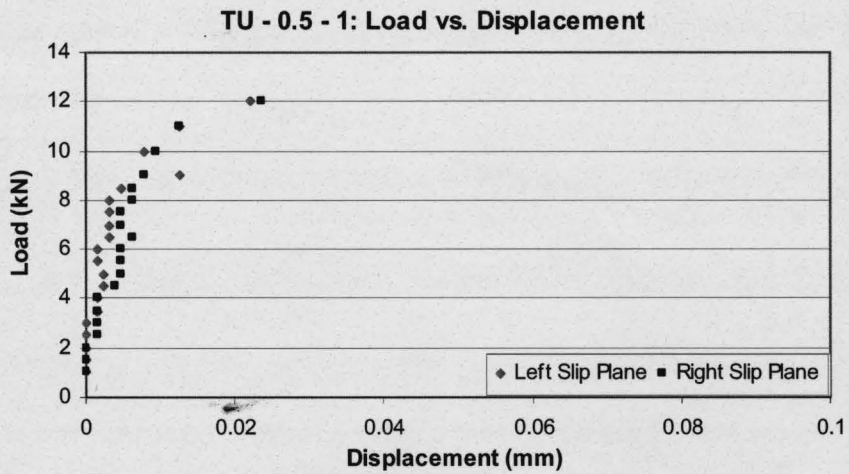
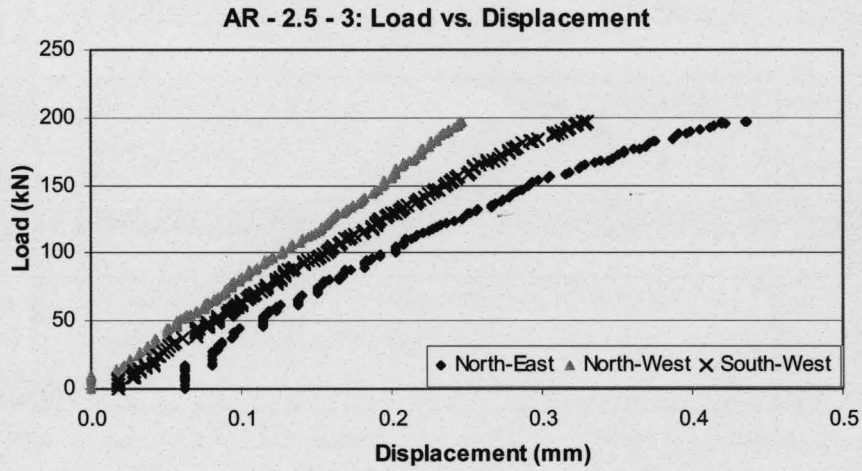
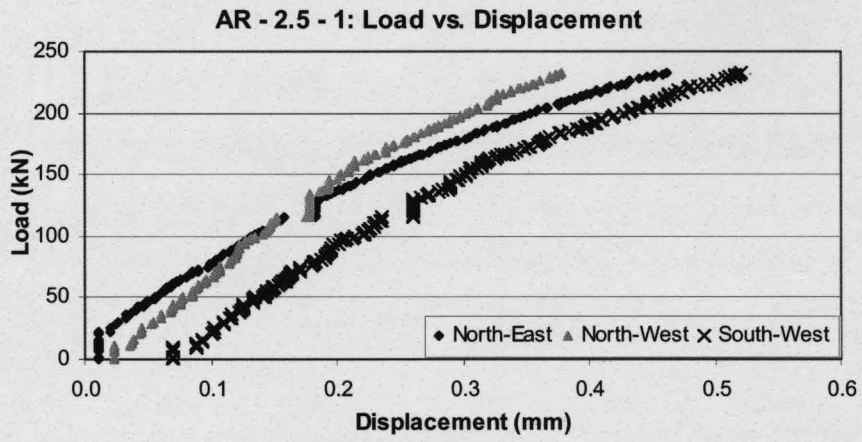




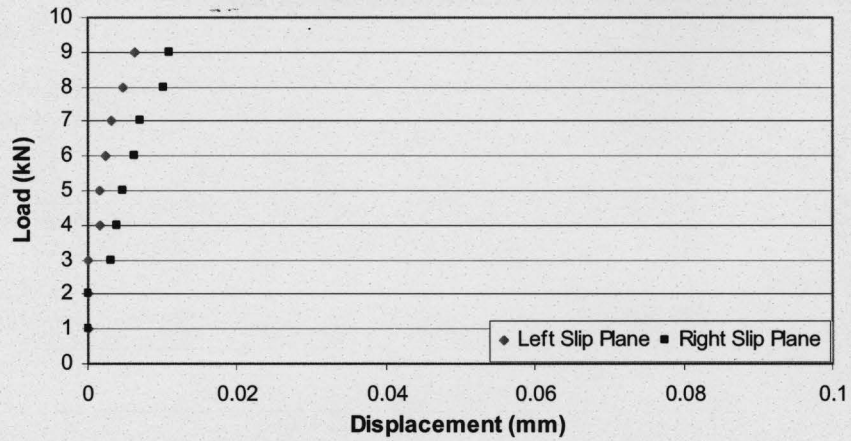




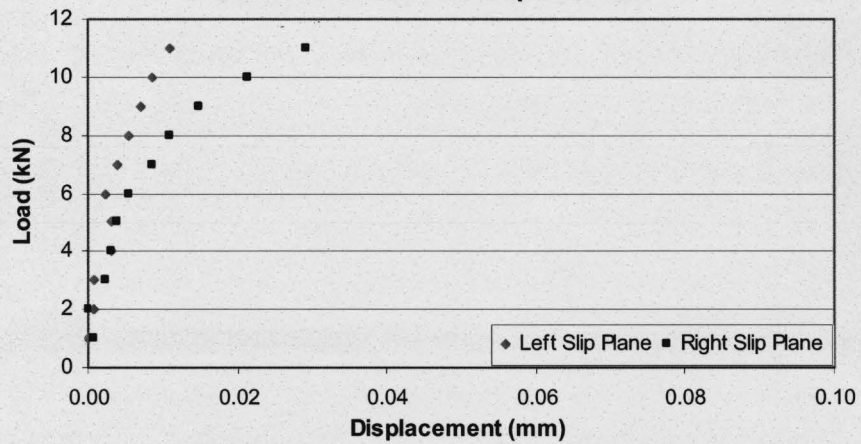




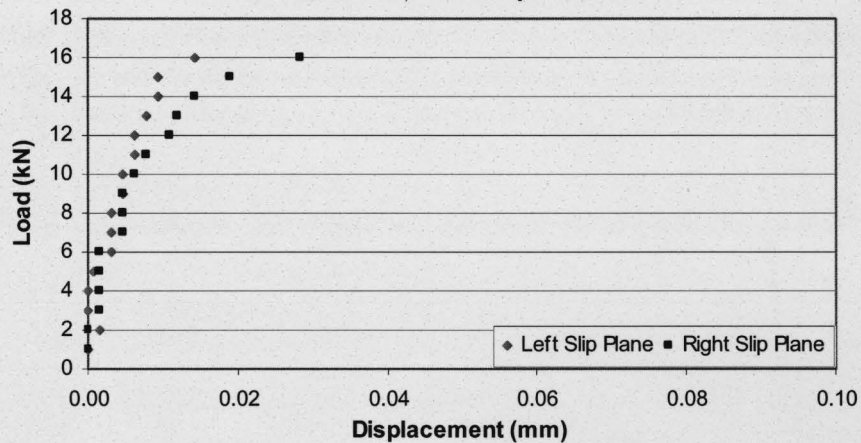
TU - 0.5 - 2: Load vs. Displacement

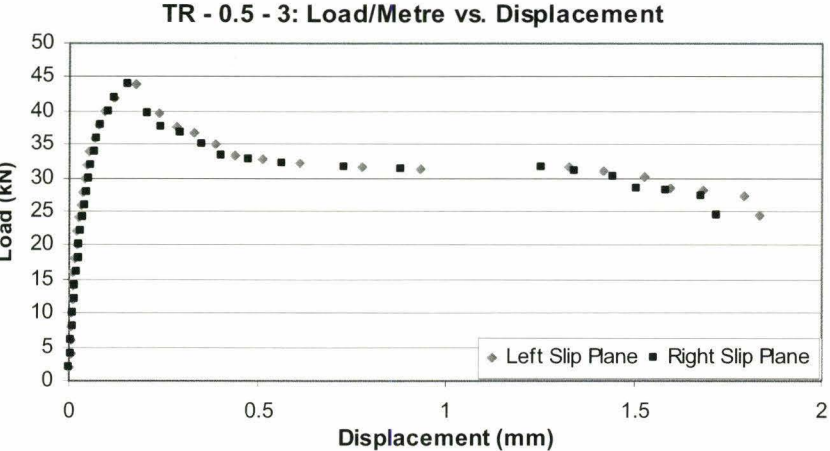
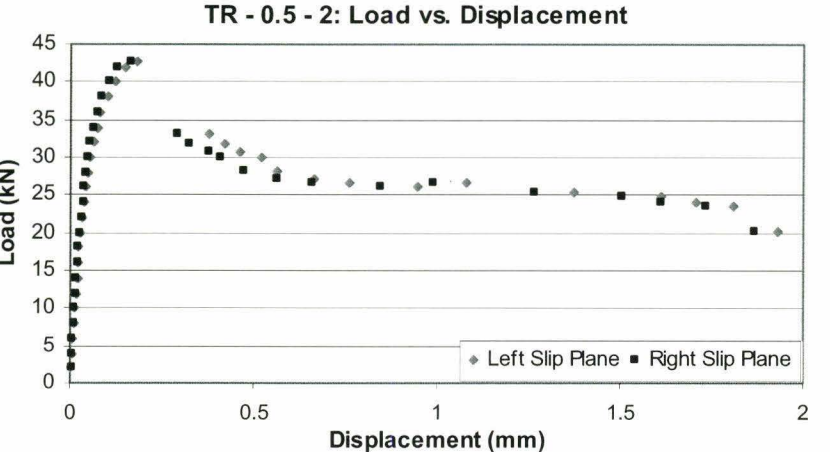
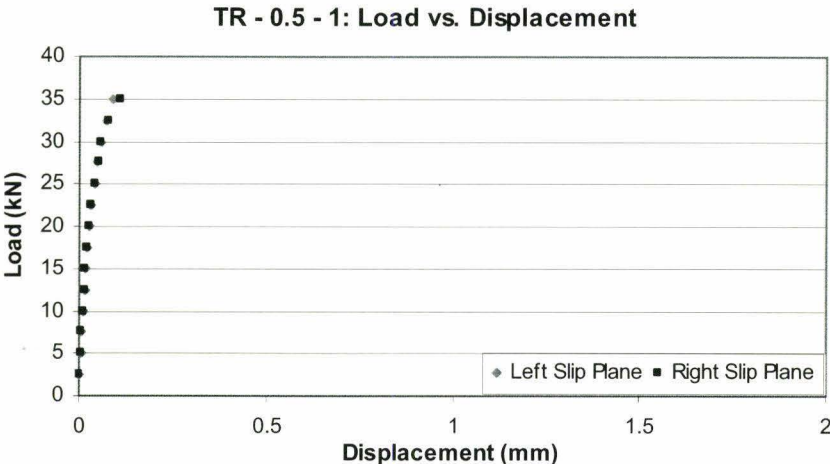


TU - 0.5 - 3: Load vs. Displacement

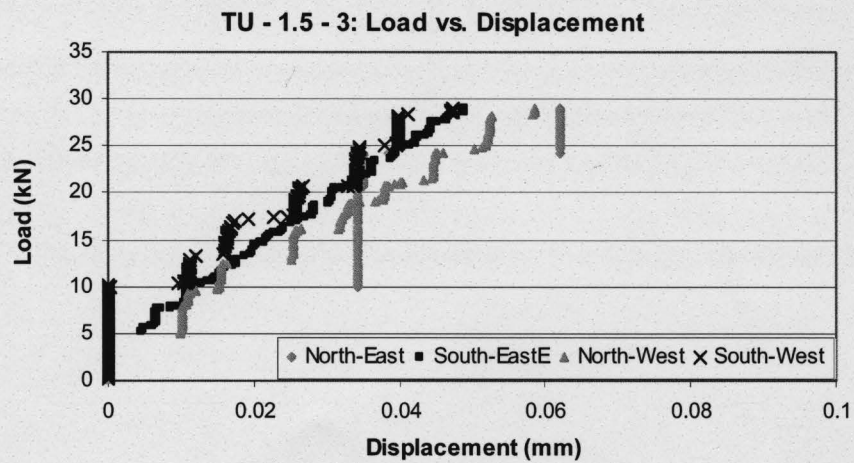
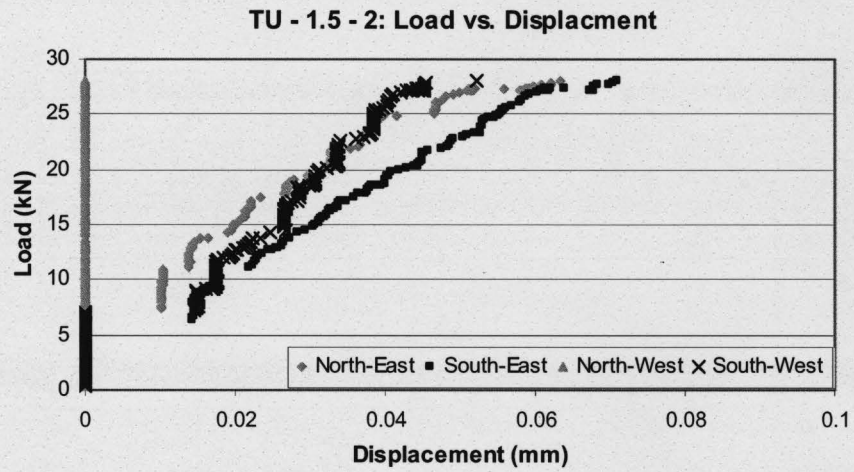
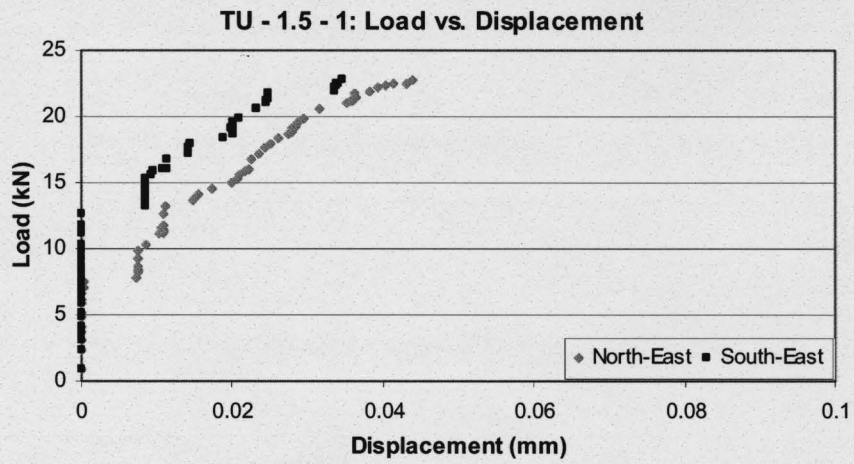


TU - 0.5 - 4: Load vs. Displacement

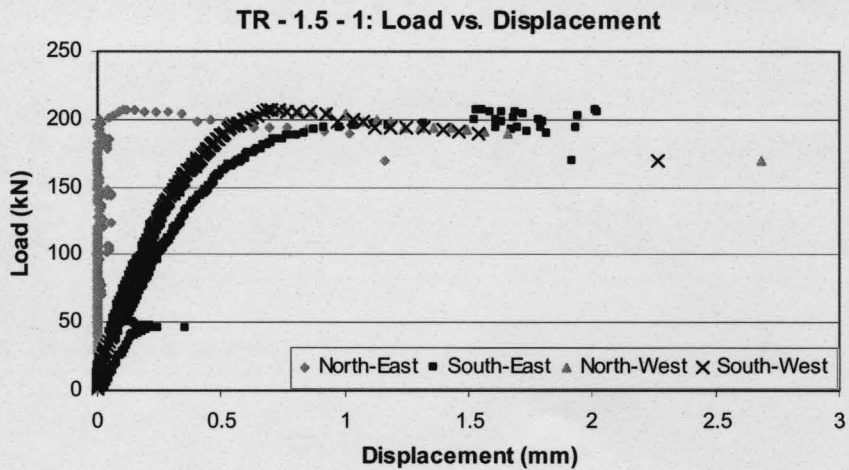
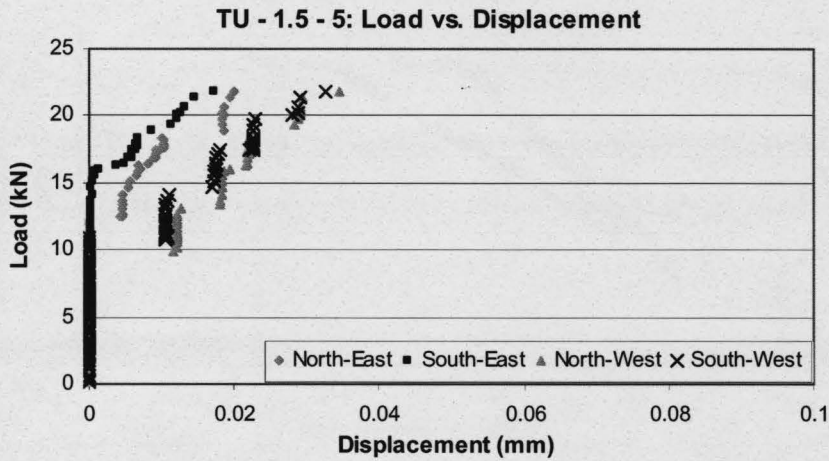
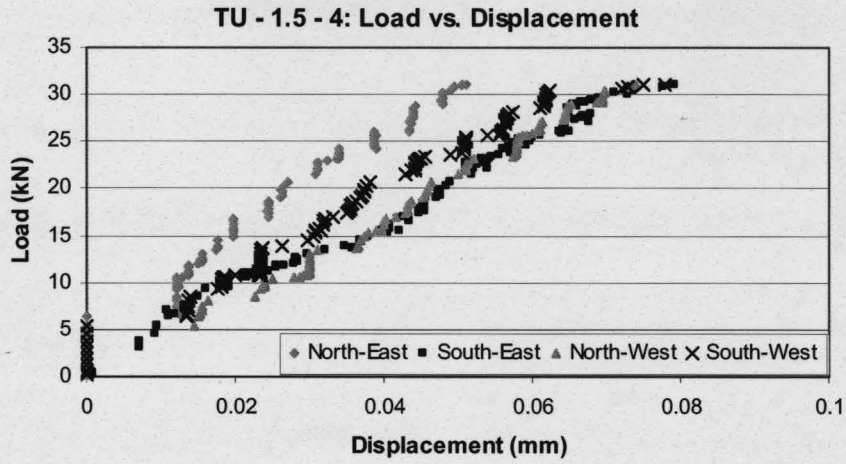


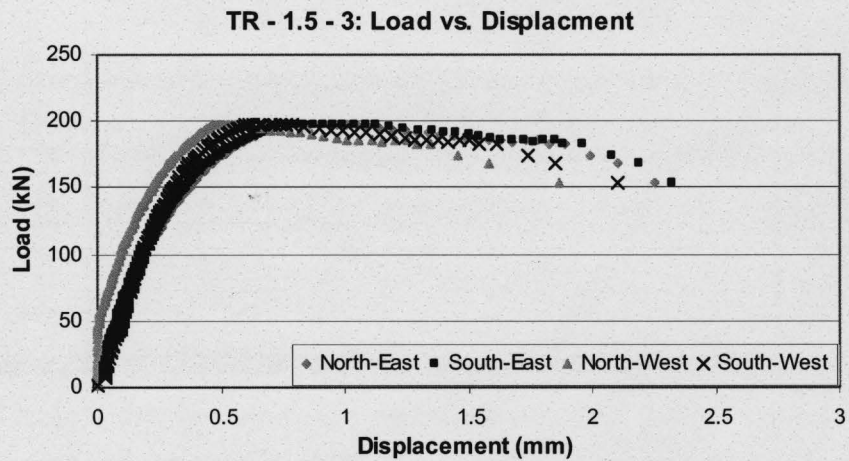
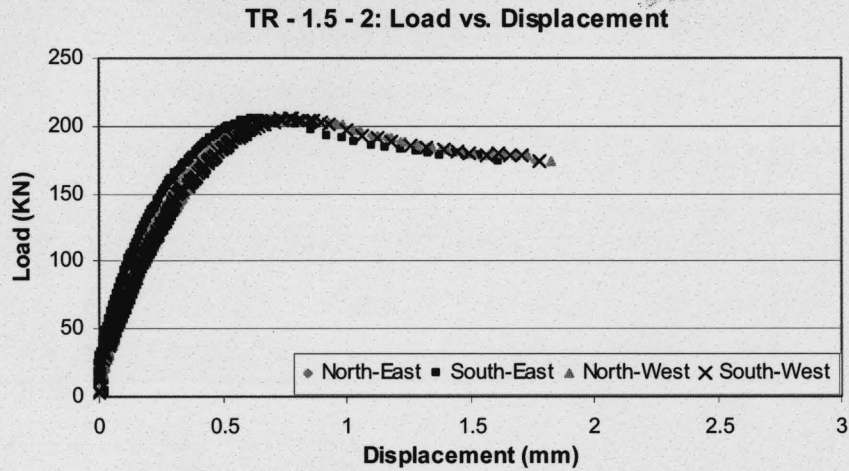








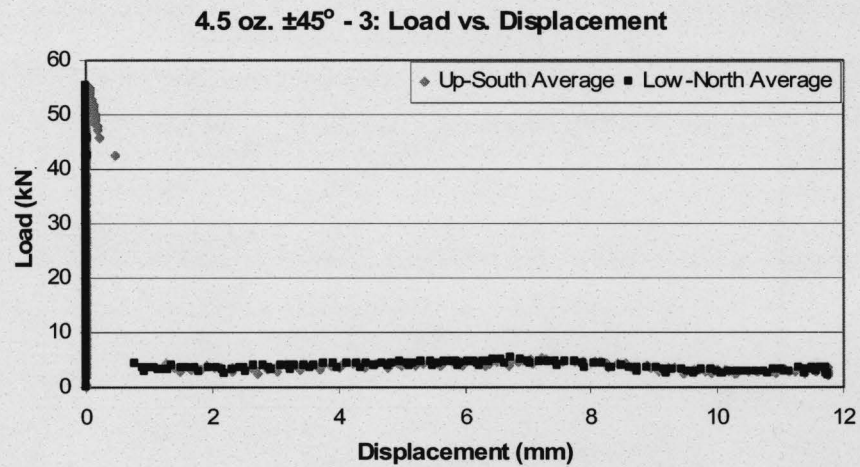
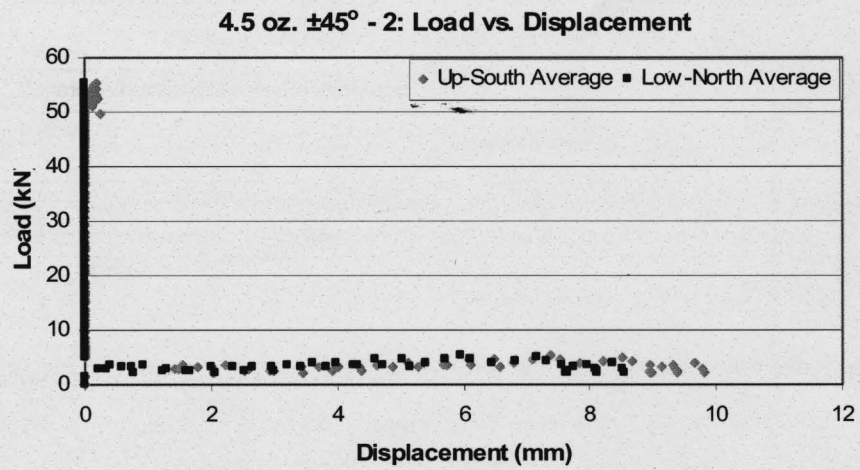
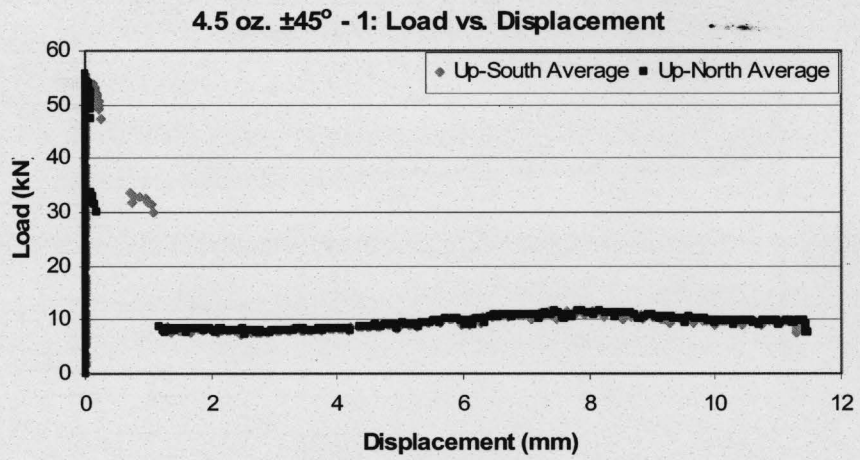




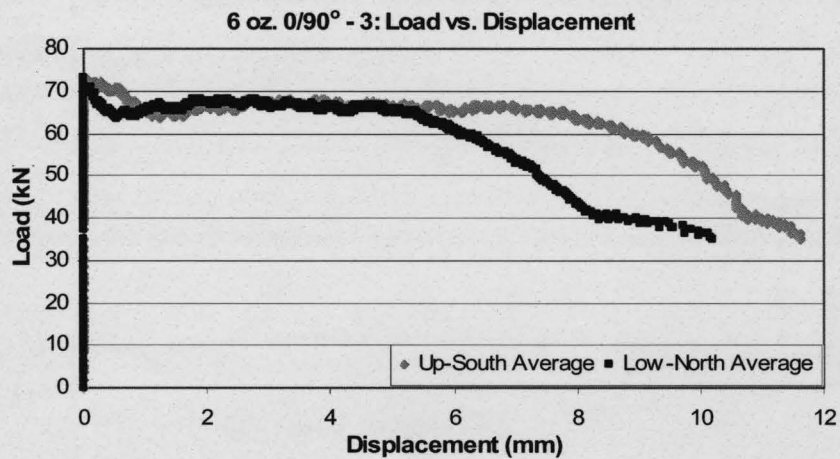
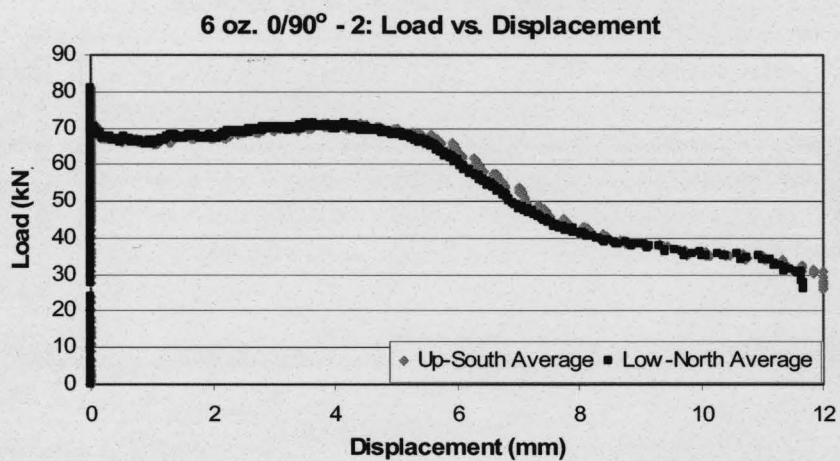
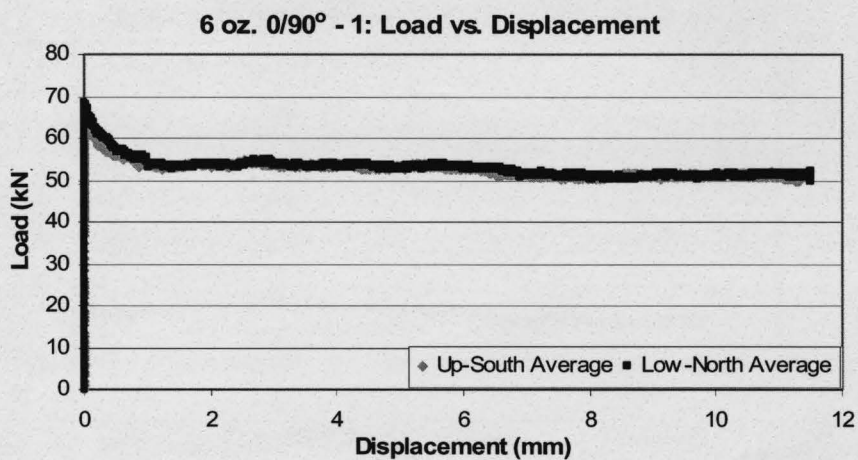
### C.3 PHASE THREE RAW DATA

Table C.2 – Phase Three Table of Contents

Specimen	Page	Specimen	Page	Specimen	Page
4.5 oz. 0°/90° – 1	176	6 oz. 0°/90° – 2	178	9 oz. 0°/90° – 3	180
4.5 oz. 0°/90° – 2	176	6 oz. 0°/90° – 3	178	9 oz. ±45° – 1	181
4.5 oz. 0°/90° – 3	176	6 oz. ±45° – 1	179	9 oz. ±45° – 2	181
4.5 oz. ±45° – 1	177	6 oz. ±45° – 2	179	9 oz. ±45° – 3	181
4.5 oz. ±45° – 2	177	6 oz. ±45° – 3	179	12 oz. 0°/90° – 1	182
4.5 oz. ±45° – 3	177	9 oz. 0°/90° – 1	180	12 oz. 0°/90° – 2	182
6 oz. 0°/90° – 1	178	9 oz. 0°/90° – 2	180	12 oz. 0°/90° – 3	182

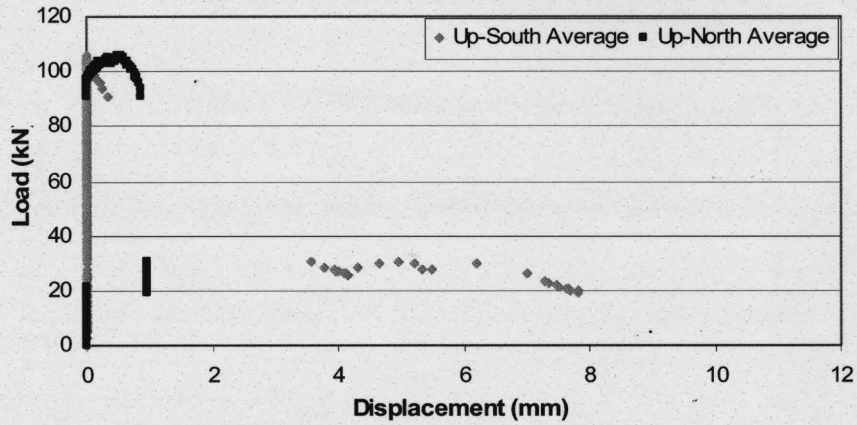




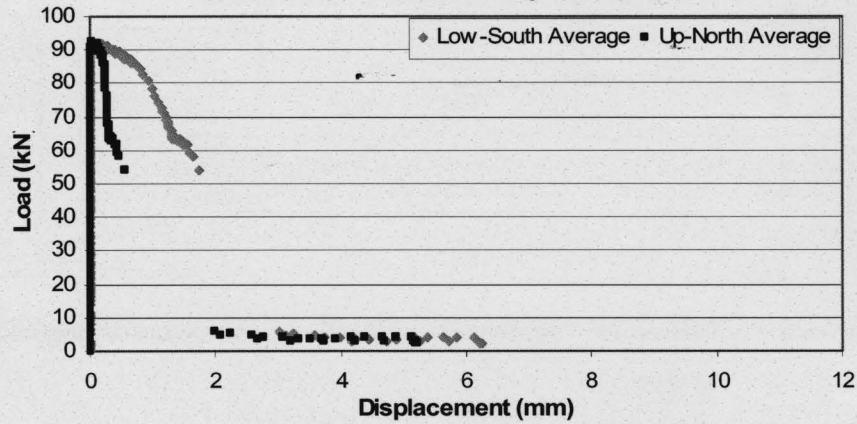




6 oz.  $\pm 45^\circ$  - 1: Load vs. Displacement



6 oz.  $\pm 45^\circ$  - 2: Load vs. Displacement



6 oz.  $\pm 45^\circ$  - 3: Load vs. Displacement

